CFD Modeling and Analysis of an Arc-jet facility using ANSYS Fluent

A Project

Presented to

The Faculty of the Department of Mechanical and Aerospace Engineering of

San José State University

In Partial Fulfillment

of the Requirements for the degree of

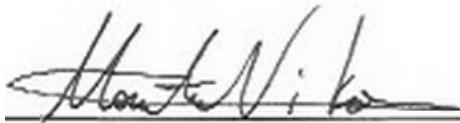MASTER OF SCIENCE IN AEROSPACE ENGINEERING

by

Srikrishna C. Srinivasa

May 2012

The Designated Project Committee Approves the Project Titled

CFD Modeling and Analysis of an Arc-jet facility using ANSYS Fluent

By

Srikrishna C. Srinivasa

APPROVED FOR THE DEPARTMENT OF MECHANICAL AND AEROSPACE
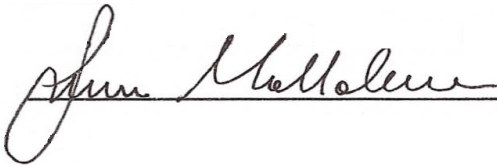ENGINEERING

SAN JOSÉ STATE UNIVERSITY

MAY 2012

Dr. Nikos J. Mourtos, Committee Chair   Date

Department of Mechanical and Aerospace Engineering

San José State University

Dr. Luca Maddalena, Committee Research Advisor   Date

Aerodynamic Research Center

University of Texas at Arlington

Marcus S. Murbach, Committee Member   Date

NASA Ames Research Center

CFD Modeling and Analysis of an Arc-jet facility using ANSYS Fluent

Srikrishna C. Srinivasa

Graduate Student, San José State University, San Jose, CA-95192.

This project attempts to develop a CFD model to support the study of aerothermodynamic features of a 1.6 MW Arc-jet wind tunnel facility. The flow field along the nozzle, test section and surface of the Thermal Protection System (TPS) specimen were modeled using ANSYS-Fluent CFD code. Chul Park's Five- Species Model was adapted in order to account the reactive nature of the flow. The CFD grids used in the project were 2D- axisymmetric and were developed using the popular Gambit 2.2.30 and ESI- Geom codes. The theoretical calculations associated with the chemistry of the problem were performed using NASA CEA code. An equation for determining theoretical convective heat flux was derived in terms of wall temperature, using Fay-Riddell approximation. The target of the project is to determine the magnitude of aerothermodynamic parameters at the exit of the nozzle and the stagnation region in front of the TPS specimen. The CFD model for the test section with specimen failed to converge due to the poor grid quality as well as the complexity of the flow near the stagnation region. The reactive nature of the flow, inadequate computational capability, and shock-shock interaction observed right after nozzle exit, increased the complexity in modeling the flow in the test section.

However, advanced CFD analysis of the nozzle for one case using air as the material and three cases with N2 only. The new nozzle grid consisted of a boundary layer mesh that was modeled using the y+ near wall modeling technique. The flow parameters at the nozzle exit obtained from the CFD analysis were in close agreement with the theoretical approximations. The flow was found to be frozen between the throat and the exit along the divergent part of the nozzle. A boundary layer analysis was performed along the wall of the nozzle near the exit of the nozzle. The thickness of the velocity boundary layer was found to be 0.3443 mm and 0.4406 mm for air and all the N2 cases respectively. The thermal boundary layer for all the cases was found to be around 0.5 mm . The project concludes with a proposal of grid independence studies and inclusion of TPS specimen material properties for the accurate modeling of the problem backed up with higher computational capabilities.

Acknowledgements

Srikrishna Chittur Srinivasa

MS-Aerospace Engineering, San José State University

CFD Modeling and Analysis of an Arc-jet facility using ANSYS Fluent

Final Project Report- Spring 2012

5/28/2011

Submitted in Partial Fulfillment towards

AE 295 Aerospace Engineering Project

Department of Mechanical and Aerospace Engineering

San José State University

Project Committee

Dr. Nikos J. Mourtos, Committee Chair

Professor & Director, Aerospace Engineering Program, SJSU.

Dr. Luca Maddalena, Committee Research Advisor

Aerodynamic Research Center, UT- Arlington.

Marcus S. Murbach, Committee Member

Research Engineer, NASA Ames Research Center, California.

Table of Contents

List of Figures:

List of Tables:

Introduction

"Scientists discover the world that exists; engineers create the world that never was."

— Theodore Von Karman. [28]

Space vehicles that enter a planetary atmosphere require the use of a thermal protection system (TPS) to protect them from aerodynamic heating. The aerodynamic heating is generated at the surface of an entering object due to the combination of compression and surface friction of the atmospheric gas. The vehicle's configuration and entry trajectory in combination with the type of thermal protection system used define the temperature distribution on the vehicle. Improvements to these materials have been the subject of much research as enhanced capability material (i.e., more durability, higher temperature capability, greater thermal shock resistance and lower thermal conductivity) improves thermal protection material and vehicle performance. Future reentry vehicles capabilities will depend upon the capabilities of TPS being developed and made available to them. [22]

An Arc-jet facility is used to simulate the aerothermodynamic heating environment that a spacecraft endures throughout atmospheric entry, study the flow features of high temperature flows and test the efficiency of the materials used in building the Thermal Protection System (TPS) of hypersonic space vehicles. The duration of such testing can range from a few seconds to more than an hour, and from one exposure to multiple exposures of the same sample. The stable, relatively long-duration arc-jet operation at high enthalpies creates opportunities for studying complex chemical and thermal interactions that cannot be easily analyzed in impulse facilities. Minimizing thermal protection mass for current, low budget planetary missions is also an important motivation for generally improving the state of knowledge of arc-jet flow stream conditions.

CFD is an important resource for aerospace vehicle design, testing, and development. Investigations into new, or poorly understood, flow problems are often undertaken with a combined experimental and computational approach. Both the experiment and the modeling benefit from the collaboration, since the CFD simulations can evaluate a wide parameter space quickly and efficiently, while the experimental results provide guidance for developing assumptions and improving model fidelity.

1.0 Literature Survey

1.1 History

On February 24th 1949, the pen plotters track the V-2 to an altitude of 100 miles at a velocity of 3500 mph, at which point the WAC Corporal is ignited. The slender upper stage accelerates to a maximum velocity of 5150 mph and reaches an altitude of 244 miles, exceeding by a healthy 130 miles previous record set by a V-2 alone. After reaching this peak, the WAC Corporal noses over and careers back into the atmosphere at over 5000 mph. In so doing, it becomes the first object of human origin to achieve hypersonic flight—the first time that any vehicle has flown faster than five times the speed of sound. [1]

Another significant event that opened up the doors for research and engineering in hypersonic flight was when Major Yuri Gagarin's orbital craft, called Vostok 1, became the world's first spaceship to carry a man onboard into space and orbit the Earth, and safely return. It was found to re-enter the earth's atmosphere at a speed in excess of 25 times the speed of sound! Therefore, on that day, 12 April 1961, Major Yuri Gagarin became the first human being in the history to experience hypersonic flight.[1]

The hypersonic era was further boosted up by the Apollo series which took the field of space exploration to the next level when Apollo 11 became the first manned mission to land on the Moon. The first steps by humans on another planetary body were taken by Neil Armstrong and Buzz Aldrin on July 20, 1969. The astronauts returned to Earth safely though a historic Mach-36 re-entry. The Apollo series paved way for so many other missions dedicated towards achieving and studying hypersonic flights.[1]

The origin of modern thermal protection systems can be traced back to two major technological developments during WW II: the development of the German V-2 rocket and the U.S. atomic bomb. When coupled, the resulting nuclear-tipped ballistic missile capability became the primary strategic objective of the U.S. and U.S.S.R. militaries after WW II and therefore the goal of major development efforts. TPS was a key enabling technology for these missile systems, because without an effective TPS, the nuclear warheads would be unable to survive the heating during the descent phase of their intercontinental trajectory. [5]

Early missile designs had sharp pointed noses and consistently failed during reentry conditions due to the high heat load and lack of a suitable TPS material. Viable reentry vehicles became possible

only after two innovations. The first was proposed by H. Julian Allen at the Ames Aeronautical Laboratory and consisted of the counter-intuitive blunt body concept, wherein much of the heat load was deflected away from the vehicle via a strong bow shock wave. The second innovation was ablative TPS, which protects the vehicle via thermochemical phenomena including: 1) an ablation process that lifts the hot shock layer gas away from the vehicle, 2) heat being absorbed by the ablative material and leaving the vehicle as the material ablates away, and 3) the creation of a char layer, which is an effective insulator and also effective at blocking radiated heat from the shock layer. Essentially, the blunt body concept coupled with ablative materials is designed to deflect, reject, and reradiate the heat load - not absorb it. [5]

President Kennedy's call for a manned Lunar mission in 1961 resulted in a massive increase in funding for ablative TPS development. Similarly, military reentry vehicles utilized the blunt body concept and ablative TPS approach, even though those flight profiles and heating environment were very different from the Apollo missions. [5]

NASA and military mission requirements led to a rapid development of practical ablative thermal protection materials. Carbon or silica based materials infused with phenolic resin composites proved to be the most suitable candidate materials for many missions. Silica based composites were found to be more efficient at lower heat fluxes (or lower entry speeds) due to lower thermal conductivity and carbon based systems, with a significantly higher temperature capability, were found to be more suitable for higher heat flux entries. [5]

There were two other critical components in the development of viable thermal protection systems in the 1960s: 1) the development of hypersonic ground test facilities including arc-jets, shock tubes, and ballistic ranges, and 2) the development of analytical models and codes that predict the aerothermal environment during entry (both convective and radiative) and the thermal and ablation response of candidate TPS materials. [5]

During the 1960s and into the mid-70s, the ablative TPS community in the U.S. was very active. However, by the late 1970s, the research, development, and testing of ablative TPS materials significantly declined as the nuclear missile programs were completed and the Apollo program was terminated after a dozen Lunar return flights. NASA shifted its focus to the Space Shuttle program that was designed to be a reusable system, including the TPS. While reusable TPS research, development and testing occurred in the late 1970s and through the 1980s, the ablative TPS community saw a

serious decline in capability. [5]

The NASA Ames Arc Jets began in the 1950's with the founding of a permanent facility in 1961. A breakthrough patented design in 1964 by Stein, Shepard and Watson of NASA Ames produced a high-enthalpy constricted-arc heater, which enabled TPS development for Mercury and Apollo missions. The Ames Arc Jet Complex enhanced the development and testing of Thermal Protection System (TPS) for every NASA Space Transportation and Planetary program including Apollo, Space Shuttle, Viking, Pioneer-Venus, Galileo, Mars Pathfinder, Stardust, NASP, X-33, X-34, SHARP-B1 and B2, and most recently X-37 and Mars Exploration Rovers. [24]

Such a history has fostered the growth of extensive local expertise in the development and refinement of the arc jet facilities.

1.2 The Facility:

A 1.6 MW Arc Jet Wind Tunnel is used to produce supersonic streams of extremely hot gas at the Aerodynamic Research Center (ARC) in University of Texas at Arlington. This high enthalpy facility consists of a nitrogen injection system, a water cooling system, a vacuum system, a probe traverse system, a facility monitoring and protection system. The facility is based on a Thermal Dynamics F-5000 arc heater, donated from the USAF Arnold Engineering Development Center, which is powered by a Halmar 1.6 MW DC power supply. [25]

The gas flowing through the arc jet is heated by a powerful electric arc to produce a gas stream with bulk temperatures ranging from 3000 to 5000 K. This high temperature gas is used to test the efficiency of the materials used in building the Thermal Protection System (TPS) of hypersonic space vehicles. A cropped conical specimen made of TPS material is placed very close to the exit of the divergent nozzle so that the high temperature gas impinges on directly on the specimen for an average test run period of 120 seconds. Hence this procedure simulates the hypersonic reentry environment around the test specimen for a short duration. [25]

Fig.1.1: Arc jet at Aerodynamic Research Center of UT-Arlington: The picture above was taken several years ago where the arc jet is not directly connected to the test section chamber. [25]

1.3 The Boundary Layer Theory:

1.3.1 History:

The boundary layer theory was first presented by Ludwig Prandtl in 1904 at the Third International Mathematical Congress at Heidelberg, Germany. This revolutionary paper was titled "Ueber Flussigkeitsbewegung Bei Sehr Kleiner Reibung" (Fluid Flow in Very Little Friction). Prandtl's boundary layer theory contributed to an understanding of skin friction drag and how streamlining reduces the drag experienced by airplane wings and other moving bodies. Prandtl examined the drag that resulted from friction that was created when a fluid such as air passed over an object's surface. [26]

1.3.2 Introduction:

As a fluid moves past over a surface, the molecules right next to the surface stick to the surface. The molecules just above the surface are slowed down as a result of their collisions with the molecules sticking to the surface. These molecules in turn slow down the flow just above them. The number of collisions reduce in the direction perpendicular to the surface. Thus the flow is less disturbed as one moves away from the surface. This creates a thin layer of fluid with a velocity gradient near the surface. This region is known as the **boundary layer.** [8]

Some of the salient features of boundary layers are as follows:

- ⌃ It is a thin region of flow adjacent to the surface, where the flow is retarded due to the friction between a solid surface and the fluid traversing over the surface.
- ⌃ Flow velocity at the surface is zero (Slip case is an exception).

 ⋏ Temperature of the fluid particles immediately adjacent to the surface is same as the temperature of the surface i.e., the wall temperature.

 ⋏ The pressure remains constant in the direction normal to the surface. [8]
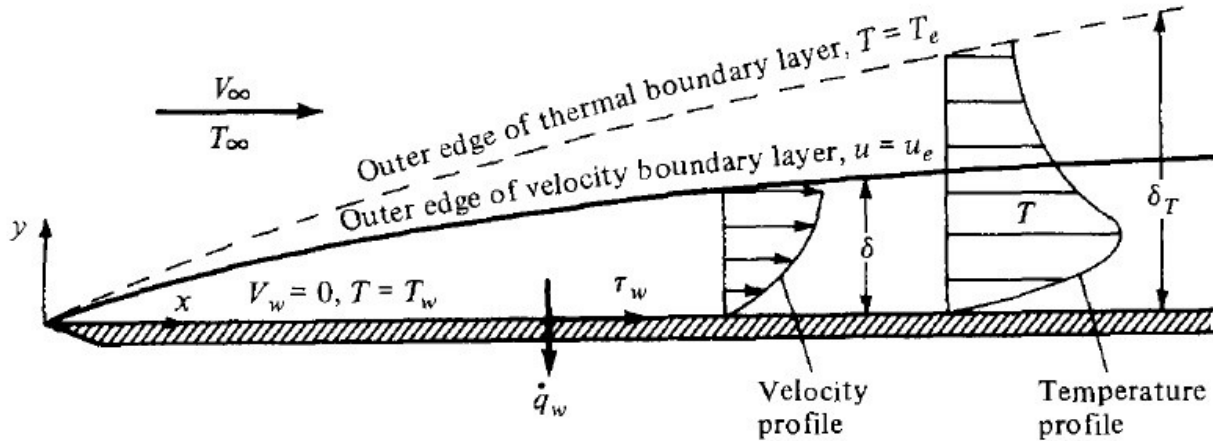
Fig.1.2: Velocity and Temperature profiles of a boundary layer on a flat plate at Pr <1. [8]

1.3.3 Velocity Boundary Layer or Momentum Boundary Layer:

It is characterized by a velocity profile that starts with a zero velocity at the surface and ends up with a velocity equal to 99% of the freestream velocity at the edge of the boundary layer in a direction perpendicular to the wall. The quantities used to describe a velocity boundary layer are:

 ⋏ Velocity Boundary Layer Thickness: It is the perpendicular distance from the surface of the object to the edge of the velocity boundary layer. It increases with the distance from the leading edge along the x-direction. It is denoted by δ.

 ⋏ Displacement Thickness: It is the height by which the streamline is displaced upwards due to the presence of a boundary layer. It is denoted by δ^* . This quantity actually leads us to the concept of effective body. Displacement thickness formula is given by

$$\delta^* \equiv \int_0^{y_1} \left(1 - \frac{\rho u}{\rho_e u_e}\right) dy$$

➤ Momentum Thickness: It is an index that is proportional to the decrement in momentum flow due to the presence of the boundary layer. It is denoted by θ. It is computed using

$$\theta = \int_0^\infty \frac{\rho(y)u(y)}{\rho_0 u_o}\left(1 - \frac{u(y)}{u_o}\right)dy$$
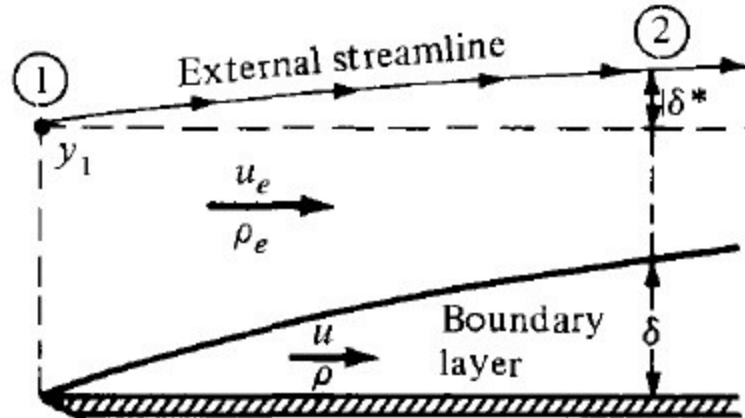
Fig.1.3: Velocity boundary layer thickness and displacement thickness. [8]

One of the major consequences of the presence of a velocity gradient at the surface is the generation of shear stress at the surface i.e., wall shear stress. It can be estimated using (du/dy)ᵥ represents the velocity gradient at the wall and μ is the coefficient of dynamic viscosity. [8]

$$\tau_w = \mu \left(\frac{\partial u}{\partial y}\right)_w$$

1.3.4 Temperature Boundary Layer or Thermal Boundary Layer:

It is characterized by a temperature profile that starts with the wall temperature at the surface and ends up with a Temperature equal to 99% of the edge Temperature of the boundary layer in a direction perpendicular to the wall. The thermal boundary layer is characterized by :

➤ Thermal Boundary Layer Thickness: It is the perpendicular distance from the surface of the object to the edge of the thermal boundary layer. It increases with the distance from the leading edge along the x-direction. It is denoted by δ_T.

➤ Heat Flux: One of the major consequences of the presence of a temperature gradient at the

surface is the generation of heat flux at the surface i.e., wall heat flux. It can be estimated using

$$\dot{q}_w = -k \left(\frac{\partial T}{\partial y} \right)_w$$

$(dT/dy)_w$ represents the temperature gradient at the wall and k is the thermal conductivity. [8]

1.3.5 Relation between δ and δ_T:

In general, δ and δ_T are not equal to each other. The relative thickness depend on the prandtl number. It can be shown that if Pr = 1, then $\delta = \delta_T$; if Pr > 1, then $\delta > \delta_T$; if Pr < 1, then $\delta < \delta_T$. However, when we are considering air at satndard conditions, the Prandtl number would be equal to 0.71 and hence the thermal boundary layer is usually thicker than the velocity boundary layer as shown in Fig.1.2. [8]

1.4 Hypersonics:

While the definition of hypersonic flow can be quite vague and is generally debatable (especially due to the lack of discontinuity between supersonic and hypersonic flows), a hypersonic flow may be characterized by certain physical phenomena become progressively important as the Mach number increases. The significant features of hypersonic flows are as follows: 1. Shock layer; 2. Aerodynamic heating; 3. Entropy layer; 4. Real gas effects; 5. Low density effects; 6. Mach number independence. [1]

1.4.1 Thin Shock Layers:

Students of aerodynamics know that when a supersonic flow passes over a wedge, a shock wave will form at the point of the wedge. This kind of shock wave is called an oblique shock because it forms at some angle to the surface of wedge (a shock wave perpendicular to the surface is known as a normal shock). As the Mach number increases, the shock angle becomes smaller, as illustrated in the figure below. Therefore, the distance between the wedge surface and the shock decreases with increasing speed. For a hypersonic body, this distance can become very small over a large portion of the body, and the resulting flowfield between the surface and shock is often referred to as a shock layer. This thin layer can produce many complications in vehicle design, e.g. the shock layer may merge with the boundary layer at low Reynolds numbers to form a fully viscous shock layer. [1]
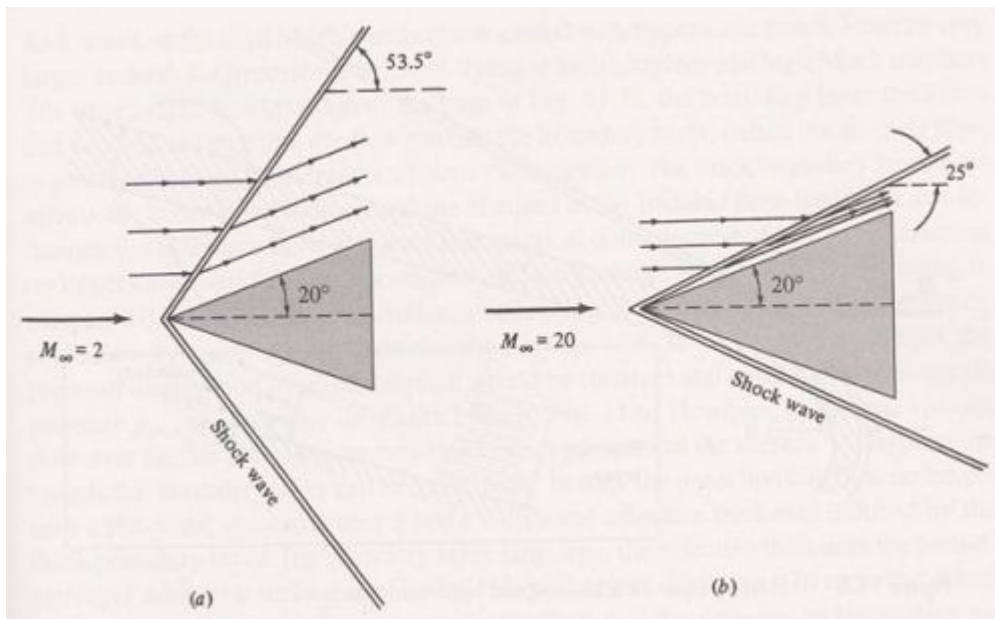
Fig.1.4.: Shock waves and streamlines over a 20° half-angle wedge at (a) Mach 2 and (b) Mach 20 [1]

At high Reynolds numbers, the shock layer can be treated as inviscid (meaning there is no friction). In the limit as Mach number goes to infinity, the shock layer forms an infinitely thin, infinitely dense sheet, or, essentially, a flat plate. The infinite flat plate is the most efficient lifting surface at hypersonic velocities, and the inviscid shock layer can therefore be used to develop simplified theories to predict hypersonic aerodynamic properties. [1]

1.4.2 Entropy Layer:

The previous discussion related to an oblique shock formed over an ideal wedge with a perfectly sharp leading edge. In practical applications, however, the leading edge must be rounded or blunted in some way both for practicality of manufacture and to ease heat fluxes. Close to this blunt leading edge, the oblique shock becomes highly curved. Shock theory tells us that entropy increases across a shock, and the entropy increase becomes greater as the shock strength increases. Since flow near the nose passes through a nearly normal shock, it will experience a much greater change in entropy compared to flow passing through the much shallower shock angle further from the body centerline. Thus, strong entropy gradients exist near the leading edge generating an "entropy layer" that flows downstream along the body surface. [1]
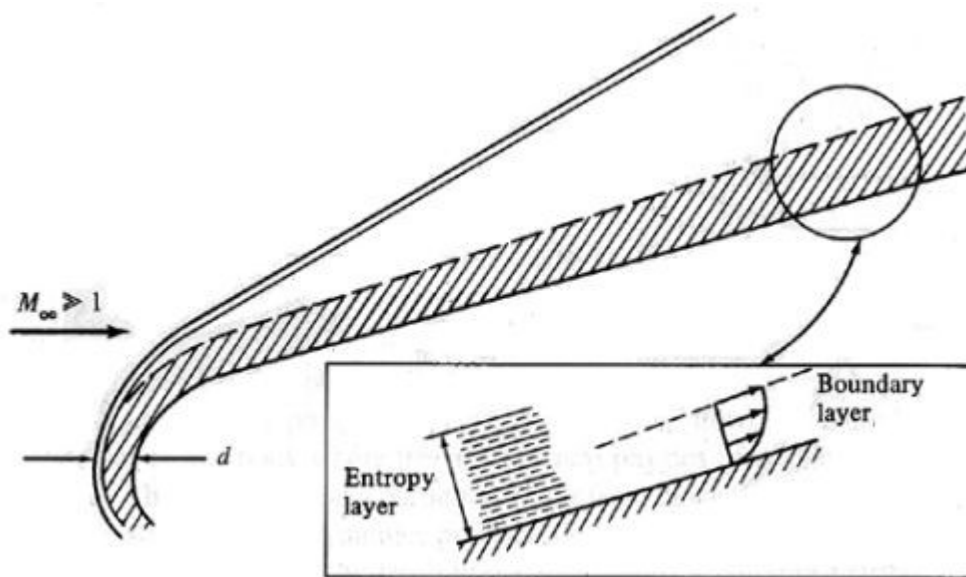
Fig.1.5: Entropy layer formation [1]

The classical boundary layer grows within this entropy layer and may be greatly affected by the entropy gradients. In addition, the entropy layer is a region of strong vorticity that can generate large gradients in the velocity flowfield near the surface, a phenomenon called "vorticity interaction." The large velocity and thermodynamic gradients induced by the sharply curved oblique shock become troublesome when attempting to predict aerodynamic performance, heat transfer results, and boundary layer shape for a hypersonic vehicle. [1]

1.4.3 Viscous Interaction:

When a body travels through the air, a thin region near the body surface called the "boundary layer" is formed. In this layer, the air slows down from the "freestream" velocity of the airflow to zero at the surface. At subsonic speeds, the thickness of the boundary layer tends to become smaller as velocity increases because the thickness is inversely proportional to the Reynolds number:

$$\delta \propto \frac{x}{\sqrt{Re_x}}$$

For compressible flow (or flow at high speeds), however, increasing flow temperature (due to

friction heat) near the body surface causes the boundary layer to become thicker as speed increases. The two primary factors driving this boundary layer growth are an increase in viscosity of the fluid and a decrease in density. The result of these factors is that boundary layer thickness varies as the square of the Mach number: [1]

$$\delta \propto \frac{M^2}{\sqrt{Re_x}}$$

Thus, as Mach number increases, the boundary layer can grow rapidly resulting in very high drag. Should the boundary layer become thick enough, it may affect the inviscid flowfield far from the body, a phenomenon called viscous interaction. Viscous interaction can have a great influence on the surface pressure distribution and skin friction on the body thereby affecting the lift, drag, stability, and heating characteristics of the body. [1]

1.4.4 High Temperature Flow:

As mentioned before, travel at high velocities produces friction and heat. Part of the kinetic energy of the body's motion is absorbed by the air and carried away from the body through a process called viscous dissipation. However, hypersonic vehicles create so much heat and such high temperatures that they can actually cause chemical changes to occur in the fluid through which they fly. The most notable changes air undergoes as temperature increases are summarized below.

Temperature [K]	Chemical Change
800	Molecular vibration
2000	Oxygen molecules (O_2) dissociate
4000	Nitrogen molecules (N_2) dissociate
	Nitric oxide (NO) forms
9000	Oxygen and nitrogen atoms ionize

Table.1.1: High Temperature Effects on Air [1]

As temperature increases, assumptions about the properties of the air are no longer valid and the

vehicle is said to be traveling through a chemically reacting boundary layer. When the properties (density and heat transfer properties) of the working fluid change, the aerodynamic characteristics and heating properties of the body can change drastically. [1]

1.4.5 Low Density Flow:

Although the properties of low density flow are not necessarily applicable to hypersonic flight, most hypersonic vehicles are intended to cruise at high altitudes in low density fluids. Therefore, these flow conditions are often important in waverider design. In low density flows, air can no longer be considered to be a continuum because the distance between individual particles of air becomes so great that each particle begins to affect the aerodynamic properties of a body. Under these conditions, common aerodynamic relations, like the Euler and Navier-Stokes equations, break down. Instead, aerodynamic properties must be analyzed using kinetic theory. Some of the most important differences between low density flows and continuous flows include

- Velocity slip: The viscous no-slip condition that says the velocity of air particles going past a body must be zero at the body surface, fails. Since friction is negligible in low density, the flow velocity at the body surface is no longer zero.
- Temperature slip: The assumption that gas temperature at the body surface becomes equal to the temperature of the body surface material fails.

Most equations derived from the continuum assumption can still be used once these slip conditions begin to take effect so long as correcting terms are added. Eventually, however, density becomes so small that fluid particles interact only with the vehicle itself and do not impact each other. In this free-molecule flow, flow structure becomes poorly defined and shocks are thick and indistinct. The aerodynamic and thermodynamic properties of the vehicle are affected at the molecular level. For example, the following figure indicates how greatly the drag coefficient of a sphere can vary when transitioning from a continuum flow to a free-molecule flow (where Kn is the Knudson number, a nondimensional parameter related to the distance between molecules). [1]
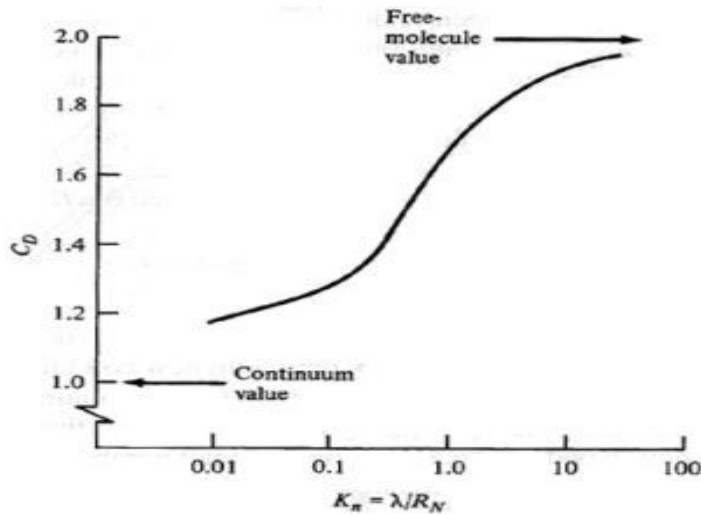
Fig.1.6: Drag coefficient of a sphere at hypersonic speeds transitioning from continuum to free-molecule flow [1]

1.4.6 Mach Number Independence:

At low supersonic Mach numbers Cp decreases rapidly as M_∞ is increased. However, at hypersonic speeds the rate of decrease diminishes considerably, and Cp becomes relatively independent of M_∞ at high Mach numbers. This is the essence of Mach-number independence principle; at high Mach numbers certain aerodynamic quantities such as pressure coefficient, lift, wave drag coefficients, and flowfield structure becomes essentially independent of Mach number. [1]
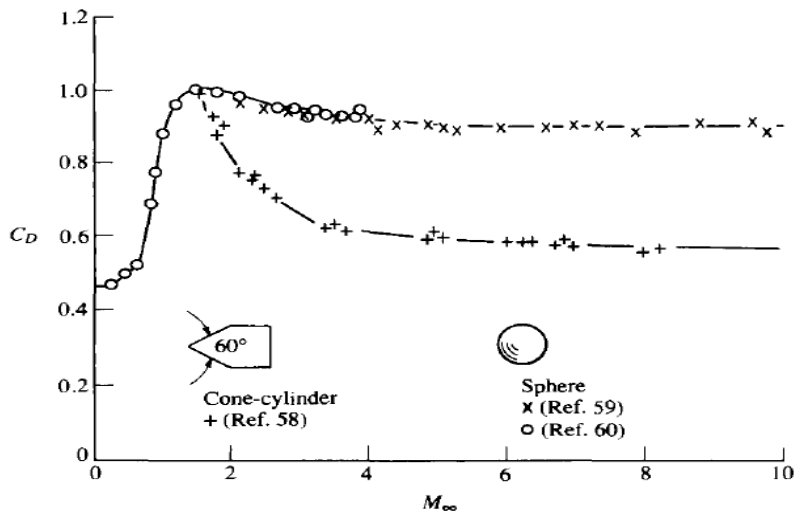
Fig.1.7: Drag coefficient for a sphere and a cone cylinder from ballistic range measurements: an example of mach number independence. [1]

1.5 Two Temperature Kinetic Model:

At a high temperature, energy in a gas is contained in the translational, rotational, vibrational, and electronic modes. If the gas is ionized, the translational energy of electron gas can be very different from that of heavy particle gas. For this reason, the translational energies of the heavy particle gas and the electron gas must be recognized as being different. Also, the vibrational energies can be different among different molecules. [3]

The energy contained in any mode in any atom or molecule is usually designated by its temperature. In a thermochemically nonequilibrium gas mixture, the temperatures that characterize these different modes of energy can be different from each other. That is, there can be several characteristic temperatures. In the so-called two-temperature model, one approximates this situation with two main assumptions. First, one assumes that there are only two different temperatures in this situation. The rotational temperature of molecules is assumed to be the same as the translational temperature of heavy particles. Vibrational temperatures of all molecules are assumed to be the same as electron temperature and electronic temperature. [3]

$$T_r = T \equiv T_{tr}, \ T_{v1} = T_{v2} = ... = T_e = T_{el} \equiv T_{ev} \ (1)^{[3]}$$

Second, the forward and reverse rate coefficients kf and kr for the chemical reactions involving molecules are assumed to be a function of a geometrically averaged temperature T_a. [3]

$$T_a = (T_{tr}T_{ev})^{1/2} \ \ (2)^{[3]}$$

$$k_f = f(T_a), \ k_r = g(T_a). \ \ (3)^{[3]}$$

There is an extension of Eq. (2) in the form [3]

$$T_a = T_{tr}^{s} T_{ev}^{1-s}$$

1.7 The Park Model:

Since the safer operating temperature of the above mentioned arc-jet facility does not exceed 9000K, the working gas does not get to reach the ionization phase. Hence, a five species model (O_2, N_2, NO, N, O) for high temperature non equilibrium reactions, proposed by Dr. Chul Park, can be chosen for the chemical modeling of the arcjet flow. The Five Species Park Model gives out finite values for Arrhenius coefficient, exponential coefficient and activation energy required to model 15 different dissociation reactions and two exchange reactions. [2]

No.	Reaction	Reaction Energy, kcal/mole	Recommended Rate Expression, $cm^3 mole^{-1} sec^{-1}$	Remark	Park (Ref. 10)
1	$O_2+O_2 \rightarrow O+O+O_2$	118.1	$2\times10^{21} T_a^{-1.5} exp(-59,500/T_a)$		$9.68\times10^{22} T_a^{-2} exp(-59,500/T_a)$
2	$O_2+NO \rightarrow O+O+NO$	118.1	$2\times10^{21} T_a^{-1.5} exp(-59,500/T_a)$	Estim	$9.68\times10^{22} T_a^{-2} exp(-59,500/T_a)$
3	$O_2+N_2 \rightarrow O+O+N_2$	118.1	$2\times10^{21} T_a^{-1.5} exp(-59,500/T_a)$		$9.68\times10^{22} T_a^{-2} exp(-59,500/T_a)$
4	$O_2+O \rightarrow O+O+O$	118.1	$10^{22} T_a^{-1.5} exp(-59,500/T_a)$		$2.90\times10^{23} T_a^{-2} exp(-59,500/T_a)$
5	$O_2+N \rightarrow O+O+N$	118.1	$10^{22} T_a^{-1.5} exp(-59,500/T_a)$	Estim	$2.90\times10^{23} T_a^{-2} exp(-59,500/T_a)$
6	$NO+O_2 \rightarrow N+O+NO$	162.5	$5\times10^{15} exp(-75,500/T_a)$		$7.95\times10^{23} T_a^{-2} exp(-75,500/T_a)$
7	$NO+NO \rightarrow N+O+NO$	162.5	$1.1\times10^{17} exp(-75,500/T_a)$		$7.95\times10^{23} T_a^{-2} exp(-75,500/T_a)$
8	$NO+N_2 \rightarrow N+O+N_2$	162.5	$5\times10^{15} exp(-75,500/T_a)$		$7.95\times10^{23} T_a^{-2} exp(-75,500/T_a)$
9	$NO+O \rightarrow N+O+O$	162.5	$1.1\times10^{17} exp(-75,500/T_a)$		$7.95\times10^{23} T_a^{-2} exp(-75,500/T_a)$
10	$NO+N \rightarrow N+O+N$	162.5	$1.1\times10^{17} exp(-75,500/T_a)$		$7.95\times10^{23} T_a^{-2} exp(-75,500/T_a)$
11	$N_2+O_2 \rightarrow N+N+O_2$	225.1	$7\times10^{21} T_a^{-1.6} exp(-113,200/T_a)$	Estim	$3.70\times10^{21} T_a^{-1.6} exp(-113,200/T_a)$
12	$N_2+NO \rightarrow N+N+NO$	225.1	$7\times10^{21} T_a^{-1.6} exp(-113,200/T_a)$	Estim	$4.98\times10^{21} T_a^{-1.6} exp(-113,200/T_a)$
13	$N_2+N_2 \rightarrow N+N+N_2$	225.1	$7\times10^{21} T_a^{-1.6} exp(-113,200/T_a)$		$3.70\times10^{21} T_a^{-1.6} exp(-113,200/T_a)$
14	$N_2+O \rightarrow N+N+O$	225.1	$3\times10^{22} T_a^{-1.6} exp(-113,200/T_a)$	Estim	$4.98\times10^{21} T_a^{-1.6} exp(-113,200/T_a)$
15	$N_2+N \rightarrow N+N+N$	225.1	$3\times10^{22} T_a^{-1.6} exp(-113,200/T_a)$		$1.60\times10^{22} T_a^{-1.6} exp(-113,200/T_a)$
17	$N_2+O \rightarrow NO+N$	75.19	$6.4\times10^{17} T^{-1} exp(-38,370/T)$		$6.4\times10^{17} T^{-1} exp(-38,370/T)$
18	$NO+O \rightarrow O_2+N$	31.83	$8.4\times10^{12} exp(-19,450/T)$		$8.4\times10^{12} exp(-19,450/T)$

Table.1.2: Park's five species chemical model [2]

1.8 CFD Modeling and Analysis:

Computational fluid dynamics, usually abbreviated as CFD, is a branch of fluid mechanics that uses numerical methods and algorithms to solve and analyze problems that involve fluid flows. Computers are used to perform the calculations required to simulate the interaction of liquids and gases with surfaces defined by boundary conditions. With high-speed supercomputers, better solutions can be achieved. Ongoing research yields software that improves the accuracy and speed of complex simulation scenarios such as transonic or turbulent flows. Initial validation of such software is performed using a wind tunnel with the final validation coming in flight tests.

CFD is an important resource for aerospace vehicle design, testing, and development. Investigations into new, or poorly understood, flow problems are often undertaken with a combined experimental and computational approach. Both the experiment and the modeling benefit from the collaboration, since the CFD simulations can evaluate a wide parameter space quickly and efficiently, while the experimental results provide guidance for developing assumptions and improving model fidelity.

A major driving force behind arcjet flow modeling is the desire to extract, the most information from tests of thermal protection systems in arcjet facilities. Testing costs are always a concern, and an investment in computational resources to avoid test article failures or to conduct, a more efficient test cycle represents a prudent strategy. Computational investigations can often be undertaken at, lower expense than experimental efforts. Unless a complete computational capability is being started from scratch, the costs of employing state-of-the-art instrumentation for experimental investigations is usually much higher, assuming that manpower for both efforts is equivalent. If more and better information could be obtained from arcjet testing, then substantial development cost savingsmay be realized from a reduced dependence on flight experiments (e.g. FIRE and Apollo) that are often required to establish thermal protection system effectiveness. [14]

2.0 Scope

Minimizing thermal protection mass for current, low budget planetary missions is also an important motivation for generally improving the state of knowledge of arcjet flow stream conditions. For these missions there is neither time nor budget for flight testing a prototype before launching. If results from arc-jet tests can be extrapolated to flight conditions with quantifiable uncertainties, then it may be possible to reduce the design safety margins that currently added to heat-shield thickness. It may ultimately be possible to establish flight performance of thermal protection materials through arc-jet testing if a sufficient understanding of arc-jet flows is developed. CFD modeling would play an indispensable and enabling role in this effort. [14]

Facility improvements and optimization for particular test configurations could also benefit from the development of CFD tools tailored to arc-jet flow modeling. Additional motivation derives from the desire to improve the general state of non-equilibrium flow modeling and the understanding of real gas effect as mentioned above, the stable, relatively long-duration arc-jet operation at high enthalpies creates opportunities for studying complex chemical and thermal interactions that cannot be easily analyzed in impulse facilities.

The details of the boundary layer on the surface of the specimen is a valuable piece of information in arc jet testing. With aid of the CFD modeling, one can obtain the details associated with the boundary layers such as the wall shear stress, heat flux, thickness etc., which are extremely hard to obtain using various instruments and experimental techniques in case of an arc jet due to very high working temperatures. This forms one of the most important advantage and scope of this project.

3.0 <u>Goals and Objectives</u>

The goals of this project are:

⚔ To gain a better understanding of the principles involved in high temperature gas dynamics, boundary layer theory and computational fluid dynamics.

⚔ To demonstrate the application of the fundamental principles in obtaining computational solutions for real time aerothermodynamic problems which are hard to be solved experimentally.

⚔ To demonstrate the understanding of the methods used by CFD solvers such as ANSYS Fluent in our case, to solve the high temperature gas dynamic problems.

Based on the background, literature survey, and the scope, the following are the objectives of the project:

- To obtain CFD solutions for the arcjet model and to validate the solutions with the experimental data obtained from Aerodynamic Research Center of UT-Arlington.

- To investigate the characteristics of the boundary layer on the specimen (Thermal Protection System) by determining the shear stress and heat flux, and comparing those results with that of analytical models.

4.0 Preliminary analysis of the nozzle

4.1 Initial Conditions:

Given test Conditions

- ⚐ Plenum Pressure = Po = Pc = 64.7 Psi
- ⚐ Exit Pressure = Pe = 7 Psi
- ⚐ Given Power = 0.6 MW
- ⚐ Cooling Efficiency = 50%
- ⚐ Final Power Input = P = 0.6*0.5 = 0.3 MW
- ⚐ Mass Flow Rate = 0.123 kg/s

Geometry of the Nozzle

- ⚐ Length of the nozzle = 64mm
- ⚐ Diameter at the chamber = 3 inch = 3*2.54/100 = 0.0762 m
- ⚐ Area of the chamber = A_i = $\pi d^2/4$ = $\pi*0.0762^2/4$ = $4.56*10^{-3}$ m^2
- ⚐ Diameter at the throat = 0.8 inch = 0.8*2.54/100 = 0.02032 m
- ⚐ Area of the throat = A* = $\pi d^2/4$ = $\pi*0.02032^2/4$ = $3.24*10^{-4}$ m^2
- ⚐ Diameter at the exit = 1 inch = 1*2.54/100 = 0.0254 m
- ⚐ Area of the exit = A_o = $\pi d^2/4$ = $\pi*0.0254^2/4$ = $5.067*10^{-4}$ m^2
- ⚐ Subsonic Area Ratio = (A_i / A*) = $4.56*10^{-3}$ / $3.24*10^{-4}$ = 14.074
- ⚐ Supersonic Area Ratio = (A_o / A*) = $5.067*10^{-4}$ / $3.24*10^{-4}$ = 1.5639

Divergent part of the nozzle is conical and hence it is a conical nozzle.

Calculation of other initial conditions

- ⚐ Specific Enthalpy = Final Power input/ Mass Flow Rate = $0.3*10^6/0.123$ = h =2439024.39 J/kg
- ⚐ h/R = 2439024.39 / 8.3144621 = 294.3472257 mol-K/g

4.2 The NASA CEA Code:

The NASA Computer program CEA (Chemical Equilibrium with Applications) calculates chemical equilibrium compositions and properties of complex mixtures. Applications include assigned thermodynamic states, theoretical rocket performance, Chapman-Jouguet detonations, and shock-tube parameters for incident and reflected shocks. CEA represents the latest in a number of computer

programs that have been developed at the NASA Lewis (now Glenn) Research Center during the last 45 years. These programs have changed over the years to include additional techniques. Associated with the program are independent databases with transport and thermodynamic properties of individual species. Over 2000 species are contained in the thermodynamic database. The program is written in ANSI standard FORTRAN-77 by Bonnie J. McBride and Sanford Gordon. It is widely used by the aerodynamics and thermodynamics community. [27]

The NASA CEA code is used in this project to estimate the chemical composition and the flow conditions at the inlet, throat and the exit of the nozzle since the current problem involves chemical reactions at high temperatures apart from regular flow features.

The results obtained from the CEA code are used to initialize the calculations in the CFD model.

4.2.1 Inputs for CEA:

- Type of problem: Rocket

- Plenum pressure = Po = Pc = 64.7 Psi

- Subsonic area ratio = 14.074

- Supersonic area ratio = 1.5639

- Freezing point: Throat

- Reactant = Air
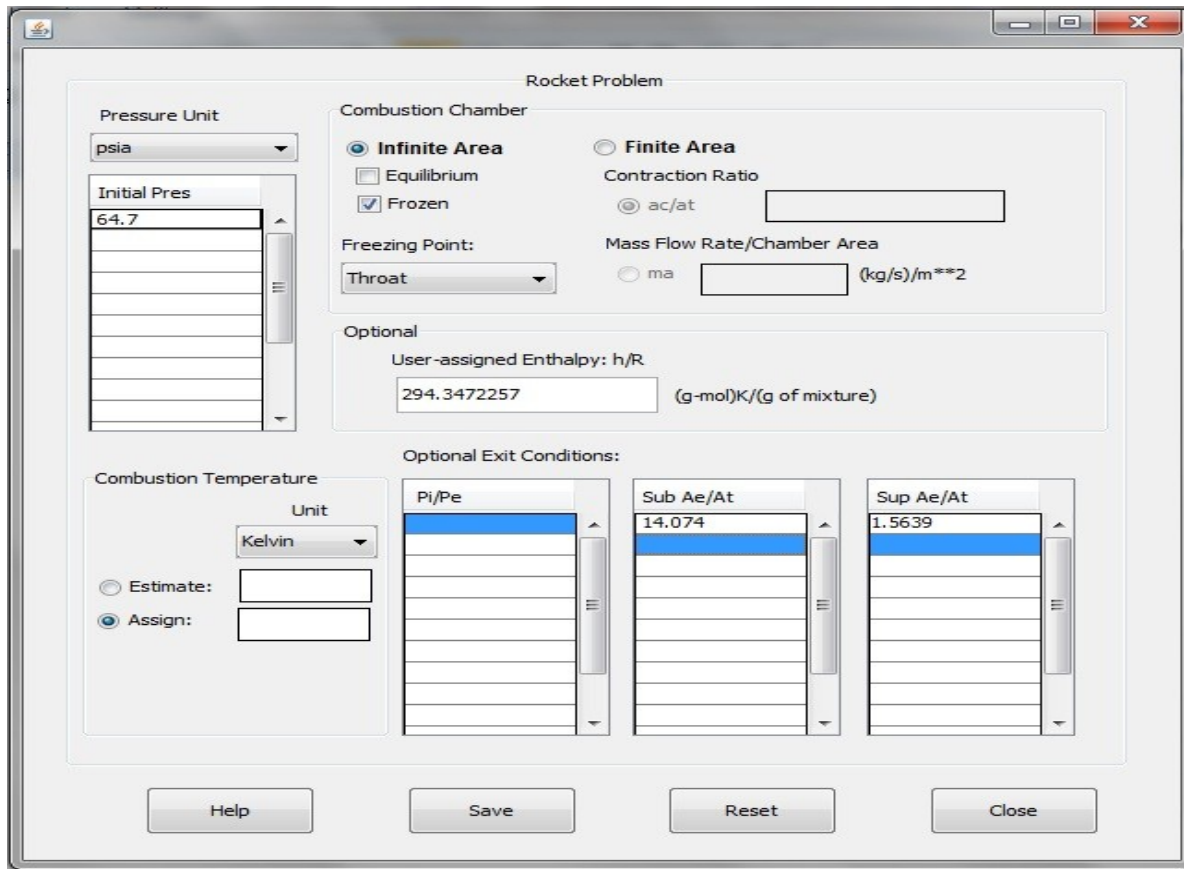
Fig.4.1: Input conditions window in the Rocket problem of CEA

4.2.2 Output obtained from CEA:

	CHAMBER	THROAT	EXIT
Pinf/P	1.0000	1.8167	6.1736
P, BAR	4.4609	2.4555	0.72258
T, K	2343.93	2070.39	1558.39
RHO, KG/CU M	6.6257-1	4.1311-1	1.6150-1
SON VEL,M/SEC	919.1	869.6	765.2
MACH NUMBER	0.000	1.000	1.859

MOLE FRACTIONS

Ar	0.00936	CO2	0.00032	NO	0.00905
NO2	0.00002	N2	0.77618	O	0.00033
O2	0.20473				

Fig.4.2: Output obtained from the CEA code for the given input conditions in our case.

The velocity of the flow at the chamber can be determined by using the density at the chamber obtained from the CEA output. Flow velocity at the chamber is denoted by Vc

Vc = mass flow rate / (density*area)$_{chamber}$ = 0.123 / (0.66257 * 4.56*10^{-3}) = 40.71 m/s

In order to cross check this value of flow velocity, we find out the mach number at the chamber. For any given plenum (chamber) condition, the mach number has to be a very small value.

Mach number at the chamber = Flow velocity / Sonic Velocity (obtained from CEA output)

M_c = 40.71 / 919.1 = 0.044

Since the mach number at the throat is found to be 0.044, this magnitude of flow velocity i.e., 40.71 m/s makes sense. We use this value in initialization process in the CFD model.

4.3 The Grid:

A 2D structured grid for the nozzle was built using ESI-GEOM. Since the geometry of the nozzle is axisymmetric in nature, only one half of the nozzle in a 2D plane needs was considered for CFD modeling. The grid was divided into 9 domains. The grid cells are absolutely rectangular in 7 domains and quadrilaterals with different shapes in the other two domains. The grid can be considered

to have medium fineness level with 67969 cells.

The specifications of the grid are as follows:

Sl. no.	Mesh Property / Parameter	Magnitude
1.	Number of Domains	9
2.	Number of Cells	67969
3.	Number of Nodes	69500
4.	X-min	0
5.	X-max	64 mm
6.	Y-min	0
7.	Y-max	38.1 mm
8.	Points	5217
9.	Curves	25
10.	Edges	25
11.	Faces	9

Table 4.1: Specifications of the 2D mesh of the nozzle

4.4 Inputs for the CFD Model:

1. Type of solver: Axisymmetric, density based, implicit, species, laminar.
2. Species Model:

    ⚹ Species transport- active

    ⚹ Reaction type- volumetric

    ⚹ Backward reactions- active

    ⚹ Reacting Species: Nitrogen (N2), Oxygen (O2), Nitrogen Oxide (NO), Atomic

Oxygen (O), Atomic Nitrogen (N).

⚔ Number of reactions: 5

⚔ Stoichiometric coefficient of reactants : 1

⚔ Rate exponent of reactants: 1

⚔ Stoichiometric coefficient of reactants : 1

⚔ Rate exponent of reactants: 0

Sl. no	Reaction	Pre- exponential factor	Activation energy(J/kg-mol)	Temperature exponent
1.	$O_2 \rightarrow O + O$	9.68e+19	4.9682e+08	-2
2.	$NO \rightarrow N + O$	7.95e+20	6.277e+08	-2
3.	$N_2 \rightarrow N + N$	4.98e+18	9.4126e+08	-1.6
4.	$NO + O \rightarrow N + O_2$	8.37e+09	1.61736e+08	0
5.	$N_2 + O \rightarrow NO + N$	6.44e+14	3.19e+08	-1

Table 4.2: Chemical reactions and magnitude of Arrhenius rate parameters associated with the reactions. (based on Park's 5-species Model [2])

Sl. no	Reaction	Third body efficiency				
		O_2	N_2	NO	N	O
1.	$O_2 \rightarrow O + O$	0.338	0.338	0.338	1	1
2.	$NO \rightarrow N + O$	1	1	1	1	1
3.	$N_2 \rightarrow N + N$	0.0743	0.0743	0.1	0.3218	1
4.	$NO + O \rightarrow N + O_2$	1	1	1	1	1
5.	$N_2 + O \rightarrow NO + N$	1	1	1	1	1

Table 4.3: Third body efficiency of each species associated with the reactions in 5-species Model [2]

3. Materials:

- o Fluid- Air, Water Vapor, Nitrogen (N2), Oxygen (O2), Nitrogen Oxide (NO), Atomic Oxygen (O), Atomic Nitrogen (N).

4. Solid- Copper (Wall)

5. Cell zone conditions

- Fluid reaction

6. Boundary Conditions

- o Wall - Adiabatic

- o Pressure-inlet

⚹	Gauge Total Pressure (pascal)	446090.78
⚹	Supersonic/Initial Gauge Pressure (pascal)	446090.78
⚹	Total Temperature (k)	2343.93
⚹	Axial-Component of Flow Direction	1
⚹	Radial-Component of Flow Direction	0
⚹	Specify Species in Mole Fractions?	yes
⚹	Mole fractions: $O_2 \rightarrow 0.20473$; $N_2 \rightarrow 0.77618$; NO$\rightarrow 0.00905$; O$\rightarrow 0$	

- ⚹ Pressure-outlet

⚹	Gauge Pressure (pascal)	72258
⚹	Backflow Total Temperature (k)	1558.39
⚹	Axial-Component of Flow Direction	1
⚹	Radial-Component of Flow Direction	0
⚹	Specify Species in Mole Fractions?	yes
⚹	Backflow mole fractions: $O_2 \rightarrow 0.18616543$; $N_2 \rightarrow 0.75946699$; NO$\rightarrow 0.018907491$; O$\rightarrow 0$	

7. Solver Settings

- ⚹ Equations to be solved- Flow i.e., Continuity, Momentum and Energy.
- ⚹ Absolute Velocity Formulation- Yes
- ⚹ Convergence criterion $\rightarrow 10^{-3}$
- ⚹ Discretization Scheme- Second Order Upwind
- ⚹ Time Marching

⊀   Solver- Implicit

⊀   Courant Number- 5

⊀   Solution Limits

⊀   Minimum Absolute Pressure   1

⊀   Maximum Absolute Pressure   5e+10

⊀   Minimum Temperature   1

⊀   Maximum Temperature   5000

Another CFD model was simulated and solved under the same conditions but with a different chemical model known as the Dunn and Kang model (Appendix). The solutions obtained from two different chemical models were compared.

4.5 CFD results for the nozzle (Park Model):
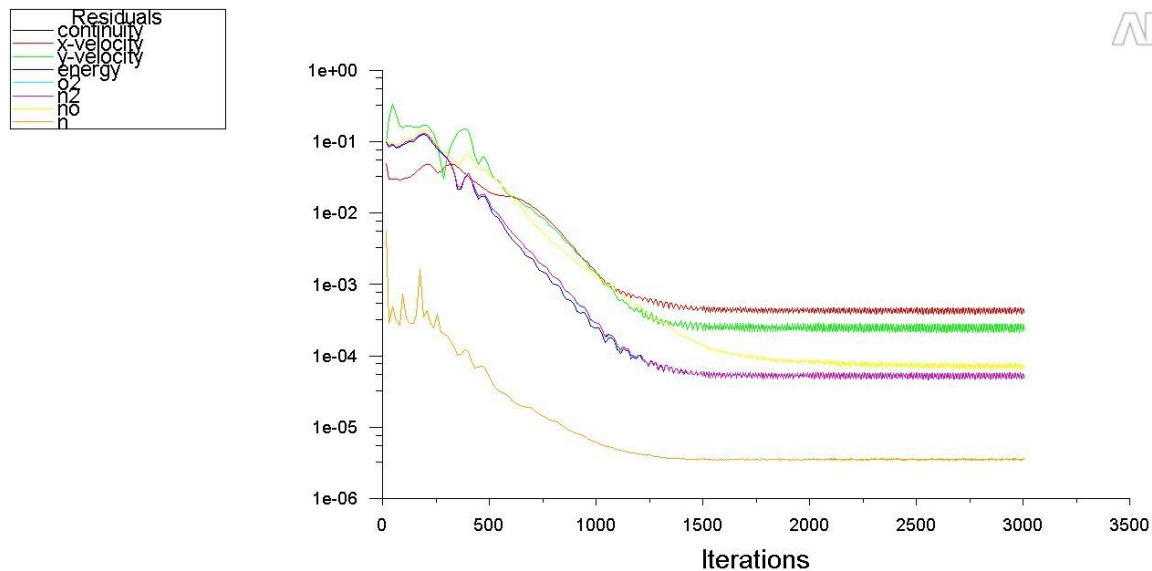
Fig.4.3: Residuals of the CFD solution for the flow through the nozzle using Park's Model. The solutions converged after 2500 iterations.
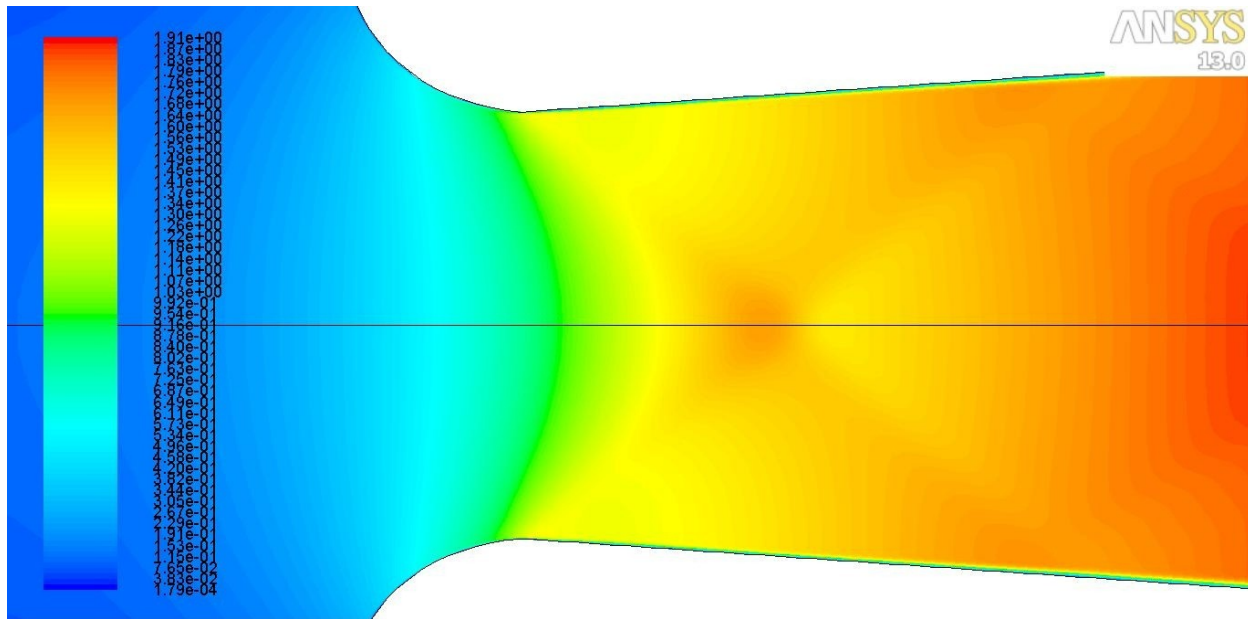
Fig.4.4: Mach contour of the flow through the nozzle obtained from the CFD solution using Park's Model.
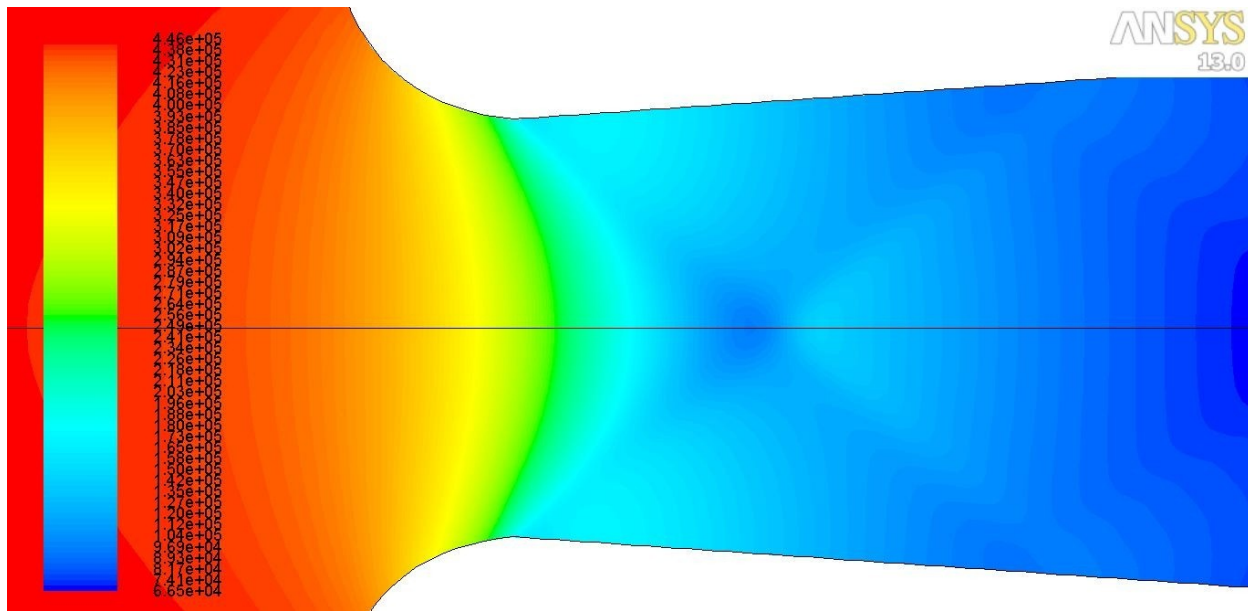
Fig.4.5: Static pressure contour of the flow through the nozzle obtained from the CFD solution using Park's Model.
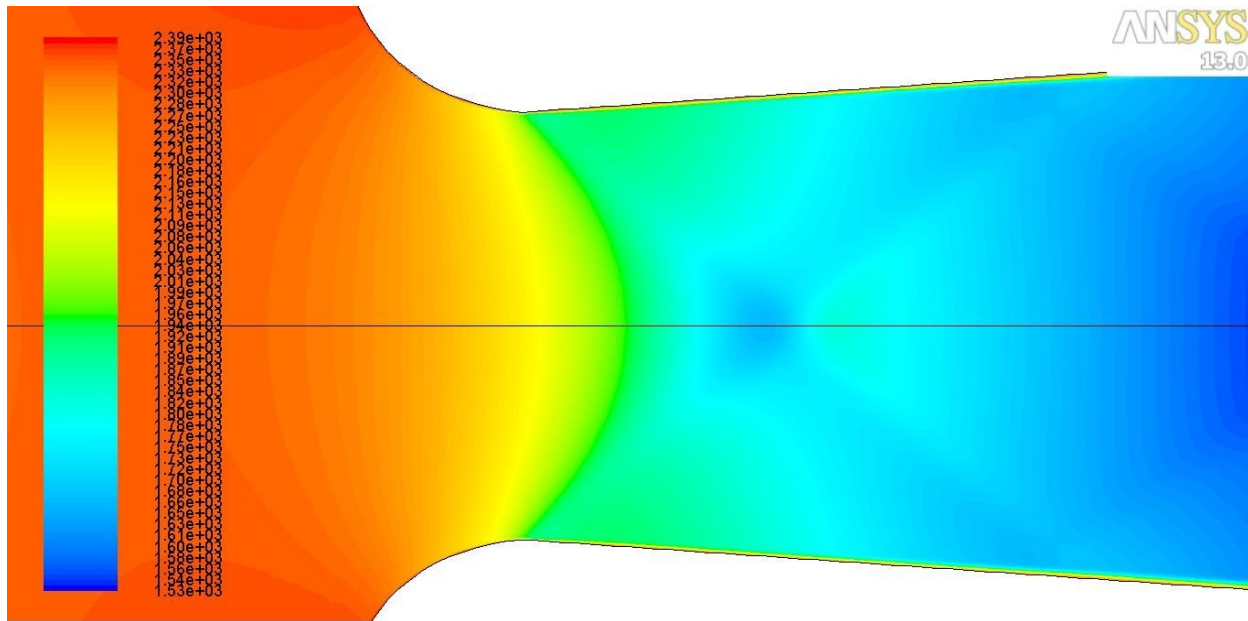
Fig.4.6: Static temperature contour of the flow though the nozzle obtained from the CFD solution using Park's Model.
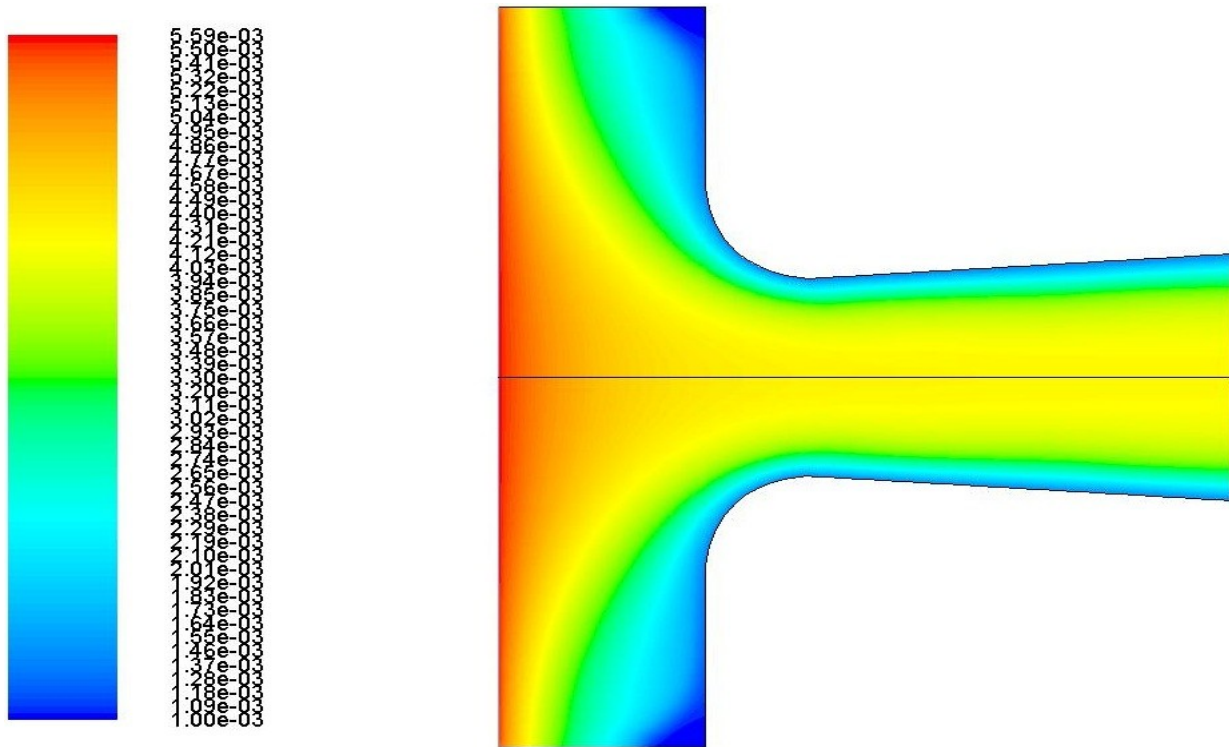
Fig.4.7: Mass fraction of atomic oxygen obtained from the CFD solution using Park's Model.
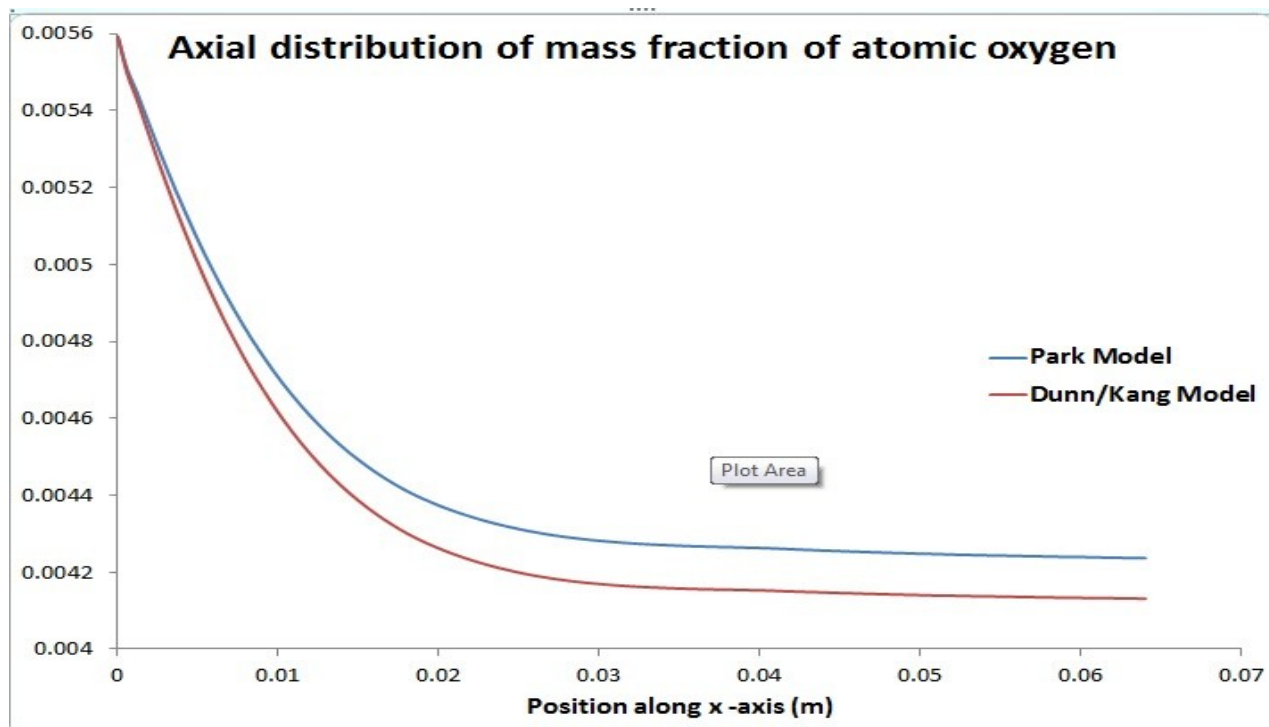
Fig.4.8: Comparison of the axial distribution of mass fraction of atomic oxygen (obtained from CFD) between Park model [2] and Dunn & Kang model [13].
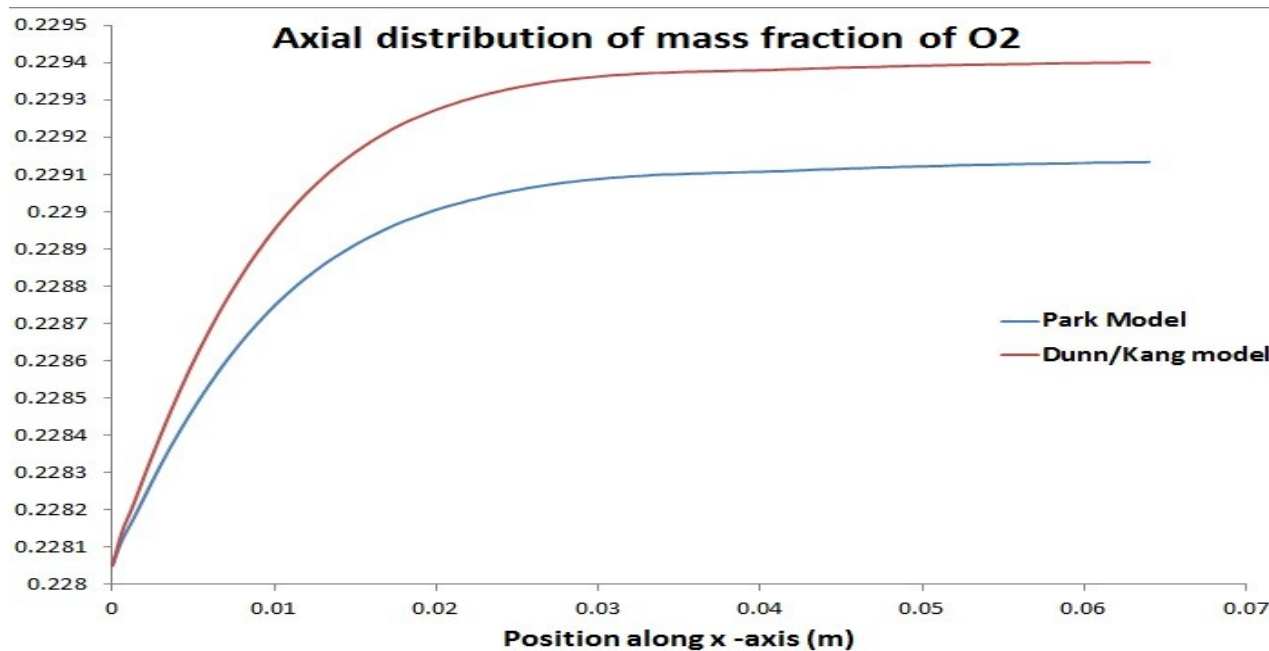
Fig.4.9: Comparison of the axial distribution of mass fraction of oxygen molecule (obtained from CFD) between Park model [2] and Dunn & Kang model [13].

4.6 Benchmarking:

The CFD solutions obtained from two different chemical models were identical. A maximum deviation of 0.12% was observed in case of mass fraction of O_2 and about 2.53% in case of mass fraction of atomic oxygen. However, the solutions obtained for Mach number, Temperature and Pressure were exactly the same. The flow properties obtained from the CFD solution at the exit of the nozzle were compared against those obtained from the output given by the NASA CEA code.

Sl.no	Flow property at the nozzle exit	CFD solution	NASA CEA output	Percentage deviation
1.	Mach Number	1.91	1.859	2.74
2.	Static Temperature(K)	1530	1558.39	1.82
3.	Static Pressure(Pa)	66500	72258	7.96
4.	Velocity (m/s)	1450	1422.5	1.93

Table 4.4: Comparison of the flow features obtained from CFD solutions and NASA CEA code.

4.7 Inference:

The flow properties obtained for the nozzle from the CFD solution using the Park Model are in close agreement with the theoretical results (CEA). Also, the Mach number at the exit from experimental data is found to be 1.85. Thus, we can confidently proceed using this chemical model for the advanced flow analysis of the entire test section with the specimen.

5.0 <u>Flow approximation:</u>

5.1 Physics of the flow:

The exit pressure from the arc jet nozzle as obtained from the CFD solutions is equal to 72258 Pascals. Whereas, the ambient pressure conditions as obtained from the experimental setup is equal to 48263.299 Pa. Since the nozzle exit pressure is greater than the ambient pressure, the flow would be "under-expanded". The under-expansion of the flow basically leads to the formation of expansion waves at the nozzle exit in order to reduce the exit pressure until it reaches the ambient value. These expansion waves are bounced back as compression waves at the boundary of the plume in order match the pressure differential.

Fig.5.1: Physics of the flow around the truncated specimen.

We have a truncated cone shaped specimen placed very close to the nozzle exit in the test

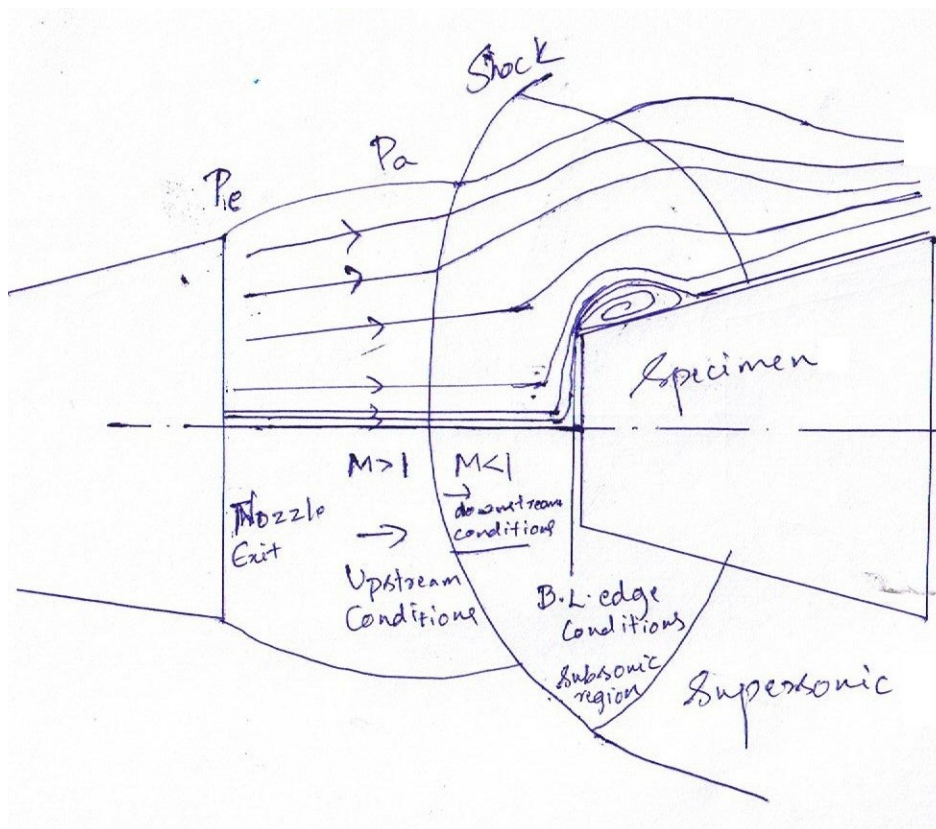chamber. Hence we can expect a bow shock between the nozzle exit and the specimen as shown in Fig.5.1. Since the distance between the nozzle exit and specimen is very small, there is not much of time available for the recombination reactions in the dissociated flow. Hence we can assume a frozen flow i.e., a constant specific heat ratio from the nozzle exit to the shock for hand calculation purposes, which makes the calculation process simpler. Another approximation that could make the calculation simpler would be considering the shock to happen exactly at the nozzle exit Mach number (~1.85). In reality, due to the crossing of the expansion fans (underexpanded jet), the centerline Mach number is different. The supersonic jet coming out of the nozzle exit goes through a normal shock and turns subsonic. The flow eventually slows down after the shock and halts at the edge of the stagnation region boundary layer. The streamlines adjacent to the stagnation stream line, traverse in a direction parallel to the flat nose. The flow is expected to separate from the specimen at the sharp corner near the end point of the flat nose. The reattachment takes place at a certain point on the surface of the specimen as a result of the acceleration of the flow from subsonic to supersonic regime.

5.2 Normal Shock Calculations:

Based on our assumptions, we can consider the shock upstream conditions to be same as the flow conditions at the exit of the nozzle. We can use the normal shock relations to determine the flow conditions after the shock. The downstream conditions obtained after normal shock calculations would then be considered as the freestream condition near the specimen.

Sl.no	Flow property at the nozzle exit	NASA CEA output
1	Mach Number	1.859
2	Static Temperature(K)	1558.39
3	Static Pressure(Pa)	72258
4	Velocity (m/s)	1422.5
5	Specific heat ratio	1.31
6	Cp (J/kg-K)	1212.81
7	Enthalpy (kJ/kg)	1435.82
8	Density (kg/m^3)	0.16

Table 5.1: Upstream Conditions (obtained from the CEA code)

5.2.1 Downstream Conditions:

- Mach-number [8]

$$M_2 = \sqrt{\frac{M_1^2 (\gamma - 1) + 2}{2\gamma M_1^2 - (\gamma - 1)}}$$

M_2 =((1.859^2 (1.31-1) +2)/(2*1.31*1.859^2-(1.31-1)))$^{1/2}$ = 0.5924

- Density (kg/m3) [8]

$$\frac{\rho_2}{\rho_1} = \frac{(\gamma + 1) M_1^2}{(\gamma - 1) M_1^2 + 2}$$

ρ_2 = 0.16(1.859^2 (1.31+1)/((1.859^2 (1.31-1)) +2)) = 0.416 kg/m^3

- Static Pressure(Pa) [8]

$$\frac{p_2}{p_1} = 1 + \frac{2\gamma}{\gamma + 1} (M_1^2 - 1)$$

P_2 = 72258(1+(2*1.31(1.859^2 -1)/(1.31-1)) = 273834.42 Pa

- Static Temperature (K) [8]

$$\frac{T_2}{T_1} = \frac{h_2}{h_1} = \frac{p_2}{p_1} \frac{\rho_1}{\rho_2}$$

T_2 = 2272.13 K

- Enthalpy (kJ/kg) [8] H_2 = Cp T_2 = 2297.91 kJ/kg

- Dynamic viscosity (from Power law) [7]

  μ_2 = $\mu_1(T_2/T_1)^{1/2}$ = 6.64 e-5 Pas

- Velocity (m/s) [8] V= $M_2 (\gamma RT_2)^{1/2}$ = 547.12 m/s

Sl.no	Flow Parameter	Downstream flow conditions
1	Mach Number	0.59
2	Static Temperature(K)	2272.13
3	Static Pressure(Pa)	273834.42
4	Velocity (m/s)	547.12 m/s
5	Density (kg/m^3)	0.42
6	Enthalpy (kJ/kg)	2297.91
7	Dynamic Viscosity (Pas)	6.64E-005

Table 5.2: Shock Downstream Conditions obtained from normal shock equations.

The calculation of Reynolds number based on the downstream conditions would tell us whether the flow is laminar or turbulent since these conditions would be considered as freestream conditions on the specimen. [8]

$$Re = \frac{\rho v L}{\mu} = \frac{v L}{\nu}$$

Re = 0.416* 547.12* 0.108/6.64e-5 = 3.702*10^5

Since the Reynolds number is lower than $5*10^5$, the freestream flow over the specimen would be *laminar.*

5.3 Stagnation point aerodynamic heating:
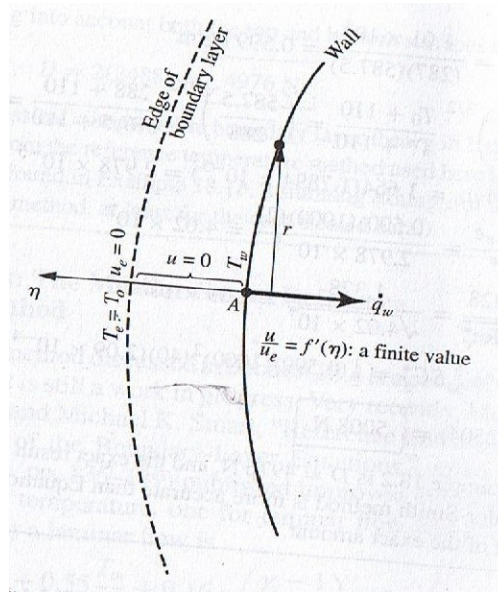
Fig.5.2: Schematic of the stagnation region boundary layer. [9]

A boundary layer at the stagnation point can be defined with a finite thickness even though the flow velocity is zero at the stagnation point. The flow conditions at the edge of the stagnation boundary layer can be determined using the inviscid solution for a stagnation point. At the edge of a stagnation boundary layer, the velocity is zero and the temperature is equal to the total temperature (Fig2.). The pressure at the edge of the boundary layer is equal to the total pressure. The temperature at the wall is different from the edge temperature and hence, there exists a temperature profile in the normal direction through the stagnation point boundary layer. This temperature gradient results in the

aerodynamic heating at the stagnation point. The purpose of obtaining a stagnation point boundary solution is to calculate the heat transfer q_w. However, the shear stress at the stagnation point is zero. [9]

5.3.1 Edge conditions:

⚑ Edge Temperature (Stagnation temperature)

$T_e = T_0 = (CpT_2 + u_2^2/2)/ Cp = 2395.62$ K

⚑ Edge Pressure $P_e = P_0 = P2 + \rho_2 u_2^2/2 = 336097.2$ Pa

⚑ Edge Density $\rho_e = P_e / RT_e = 0.488$ kg/ m^3

⚑ Edge Enthalpy $H_e = H_0 = H_2 + u_2^2/2 = 2447.58$ kJ /kg

⚑ Edge Viscosity (Power Law) $\mu_e = \mu_2(T_e/T_2)^{1/2} = 6.82$ e-5 Pas

Sl.no	Flow Parameter	Edge flow conditions
1	Edge Temperature(K)	2395.62
2	Edge Pressure(Pa)	336097.2
3	Edge Density (kg/m^3)	0.49
4	Edge Enthalpy (kJ/kg)	2447.58
5	Edge Dynamic Viscosity (Pas)	6.82E-005

Table 5.3: Stagnation boundary edge conditions obtained from downstream flow solution.

5.3.2 Stagnation heat flux :

The stagnation point heat transfer due to convection for an equilibrium case could be approximated with the help of Fay-Riddell equation [21]. Fay-Riddell equation is a relatively compact closed form equation used to model the convective and catalytic heat flux at the stagnation point of an aeroshell. The Fay-Riddell equation is remarkably accurate and sometimes used to validate modern computational fluid dynamics (CFD) solutions. Though virtually unknown outside the aerospace profession, the Fay-Riddell equation is amongst the most brilliant mathematical derivations in the history of science. The Fay-Riddell equation is given by [21]

- **Final result for heat transfer at stagnation point:**

$$\dot{q}_w = \frac{0.763}{(\mathrm{Pr}_w)^{0.6}} (\rho_e \mu_e)^{0.4} (\rho_w \mu_w)^{0.1} \left[(h_o)_e - h_w\right] \left[1 + (Le^{0.52} - 1)\frac{h_d}{(h_o)_e}\right] \left[\left(\frac{du_e}{dx}\right)_t\right]^{0.5}$$

- **Modified Newtonian model at stag pt yields:**

$$\left(\frac{du_e}{dx}\right)_t = \frac{1}{R_N}\sqrt{\frac{2(p_e - p_\infty)}{\rho_e}}$$

The equation uses flow properties at the edge and wall. The stagnation point velocity gradient is found using the modified Newtonian theory. The Fay-Riddell equation is based on assumptions [21] such as:

- Air is assumed to be comprised of only oxygen and nitrogen, and all the oxygen dissociates before the nitrogen starts dissociation.
- Air is assumed to behave as a Newtonian fluid.
- It is applicable only for air in steady, equilibrium flow.
- Applicable only for 2D-planar or axially symmetric bodies.
- The boundary layer thickness is assumed to be negligible as compared to the blunt body radius

The stagnation point heat transfer due to convection was estimated using the Fay-Riddell equation for two different cases namely the peak heat flux and radiative specimen in equilibrium. The equilibrium wall temperature for a radiative specimen and a non radiative specimen was found using a ms-excel program based on an equation that was derived from the Fay-Riddell approximation for our case. The equation derived basically has the wall temperature as an independent variable and stagnation point heat flux as a dependent variable.

The following were the assumptions used in our calculations in order to implement the Fay-Riddell approximation technique in our calculations:

- The flat nose is considered as a part of a large sphere with $R_N = 0.1$ m.
- Lewis number is assumed to be nearly equal to 1.
- The velocity of the flow at the wall in the direction perpendicular to the wall is assumed to be

zero.

Based on our assumptions, the Fay-Riddell eqaution is simplified to the following form:

$$\dot{q}_w = \frac{0.763}{\left(\text{Pr}_w\right)^{0.6}} \left(\rho_e \mu_e\right)^{0.4} \left(\rho_w \mu_w\right)^{0.1} \left[\left(h_o\right)_e - h_w\right] \left[\left(\frac{du_e}{dx}\right)_t\right]^{0.5}$$

According to this equation the peak flux can be obtained when the difference between the edge enthalpy and wall enthalpy is the maximum. In the experiment, the difference is maximum when the temperature at the wall is minimum i.e., before the jet is impinged on the specimen. Thus, the wall temperature that gives the peak heat flux is the ambient temperature that exists on the surface before it is exposed to the jet. Hence, the wall temperature T_w was considered to be equal to 300K for the peak heat flux calculation.

Case 1: Peak heat flux

- ⋏ Stagnation point velocity gradient $(du_e/dx)_t$ = 10398.597 /s
- ⋏ Wall Temperature T_w = 300 K
- ⋏ Wall Pressure P_w = Stagnation Pressure = P_0 = 336097.2 Pa
- ⋏ Wall Density $\rho_w = P_w / RT_w$ = 3.9 kg/ m³
- ⋏ Wall Viscosity $\mu_w = \mu_e(T_w/T_e)^{1/2}$ = 2.41 e-5 Pas
- ⋏ Wall Prandtl Number = 0.71
- ⋏ Wall Enthalpy $H_w = CpT_w$ = 363.843 kJ/kg
- ⋏ Peak flux q_w = 1276.865 kW/m²

Case 2: Radiative specimen

In this case the specimen radiates heat with an emissivity equal to 0.9. The net heat flux becomes equal to zero when the sum of radiative heat flux and convective heat flux comes down to

zero. Since radiative heat transfer is taking place is exactly opposite direction of the convective heat transfer, the equilibrium temperature is reached when the radiative heat flux becomes equal to convective heat flux.

The equation for convective heat flux in terms of wall temperature for our case was found to be:

$$(q_w)_{conv} = \mathbf{1994777.7}\ T_w^{-0.05} - \mathbf{988.432}\ T_w^{0.95}$$

The Stefan-Boltzmann equation was used to calculate the radiative heat flux

$$(q_w)_{rad} = \varepsilon\ \sigma\ T_w^{4}$$

At $T_w = 1567.665$ K, $(q_w)_{conv} = (q_w)_{rad} = 308.204$ kW/m²

Hence, for the case of a radiative specimen

- Equilibrium Wall Temperature $T_w = 1567.665$ K
- Convective Heat Flux at the stagnation point = 308.204 kW/m²
- Radiative Heat Flux at the stagnation point = 308.204 kW/m²
- Equilibrium Wall enthalpy = $h_w = CpT_w = 1901.279$ kJ/kg

Case 3: Non Radiative Specimen:

In this case the wall temperature reaches equilibrium when there is no heat transfer from the fluid to the surface. This happens when the convective heat flux becomes equal to zero. Using the same equation for convective heat flux as shown in case two, the equilibrium wall temperature was found to be 2018.123 K.

Hence for the case of a non radiative specimen:

- When $(q_w)_{conv} = 0$, Equilibrium Wall Temperature $T_w = 2018.123$ K
- Equilibrium Wall enthalpy = $h_w = CpT_w = 2447.599$ kJ/kg

5.4 Shear stress calculations:

Shear stress on the wall away from the stagnation point was found using the Reynolds analogy. Reynolds analogy is a relates momentum transfer to heat transfer as function of Prandtl number. For a compressible boundary layer the Reynolds analogy can be written is

$C_h / C_f = Pr^{-2/3} / 2$ wher C_f is the coefficient of skin friction and C_h is the Stanton number.

Stanton number is given by [6]

$C_h = q_w / \rho u \, (h_{aw} - h_w)$ where ρ and u are the density and velocity of the freestream obtained from inviscid solution.

Adiabatic wall enthalpy [6] $h_{aw} = h_2 + Pr^{1/2} \, u_2^2 /2 = 2424.019$ kJ/kg

Considering the results from the radiative specimen case, which in reality, is the case of arc-jet specimen that we are studying, we get,

- Stanton number $C_h = 308.204 / (0.416*547.12*(2424.019 - 1901.279)) = 2.59$ e -3
- Skin friction coefficient $C_f = 2*2.59$ e -5 $/0.71^{-2/3} = 4.1233$ e-3
- Wall shear stress $\tau_w = \rho u^2 \, C_f / 2 = 0.416* 547.12^2 *4.1233$ e-5 $/ 2 = 256.73$ N /m2

6.0 The Grid

The y+ wall technique [20] was used to determine the distance of the 1st grid point from the wall in a direction normal to the wall. The wall y+ is a non-dimensional distance used in CFD to describe how coarse or fine a mesh is for a particular flow. It is the ratio between the turbulent and laminar influences in a cell. Very close to the wall, viscous damping reduces the tangential velocity fluctuations, while kinematic blocking reduces the normal fluctuations. Towards the outer part of the near-wall region, however, the turbulence is rapidly augmented by the production of turbulent kinetic energy due to the large gradients in mean velocity. The momentum and other scalar transports occur most vigorously near the wall regions leading to larger gradients in the solution variables . The viscosity-affected region (the *inner layer* in this case) is made up of three zones (with their corresponding wall y+), namely the:

- ⚐ Viscous sublayer (y+ < 5)
- ⚐ Buffer layer or blending region (5 < y+ < 30)
- ⚐ Fully turbulent or log-law region (y+ > 30 to 60) [20]

Accurate presentation of the flow in the near-wall region determines successful prediction of wall-bounded turbulent flows. Values of y+ close to the lower bound (y+≈30) are most desirable for *wall function*s whereas y+≈1 are most desirable for *near-wall modeling*.[20] In our case, for y+ =1 , we obtain the actual size of wall adjacent cells using the following equations. [18]

$$u_t = (\tau_w / \rho)^{1/2} = (256.73 / 0.416)^{1/2} = 24.84 \text{ m/s}$$

$$y = \mu / \rho u_t = 6.64 \text{ e -5} / (0.416 * 24.84) = 6.426 \text{ e -6 m}$$

Therefore, the distance of the first grid point from the wall should be 6.426 e -6 m in a direction perpendicular to the wall. Placing the first grid point at this location would result in effective capturing of the boundary layer in the CFD solutions.

A 2D- axisymmetric grid including the nozzle, test section and the specimen was modeled using the GAMBIT 2.2.30 program. The grid initially consisted of quadrilateral cells throughout the flow domain but it caused abrupt divergence during simulations due to discontinuous aspect ratios. Hence a blend of quadrilateral grid in the nozzle domain and triangular cells in the rest of the flow domain inside the test section was modeled for convergence. It also reduced the number of cells, reducing the computational time. A Boundary layer mesh was modeled over the surface of the specimen, purely based on the y+ calculations (refer to previous section) in order to capture the physics of the flow near the stagnation region and the tapering surface of the specimen. The flow domain was extended till the wall of the test section in the radial direction and the exit of the test section in the axial direction. The trailing edge of the specimen was extended into a straight cylindrical surface so as to minimize the computational effort that goes in determining the complex flow field behind the specimen, which is not subject of interest in this project.
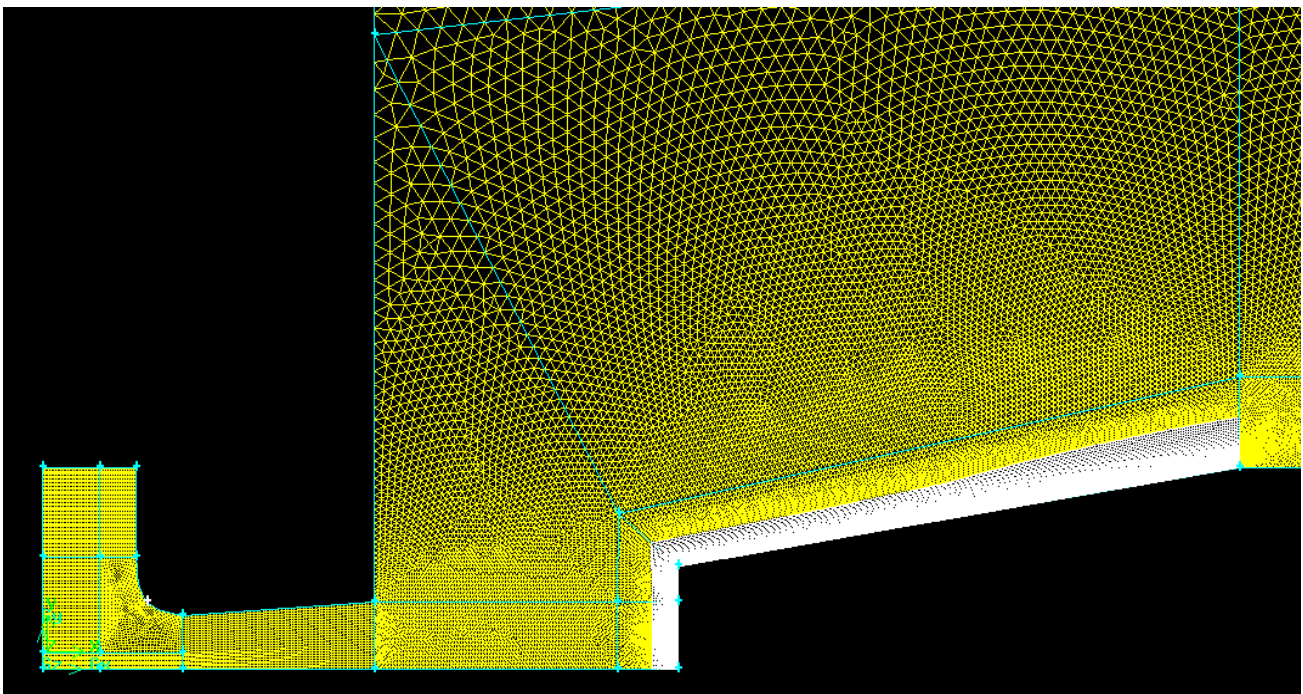

Fig.6.1: 2D- Axisymmetric grid including the nozzle and test section with the specimen modeled in using GAMBIT- 2.2.30.

Specifications of the Mesh:
- ⚐ Number of cells – 80723
- ⚐ Number of Faces - 138359
- ⚐ Number of Nodes - 57637
- ⚐ Number of Zones - 8
- ⚐ Minimum Orthogonal Quality – 1.89 E-3
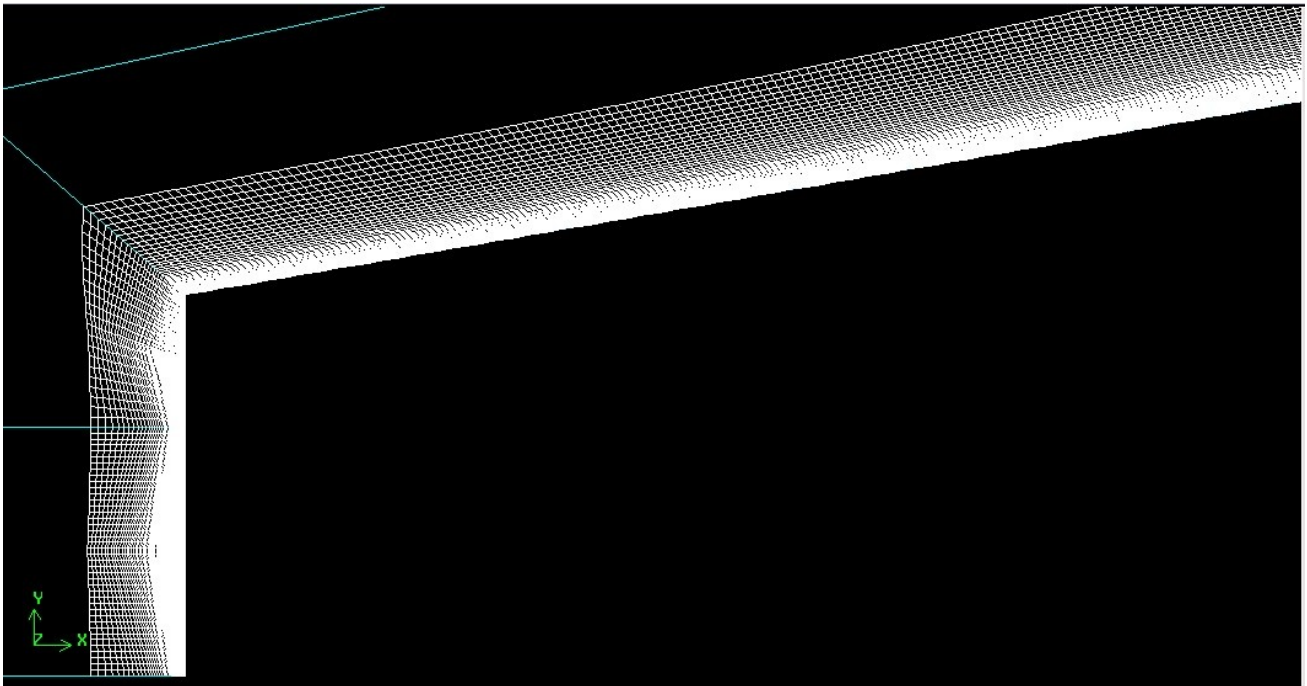- ⚐ Maximum Aspect Ratio – 2.566 E3

Fig.6.2 : Boundary layer mesh on the specimen surface modeled with cell wall distance = 6.426 e-6 m

7.0 <u>CFD- Test Section:</u>

Initially, the test section grid was imported into the case file used in the nozzle analysis. But the residuals diverged after 6000 iterations every time irrespective of the solution control settings. So the entire model was carefully reviewed and remodeled based on the solver settings recommended in a Hypersonic Re-entry modeling tutorial [29] obtained from ANSYS Inc.,. This particular document provides detailed specifications for the solver settings recommended for high temperature reactive cases modeled using FLUENT. The details of the remodeled CFD case file are mentioned below :

1. Type of solver: Axisymmetric, density based, implicit, species, laminar.
2. Species Model:

    ⚒ Species transport- active

    ⚒ Reaction type- volumetric

    ⚒ Backward reactions- active

    ⚒ Reacting Species: Nitrogen (N_2), Oxygen (O_2), Nitrogen Oxide (NO), Atomic Oxygen (O), Atomic Nitrogen (N).

    ⚒ Number of reactions: 5

    ⚒ Stoichiometric coefficient of reactants : 1

    ⚒ Rate exponent of reactants: 1

    ⚒ Stoichiometric coefficient of reactants : 1

    ⚒ Rate exponent of reactants: 0

Sl. no	Reaction	Pre- exponential factor	Activation energy(J/kg-mol)	Temperature exponent
1.	$O_2 \rightarrow O + O$	2.90E+020	4.9682e+08	-2
2.	$NO \rightarrow N + O$	7.95e+20	6.28E+008	-2
3.	$N_2 \rightarrow N + N$	4.98e+18	9.4126e+08	-1.6
4.	$NO + O \rightarrow N + O_2$	8.37e+09	1.62E+008	0
5.	$N_2 + O \rightarrow NO + N$	6.44e+14	3.19e+08	-1

Table 7.1: Chemical reactions and magnitude of Arrhenius rate parameters associated with the reactions used in test section analysis. (based on Park's 5-species Model [2])

Sl. no	Reaction	Third body efficiency				
		O_2	N_2	NO	N	O
1.	$O_2 \rightarrow O + O$	0.338	0.338	0.338	1	1
2.	$NO \rightarrow N + O$	1	1	1	1	1
3.	$N_2 \rightarrow N + N$	0.0743	0.0743	0.1	0.32	1
4.	$NO + O \rightarrow N + O_2$	1	1	1	1	1
5.	$N_2 + O \rightarrow NO + N$	1	1	1	1	1

Table 7.2: Third body efficiency of each species for test section analysis. [2]

3. Materials:

    o Fluid- Air, Water Vapor, Nitrogen (N2), Oxygen (O2), Nitrogen Oxide (NO), Atomic Oxygen (O), Atomic Nitrogen (N).

4. Solid- Copper (Wall)

5. Cell zone conditions

    • Fluid reaction

6. Boundary Conditions

    o Wall - Adiabatic

    o Pressure-inlet

          ⚔   Gauge Total Pressure (pascal)   446090.78

          ⚔   Supersonic/Initial Gauge Pressure (pascal)   446090.78

          ⚔   Total Temperature (k)   2343.93

          ⚔   Axial-Component of Flow Direction   1

          ⚔   Radial-Component of Flow Direction   0

          ⚔   Specify Species in Mole Fractions?   yes

   ⚔   Mole fractions: $O_2 \rightarrow 0.20473$; $N_2 \rightarrow 0.77618$; $NO \rightarrow 0.00905$; $O \rightarrow 0$

        ⚔ Pressure-outlet

⚚ Gauge Pressure (pascal)   48263.3

⚚ Backflow Total Temperature (k)   300

⚚ Axial-Component of Flow Direction   1

⚚ Radial-Component of Flow Direction   0

⚚ Specify Species in Mole Fractions?   yes

⚚ Backflow mole fractions: $O_2 \rightarrow$ 0.18616543; $N_2 \rightarrow$ 0.75946699; $NO \rightarrow$ 0.018907491; $O \rightarrow$ 0

7. Solver Settings

⚚ Equations to be solved- Flow i.e., Continuity, Momentum and Energy.

⚚ Absolute Velocity Formulation- Yes

⚚ Convergence criterion $\rightarrow$ 10^{-3}

⚚ Discretization Gradient- Green Gauss Node based

⚚ Discretization Scheme- Second Order Upwind

⚚ Flux Type: AUSM

⚚ Solver- Implicit

⚚ Solution Steering with FMG initialization for supersonic flow

⚚ Courant Number- 0.005 to 1
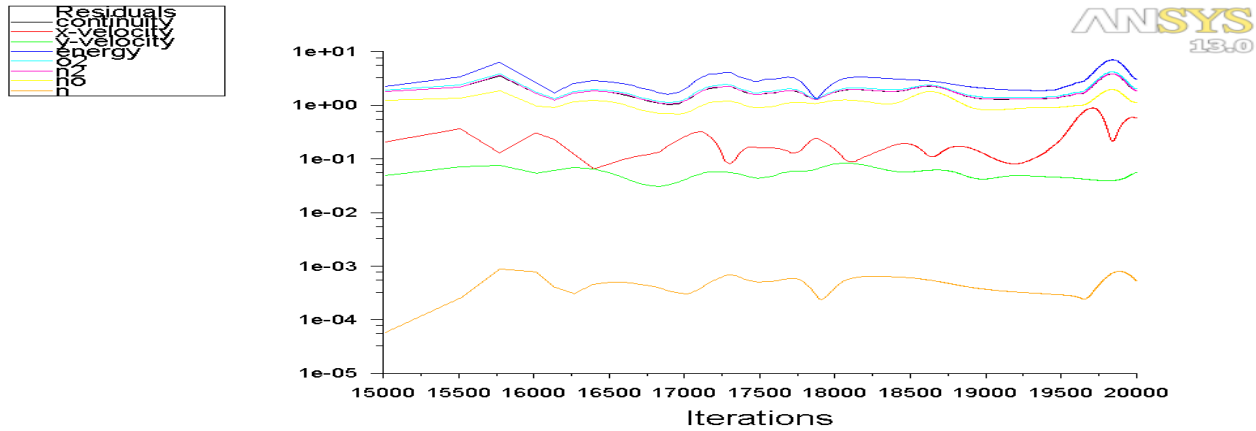
Fig 7.1: Residuals neither converged nor diverged after 20000 iterations for the test section case.
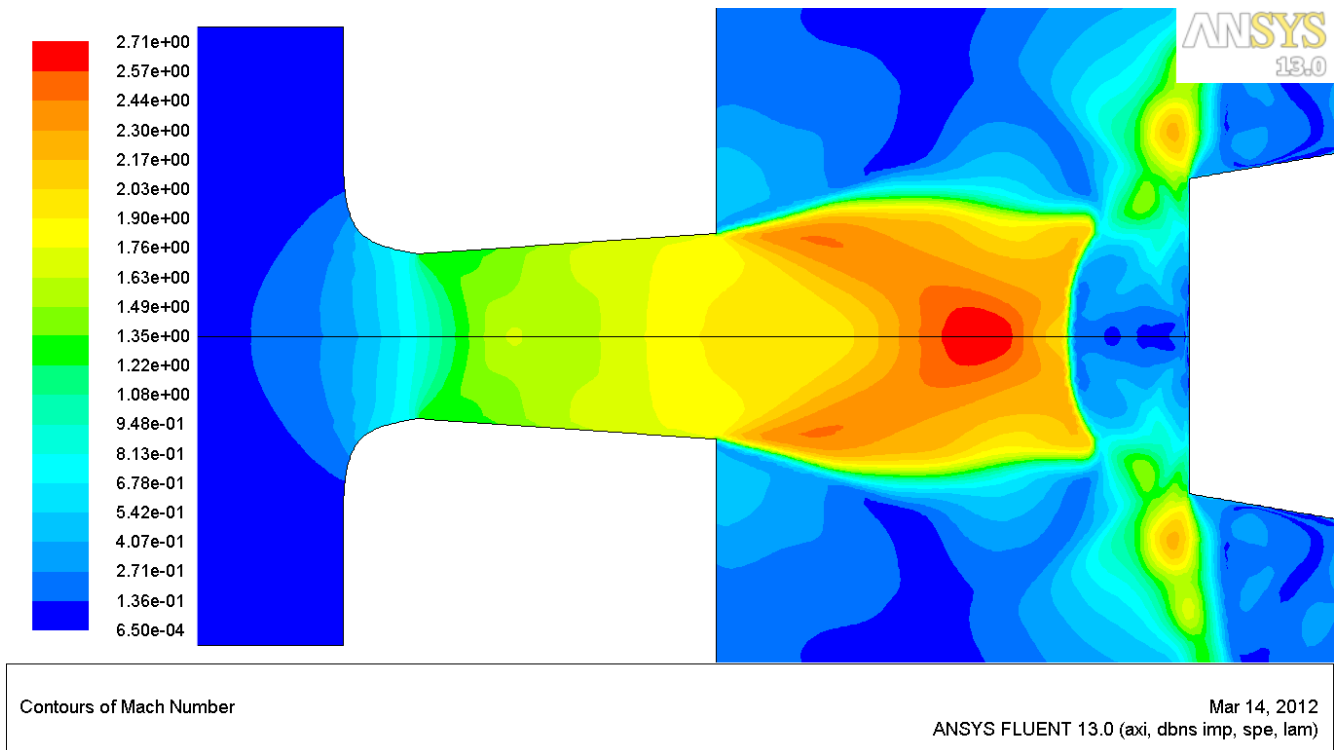
Fig 7.2: Mach contours of the flow through the nozzle, specimen and test section.
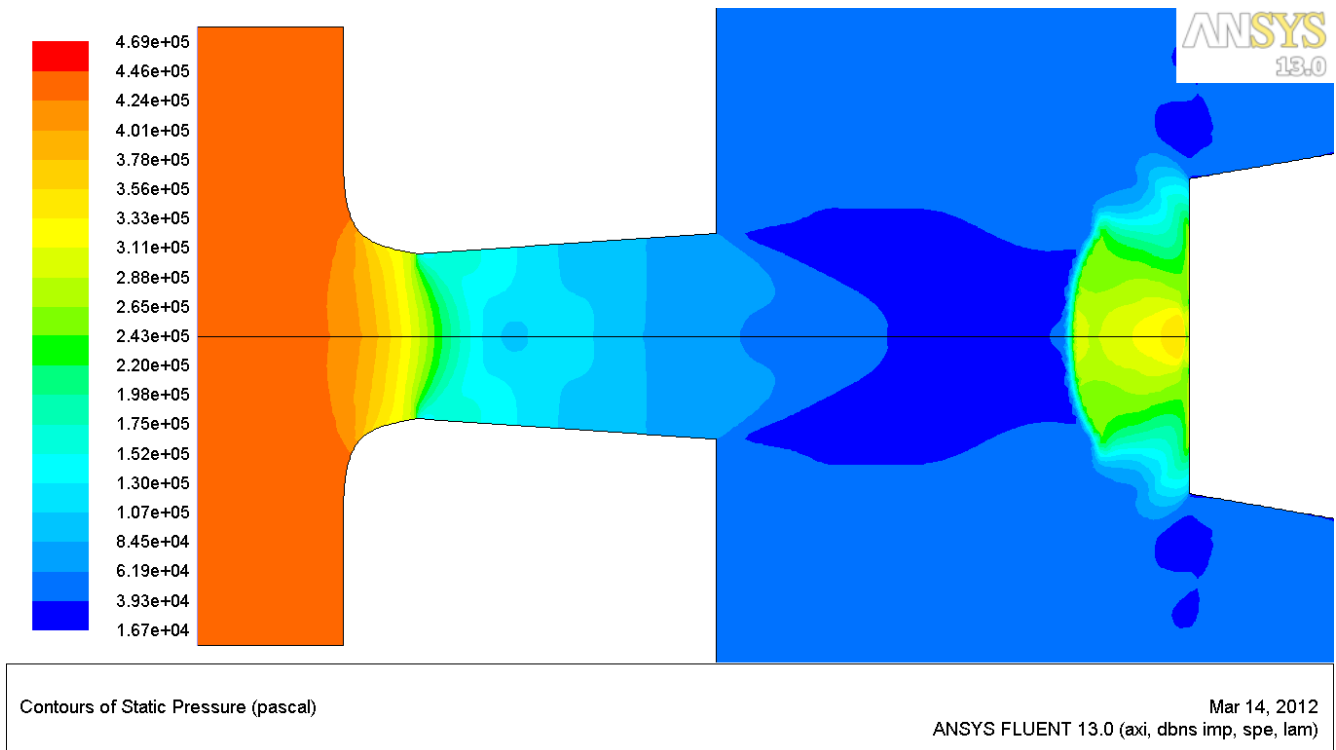

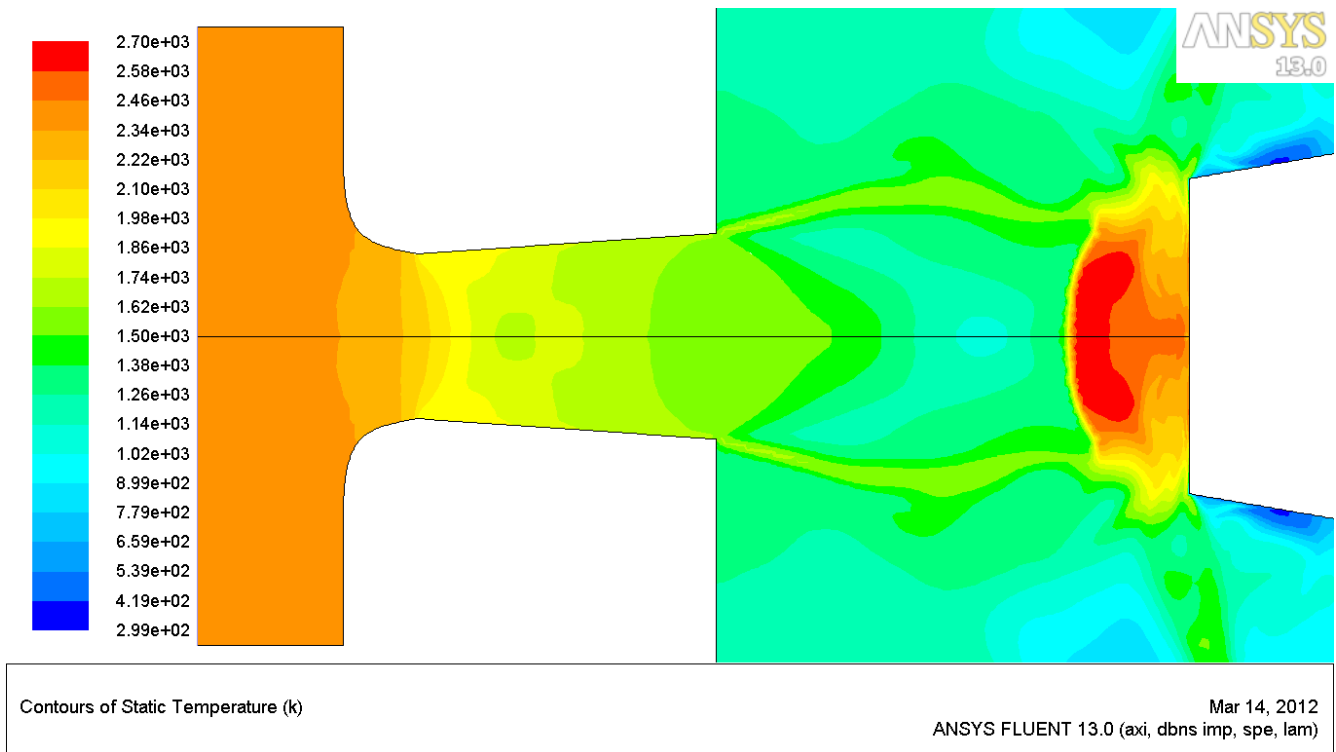**Fig 7.3**: Static Pressure contours of the flow through the nozzle, specimen and test section.

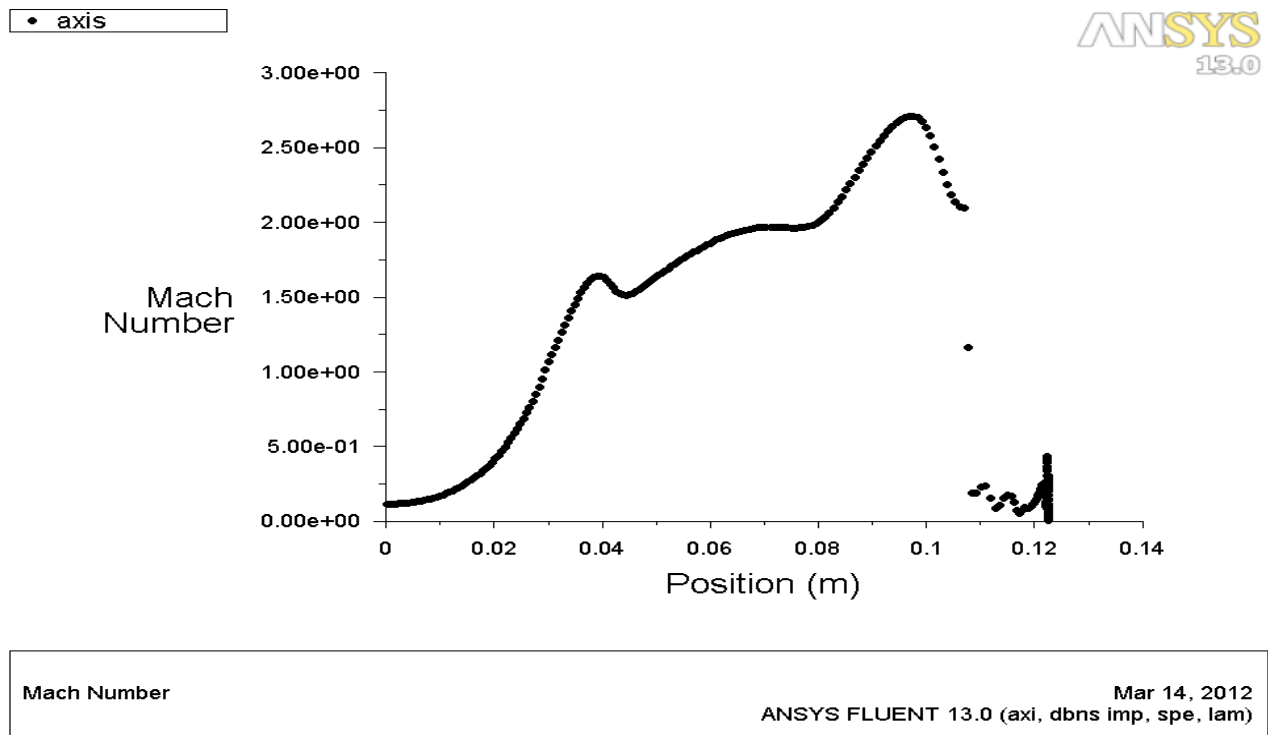**Fig 7.4**: Static temperature contours of the flow through the nozzle, specimen and test section.

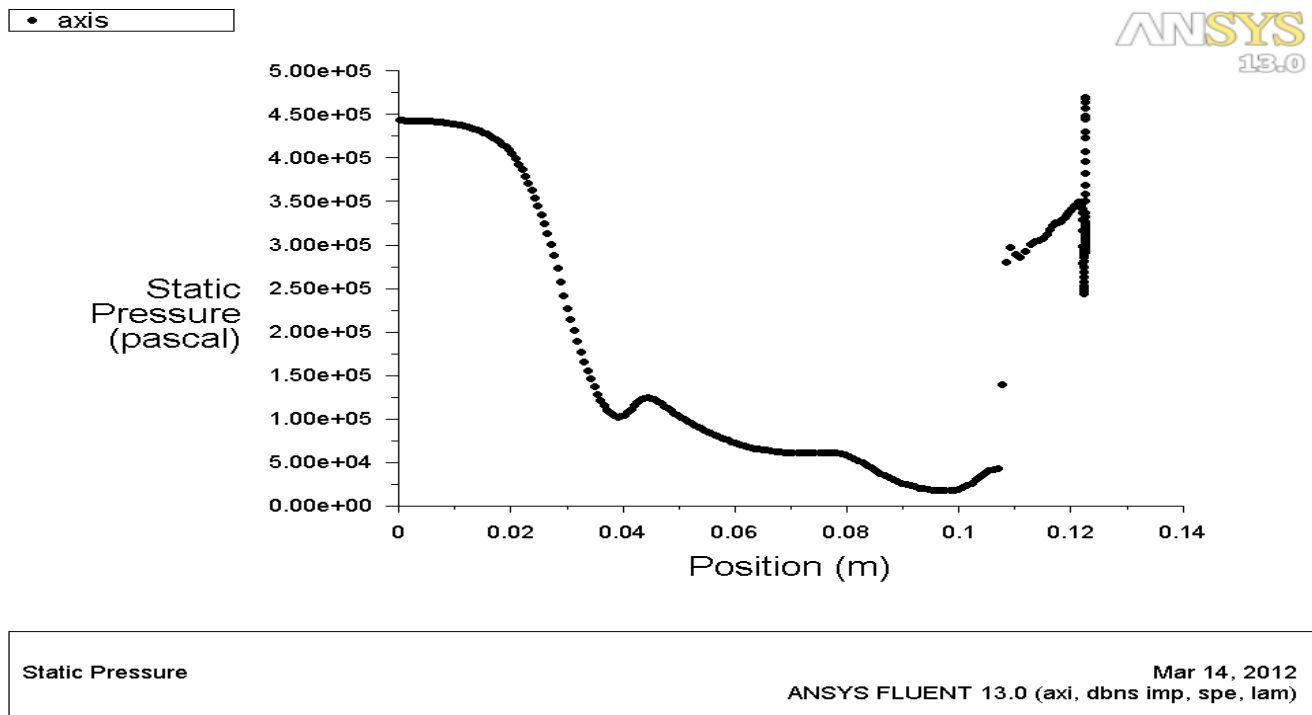**Fig 7.5**: Mach number variation along the axis of symmetry.

Fig 7.6: Static Pressure variation along the axis of symmetry.
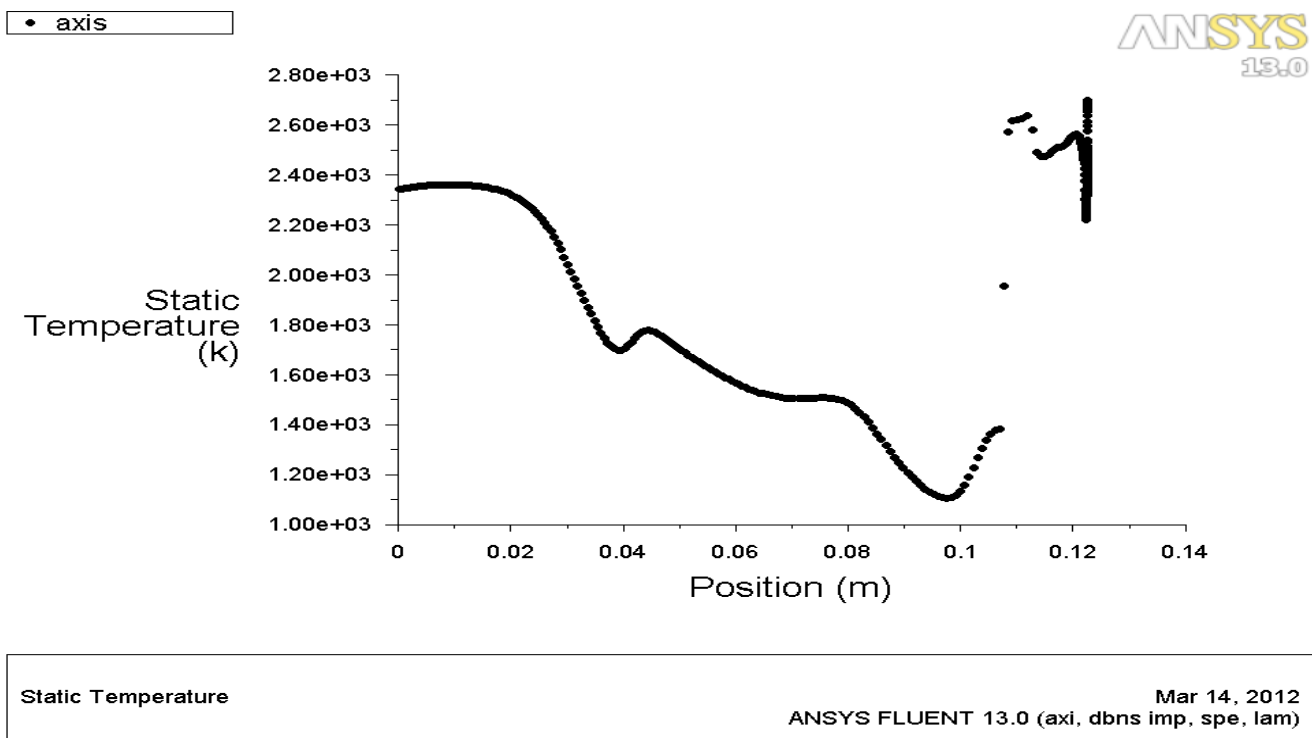

Fig 7.7: Static Temperature variation along the axis of symmetry.

The following inferences were drawn from the CFD solutions:

⮞ The flow expands after the nozzle exit throwing expansion waves and forming the plume

⮞ The plume is interrupted by a bow shock thrown by the specimen very near to the exit of the nozzle.

⮞ The flow attains a maximum mach number of 2.7085 at the intersection of 1st set of expansion waves in the plume. This location is about 97.4941 mm away from the chamber along the axis of symmetry.

⮞ The flow attains a maximum temperature of 2697.66 K at the stagnation region right in from of the flat surface of the specimen.

⮞ The enthalpy at the wall was found to be 2964.03 KJ/kg at the stagnation region right in from of the flat surface of the specimen.

⮞ The flow attains a maximum Static pressure of 468857 Pa at the stagnation region right in from of the flat surface of the specimen.

⮞ The separation bubbles are seen near the top corners of the of specimen surface exposed to the flow exiting the nozzle.

⮞ The deviation of the CFD solutions from the theoretical flow approximation (non radiative specimen) was about 21 % and 33.67 % for wall enthalpy and wall temperature respectively. This large deviation can be attributed towards the assumption of frozen flow in theoretical calculations and the non convergence of grid during computation.

The residuals neither converged nor diverged even after 20000 iterations. The CFD solutions obtained did match reasonably with the experimental results but showed a drastic deviation from theoretical approximation. About eight to ten grids with lower grid resolution and finer orthogonality were modeled and tested with the above mentioned model but all of them ended up with no-convergence-no divergence situation just like the first one. The solver settings were changed to simpler schemes in the first order but that did not help either. The failure of the model to converge was attributed to the quality of the grid as well as the complexity of the flow near the stagnation region. The flow is under expanded, reactive and interfering with a shock wave right after it exits the nozzle. This is due to the small distance between the nozzle exit and the specimen. One of the other constraints in

solving such complicated flows is the computational power required to support the solver at higher order schemes with a high resolution grid with superior orthogonal quality.

Hence, the goals of the project were redefined as follows:

- ⚔ To build a CFD model for the nozzle of the arc jet facility and to analyze the same based on the flow conditions at the exit of the nozzle using a CFD model.

- ⚔ To capture and analyze the velocity and thermal boundary layer profiles at the exit of the nozzle using the CFD model of the nozzle.

- ⚔ To establish a correlation between the flow conditions at the exit and the total pressure and total enthalpy at the chamber.

This new set of objectives were actually defined based on a technical publication titled " The GHIBLI plasma wind tunnel: Description of the new CIRA-PWT facility" [11] published by CIRA, Italy. GHIBLI is a 2MW arc jet facility developed by the Italian Aerospace Research Center (CIRA) located at Capua. This particular work tries to identify analytical correlations between the main aerodynamic parameters and the chamber conditions in the arc heater column in terms of Total Enthalpy and Total Pressure.

8.0 Advanced Analysis of the Nozzle:

A 2D structured grid for the nozzle was modeled using GAMBIT 2.2.30. Since the geometry of the nozzle is axisymmetric in nature, only one half of the nozzle in a 2D plane was considered for CFD modeling. The grid consisted of 5 domains. The grid cells are absolutely rectangular in two domains and quadrilaterals with different shapes in the other three domains. Three grids with same topology but different grid resolutions(coarse, fine-1 and fine-2) were modeled for the purpose of grid convergence. The fine grids consisted of a boundary layer mesh starting from the beginning of the throat and extending till the exit of the nozzle. The BL mesh was more focused towards capturing the flow near the wall region in the divergent part of the nozzle. Hence, the BL mesh for fine-2 grid was modeled for y+ =1 with a cell wall distance of 1.1E-6 m. This value was obtained using the flow conditions at the throat obtained from the case with fine-1 resolution grid.

Y+ Wall Distance Estimation

Input

Freestream velocity:	720.787	[m/s]
Density:	0.46972	[kg/m3]
Dynamic viscosity:	1.7158e-5	[kg/ms]
Boundary layer length:	0.037	[m]
Desired Y+ value:	1.0	[]

Output

Reynolds number:	7.3e+5	[]
Estimated wall distance:	1.1e-6	[m]

Fig 8.1: Y+ wall distance estimation for the boundary layer mesh in the divergent part of the nozzle.

The new CFD models of the nozzle were developed considering the solver setup used in the GHIBLI model[11]. Two different models were developed specifically for air and N2. The air model was run with one set of inputs on a coarse, intermediate and fine grid in the same order. The N2 model was run with 3 different chamber conditions over a coarse, intermediate and a fine grid. Hence, a total of 12 CFD simulations were performed under the following conditions and solver settings :

1. Type of solver: Axisymmetric, density based, implicit, species, laminar.
2. Species Model:

    ⅄ Species transport- active

    ⅄ Reaction type- volumetric

    ⅄ Backward reactions- active

    ⅄ Reacting Species: Nitrogen (N2), Oxygen (O2), Nitrogen Oxide (NO), Atomic Oxygen (O), Atomic Nitrogen (N).

    ⅄ Number of reactions: 5

    ⅄ Stoichiometric coefficient of reactants : 1

    ⅄ Rate exponent of reactants: 1

    ⅄ Stoichiometric coefficient of reactants : 1

    ⅄ Rate exponent of reactants: 0

Sl. no	Reaction	Pre- exponential factor	Activation energy(J/kg-mol)	Temperature exponent
1.	$O_2 \rightarrow O + O$	2.90E+020	4.9682e+08	-2
2.	$NO \rightarrow N + O$	7.95e+20	6.28E+008	-2
3.	$N_2 \rightarrow N + N$	4.98e+18	9.4126e+08	-1.6
4.	$NO + O \rightarrow N + O_2$	8.37e+09	1.62E+008	0
5.	$N_2 + O \rightarrow NO + N$	6.44e+14	3.19e+08	-1

Table 8.1: Park-5 species chemical model used in the advanced nozzle analysis [2].

Sl. no	Reaction	Third body efficiency				
		O_2	N_2	NO	N	O
1.	$O_2 \rightarrow O + O$	0.3338	0.3338	0.3338	1	1
2.	$NO \rightarrow N + O$	1	1	1	1	1
3.	$N_2 \rightarrow N + N$	0.0743	0.0743	0.1	0.3213	1
4.	$NO + O \rightarrow N + O_2$	1	1	1	1	1
5.	$N_2 + O \rightarrow NO + N$	1	1	1	1	1

Table 8.2: Third Body efficiencies of the Park-5 species chemical model used in the advanced nozzle analysis. [2]

The kinetic theory was applied for determining flow properties like thermal conductivity and viscosity. A 7th polynomial law of temperature has been assumed for specific heat flux calculations. Chemical and thermodynamic non-equilibrium was considered during the process. [11]

3. Materials:
   o Fluid- Air, Water Vapor, Nitrogen (N2), Oxygen (O2), Nitrogen Oxide (NO), Atomic Oxygen (O), Atomic Nitrogen (N).
4. Solid- Copper (Wall)
5. Cell zone conditions
   • Fluid reaction
6. Solver Settings
   ⚐ Equations to be solved- Flow i.e., Continuity, Momentum and Energy.
   ⚐ Absolute Velocity Formulation- Yes

⋏ Convergence criterion → 10^{-3}

⋏ Discretization Gradient- Least Squares Cell based

⋏ Discretization Scheme- Second Order Upwind

⋏ Flux Type: Roe-FDS

⋏ Solver- Implicit

⋏ Solution Steering with FMG initialization for supersonic flow

⋏ Courant Number- 5 to 50

The experimental data consisted of total pressure and total enthalpy at the chamber for all the four cases based on the test runs at the facility. Hence, the remaining inlet boundary conditions that are required to model the problem in CFD were approximated from the outputs of the CEA code following the same process as mentioned in preliminary nozzle analysis section in the beginning of the report. The detailed inputs and outputs for CEA for all the four cases are mentioned in the appendix section.

1. Boundary Conditions for Air- case 1:

○ Wall - Adiabatic

○ Pressure-inlet

⋏ Gauge Total Pressure (pascal)   446090.78

⋏ Supersonic/Initial Gauge Pressure (pascal)   446090.78

⋏ Total Temperature (k)   2343.93

⋏ Axial-Component of Flow Direction   1

⋏ Radial-Component of Flow Direction   0

⋏ Specify Species in Mole Fractions?   yes

⋏ Mole fractions: O_2 →0.20473; N_2→ 0.77618; NO→ 0.00905; O→ 0.00033

⋏ Pressure-outlet

⋏ Gauge Pressure (pascal)   48263.3

⋏ Backflow Total Temperature (k)   300

⋏ Axial-Component of Flow Direction   1

⋏ Radial-Component of Flow Direction   0

⋏ Specify Species in Mole Fractions?   yes

⋏ Backflow mole fractions: O_2 → 0.20939; N_2 → 0.78101;

$$NO \rightarrow 0; O \rightarrow 0$$

2. Boundary Conditions for N2- case 1:

- ○ Wall - Adiabatic

- ○ Pressure-inlet

  - ⚹   Gauge Total Pressure (pascal)   413685.4
  - ⚹   Supersonic/Initial Gauge Pressure (pascal) 413685.4
  - ⚹   Total Temperature (k)   4028.43
  - ⚹   Axial-Component of Flow Direction   1
  - ⚹   Radial-Component of Flow Direction   0
  - ⚹   Specify Species in Mole Fractions?   yes
  - ⚹   Mole fractions: $O_2 \rightarrow 0$; $N_2 \rightarrow 0.99952$; $NO \rightarrow 0$; $N \rightarrow 0.00048$

  - ⚹ Pressure-outlet

    - ⚹   Gauge Pressure (pascal)   67550 Pa
    - ⚹   Backflow Total Temperature (k)   300
    - ⚹   Axial-Component of Flow Direction   1
    - ⚹   Radial-Component of Flow Direction   0
    - ⚹   Specify Species in Mole Fractions?   yes
    - ⚹   Backflow mole fractions: $O_2 \rightarrow 0.20939$; $N_2 \rightarrow 0.78101$;

$$NO \rightarrow 0; O \rightarrow 0$$

3. Boundary Conditions for N2- case 2:

- ○ Wall - Adiabatic

- ○ Pressure-inlet

  - ⚹   Gauge Total Pressure (pascal)   413685.4
  - ⚹   Supersonic/Initial Gauge Pressure (pascal) 413685.4
  - ⚹   Total Temperature (k)   4091.96
  - ⚹   Axial-Component of Flow Direction   1
  - ⚹   Radial-Component of Flow Direction   0
  - ⚹ Specify Species in Mole Fractions?   yes
  - ⚹   Mole fractions: $O_2 \rightarrow 0$; $N_2 \rightarrow 0.99939$; $NO \rightarrow 0$; $N \rightarrow 0.00061$

  - ⚹ Pressure-outlet

⟡   Gauge Pressure (pascal)   67550 Pa

⟡   Backflow Total Temperature (k)   300

⟡   Axial-Component of Flow Direction   1

⟡   Radial-Component of Flow Direction   0

⟡   Specify Species in Mole Fractions?   yes

⟡   Backflow mole fractions: $O_2 \rightarrow$ 0.20939; $N_2 \rightarrow$ 0.78101;

                       $NO \rightarrow$ 0; $O \rightarrow$ 0

4. Boundary Conditions for N2- case 3:

- ◦   Wall - Adiabatic

- ◦   Pressure-inlet

     ⟡   Gauge Total Pressure (pascal)   39211.6

     ⟡   Supersonic/Initial Gauge Pressure (pascal)   39211.6

     ⟡   Total Temperature (k)   3736.85

     ⟡   Axial-Component of Flow Direction   1

     ⟡   Radial-Component of Flow Direction   0

     ⟡   Specify Species in Mole Fractions?   yes

     ⟡   Mole fractions: $O_2 \rightarrow$ 0; $N_2 \rightarrow$ 0.99984; $NO \rightarrow$ 0; $N \rightarrow$ 0.00016

⟡   Pressure-outlet

     ⟡   Gauge Pressure (pascal)   67550 Pa

     ⟡   Backflow Total Temperature (k)   300

     ⟡   Axial-Component of Flow Direction   1

     ⟡   Radial-Component of Flow Direction   0

     ⟡   Specify Species in Mole Fractions?   yes

     ⟡   Backflow mole fractions: $O_2 \rightarrow$ 0.20939; $N_2 \rightarrow$ 0.78101;

                       $NO \rightarrow$ 0; $O \rightarrow$ 0

      The nozzle exit was considered as a monitoring point along the axis of symmetry for all the results. The flow parameters such as Static Pressure, Static Temperature, Mach Number, Velocity Magnitude, Density and Specific Heat Ratio obtained from the CFD simulations on the fine-2 grid have been considered for comparison and analysis with respect to theoretical approximations. The flow was evaluated for equilibrium/frozen chemistry based on the species concentration along the axis of

symmetry. The contours and plots of all the N2 cases are included in the appendix section. The boundary layer analysis is discussed in detail in the next section.
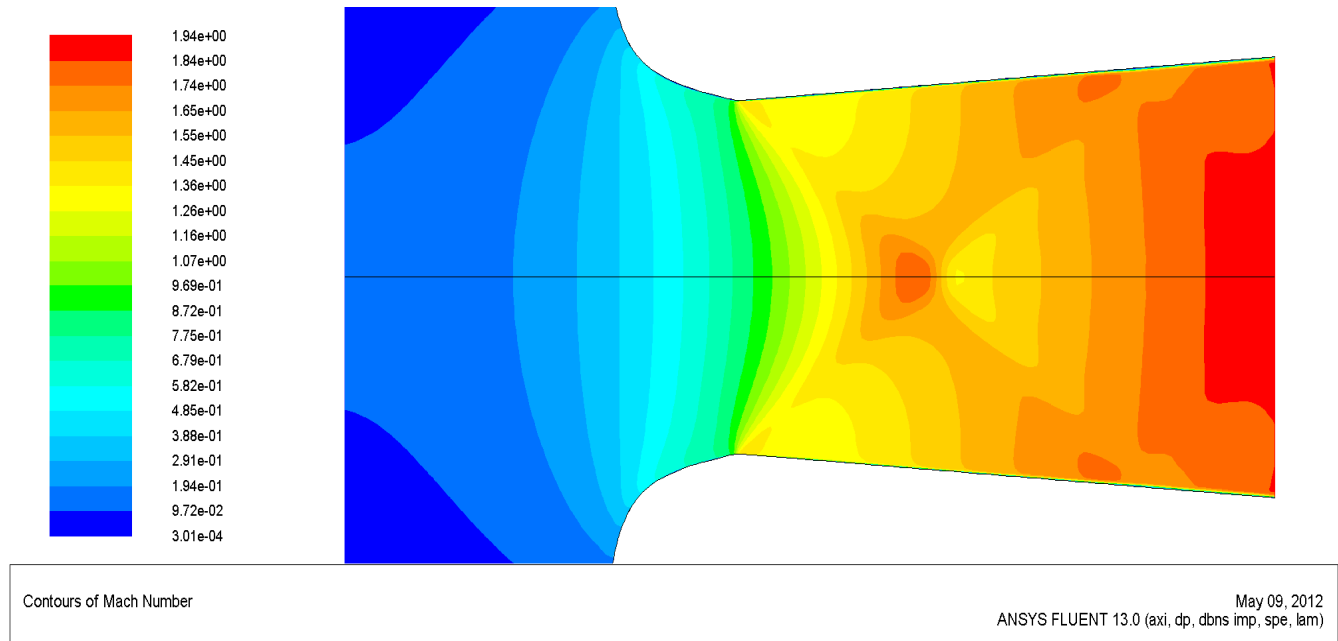
Fig 8.2: Mach Contours of the nozzle obtained from CFD solutions for the air-case using fine-2 grid.
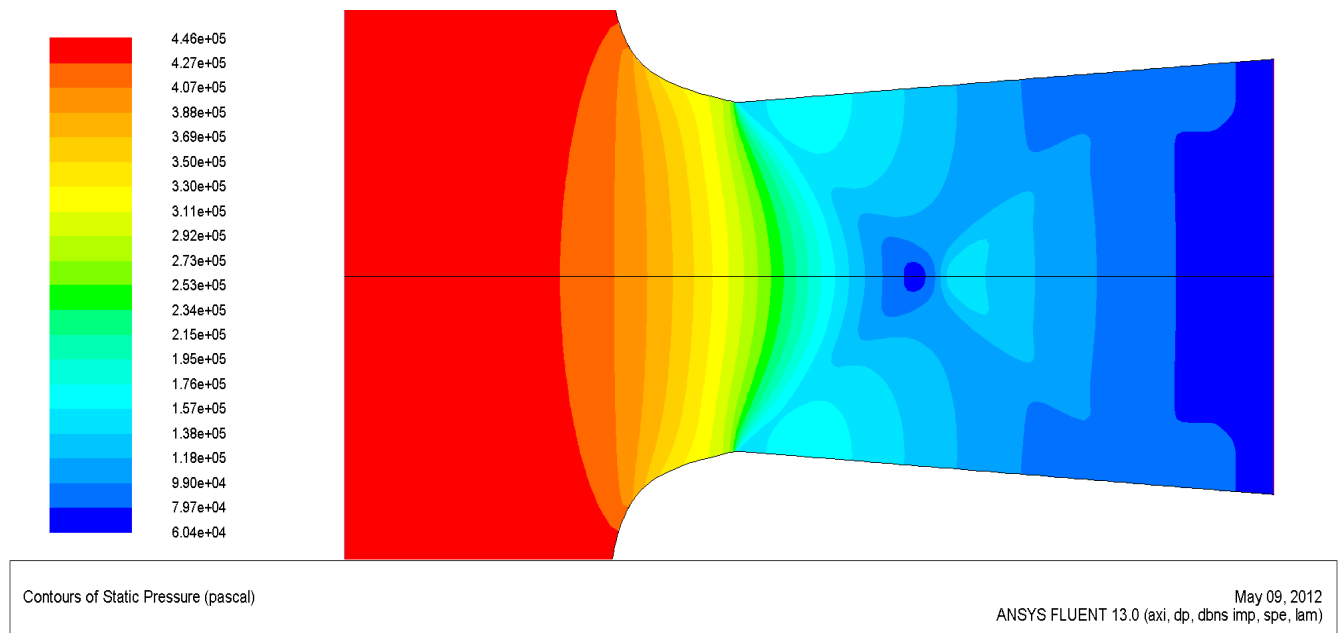
Fig 8.3: Static Pressure Contours of the nozzle obtained from CFD solutions for the air-case using fine-2 grid.
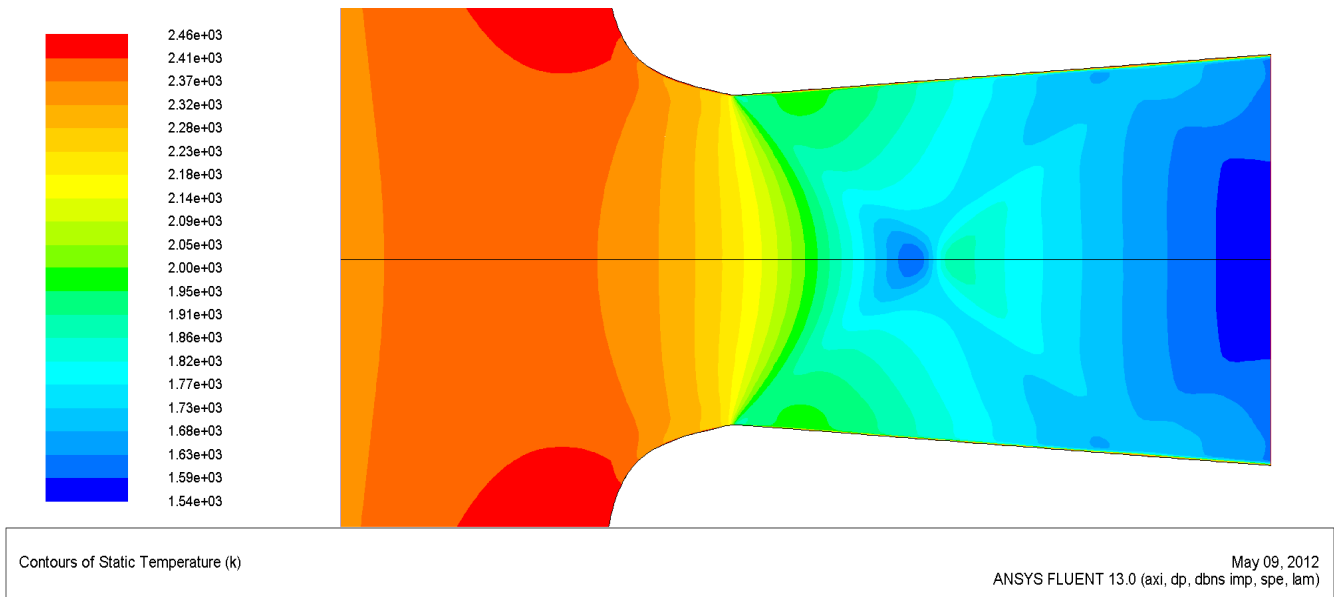
Fig 8.4: Static Temperature Contours of the nozzle obtained from CFD solutions for the air-case using fine-2 grid.
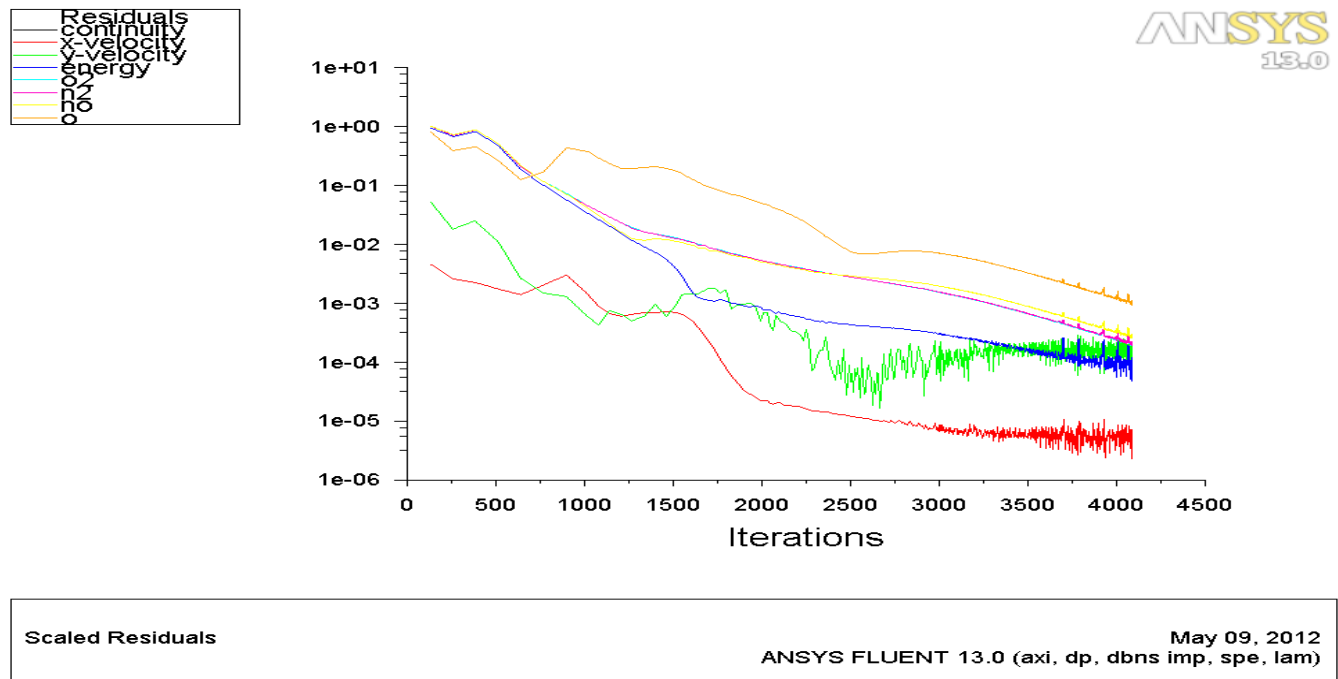
Fig 8.5: Residuals of the CFD solutions converging at 4090 iterations for the air-case using fine-2 grid.
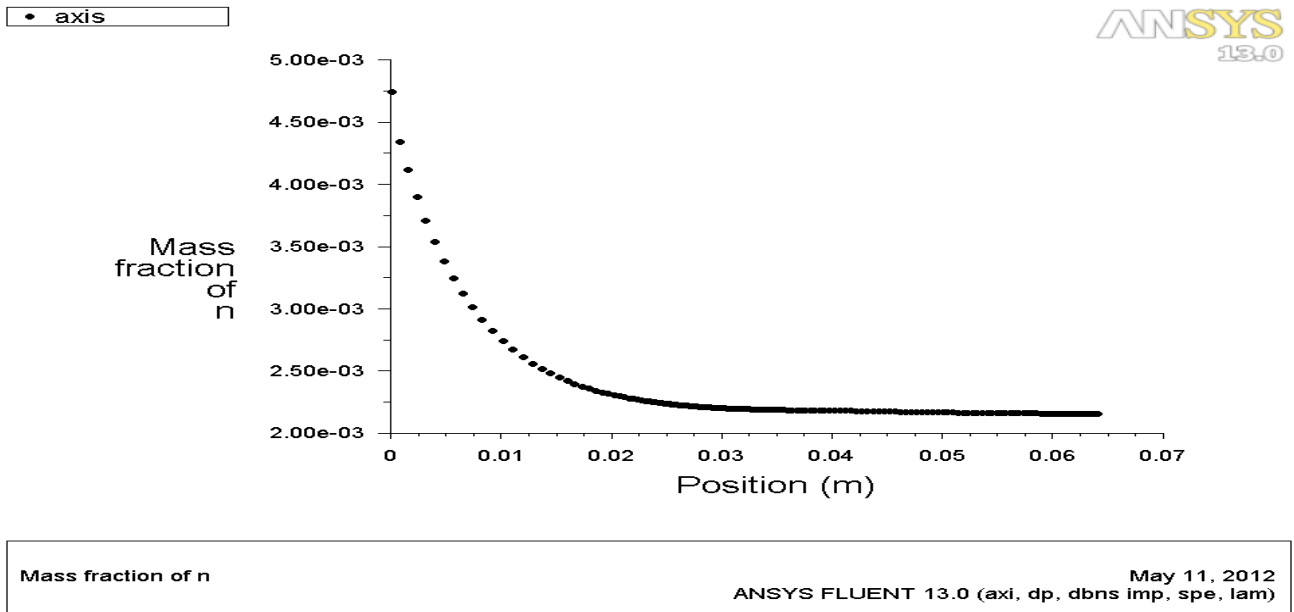
Fig 8.6: Mass fraction of N along the axis of symmetry of the nozzle for the air-case using fine-2 grid.
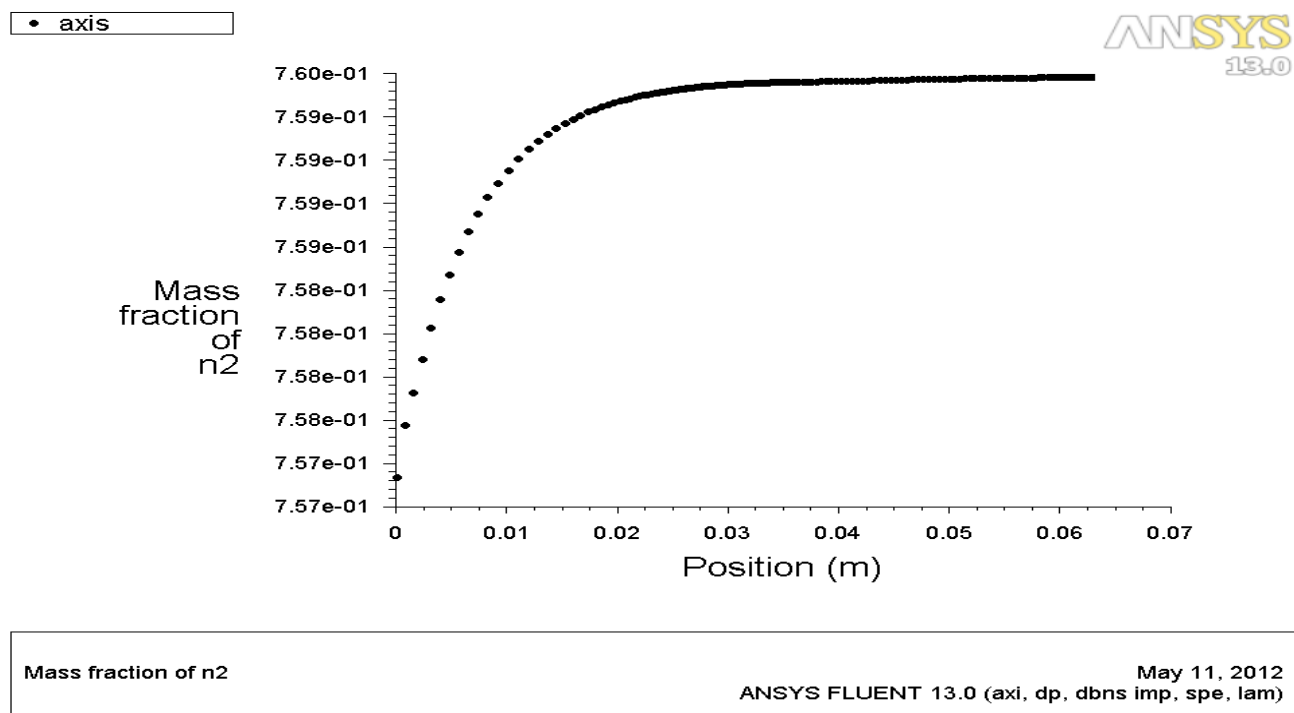
Fig 8.7: Mass fraction of N2 along the axis of symmetry of the nozzle for the air-case using fine-2 grid.
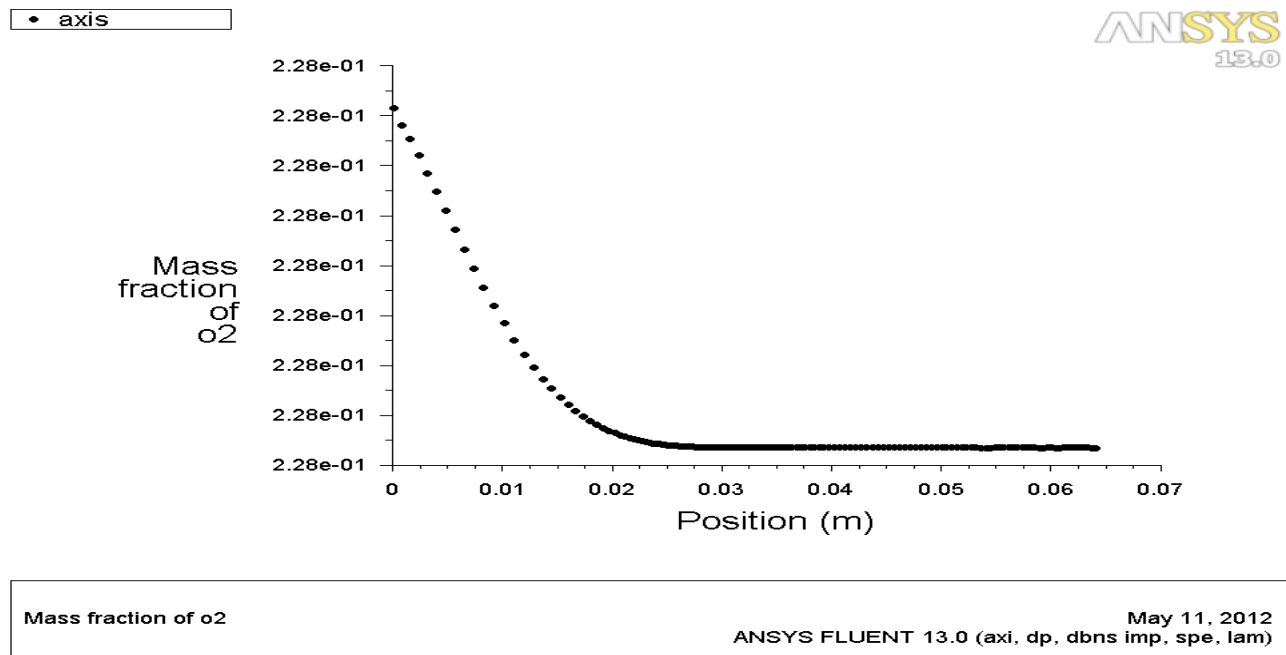
Fig 8.8: Mass fraction of O2 along the axis of symmetry of the nozzle for the air-case using fine-2 grid.
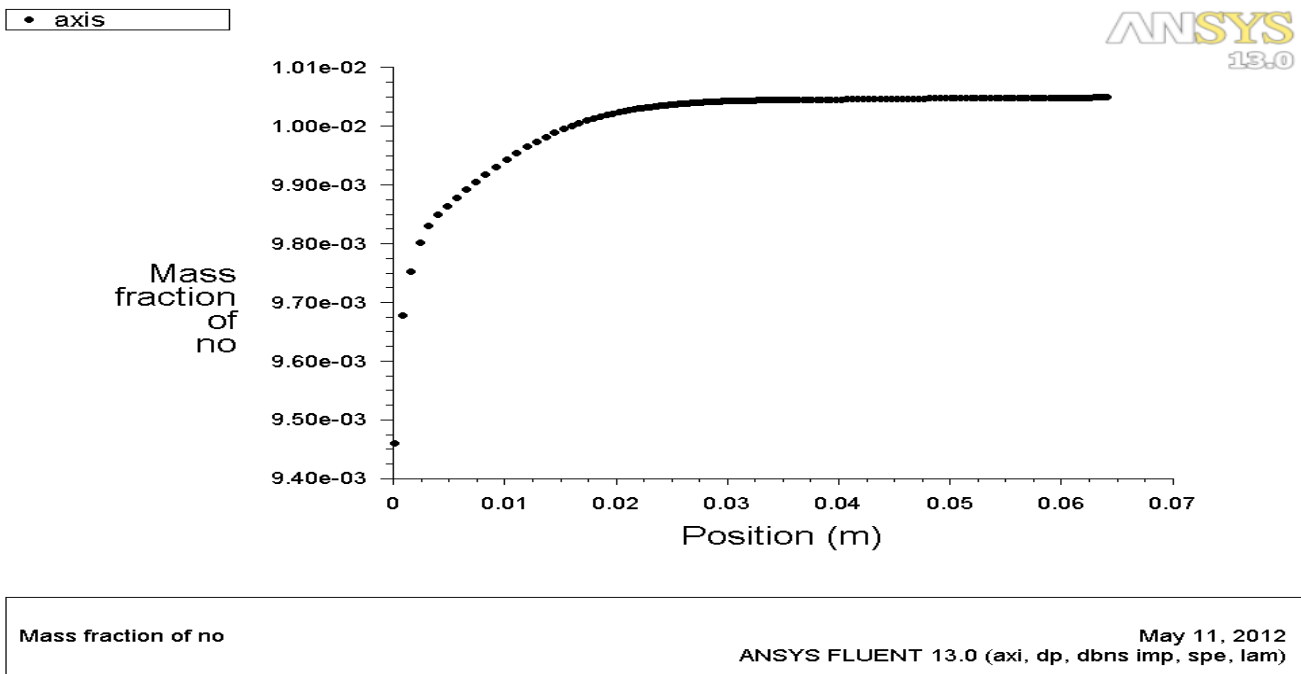
Fig 8.9: Mass fraction of NO along the axis of symmetry of the nozzle for the air-case using fine-2 grid.

Material	m-flow	P0	H0	Pexit-eq	Pexit-fr	Pexit-CFD	% deviation	% deviation
	kg/s	psi	MJ/kg	Pa	Pa	Pa	equilibrium	frozen
Air	0.123	64.7	2.439	73504	72258	63256.3	13.9416902	12.4577209
N2-case1	0.107	60	4.696	68316	68280	59670.1	12.6557468	12.6096954
N2-case2	0.105	60	4.785	68348	68300	59699	12.6543571	12.5929722
N2-case3	0.117	55	4.295	62500	62492	54668.4	12.53056	12.5193625

Table 8.3: Comparison of nozzle exit Static Pressure obtained from CFD with Theoretical estimation

Material	m-flow	P0	H0	Mexit-eq	Mexit-fr	Mexit-CFD	% deviation	% deviation
	kg/s	psi	MJ/kg				equilibrium	frozen
Air	0.123	64.7	2.439	1.848	1.859	1.93804	-4.872294372	-4.251748252
N2-case1	0.107	60	4.696	1.853	1.854	1.93357	-4.348084188	-4.29180151
N2-case2	0.105	60	4.785	1.853	1.854	1.93336	-4.336751214	-4.280474649
N2-case3	0.117	55	4.295	1.854	1.854	1.93346	-4.285868393	-4.285868393

Table 8.4: Comparison of nozzle exit Mach Number obtained from CFD with Theoretical estimation

Material	m-flow	P0	H0	Texit-eq	Texit-fr	Texit-CFD	% deviation	% deviation
	kg/s	psi	MJ/kg	K	K	K	equilibrium	frozen
Air	0.123	64.7	2.439	1582.61	1558.39	1541.67	2.586866	1.07290216
N2-case1	0.107	60	4.696	2702.57	2692.7	2613.4	3.299452	2.94499944
N2-case2	0.105	60	4.785	2748.53	2736.11	2655.68	3.37816942	2.9395748
N2-case3	0.117	55	4.295	2496.42	2493.13	2420.06	3.05878017	2.93085399

Table 8.5: Comparison of nozzle exit Static Temperature obtained from CFD with Theoretical estimation

Material	m-flow	P0	H0	Υexit-eq	Υexit-fr	Υexit-CFD	% deviation	% deviation
	kg/s	psi	MJ/kg				equilibrium	frozen
Air	0.123	64.7	2.439	1.2999	1.3088	1.30897	-0.69774598	-0.012988998
N2-case1	0.107	60	4.696	1.2918	1.2921	1.29255	-0.05805852	-0.034827026
N2-case2	0.105	60	4.785	1.2914	1.2918	1.29222	-0.06349698	-0.032512773
N2-case3	0.117	55	4.295	1.2938	1.2939	1.29435	-0.04251043	-0.034778576

Table 8.6: Comparison of nozzle exit Specific Heat Ratio (Gamma) obtained from CFD with Theoretical estimation

Material	m-flow kg/s	P0 psi	H0 MJ/kg	ρexit-eq kg/m3	ρexit-fr kg/m3	ρexit-CFD kg/m3	% deviation equilibrium	% deviation frozen
Air	0.123	64.7	2.439	0.1618	0.1615	0.14196	12.26205192	12.09907121
N2-case1	0.107	60	4.696	0.085168	0.085394	0.0768372	9.781608116	10.02037614
N2-case2	0.105	60	4.785	0.083782	0.084053	0.0756407	9.717242367	10.00832808
N2-case3	0.117	55	4.295	0.084352	0.084437	0.0760445	9.848610584	9.939363075

Table 8.7: Comparison of nozzle exit density obtained from CFD with Theoretical estimation

Material	m-flow kg/s	P0 psi	H0 MJ/kg	Vexit-eq m/s	Vexit-fr m/s	Vexit-CFD m/s	% deviation equilibrium	% deviation frozen
Air	0.123	64.7	2.439	1420.188	1422.5068	1480.12	-4.220004675	-4.050117722
N2 only	0.107	60	4.696	1886.1687	1884.4	1937.2	-2.705553326	-2.801952876
N2 only	0.105	60	4.785	1901.9192	1899.423	1952.49	-2.658935248	-2.793848448
N2 only	0.117	55	4.295	1815.2514	1814.3244	1865.07	-2.744446306	-2.796941936

Table 8.8: Comparison of nozzle exit Velocity obtained from CFD with Theoretical estimation

The following observations and inferences were made from the "converged" CFD solutions and the calculations based on those solutions for all the four cases:

⚔ A shock wave was observed at the beginning of the divergent part of the nozzle. It intersects at a distance of 39.5 mm from the beginning of the chamber opening. This phenomenon could be attributed towards the geometrical nature of the divergent part of the nozzle. A shock wave is often observed in case of a conical nozzle.

⚔ The mass fraction of O2 decreases from chamber to the throat. The mass fraction of N2 increases from chamber to the throat. The mass fraction of NO increases from chamber to the throat. The mass fraction of O increases from chamber to the throat. The mass fraction of N decreases from chamber to the throat.

⚔ The mass fractions of all the species varied drastically from the beginning of the chamber till the throat. But they all remained the same from throat to the exit of the nozzle. Hence, the flow can be considered as **"frozen"** from the throat till the end of the nozzle. This is purely based on species concentration plots and the specific heat ration plot along the axis of symmetry. This actually validates our initial assumption used in the theoretical approximation.

⚔ The static pressure at the exit of the nozzle along the axis of symmetry showed a highest average deviation of 12.54% and 12.94% from that of theoretical estimations of the frozen and the equilibrium flows respectively. This strongly represents the poor quality of the grid since the pressure is the one of the very few flow parameters that could be matched within 1% accuracy

with a good quality grid.

⚔ The static pressure at the exit of the nozzle decreases with increase in the total enthalpy and increases with the increase in total pressure at the chamber.

⚔ The density at the exit of the nozzle along the axis of symmetry showed a next highest average deviation of 10.517% and 10.4% from that of theoretical estimations of the frozen and the equilibrium flows respectively. The reason for such a large deviation is the same as mentioned in the corresponding case of static pressure.

⚔ The density at the exit of the nozzle decreases with increase in the total enthalpy and increases with the increase in total pressure at the chamber.

⚔ The Mach number at the exit of the nozzle along the axis of symmetry matched closely with that of theoretical estimations of the frozen and the equilibrium flows with an average deviation of 4.28% and 4.46% respectively.

⚔ The Mach number was at the exit of the nozzle remained the same (1.933) for all the four cases irrespective of the chamber pressure and chamber enthalpies.

⚔ The velocity magnitude at the exit of the nozzle along the axis of symmetry matched closely with that of theoretical estimations of the frozen and the equilibrium flows with an average deviation of 3.11% and 3.082% respectively.

⚔ The velocity magnitude at the exit of the nozzle increases with increase in the total enthalpy and decreases with the increase in total pressure at the chamber.

⚔ The static temperature at the exit of the nozzle along the axis of symmetry matched closely with that of theoretical estimations of the frozen and the equilibrium flows with an average deviation of 2.472% and 3.08% respectively. This indicates the successful chemical modeling of the problem. Since temperature has a direct relation with the chemistry in our case.

⚔ The static temperature at the exit of the nozzle increases with increase in the total enthalpy and decreases with the increase in total pressure at the chamber.

⚔ The specific heat ratio at the exit of the nozzle along the axis of symmetry showed a least average deviation of 0.028% and 0.215% from that of theoretical estimations of the frozen and the equilibrium flows respectively. Since the flow is considered to be *frozen* we can say that the chemical modeling part of the CFD solutions have matched the theoretical approximations with almost 100% accuracy!!!!!!!

9.0 Boundary Layer Analysis- CFD:

The CFD solutions obtained after convergence of all the cases were zoomed in for boundary layer analysis. The velocity magnitude and static temperature of the flow were plotted against the distance from the inner wall of the nozzle at the exit. Since the boundary layer mesh had the first grid point placed at y+ = 1, the velocity and thermal boundary layers were captured with a very good resolution. The thickness of the velocity boundary layer was found to be 0.3443 mm and 0.4406 mm for air and all the N2 cases respectively. The thermal boundary layer for all the cases was found to be around 0.5 mm . It was found that the presence of 29 grid points within the boundary layers enhanced the accuracy of the solution since the minimum number of grid points for effectively capturing a boundary layer is 10. The air had lower thicknesses compared to all the N2 cases. This phenomenon could be attributed to air being less viscous as compared to N2 gas.
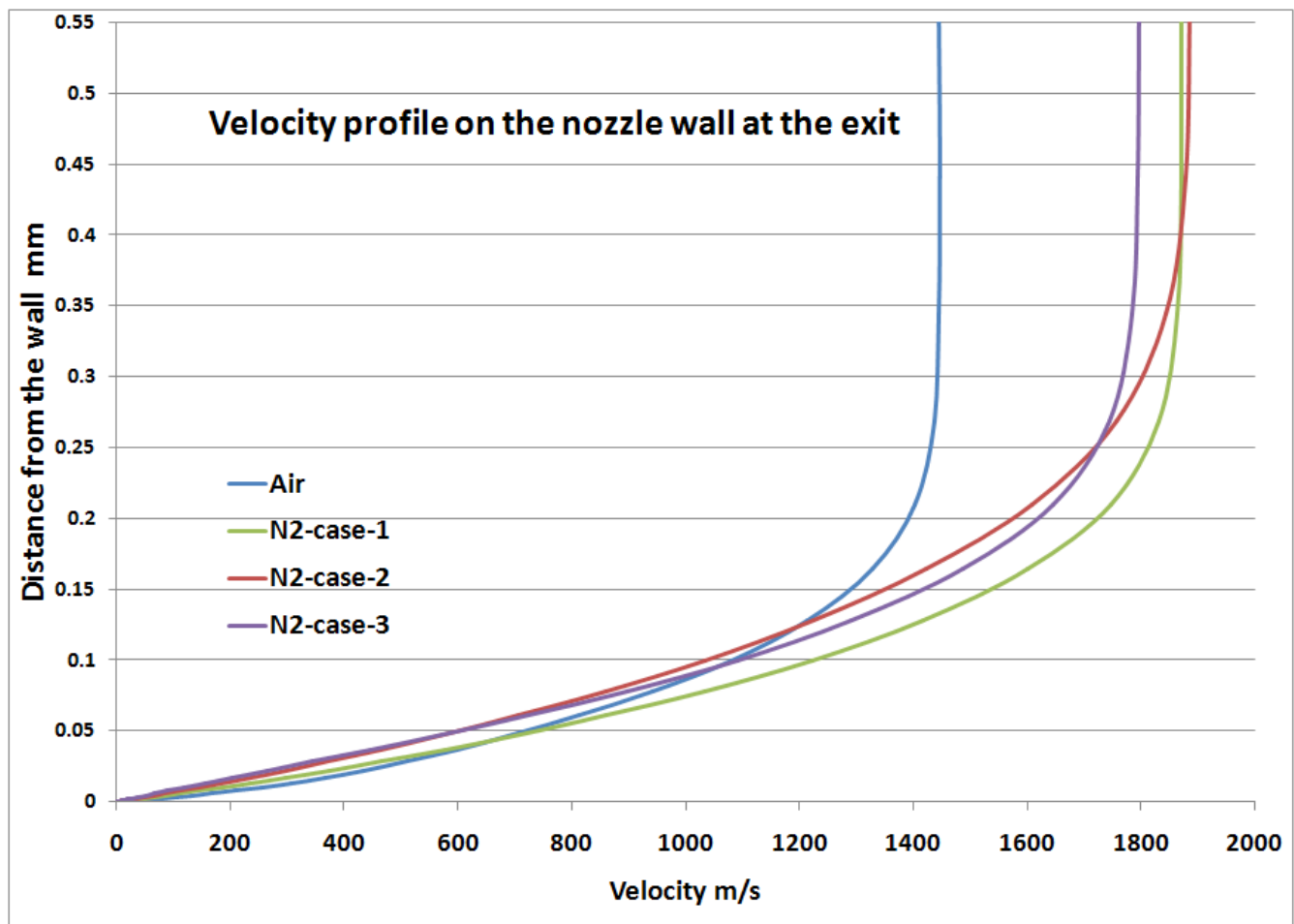
Fig 9.1: Velocity boundary layer plots of Air and N2 cases from the nozzle wall at the exit.
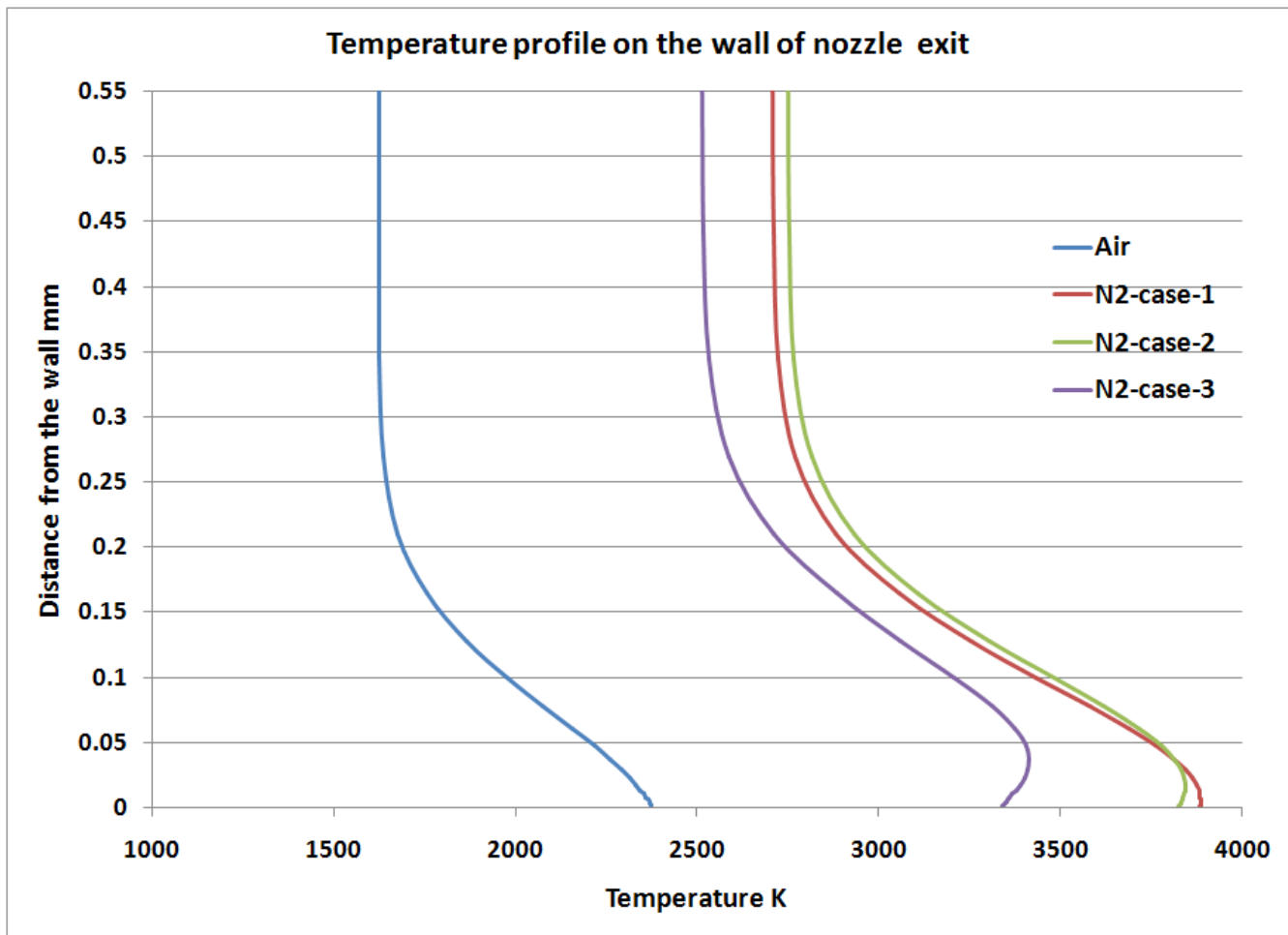
Fig 9.2: Velocity boundary layer plots of Air and N2 cases from the nozzle wall at the exit.

The bulge seen in the thermal boundary layers could be the result of viscous dissipation effects. It can also be observed that increase in total enthalpy at the chamber increases the wall temperature at the exit. This is found by comparing N2-case-1 and N2- case-2 which have the exact same total pressure conditions but slightly different total enthalpies. Similarly, the velocity profile of N2- case-2 is steeper than that of N2-case-1 clearly indicating that the increase in total enthalpy decreases the shear stress induced by the velocity boundary layer along the wall of the nozzle. This correlation is supported by the direct shear stress values obtained from FLUENT for the divergent part of the nozzle. The shear stress values provided by the code were 312.929 N/m2 and 310.068 N/m2 for N2-case-1 and N2-case 2 respectively. The shear stress difference is very small because the difference in enthalpy between these two cases were small.
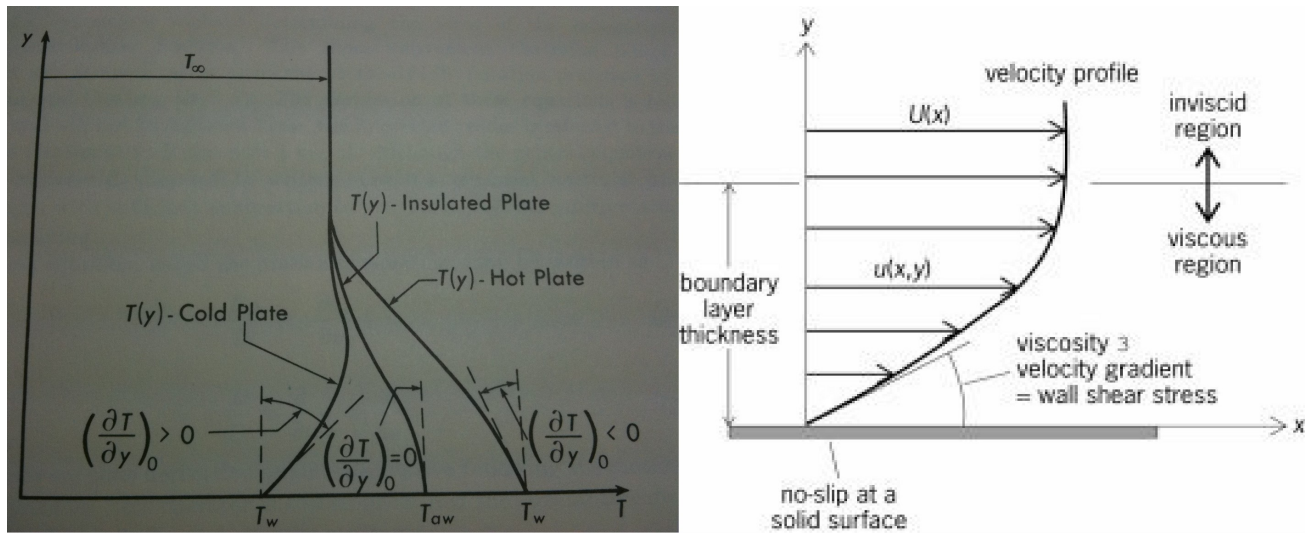
Fig 9.3: Theoretical thermal boundary layer profile for an adiabatic wall and velocity boundary layer profile for laminar flow over a flat plate. [6]

The velocity and thermal boundary layer profiles obtained from CFD at the wall of the nozzle resembles closely with theoretical thermal boundary layer profile for an adiabatic wall and velocity boundary layer profile for laminar flow over a flat plate.

10.0 **Proposed work for future:**

      The initial objectives of the entire project were accomplished only to a certain extent due to the reasons explained at the end of section 8.0. However, the objectives that were defined afresh at the latter stage of the project were achieved quite successfully. The following improvisations could definitely help modeling the entire test section for such complicated flows:

- ⚔ The existing nozzle grid can be modified for better orthogonality and lower aspect ratio, with the aid of a powerful computing capability. The grid can be taken through an iterative process of grid refinement for obtaining an optimum grid thus saving tremendous computational effort.

- ⚔ Grid convergence is one of the key milestones that mark the successful modeling of any problem in CFD. Hence, the nozzle should be tested thoroughly for the grid convergence, with the aid of a powerful computing capability.

- ⚔ The nozzle wall is considered as adiabatic in our cases as well as the one published by the GHIBLI facility. [11] [12] However, more accurate near modeling solutions can be obtained with the determination of the "exact" temperature and the nature of heat transfer at the wall considering the material properties of the wall.

- ⚔ While modeling the flow through the test section over the TPS specimen, it makes more sense to accommodate the chemical properties and radiative features of the specimen. This modification would definitely match the experimental results with very less amount of errors.

- ⚔ Convergence criteria of 1e-3 was used throughout the project. However, a more accurate set of solutions can be obtained if one can get the residuals of the same models to converge at 1e-5 .

- ⚔ We can run 15 to 20 different cases based on the possible range of total pressure and total enthalpy at the chamber. It would then be easy and make more sense to determine the correlation equations between the flow conditions at the nozzle exit and the total pressure and total enthalpy at the chamber. This is the exact same procedure explained and successfully validated in the GHIBLI publication.

- ⚔ The same set of studies can be extended to modeling of the same facility different materials such as O2.

- ⚔ The successful modeling the arc jet can be really helpful in the modeling and analysis of the reentry phenomena which is considered to me one of the most complicated flow problems.

References

1. Anderson, J. D., Jr (2006). *Hypersonics and High-Temperature Gas Dynamics (2nd ed.).* Virginia: AIAA Education Series.

2. Park, Chul (1989). *Assessment of Two-Temperature Kinetic Model for Ionizing Air   (Vol 3. No 3.)* Journal of Thermophysics.

3. Park, Chul (1989). *A Review of Reaction Rates in High Temperature Air (AIAA-89-1740).* New York: AIAA 24th Thermophysics Conference.

4. Deutshmann, O.; Riedel, U.; and Warnatz, J. *Modelling Of Surface Reactions In Hypersonic Re-entry Flow Fields.* Germany: Im Neuenheimer Feld (368, D-69120)

5. Ethiraj Venkatapathy* (Lead), Christine E. Szalai***, Bernard Laub*, Helen H. Hwang*, Joseph L. Conley*, James Arnold**, and 90 Co-authors .WHITE PAPER TO THE NRC DECADAL PRIMITIVE BODIES SUB-PANEL *Thermal Protection System Technologies for Enabling Future Sample Return Missions.* * NASA ARC, ** UC Santa Cruz, *** JPL.

6. Trutt, R.W (1960). *Fundamentals of Aerodynamic Heating.* New York: THE RONALD PRESS COMPANY.

7. Schlichting, Dr. H (1979). *Boundary Layer Theory.* New York: Mc-GRAW HILL BOOK COMPANY.

8. Anderson, J. D., Jr (2005). *Fundamentals of Aerodynamics* (5th ed.). New Delhi: Tata McGraw-Hill.

9. Anderson, J. D., Jr (2003). *Modern Compressible Flow with historical perspective* (3rd ed.). New York: Tata McGraw-Hill.

10. Anderson, J.D., Jr (1995). *Computational Fluid Dynamics: THE BASICS WITH APPLICATIONS.* United States of America: McGraw-Hill.

11. Purpura, C.; Filippis, F.D.; Graps, E.; Trifoni, E.; Savino, R (2007). *The GHIBLI plasma wind tunnel: Description of the new CIRA-PWT facility.* Italy: Acta Astronautica 61 (2007) 331 – 340.

12. Borrelli, S.; Filippis, F.D.; Marini, M.; Schettino, A. *CFD FOR SCIROCCO PROJECT.* CIRA, Italy.

13. Viviani, A.; Pezzella, G. *Computational Flowfield Analysis of a Planetary Entry Vehicle*. CIRA, Italy.

14. Fletcher, D.G. *Measurement Requirements for Improved Modeling of Arcjet Facility Flows*. Reacting Flow Environments Branch, NASA Ames Research Center.

15. Gnoffo, P, A (1999). *PLANETARY-ENTRY GAS DYNAMICS[1]*. Hampton: Annu. Rev. Fluid Mech. 1999. 31:459–94

16. Witte, A.B (1967). *PART I. EXPERIMENTAL INVESTIGATION OF AN ARC-HEATED SUPERSONIC FREE JET PART 11. ANALYSIS OF ONE-DIMENSIONAL ISENTROPIC FLOW FOR PARTIALLY IONIZED ARGON.* Pasadena: Thesis submitted towards Doctor of Philosophy at California Insitute of Technology.

17. Fletcher, D.G (2004). *FUNDAMENTALS OF HYPERSONIC FLOW- AEROTHERMODYNAMICS* (RTO-EN-AVT-116). Belgium: RTO-AVT Lecture Series on " Critical Technologies for Hypersonic Vehicle Development" .

18. Dr. Gerasimov, A (2006). *Modelling Turbulent Flows with Fluent*. Fluent Europe Ltd. ANSYS Inc.

19. Kalitzin, G.; Medic, G.; Iaccarino, G.; Durbin, P (2004). *Near-wall behavior of RANS turbulence models and implications for wall functions*. Stanford: JOURNAL OF COMPUTATIONAL PHYSICS.

20. Salim, S.M.; Cheah, S.C (2009). *Wall y+ Strategy for Dealing with Wall-bounded Turbulent Flows* (ISBN: 978-988-17012-7-5) . Hong Kong: Proceedings of the International MultiConference of Engineers and Computer Scientists 2009 Vol II.

21. Steinfeld, D.E (1989). *The determination of the free stream temperature of air in a shock tube*, The University of Texas at Arlington.

Web References:

22. *Thermal Protection System (TPS) and Materials*, Humans in Space, NASA Ames official website
http://www.nasa.gov/centers/ames/research/humaninspace/humansinspace-thermalprotectionsystem.html

23. *NASA Ames Arc Jet Complex*, NASA Ames official website
http://www.nasa.gov/centers/ames/pdf/146635main_rtf_arcjet.pdf

24. *Ames Technology Capabilities and Facilities*, NASA Ames official website.
http://www.nasa.gov/centers/ames/research/technology-onepagers/arcjetcomplex.html

25. *Arc Jet Tunnel*, Aerodynamics Research Center UT-Arlington official website.
http://arc.uta.edu/facilities/archeater.htm

26. *The Work of Ludwig Prandtl*, U.S Centennial of Flight Commission official website.

http://www.centennialofflight.gov/essay/Theories_of_Flight/Prandtl/TH10.htm

27. *Chemical Equilibrium with Applications*, NASA GLENN RESEARCH CENTER.

http://www.grc.nasa.gov/WWW/CEAWeb/ceaWhat.htm

28. THEODORE VON KARMAN, International Space Hall of Fame-New Mexico Museum of Space History Official Website.

http://www.nmspacemuseum.org/halloffame/detail.php?id=31

Tutorials:

29. *Hypersonic Flow over a Re-entry Pod*, FLUENT code – ANSYS Inc.

NASA JPL Technical Presentations:

30. White, T., and Tang, C (2008). *Arc-Jet Computational Simulations of Ablators for the Mars Science Laboratory Program* (*Session V: Ongoing and Proposed EDL Technology Development*). 6th Annual International Planetary Probes Workshop- Georgia Institute of Technology.

Appendix:

A1. CEA output files for all the four cases used in the advanced nozzle analysis

1 a) Air-equilibrium

problem

  rocket equilibrium tcest,k= 3800

  p,psia=64.7,

  sub,ae/at=14.074,

  sup,ae/at=1.5639,

  h/r=294.3472257

 react

  name=Air wt=1 t,k=300

output massf

   plot p t rho h s cp gam son mach vis cond condfz pran pranfz

 end

OPTIONS: TP=F HP=F SP=F TV=F UV=F SV=F DETN=F SHOCK=F REFL=F INCD=F

RKT=T FROZ=F EQL=T IONS=F SIUNIT=T DEBUGF=F SHKDBG=F DETDBG=F
TRNSPT=F

TRACE= 0.00E+00 S/R= 0.000000E+00 H/R= 2.943472E+02 U/R= 0.000000E+00

AE295- CFD Modeling and analysis of an Arc-jet facility using ANSYS Fluent

Pc,BAR =   4.460891

Pc/P =

SUBSONIC AREA RATIOS =   14.0740

SUPERSONIC AREA RATIOS =   1.5639

NFZ= 1 Mdot/Ac= 0.000000E+00 Ac/At= 0.000000E+00

   REACTANT   WT.FRAC   (ENERGY/R),K   TEMP,K DENSITY

      EXPLODED FORMULA

N: Air   1.000000 -0.862210E+01   300.00 0.0000

    N 1.56168 O 0.41959 AR 0.00937 C 0.00032

 SPECIES BEING CONSIDERED IN THIS SYSTEM

(CONDENSED PHASE MAY HAVE NAME LISTED SEVERAL TIMES)

 LAST thermo.inp UPDATE: 10/22/02

g 3/98 *Ar   g 7/97 *C   g 8/99 *CN

g12/99 CNN   tpis79 *CO   g 9/99 *CO2

tpis91 *C2   g 7/00 CCN   tpis91 CNC

srd 01 OCCN   tpis79 C2N2   g 8/00 C2O

tpis79 *C3   srd 01 CNCOCN   g 7/88 C3O2

g tpis *C4   g 6/01 C4N2   g 8/00 *C5

g 5/97 *N   g 6/01 NCO   tpis89 *NO

g 4/99 NO2   j12/64 NO3   tpis78 *N2

g 6/01 NCN   g 4/99 N2O   g 4/99 N2O3

tpis89 N2O4   g 4/99 N2O5   tpis89 N3

g 5/97 *O   tpis89 *O2   g 8/01 O3

n 4/83 C(gr)   n 4/83 C(gr)   n 4/83 C(gr)

O/F = 0.000000

	EFFECTIVE FUEL	EFFECTIVE OXIDANT	MIXTURE
ENTHALPY	h(2)/R	h(1)/R	h0/R
(KG-MOL)(K)/KG	-0.29767190E+00	0.00000000E+00	0.29434723E+03

| KG-FORM.WT./KG | bi(2) | bi(1) | b0i |

*N   0.53915890E-01   0.00000000E+00   0.53915890E-01

*O   0.14486046E-01   0.00000000E+00   0.14486046E-01

*Ar   0.32331996E-03   0.00000000E+00   0.32331996E-03

*C   0.11013248E-04   0.00000000E+00   0.11013248E-04

POINT ITN   T   N   O   AR   C

 1 20   2343.926   -13.126   -14.728   -24.773   -29.902

Pinf/Pt = 1.804957

 2   4   2073.258   -13.206   -14.788   -25.098   -32.300

Pinf/Pt = 1.816572

 2   2   2070.421   -13.207   -14.788   -25.101   -32.329

Pinf/Pt = 1.816681

 2   1   2070.394   -13.207   -14.788   -25.101   -32.329

 3   1   2343.841   -13.126   -14.728   -24.773   -29.903

3	1	2343.687	-13.126	-14.728	-24.773	-29.904
3	2	2343.500	-13.126	-14.728	-24.773	-29.906
3	1	2343.414	-13.126	-14.728	-24.773	-29.906
3	1	2343.405	-13.126	-14.728	-24.773	-29.906
4	4	1599.613	-13.361	-14.912	-25.722	-38.592
4	2	1582.502	-13.368	-14.918	-25.746	-38.893
4	1	1582.610	-13.368	-14.918	-25.746	-38.891

THEORETICAL ROCKET PERFORMANCE ASSUMING EQUILIBRIUM

COMPOSITION DURING EXPANSION FROM INFINITE AREA COMBUSTOR

Pin =   64.7 PSIA

CASE =

REACTANT   WT FRACTION   ENERGY   TEMP

(SEE NOTE)   KJ/KG-MOL   K

NAME   Air   1.0000000   -71.689   300.000

O/F=   0.00000 %FUEL= 0.000000 R,EQ.RATIO= 0.001521 PHI,EQ.RATIO= 0.000000

CHAMBER THROAT   EXIT   EXIT

	CHAMBER	THROAT	EXIT	EXIT
Pinf/P	1.0000	1.8167	1.0011	6.0689
P, BAR	4.4609	2.4555	4.4560	0.73504
T, K	2343.93	2070.39	2343.40	1582.61
RHO, KG/CU M	6.6257-1	4.1311-1	6.6198-1	1.6180-1
H, KJ/KG	2447.35	2069.23	2446.61	1439.50
U, KJ/KG	1774.08	1474.82	1773.49	985.21
G, KJ/KG	-18112.5	-16091.4	-18108.7	-12442.4
S, KJ/(KG)(K)	8.7716	8.7716	8.7716	8.7716
M, (1/n)	28.946	28.961	28.946	28.965
(dLV/dLP)t	-1.00035	-1.00009	-1.00035	-1.00000
(dLV/dLT)p	1.0088	1.0024	1.0088	1.0001

Cp, KJ/(KG)(K)   1.4371   1.3473   1.4369   1.2442

GAMMAs   1.2548   1.2723   1.2548   1.2999

SON VEL,M/SEC   919.1   869.6   919.1   768.5

MACH NUMBER   0.000   1.000   0.042   1.848

PERFORMANCE PARAMETERS

Ae/At   1.0000   14.074   1.5639

CSTAR, M/SEC   1241.7   1241.7   1241.7

CF   0.7003   0.0311   1.1434

Ivac, M/SEC   1553.1   17496.7   1739.7

Isp, M/SEC   869.6   38.6   1419.8

MASS FRACTIONS

*Ar   0.01292 0.01292 0.01292 0.01292

*CO2   0.00048 0.00048 0.00048 0.00048

*NO   0.01720 0.00938 0.01718 0.00184

NO2   0.00006 0.00003 0.00006 0.00001

*N2   0.74714 0.75080 0.74714 0.75432

*O   0.00075 0.00018 0.00075 0.00000

*O2   0.22146 0.22621 0.22147 0.23042

 * THERMODYNAMIC PROPERTIES FITTED TO 20000.K

PRODUCTS WHICH WERE CONSIDERED BUT WHOSE MASS FRACTIONS WERE LESS THAN 5.000000E-06 FOR ALL ASSIGNED CONDITIONS

*C   *CN   CNN   *CO   *C2

CCN   CNC   OCCN   C2N2   C2O

*C3   CNCOCN   C3O2   *C4   C4N2

*C5   *N   NCO   NO3   NCN

N2O   N2O3   N2O4   N2O5   N3

O3   C(gr)

NOTE. WEIGHT FRACTION OF FUEL IN TOTAL FUELS AND OF OXIDANT IN TOTAL OXIDANTS

AE295- CFD Modeling and analysis of an Arc-jet facility using ANSYS Fluent

1 b) Air-frozen

 problem

  rocket frozen nfz=2

  p,psia=64.7,

  sub,ae/at=14.074,

  sup,ae/at=1.5639,

  h/r= 294.3472257

react

  name=Air wt=1 t,k=300

 end

OPTIONS: TP=F HP=F SP=F TV=F UV=F SV=F DETN=F SHOCK=F REFL=F INCD=F

RKT=T FROZ=T EQL=F IONS=F SIUNIT=T DEBUGF=F SHKDBG=F DETDBG=F
TRNSPT=F

TRACE= 0.00E+00 S/R= 0.000000E+00 H/R= 2.943472E+02 U/R= 0.000000E+00

Pc,BAR =   4.460891

Pc/P =

SUBSONIC AREA RATIOS =   14.0740

SUPERSONIC AREA RATIOS =   1.5639

NFZ= 2 Mdot/Ac= 0.000000E+00 Ac/At= 0.000000E+00

   REACTANT   WT.FRAC   (ENERGY/R),K   TEMP,K DENSITY

      EXPLODED FORMULA

N: Air   1.000000 -0.862210E+01   300.00 0.0000

      N 1.56168 O 0.41959 AR 0.00937 C 0.00032

 SPECIES BEING CONSIDERED IN THIS SYSTEM

(CONDENSED PHASE MAY HAVE NAME LISTED SEVERAL TIMES)

 LAST thermo.inp UPDATE: 10/22/02

  g 3/98 *Ar   g 7/97 *C   g 8/99 *CN

  g12/99 CNN   tpis79 *CO   g 9/99 *CO2

  tpis91 *C2   g 7/00 CCN   tpis91 CNC

  srd 01 OCCN   tpis79 C2N2   g 8/00 C2O

tpis79 *C3   srd 01 CNCOCN   g 7/88 C3O2

g tpis *C4   g 6/01 C4N2   g 8/00 *C5

g 5/97 *N   g 6/01 NCO   tpis89 *NO

g 4/99 NO2   j12/64 NO3   tpis78 *N2

g 6/01 NCN   g 4/99 N2O   g 4/99 N2O3

tpis89 N2O4   g 4/99 N2O5   tpis89 N3

g 5/97 *O   tpis89 *O2   g 8/01 O3

n 4/83 C(gr)   n 4/83 C(gr)   n 4/83 C(gr)

WARNING!! FOR FROZEN PERFORMANCE, SUBSONIC AREA

RATIOS WERE OMITTED SINCE nfz IS GREATER THAN 1 (ROCKET)

O/F = 0.000000

	EFFECTIVE FUEL	EFFECTIVE OXIDANT	MIXTURE
ENTHALPY	h(2)/R	h(1)/R	h0/R
(KG-MOL)(K)/KG	-0.29767190E+00	0.00000000E+00	0.29434723E+03

KG-FORM.WT./KG	bi(2)	bi(1)	b0i
*N	0.53915890E-01	0.00000000E+00	0.53915890E-01

*O   0.14486046E-01 0.00000000E+00 0.14486046E-01

*Ar   0.32331996E-03 0.00000000E+00 0.32331996E-03

*C   0.11013248E-04 0.00000000E+00 0.11013248E-04

POINT ITN T N O AR C

1 20 2343.926 -13.126 -14.728 -24.773 -29.902

Pinf/Pt = 1.804957

2 4 2073.258 -13.206 -14.788 -25.098 -32.300

Pinf/Pt = 1.816572

2 2 2070.421 -13.207 -14.788 -25.101 -32.329

Pinf/Pt = 1.816681

2 1 2070.394 -13.207 -14.788 -25.101 -32.329

THEORETICAL ROCKET PERFORMANCE ASSUMING FROZEN COMPOSITION

AFTER POINT 2

Pin = 64.7 PSIA

CASE =

REACTANT	WT FRACTION (SEE NOTE)	ENERGY KJ/KG-MOL	TEMP K
NAME Air	1.0000000	-71.689	300.000

O/F=   0.00000 %FUEL= 0.000000 R,EQ.RATIO= 0.001521 PHI,EQ.RATIO= 0.000000

	CHAMBER	THROAT	EXIT
Pinf/P	1.0000	1.8167	6.1736
P, BAR	4.4609	2.4555	0.72258
T, K	2343.93	2070.39	1558.39
RHO, KG/CU M	6.6257-1	4.1311-1	1.6150-1
H, KJ/KG	2447.35	2069.23	1435.82
U, KJ/KG	1774.08	1474.82	988.41
G, KJ/KG	-18112.5	-16091.4	-12233.7
S, KJ/(KG)(K)	8.7716	8.7716	8.7716

	CHAMBER	THROAT	EXIT
M, (1/n)	28.946	28.961	28.961
Cp, KJ/(KG)(K)	1.4371	1.3473	1.2167

GAMMAs   1.2548   1.2723   1.3088

SON VEL,M/SEC   919.1   869.6   765.2

MACH NUMBER   0.000   1.000   1.859

PERFORMANCE PARAMETERS

Ae/At   1.0000   1.5639

CSTAR, M/SEC   1241.7   1241.7

CF   0.7003   1.1455

Ivac, M/SEC   1553.1   1736.9

Isp, M/SEC   869.6   1422.3

MOLE FRACTIONS

*Ar   0.00936 *CO2   0.00032 *NO   0.00905

NO2   0.00002 *N2   0.77618 *O   0.00033

*O2   0.20473

* THERMODYNAMIC PROPERTIES FITTED TO 20000.K

PRODUCTS WHICH WERE CONSIDERED BUT WHOSE MOLE FRACTIONS WERE LESS THAN 5.000000E-06 FOR ALL ASSIGNED CONDITIONS

NOTE. WEIGHT FRACTION OF FUEL IN TOTAL FUELS AND OF OXIDANT IN TOTAL OXIDANTS

AE295- CFD Modeling and analysis of an Arc-jet facility using ANSYS Fluent

1 c) N2 case-1 – equilibrium

problem

  rocket equilibrium tcest,k=3800

  p,psia=60,

  sup,ae/at=1.5625,

  h/r= 564.829815

 react

  name=N2 moles=3.819601 t,k=300

output massf

    plot p t rho h s cp gam son mach vis cond condfz pran pranfz

 end

OPTIONS: TP=F HP=F SP=F TV=F UV=F SV=F DETN=F SHOCK=F REFL=F INCD=F

RKT=T FROZ=F EQL=T IONS=F SIUNIT=T DEBUGF=F SHKDBG=F DETDBG=F
TRNSPT=F

TRACE= 0.00E+00 S/R= 0.000000E+00 H/R= 5.648298E+02 U/R= 0.000000E+00

Pc,BAR =   4.136838

Pc/P =

SUBSONIC AREA RATIOS =

SUPERSONIC AREA RATIOS =   1.5625

NFZ= 1 Mdot/Ac= 0.000000E+00 Ac/At= 0.000000E+00

   REACTANT   MOLES   (ENERGY/R),K   TEMP,K DENSITY

      EXPLODED FORMULA

N: N2   3.819601   0.648034E+01   300.00 0.0000

      N 2.00000

 SPECIES BEING CONSIDERED IN THIS SYSTEM

(CONDENSED PHASE MAY HAVE NAME LISTED SEVERAL TIMES)

 LAST thermo.inp UPDATE: 10/22/02

 g 5/97 *N   tpis78 *N2   tpis89 N3

O/F =   0.000000

	EFFECTIVE FUEL	EFFECTIVE OXIDANT	MIXTURE
ENTHALPY	h(2)/R	h(1)/R	h0/R
(KG-MOL)(K)/KG	0.23132989E+00	0.00000000E+00	0.56482982E+03

KG-FORM.WT./KG	bi(2)	bi(1)	b0i
*N	0.71394404E-01	0.00000000E+00	0.71394404E-01

POINT ITN   T   N

 1 10   4028.426   -14.045

Pinf/Pt = 1.816237

 2   3   3537.889   -14.091

Pinf/Pt = 1.823013

 2   2   3534.983   -14.091

 3   3   2728.572   -14.186

 3   2   2702.418   -14.190

 3   1   2702.574   -14.190

THEORETICAL ROCKET PERFORMANCE ASSUMING EQUILIBRIUM

COMPOSITION DURING EXPANSION FROM INFINITE AREA COMBUSTOR

Pin =   60.0 PSIA

CASE =

REACTANT	MOLES	ENERGY	TEMP
		KJ/KG-MOL	K
NAME N2	3.8196010	53.881	300.000

O/F=   0.00000 %FUEL= 0.000000 R,EQ.RATIO= 0.000000 PHI,EQ.RATIO= 0.000000

	CHAMBER	THROAT	EXIT
Pinf/P	1.0000	1.8230	6.0554
P, BAR	4.1368	2.2692	0.68316
T, K	4028.43	3534.98	2702.57
RHO, KG/CU M	3.4582-1	2.1626-1	8.5168-2
H, KJ/KG	4696.28	4022.83	2917.65
U, KJ/KG	3500.05	2973.54	2115.52
G, KJ/KG	-33584.9	-29569.3	-22764.3
S, KJ/(KG)(K)	9.5028	9.5028	9.5028

M, (1/n)   28.000   28.011   28.013

(dLV/dLP)t   -1.00024 -1.00004 -1.00000

(dLV/dLT)p   1.0070   1.0014   1.0000

Cp, KJ/(KG)(K)   1.4011   1.3468   1.3140

GAMMAs   1.2734   1.2837   1.2918

SON VEL,M/SEC   1234.2   1160.6   1017.9

MACH NUMBER   0.000   1.000   1.853

PERFORMANCE PARAMETERS

Ae/At   1.0000   1.5625

CSTAR, M/SEC   1648.2   1648.2

CF   0.7041   1.1443

Ivac, M/SEC   2064.7   2311.4

Isp, M/SEC   1160.6   1886.1

MASS FRACTIONS

*N   0.00048 0.00009 0.00000

*N2   0.99952 0.99991 1.00000

* THERMODYNAMIC PROPERTIES FITTED TO 20000.K

PRODUCTS WHICH WERE CONSIDERED BUT WHOSE MASS FRACTIONS WERE LESS THAN 5.000000E-06 FOR ALL ASSIGNED CONDITIONS

1 d) N2-case-1 frozen

problem

 ro frozen nfz=1

p,bar=4.136855

sup,ae/at=1.562500,

h/r=564.829815

react

name=N2 moles=3.819601 t,k=300

output massf transport

plot p t rho h son cp gam vis

end

OPTIONS: TP=F HP=F SP=F TV=F UV=F SV=F DETN=F SHOCK=F REFL=F INCD=F

RKT=T FROZ=T EQL=F IONS=F SIUNIT=T DEBUGF=F SHKDBG=F DETDBG=F
TRNSPT=T

TRACE= 0.00E+00 S/R= 0.000000E+00 H/R= 5.648298E+02 U/R= 0.000000E+00

Pc,BAR =   4.136855

Pc/P =

SUBSONIC AREA RATIOS =

SUPERSONIC AREA RATIOS =   1.5625

NFZ= 1 Mdot/Ac= 0.000000E+00 Ac/At= 0.000000E+00

   REACTANT   MOLES   (ENERGY/R),K   TEMP,K DENSITY

      EXPLODED FORMULA

N: N2   3.819601   0.648034E+01   300.00 0.0000

      N 2.00000

 SPECIES BEING CONSIDERED IN THIS SYSTEM

(CONDENSED PHASE MAY HAVE NAME LISTED SEVERAL TIMES)

 LAST thermo.inp UPDATE: 9/09/04

 g 5/97 *N   tpis78 *N2   tpis89 N3

 SPECIES WITH TRANSPORT PROPERTIES

PURE SPECIES

N   N2

BINARY INTERACTIONS

N   N2

O/F =   0.000000

	EFFECTIVE FUEL	EFFECTIVE OXIDANT	MIXTURE
ENTHALPY	h(2)/R	h(1)/R	h0/R
(KG-MOL)(K)/KG	0.23132989E+00	0.00000000E+00	0.56482982E+03

KG-FORM.WT./KG	bi(2)	bi(1)	b0i
*N	0.71394404E-01	0.00000000E+00	0.71394404E-01

POINT	ITN	T	N
1	10	4028.426	-14.045

THEORETICAL ROCKET PERFORMANCE ASSUMING FROZEN COMPOSITION

Pin =   60.0 PSIA

CASE =

REACTANT		MOLES	ENERGY	TEMP
			KJ/KG-MOL	K
NAME	N2	3.8196010	53.881	300.000

O/F=   0.00000 %FUEL= 0.000000 R,EQ.RATIO= 0.000000 PHI,EQ.RATIO= 0.000000

	CHAMBER	THROAT	EXIT
Pinf/P	1.0000	1.8245	6.0587
P, BAR	4.1369	2.2674	0.68280
T, K	4028.43	3524.77	2692.70

RHO, KG/CU M   3.4582-1 2.1663-1 8.5394-2

H, KJ/KG   4696.28 4022.91 2921.26

U, KJ/KG   3500.05 2976.24 2121.67

G, KJ/KG   -33584.9 -29472.2 -22666.8

S, KJ/(KG)(K)   9.5028   9.5028   9.5028

M, (1/n)   28.000   28.000   28.000

Cp, KJ/(KG)(K)   1.3409   1.3328   1.3135

GAMMAs   1.2845   1.2867   1.2921

SON VEL,M/SEC   1239.6   1160.5   1016.4

MACH NUMBER   0.000   1.000   1.854

TRANSPORT PROPERTIES (GASES ONLY)

 CONDUCTIVITY IN UNITS OF MILLIWATTS/(CM)(K)

VISC,MILLIPOISE   1.0861 0.98268 0.80768

 WITH FROZEN REACTIONS

Cp, KJ/(KG)(K)   1.3409   1.3328   1.3135

CONDUCTIVITY   2.0301   1.8121   1.4441

PRANDTL NUMBER   0.7174   0.7227   0.7346

PERFORMANCE PARAMETERS

Ae/At   1.0000   1.5625

CSTAR, M/SEC   1645.5   1645.5

CF   0.7052   1.1450

Ivac, M/SEC   2062.4   2308.5

Isp, M/SEC   1160.5   1884.2

MASS FRACTIONS

*N   0.00048   *N2   0.99952

 * THERMODYNAMIC PROPERTIES FITTED TO 20000.K

   PRODUCTS WHICH WERE CONSIDERED BUT WHOSE MASS FRACTIONS

   WERE LESS THAN 5.000000E-06 FOR ALL ASSIGNED CONDITIONS

1 e) N2-case-2 equilibrium

 problem

  rocket equilibrium tcest,k=3800

  p,bar=4.136855,

  sup,ae/at=1.5625,

  h/r=575.588478

react

  name=N2 moles=3.748206 t,k=300

output

    plot p t rho h s cp gam son mach vis cond condfz pran pranfz

 end

OPTIONS: TP=F HP=F SP=F TV=F UV=F SV=F DETN=F SHOCK=F REFL=F INCD=F

RKT=T FROZ=F EQL=T IONS=F SIUNIT=T DEBUGF=F SHKDBG=F DETDBG=F
TRNSPT=F

TRACE= 0.00E+00 S/R= 0.000000E+00 H/R= 5.755885E+02 U/R= 0.000000E+00

Pc,BAR =   4.136855

Pc/P =

SUBSONIC AREA RATIOS =

SUPERSONIC AREA RATIOS =   1.5625

NFZ= 1 Mdot/Ac= 0.000000E+00 Ac/At= 0.000000E+00

   REACTANT   MOLES   (ENERGY/R),K   TEMP,K DENSITY

     EXPLODED FORMULA

N: N2   3.748206   0.648034E+01   300.00 0.0000

     N 2.00000

 SPECIES BEING CONSIDERED IN THIS SYSTEM

(CONDENSED PHASE MAY HAVE NAME LISTED SEVERAL TIMES)

 LAST thermo.inp UPDATE: 10/22/02

 g 5/97 *N   tpis78 *N2   tpis89 N3

O/F =   0.000000

	EFFECTIVE FUEL	EFFECTIVE OXIDANT	MIXTURE
ENTHALPY	h(2)/R	h(1)/R	h0/R
(KG-MOL)(K)/KG	0.23132989E+00	0.00000000E+00	0.57558848E+03

	bi(2)	bi(1)	b0i
KG-FORM.WT./KG			
*N	0.71394404E-01	0.00000000E+00	0.71394404E-01

POINT ITN   T   N

 1 10   4091.964   -14.075

Pinf/Pt = 1.814808

 2   3   3596.754   -14.122

Pinf/Pt = 1.822478

 2   2   3593.418   -14.123

 3   3   2774.836   -14.217

 3   2   2748.372   -14.220

 3   1   2748.530   -14.220

THEORETICAL ROCKET PERFORMANCE ASSUMING EQUILIBRIUM

COMPOSITION DURING EXPANSION FROM INFINITE AREA COMBUSTOR

Pin =   60.0 PSIA

CASE =

REACTANT	MOLES	ENERGY	TEMP
		KJ/KG-MOL	K
NAME N2	3.7482060	53.881	300.000

O/F=   0.00000 %FUEL= 0.000000 R,EQ.RATIO= 0.000000 PHI,EQ.RATIO= 0.000000

	CHAMBER	THROAT	EXIT
Pinf/P	1.0000	1.8225	6.0527
P, BAR	4.1369	2.2699	0.68348
T, K	4091.96	3593.42	2748.53
RHO, KG/CU M	3.4041-1	2.1280-1	8.3782-2
H, KJ/KG	4785.74	4101.66	2978.07
U, KJ/KG	3570.49	3035.00	2162.30
G, KJ/KG	-34189.4	-30124.9	-23201.1
S, KJ/(KG)(K)	9.5248	9.5248	9.5248

M, (1/n)   27.996   28.010   28.013

(dLV/dLP)t   -1.00030 -1.00006 -1.00000

(dLV/dLT)p   1.0086   1.0018   1.0000

Cp, KJ/(KG)(K)   1.4150   1.3515   1.3155

GAMMAs   1.2710   1.2827   1.2914

SON VEL,M/SEC   1242.8   1169.7   1026.4

MACH NUMBER   0.000   1.000   1.853

PERFORMANCE PARAMETERS

Ae/At   1.0000   1.5625

CSTAR, M/SEC   1662.0   1662.0

CF   0.7038   1.1441

Ivac, M/SEC   2081.6   2330.4

Isp, M/SEC   1169.7   1901.4

 MOLE FRACTIONS

*N   0.00121 0.00023 0.00000

*N2   0.99879 0.99977 1.00000

 * THERMODYNAMIC PROPERTIES FITTED TO 20000.K

   PRODUCTS WHICH WERE CONSIDERED BUT WHOSE MOLE FRACTIONS WERE LESS THAN 5.000000E-06 FOR ALL ASSIGNED CONDITIONS

1 f) N2-case-2 frozen

problem

 ro frozen nfz=1

p,bar=4.136855

sup,ae/at=1.562500,

h/r=575.588478

react

name=N2 moles=3.748206 t,k=300

output massf transport

plot p t rho h son cp gam vis

end

OPTIONS: TP=F HP=F SP=F TV=F UV=F SV=F DETN=F SHOCK=F REFL=F INCD=F

RKT=T FROZ=T EQL=F IONS=F SIUNIT=T DEBUGF=F SHKDBG=F DETDBG=F
TRNSPT=T

TRACE= 0.00E+00 S/R= 0.000000E+00 H/R= 5.755885E+02 U/R= 0.000000E+00

Pc,BAR =   4.136855

Pc/P =

SUBSONIC AREA RATIOS =

SUPERSONIC AREA RATIOS =   1.5625

NFZ= 1 Mdot/Ac= 0.000000E+00 Ac/At= 0.000000E+00

   REACTANT   MOLES   (ENERGY/R),K TEMP,K DENSITY

     EXPLODED FORMULA

N: N2   3.748206 0.648034E+01   300.00 0.0000

     N 2.00000

 SPECIES BEING CONSIDERED IN THIS SYSTEM

(CONDENSED PHASE MAY HAVE NAME LISTED SEVERAL TIMES)

 LAST thermo.inp UPDATE: 9/09/04

 g 5/97 *N   tpis78 *N2   tpis89 N3

 SPECIES WITH TRANSPORT PROPERTIES

PURE SPECIES

N   N2

BINARY INTERACTIONS

N   N2

O/F =   0.000000

	EFFECTIVE FUEL	EFFECTIVE OXIDANT	MIXTURE
ENTHALPY	h(2)/R	h(1)/R	h0/R
(KG-MOL)(K)/KG	0.23132989E+00	0.00000000E+00	0.57558848E+03

KG-FORM.WT./KG	bi(2)	bi(1)	b0i
*N	0.71394404E-01	0.00000000E+00	0.71394404E-01

POINT	ITN	T	N
1	10	4091.964	-14.075

THEORETICAL ROCKET PERFORMANCE ASSUMING FROZEN COMPOSITION

Pin =   60.0 PSIA

CASE =

REACTANT		MOLES	ENERGY	TEMP
			KJ/KG-MOL	K
NAME	N2	3.7482060	53.881	300.000

O/F=   0.00000 %FUEL= 0.000000 R,EQ.RATIO= 0.000000 PHI,EQ.RATIO= 0.000000

	CHAMBER	THROAT	EXIT
Pinf/P	1.0000	1.8243	6.0569
P, BAR	4.1369	2.2676	0.68300
T, K	4091.96	3580.71	2736.11

RHO, KG/CU M   3.4041-1 2.1324-1 8.4053-2

H, KJ/KG   4785.74 4101.72 2982.52

U, KJ/KG   3570.49 3038.30 2169.94

G, KJ/KG   -34189.4 -30003.9 -23078.4

S, KJ/(KG)(K)   9.5248 9.5248 9.5248

M, (1/n)   27.996 27.996 27.996

Cp, KJ/(KG)(K)   1.3418 1.3338 1.3148

GAMMAs   1.2842 1.2864 1.2918

SON VEL,M/SEC   1249.3 1169.6 1024.5

MACH NUMBER   0.000 1.000 1.854

TRANSPORT PROPERTIES (GASES ONLY)

 CONDUCTIVITY IN UNITS OF MILLIWATTS/(CM)(K)

VISC,MILLIPOISE 1.0992 0.99432 0.81702

 WITH FROZEN REACTIONS

Cp, KJ/(KG)(K)   1.3418 1.3338 1.3148

CONDUCTIVITY   2.0575   1.8367   1.4638

PRANDTL NUMBER   0.7168   0.7221   0.7339

PERFORMANCE PARAMETERS

Ae/At   1.0000   1.5625

CSTAR, M/SEC   1658.7   1658.7

CF   0.7052   1.1449

Ivac, M/SEC   2078.8   2326.9

Isp, M/SEC   1169.6   1899.1

MASS FRACTIONS

*N   0.00061   *N2   0.99939

 * THERMODYNAMIC PROPERTIES FITTED TO 20000.K

   PRODUCTS WHICH WERE CONSIDERED BUT WHOSE MASS FRACTIONS WERE LESS THAN 5.000000E-06 FOR ALL ASSIGNED CONDITIONS

1 g) N2-case-3- equilibrium

problem

  rocket equilibrium tcest,k=3800

  p,bar=3.792117,

  sup,ae/at=1.5625,

  h/r= 516.553763

 react

  name=N2 wt=4.176573 t,k=300

output massf

    plot p t rho h s cp gam son mach vis cond condfz pran pranfz

 end

OPTIONS: TP=F HP=F SP=F TV=F UV=F SV=F DETN=F SHOCK=F REFL=F INCD=F

RKT=T FROZ=F EQL=T IONS=F SIUNIT=T DEBUGF=F SHKDBG=F DETDBG=F
TRNSPT=F

TRACE= 0.00E+00 S/R= 0.000000E+00 H/R= 5.165538E+02 U/R= 0.000000E+00

Pc,BAR =   3.792117

Pc/P =

SUBSONIC AREA RATIOS =

SUPERSONIC AREA RATIOS =   1.5625

NFZ= 1 Mdot/Ac= 0.000000E+00 Ac/At= 0.000000E+00

   REACTANT   WT.FRAC   (ENERGY/R),K   TEMP,K DENSITY

      EXPLODED FORMULA

N: N2   1.000000   0.648034E+01   300.00 0.0000

      N 2.00000

 SPECIES BEING CONSIDERED IN THIS SYSTEM

(CONDENSED PHASE MAY HAVE NAME LISTED SEVERAL TIMES)

 LAST thermo.inp UPDATE: 10/22/02

 g 5/97 *N   tpis78 *N2   tpis89 N3

O/F =   0.000000

	EFFECTIVE FUEL	EFFECTIVE OXIDANT	MIXTURE
ENTHALPY	h(2)/R	h(1)/R	h0/R
(KG-MOL)(K)/KG	0.23132989E+00	0.00000000E+00	0.51655376E+03

	bi(2)	bi(1)	b0i
KG-FORM.WT./KG			
*N	0.71394404E-01	0.00000000E+00	0.71394404E-01

POINT ITN   T   N

 1 10   3736.853   -13.942

Pinf/Pt = 1.820848

 2   3   3273.044   -13.988

Pinf/Pt = 1.824788

 2   2   3271.468   -13.988

 3   3   2521.127   -14.087

 3   2   2496.265   -14.091

 3   1   2496.416   -14.091

THEORETICAL ROCKET PERFORMANCE ASSUMING EQUILIBRIUM

COMPOSITION DURING EXPANSION FROM INFINITE AREA COMBUSTOR

Pin =   55.0 PSIA

CASE =

	REACTANT	WT FRACTION	ENERGY	TEMP
		(SEE NOTE)	KJ/KG-MOL	K
NAME	N2	1.0000000	53.881	300.000

O/F=   0.00000 %FUEL= 0.000000 R,EQ.RATIO= 0.000000 PHI,EQ.RATIO= 0.000000

	CHAMBER	THROAT	EXIT
Pinf/P	1.0000	1.8248	6.0673
P, BAR	3.7921	2.0781	0.62500
T, K	3736.85	3271.47	2496.42
RHO, KG/CU M	3.4185-1	2.1402-1	8.4352-2
H, KJ/KG	4294.89	3670.09	2647.47
U, KJ/KG	3185.59	2699.08	1906.52
G, KJ/KG	-30925.7	-27164.1	-20881.7
S, KJ/(KG)(K)	9.4252	9.4252	9.4252
M, (1/n)	28.009	28.013	28.013

(dLV/dLP)t   -1.00008 -1.00001 -1.00000

(dLV/dLT)p   1.0025   1.0004   1.0000

Cp, KJ/(KG)(K)   1.3599   1.3323   1.3070

GAMMAs   1.2809   1.2869   1.2938

SON VEL,M/SEC   1192.0   1117.9   979.1

MACH NUMBER   0.000   1.000   1.854

PERFORMANCE PARAMETERS

Ae/At   1.0000   1.5625

CSTAR, M/SEC   1585.1   1585.1

CF   0.7052   1.1452

Ivac, M/SEC   1986.5   2223.4

Isp, M/SEC   1117.9   1815.2

MASS FRACTIONS

*N   0.00016 0.00002 0.00000

*N2   0.99984 0.99998 1.00000

* THERMODYNAMIC PROPERTIES FITTED TO 20000.K

   PRODUCTS WHICH WERE CONSIDERED BUT WHOSE MASS FRACTIONS WERE LESS THAN 5.000000E-06 FOR ALL ASSIGNED CONDITIONS

 NOTE. WEIGHT FRACTION OF FUEL IN TOTAL FUELS AND OF OXIDANT IN TOTAL OXIDANTS

1 h) N2-case-3 frozen

problem

 ro frozen nfz=1

p,bar=3.792117

sup,ae/at=1.562500,

h/r=516.553763

react

name=N2 moles=4.176573 t,k=300

output massf transport

plot p t rho h son cp gam vis

end

OPTIONS: TP=F HP=F SP=F TV=F UV=F SV=F DETN=F SHOCK=F REFL=F INCD=F

RKT=T FROZ=T EQL=F IONS=F SIUNIT=T DEBUGF=F SHKDBG=F DETDBG=F
TRNSPT=T

TRACE= 0.00E+00 S/R= 0.000000E+00 H/R= 5.165538E+02 U/R= 0.000000E+00

Pc,BAR =   3.792117

Pc/P =

SUBSONIC AREA RATIOS =

SUPERSONIC AREA RATIOS =   1.5625

NFZ= 1 Mdot/Ac= 0.000000E+00 Ac/At= 0.000000E+00

  REACTANT   MOLES   (ENERGY/R),K   TEMP,K DENSITY

    EXPLODED FORMULA

N: N2   4.176573   0.648034E+01   300.00 0.0000

     N 2.00000

 SPECIES BEING CONSIDERED IN THIS SYSTEM

(CONDENSED PHASE MAY HAVE NAME LISTED SEVERAL TIMES)

 LAST thermo.inp UPDATE: 9/09/04

 g 5/97 *N   tpis78 *N2   tpis89 N3

SPECIES WITH TRANSPORT PROPERTIES

    PURE SPECIES

 N   N2

BINARY INTERACTIONS

    N   N2

O/F =   0.000000

                EFFECTIVE FUEL   EFFECTIVE OXIDANT   MIXTURE

ENTHALPY   h(2)/R   h(1)/R   h0/R

(KG-MOL)(K)/KG   0.23132989E+00   0.00000000E+00   0.51655376E+03

KG-FORM.WT./KG   bi(2)   bi(1)   b0i

 *N   0.71394404E-01   0.00000000E+00   0.71394404E-01

POINT ITN   T   N

 1   10   3736.853   -13.942

            THEORETICAL ROCKET PERFORMANCE ASSUMING FROZEN COMPOSITION

Pin =   55.0 PSIA

CASE =

            REACTANT   MOLES   ENERGY   TEMP

                                 KJ/KG-MOL   K

NAME   N2   4.1765730   53.881   300.000

O/F=   0.00000 %FUEL= 0.000000 R,EQ.RATIO= 0.000000 PHI,EQ.RATIO= 0.000000

```
                  CHAMBER   THROAT    EXIT

Pinf/P            1.0000   1.8253   6.0682

P, BAR            3.7921   2.0776  0.62492

T, K              3736.85  3267.92  2493.13

RHO, KG/CU M   3.4185-1 2.1416-1 8.4437-2

H, KJ/KG          4294.89  3670.18  2648.78

U, KJ/KG          3185.59  2700.09  1908.68

G, KJ/KG         -30925.7 -27130.6 -20849.5

S, KJ/(KG)(K)     9.4252   9.4252   9.4252

M, (1/n)          28.009   28.009   28.009

Cp, KJ/(KG)(K)    1.3363   1.3278   1.3068

GAMMAs            1.2856   1.2879   1.2939

SON VEL,M/SEC     1194.2   1117.8   978.6

MACH NUMBER       0.000    1.000    1.854
```

TRANSPORT PROPERTIES (GASES ONLY)

  CONDUCTIVITY IN UNITS OF MILLIWATTS/(CM)(K)

VISC,MILLIPOISE 1.0263 0.92910 0.76464

AE295- CFD Modeling and analysis of an Arc-jet facility using ANSYS Fluent

 WITH FROZEN REACTIONS

Cp, KJ/(KG)(K)   1.3363   1.3278   1.3068

CONDUCTIVITY   1.9038   1.6992   1.3537

PRANDTL NUMBER   0.7204   0.7260   0.7381

PERFORMANCE PARAMETERS

Ae/At   1.0000   1.5625

CSTAR, M/SEC   1584.1   1584.1

CF   0.7056   1.1454

Ivac, M/SEC   1985.7   2222.3

Isp, M/SEC   1117.8   1814.4

MASS FRACTIONS

*N   0.00016   *N2   0.99984

 * THERMODYNAMIC PROPERTIES FITTED TO 20000.K

  PRODUCTS WHICH WERE CONSIDERED BUT WHOSE MASS FRACTIONS

  WERE LESS THAN 5.000000E-06 FOR ALL ASSIGNED CONDITIONS

A2. 2D- Axisymmetric grids used for CFD modeling of the arc-jet nozzle for advanced analysis.

2 a) Coarse grid

- ⚐ Number of Cells – 650

- ⚐ Number of zones – 7

- ⚐ Minimum orthogonal quality – 0.7797

- ⚐ Maximum Aspect Ratio – 3.297

Fig A-2.1: Coarse grid used in the CFD modeling of the arc-jet nozzle for advanced analysis.
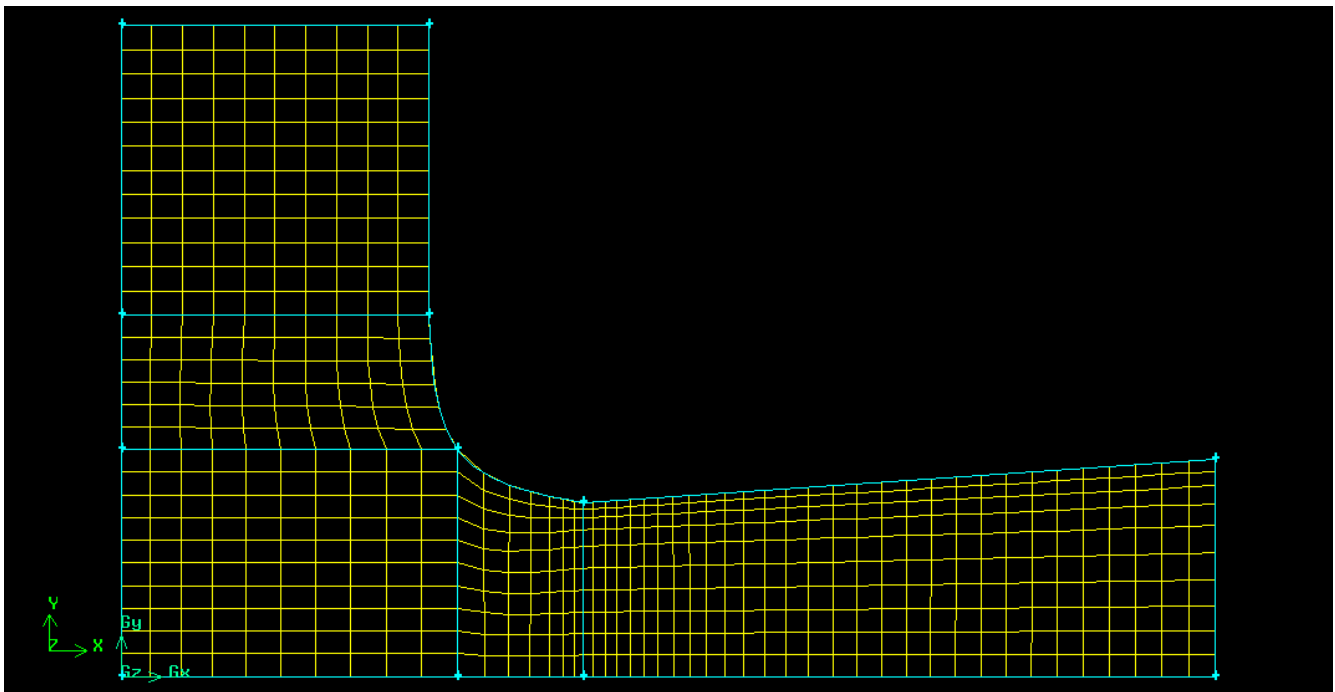
2 b) Fine-1 grid

- ⚐ Number of Cells – 10600

- ⚐ Number of zones – 7

- ⚐ Minimum orthogonal quality – 0.63727

- ⚐ Maximum Aspect Ratio – 51.189

- ⚐ y+ value used - 10

- ⚐ Cell wall distance (BL Mesh) - 0.01 mm

- ⚐ Thickness of Boundary Layer mesh – 1.55 mm

- ⚐ Number of rows inside the Boundary Layer mesh- 25

Fig A-2.2: Fine-1 grid used in the CFD modeling of the arc-jet nozzle for advanced analysis.
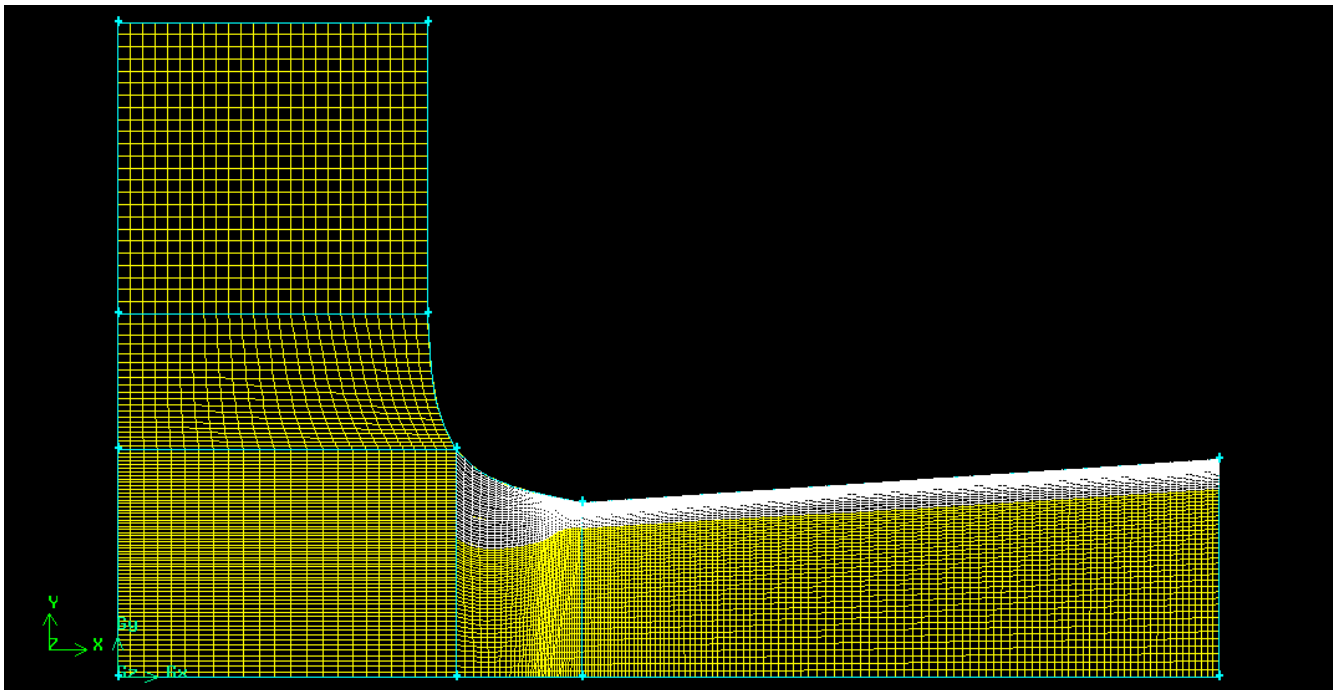
2 c) Fine2 grid

- ⚜ Number of Cells – 10760

- ⚜ Number of zones – 7

- ⚜ Minimum orthogonal quality – 0.0427

- ⚜ Maximum Aspect Ratio – 1646.36

- ⚜ y+ value used - 1

- ⚜ Cell wall distance (BL Mesh) - 0.0011 mm

- ⚜ Thickness of Boundary Layer mesh – 0.96 mm

- ⚜ Number of rows inside the Boundary Layer mesh- 30

Fig A-2.3: Fine-2 grid used in the CFD modeling of the arc-jet nozzle for advanced analysis.
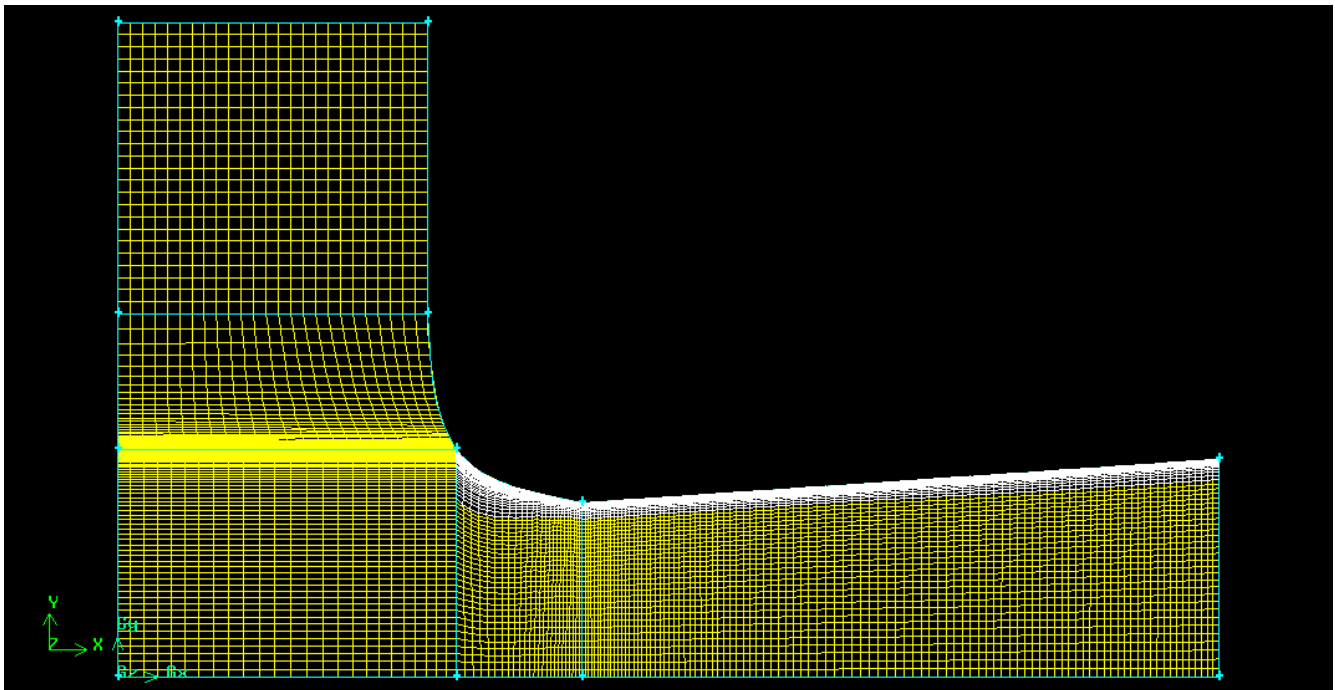
A3. <u>**Results obtained from the CFD simulation of the nozzle for all the three grids and four cases.**</u>

3.1 a) Air-coarse grid

Fig A-3.1.1: Mach contours in the nozzle obtained from the CFD model for air using coarse grid.
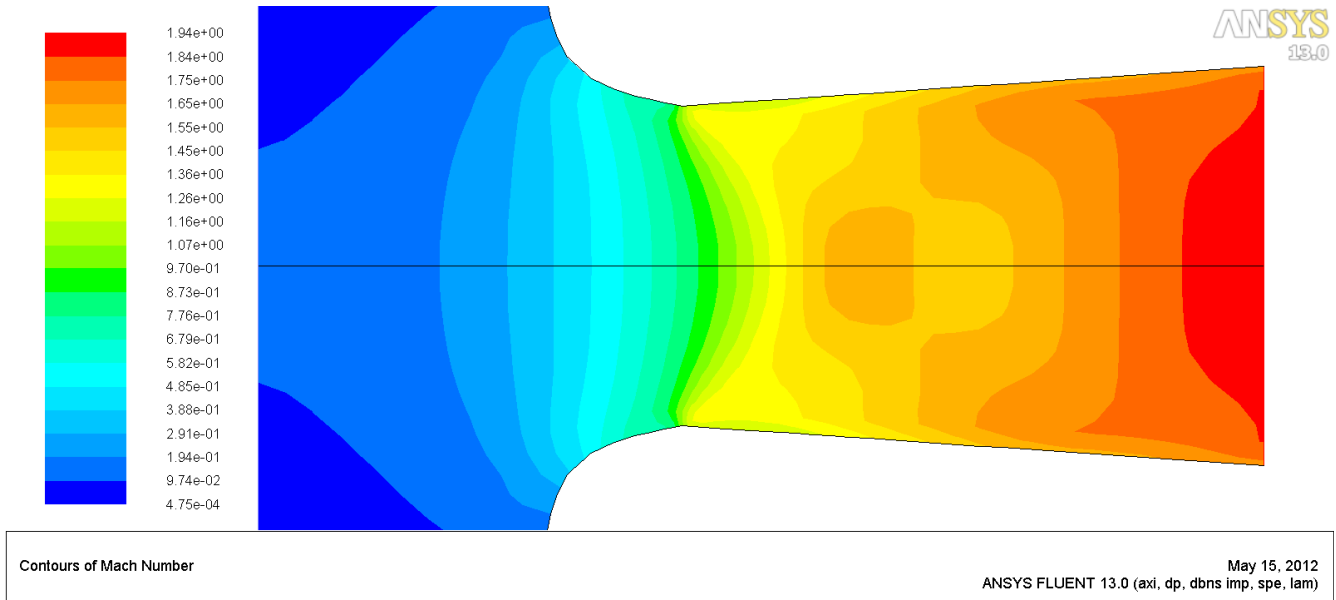
Fig A-3.1.2: Static Pressure contours in the nozzle obtained from the CFD model for air using coarse grid.
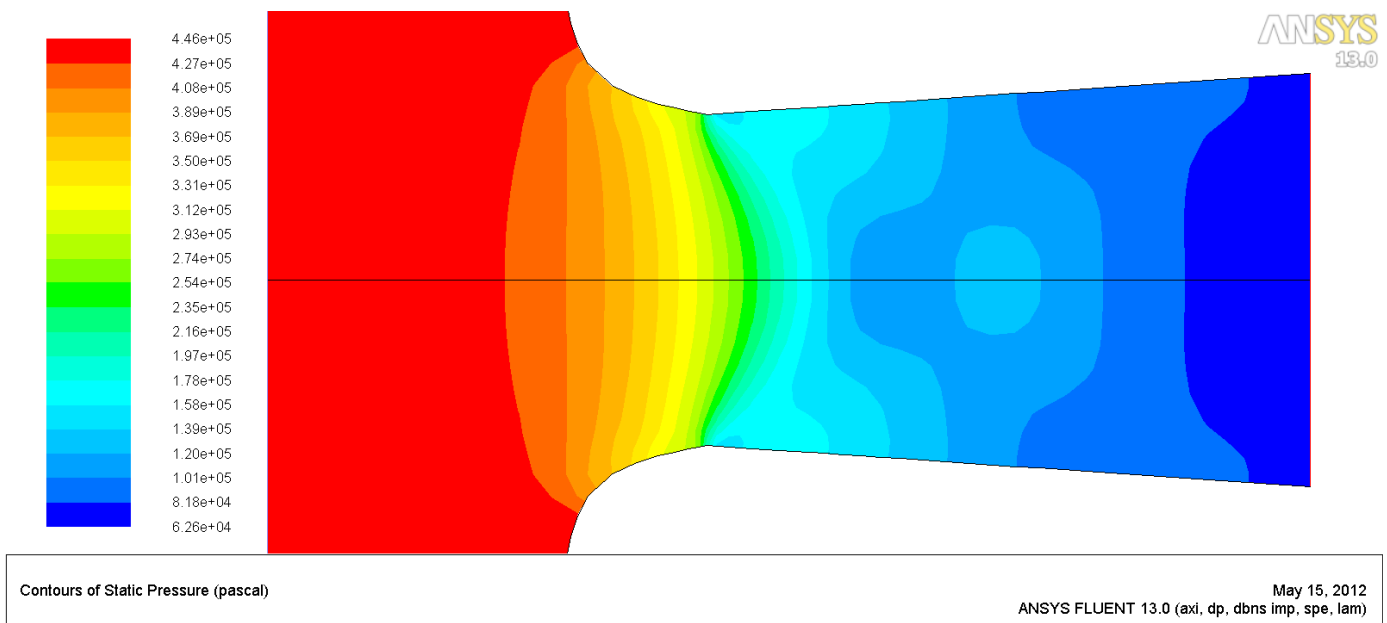
Fig A-3.1.3: Static Temperature contours in the nozzle obtained from the CFD model for air using

Contours of Static Temperature (k)

May 15, 2012
ANSYS FLUENT 13.0 (axi, dp, dbns imp, spe, lam)
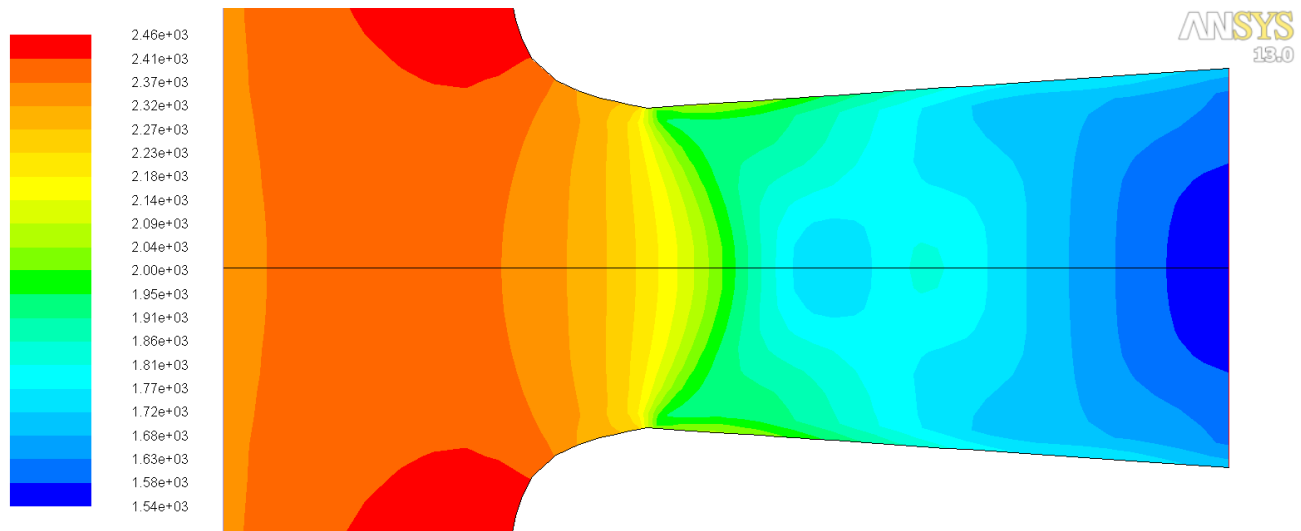
coarse grid.

Fig A-3.1.4: Velocity Magnitude contours in the nozzle obtained from the CFD model for air using coarse grid.

Contours of Velocity Magnitude (m/s)

May 15, 2012
ANSYS FLUENT 13.0 (axi, dp, dbns imp, spe, lam)
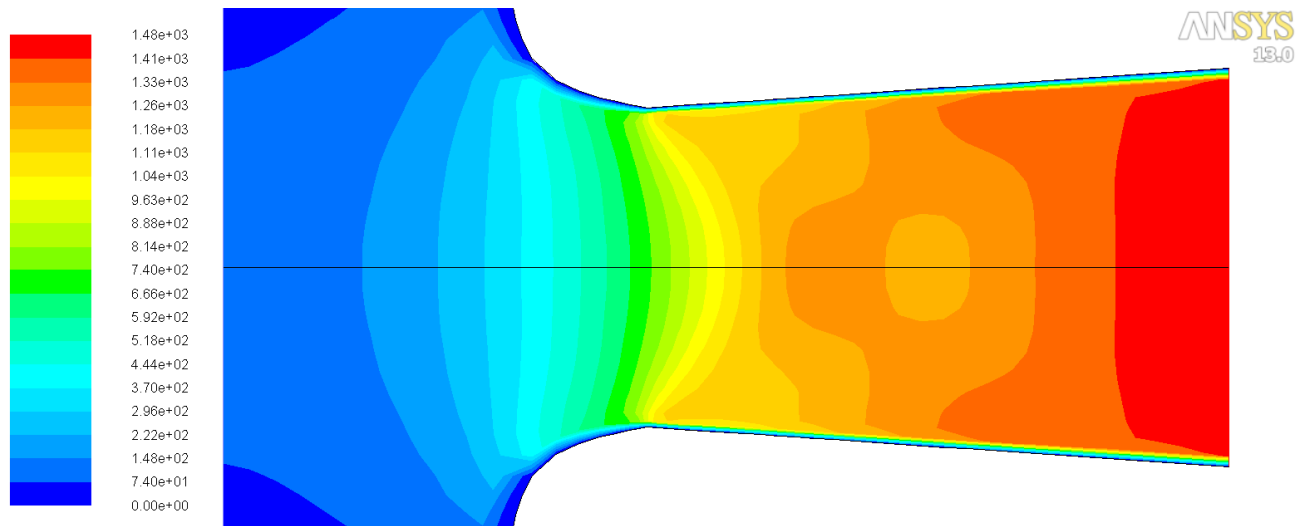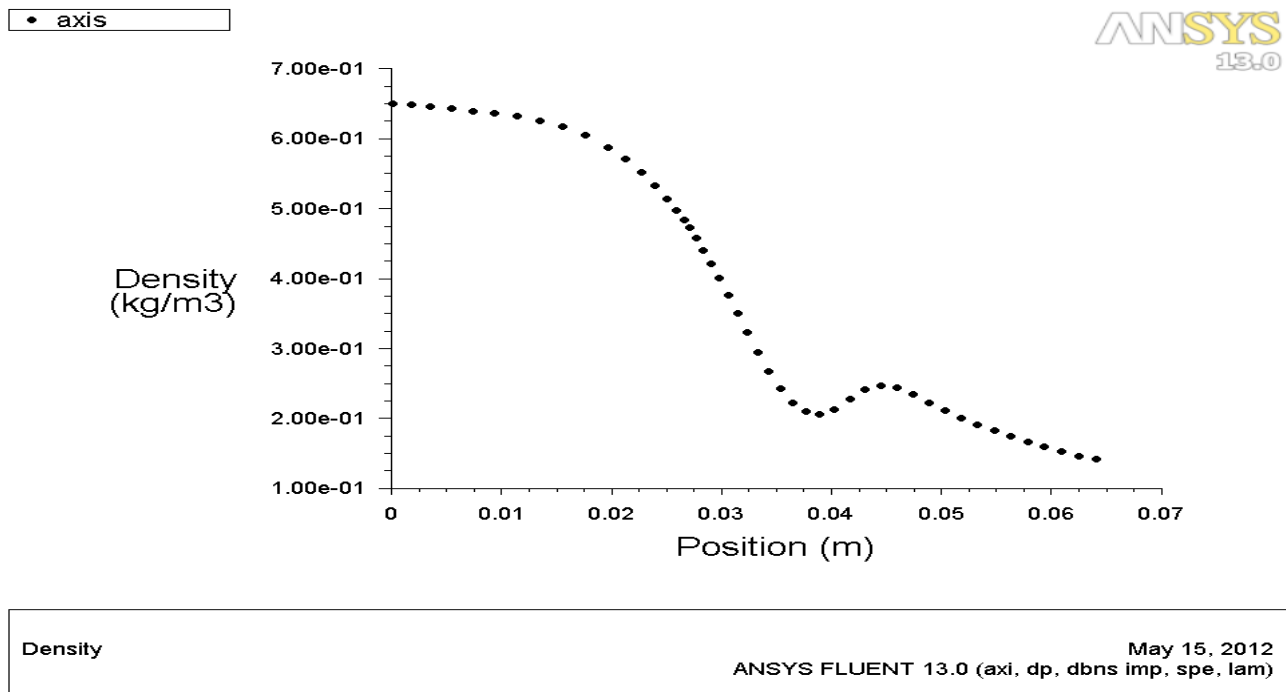
Fig A-3.1.5: Density plot along the axis of symmetry in the nozzle obtained from the CFD model for air using coarse grid.

Fig A-3.1.6: Enthalpy plot along the axis of symmetry in the nozzle obtained from the CFD model for air using coarse grid.
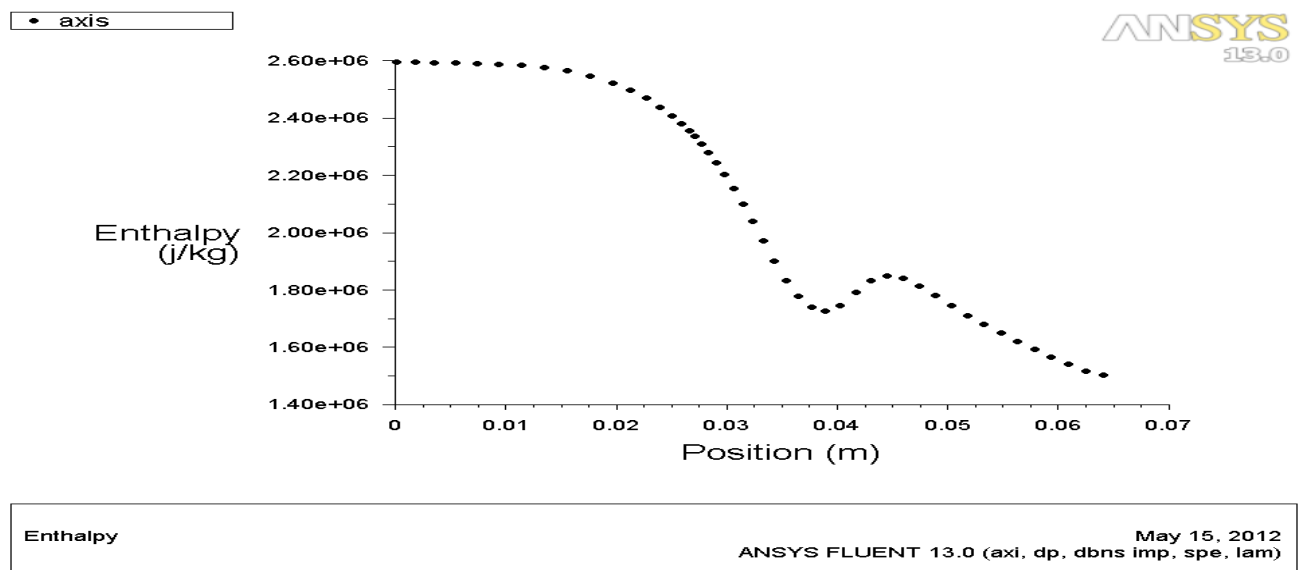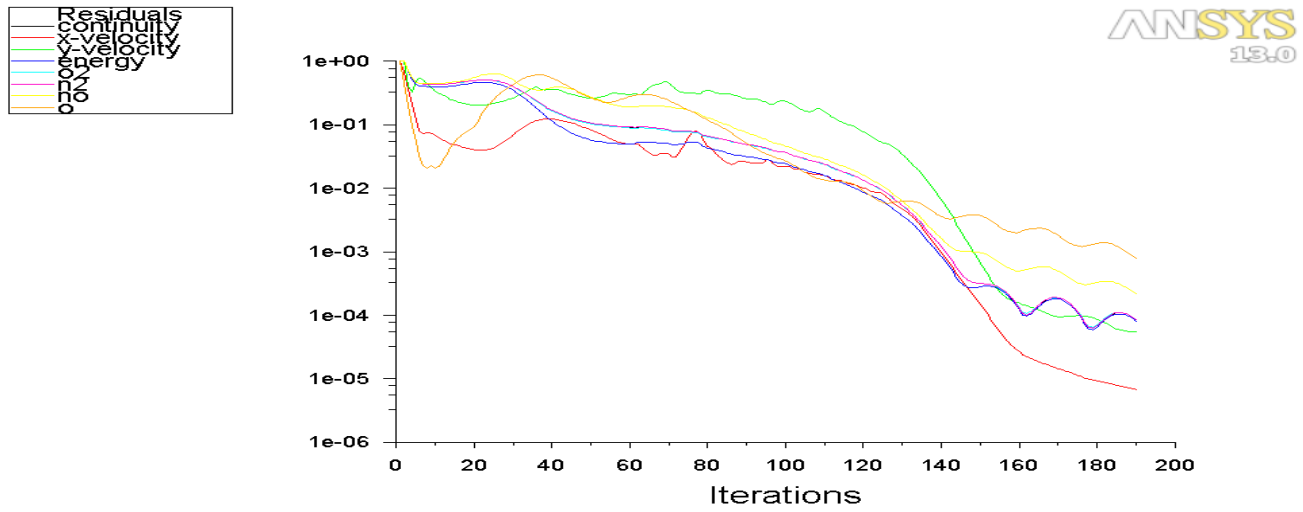
Fig A-3.1.7: Residual plot for the CFD model of the nozzle for air using coarse grid.

3.1   b) Air-fine-1 grid

Fig A-3.1.8: Mach Contours obtained from the CFD model of the nozzle for air using fine-1 grid.
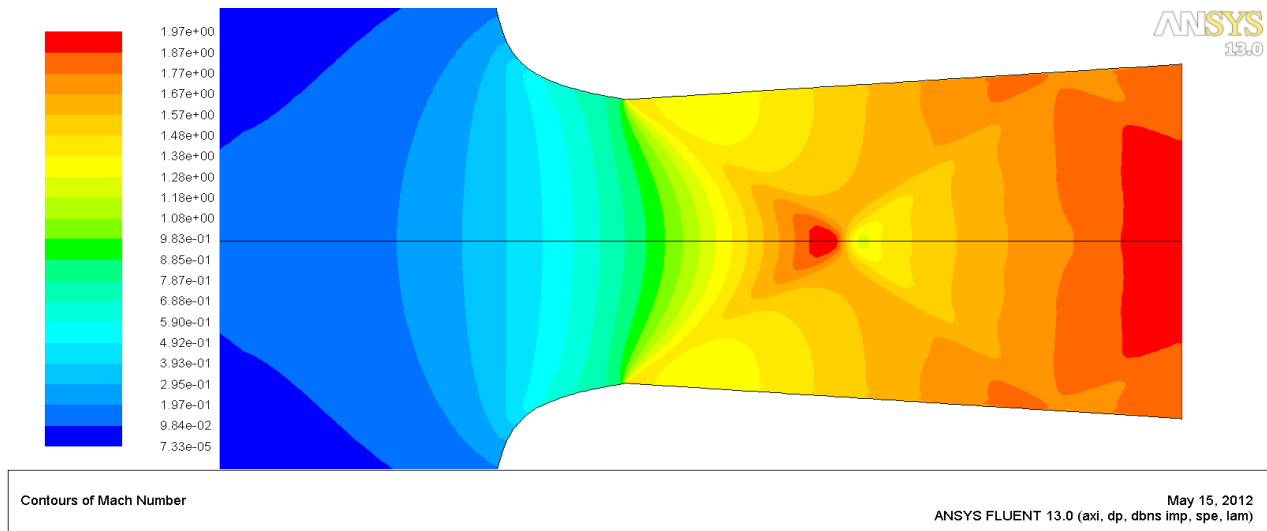
Fig A- 3.1.9: Static Pressure contours obtained from the CFD model of the nozzle for air using fine-1 grid.
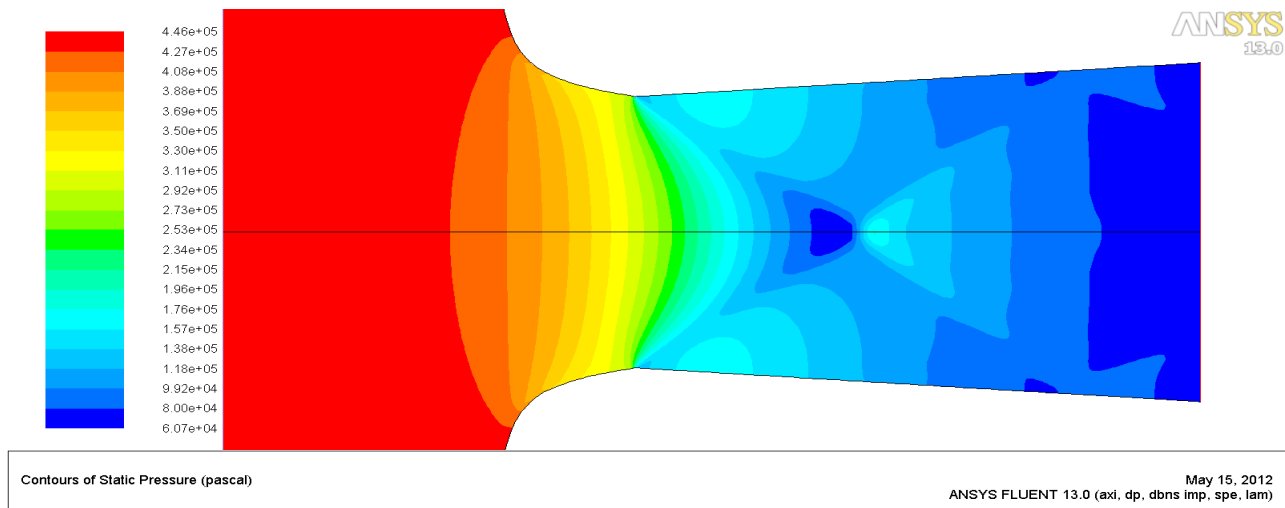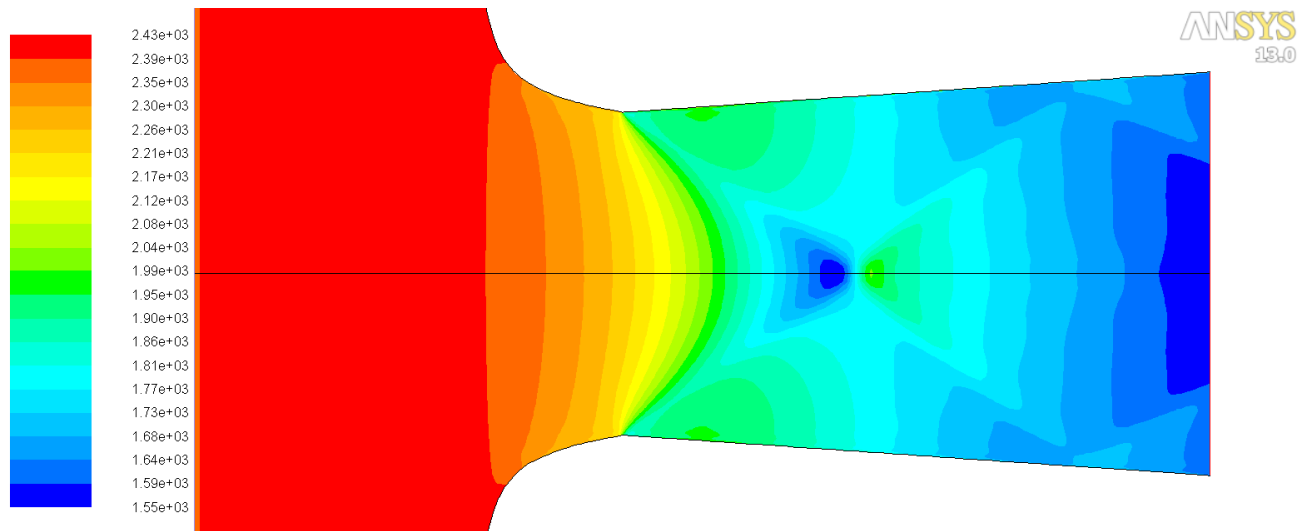
Fig A-3.1.10: Static Temperature contours obtained from the CFD model of the nozzle for air using fine-1 grid.

Fig A-3.1.11: Velocity Magnitude contours obtained from the CFD model of the nozzle for air using fine-1 grid.
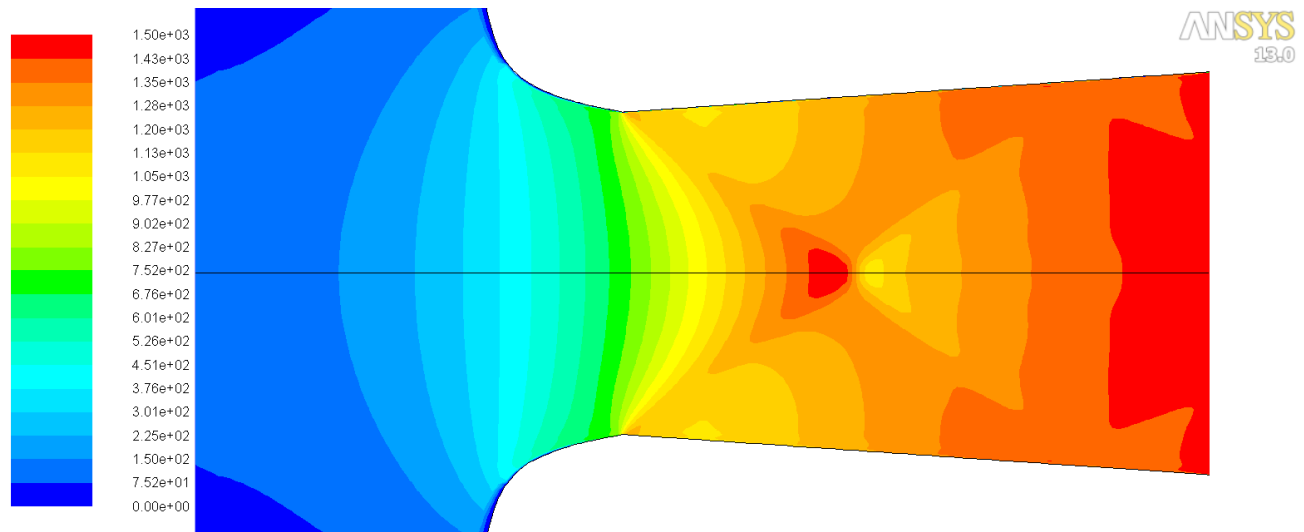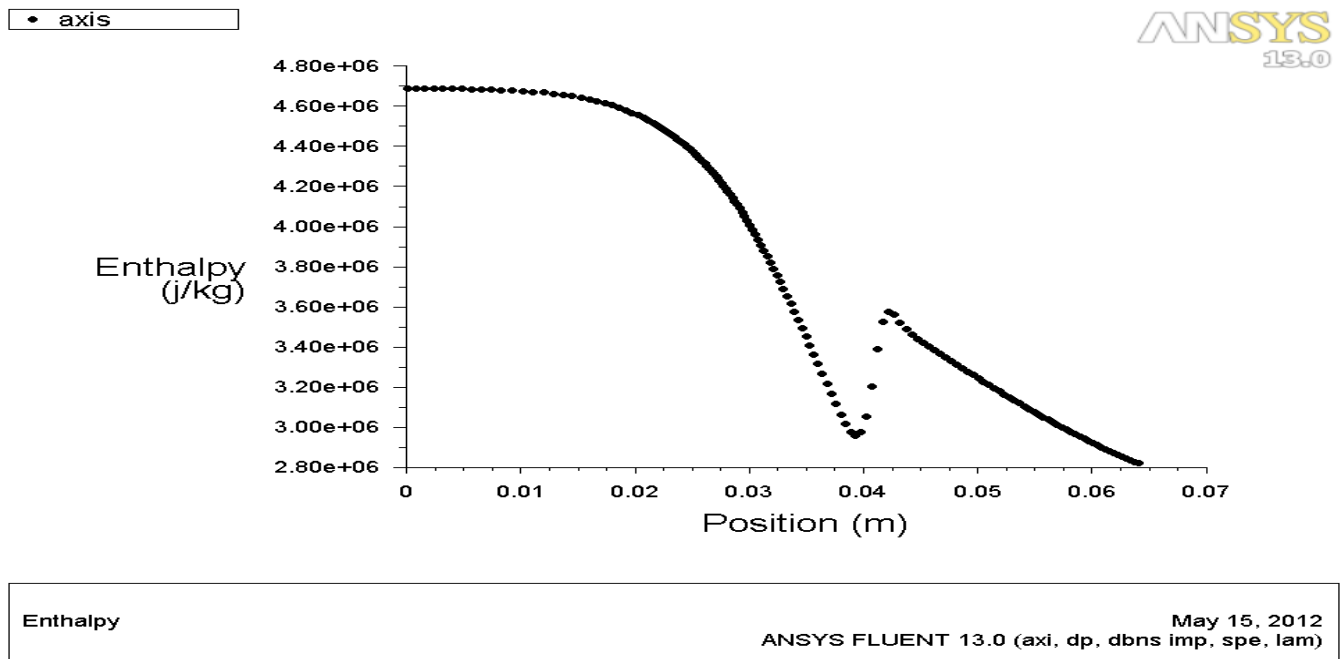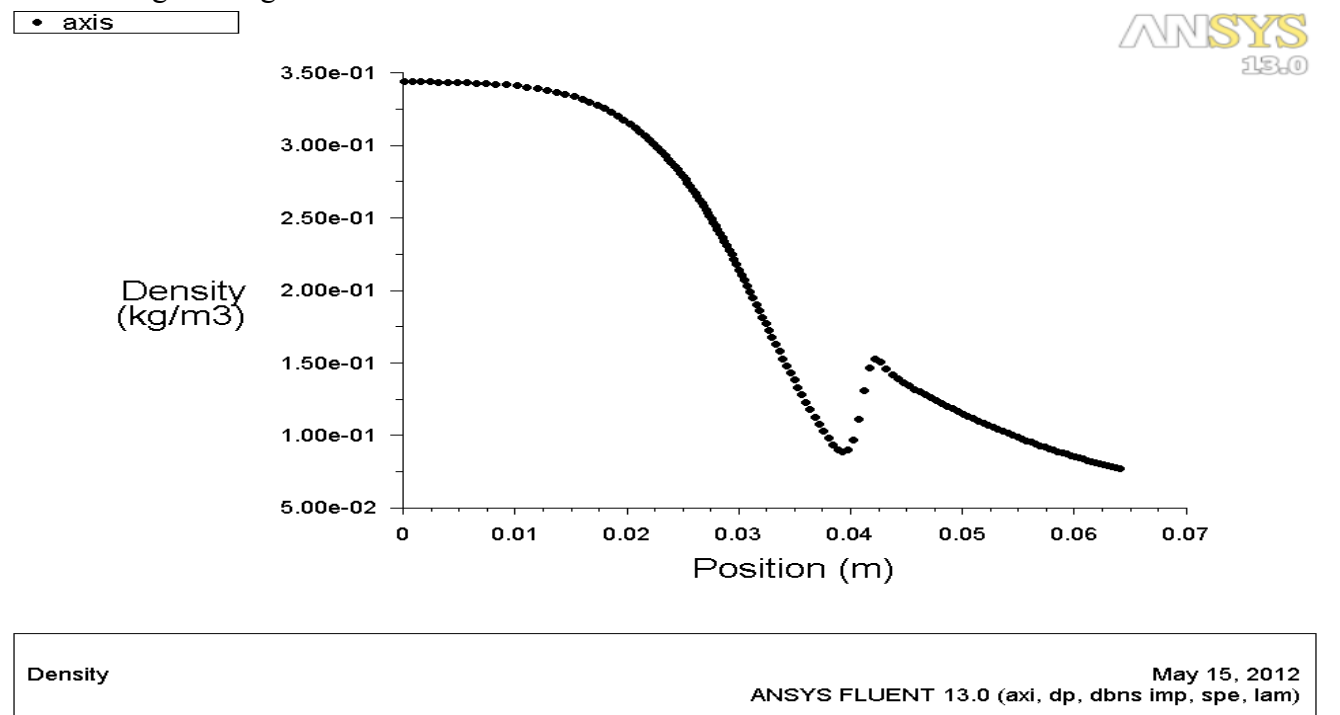
Fig A-3.1.12: Enthalpy along the axis of symmetry obtained from the CFD model of the nozzle for air
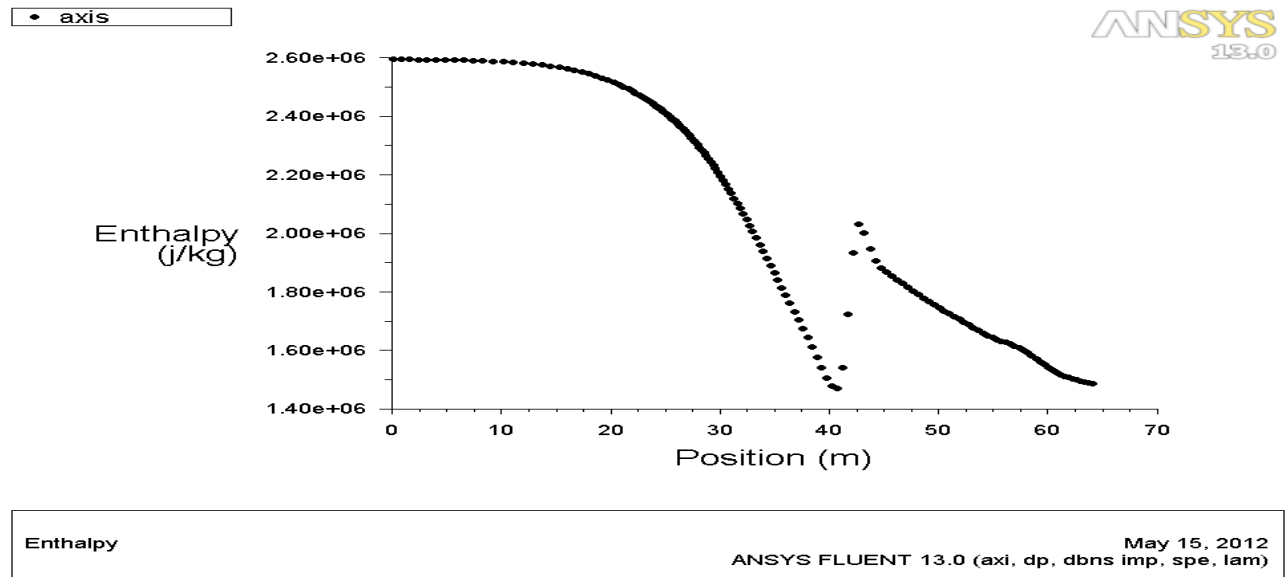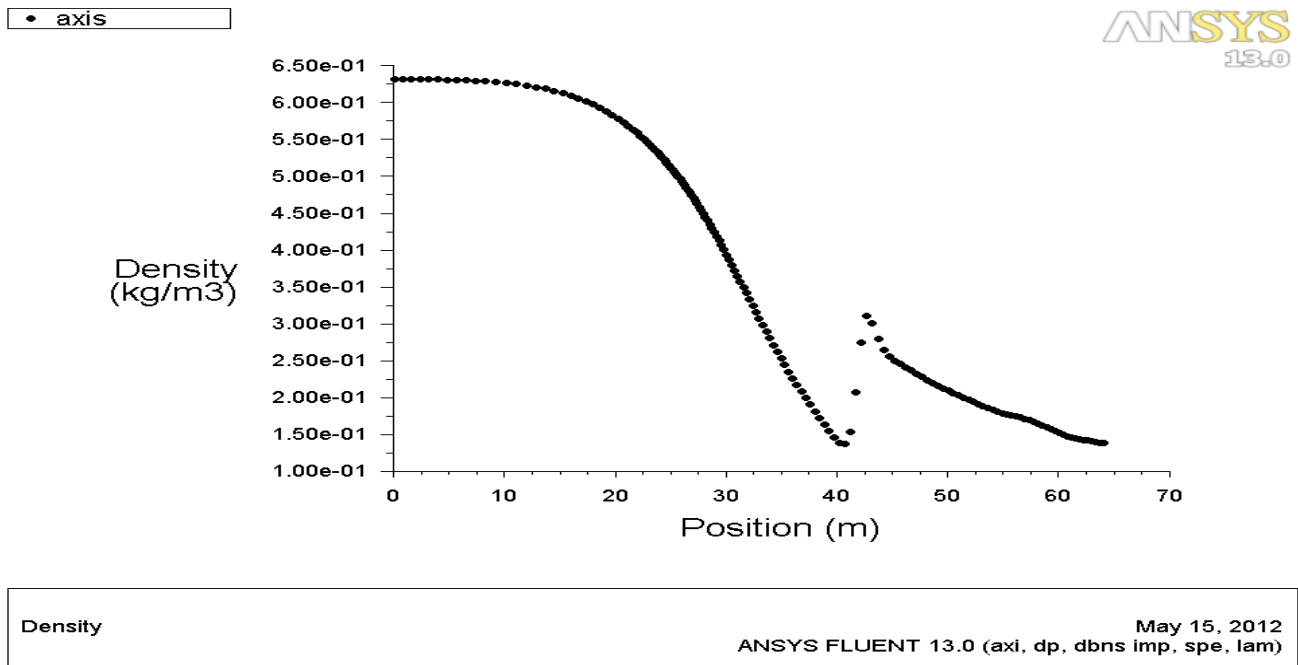
using fine-1 grid.

Fig A-3.1.13: Density along the axis of symmetry obtained from the CFD model of the nozzle for air using fine-1 grid.
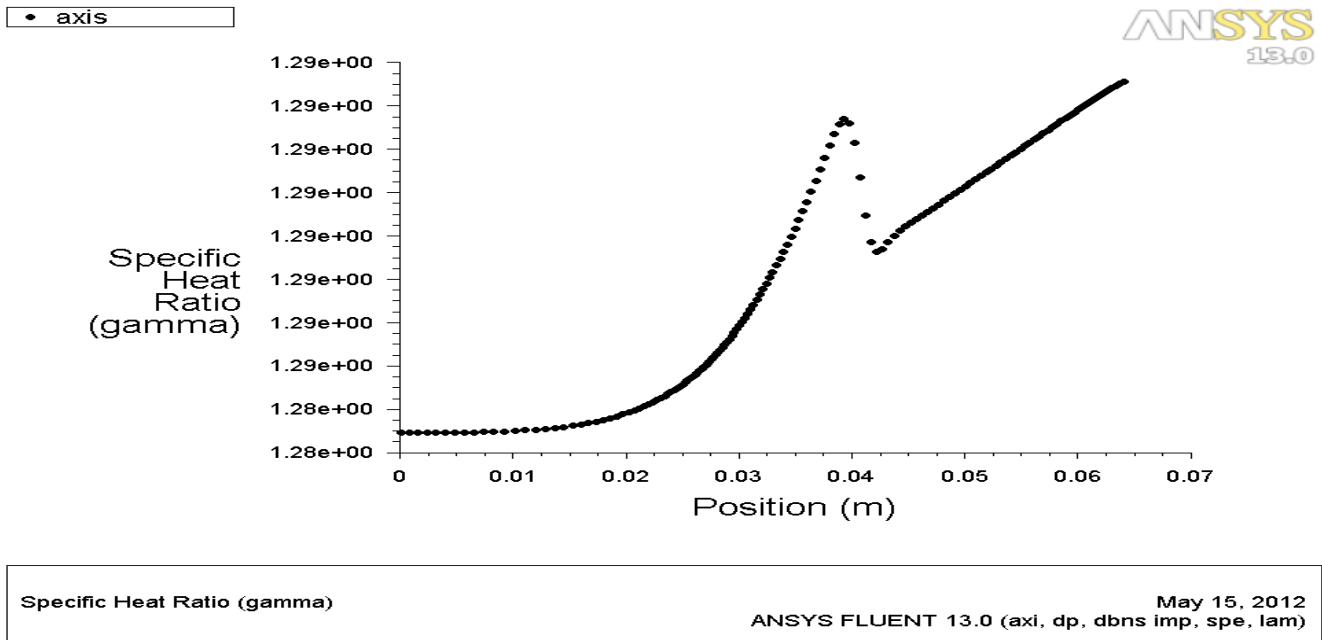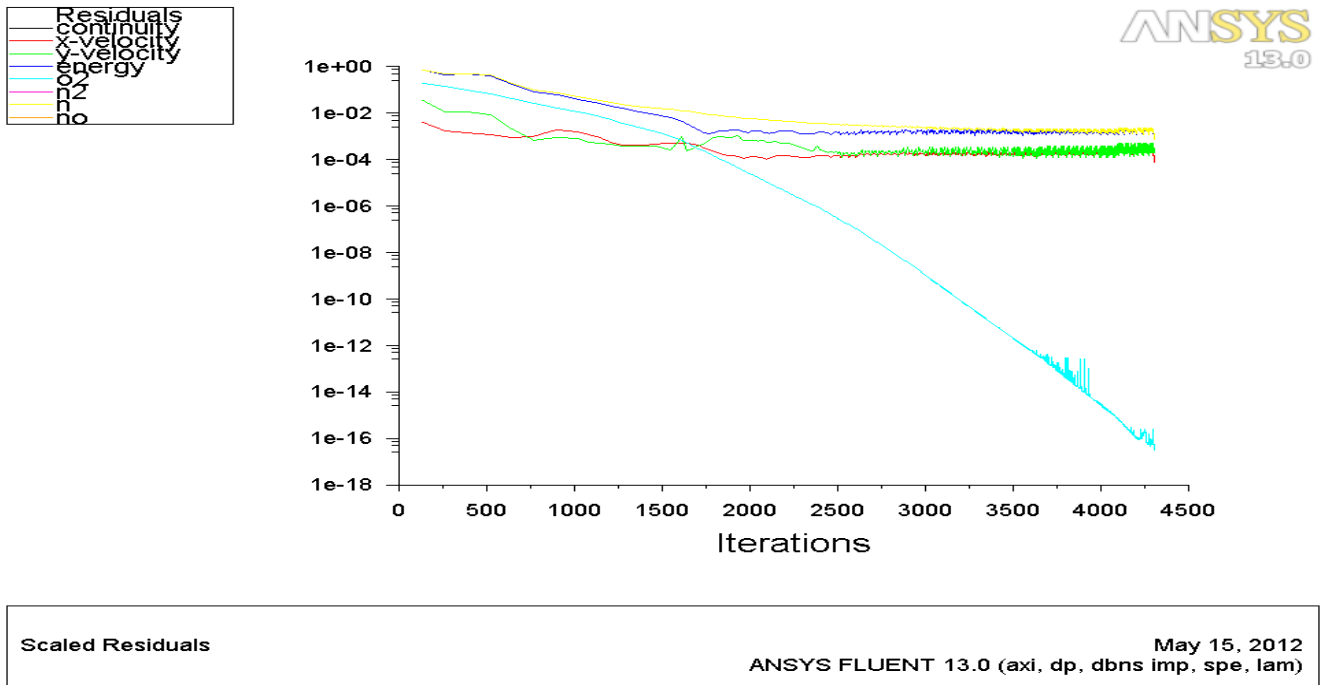
Fig A-3.1.14: Scaled Residuals obtained from the CFD model of the nozzle for air using fine-1 grid.
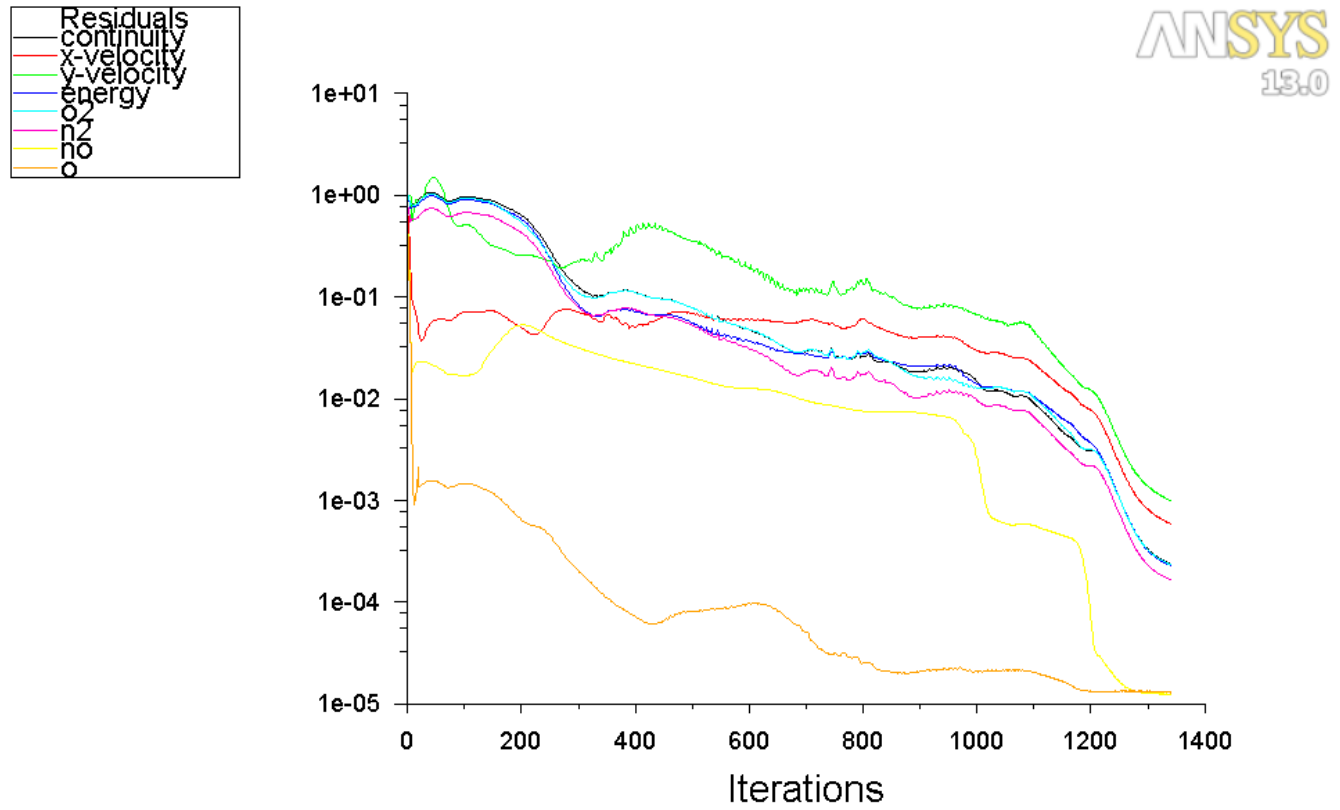
3.1 c) Air-Fine-2 grid

Fig A-3.1.15: Mach contours obtained from the CFD model of the nozzle for air using fine-2 grid.
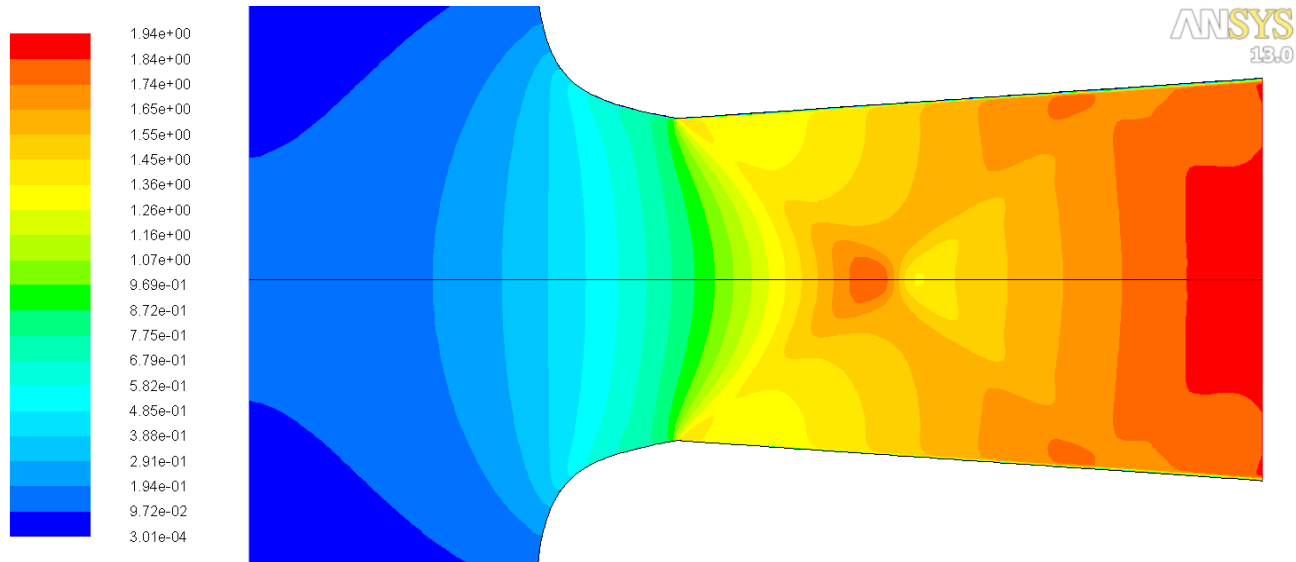
Contours of Mach Number

May 15, 2012
ANSYS FLUENT 13.0 (axi, dp, dbns imp, spe, lam)

Fig A-3.1.16: Static Pressure contours obtained from the CFD model of the nozzle for air using fine-2 grid.
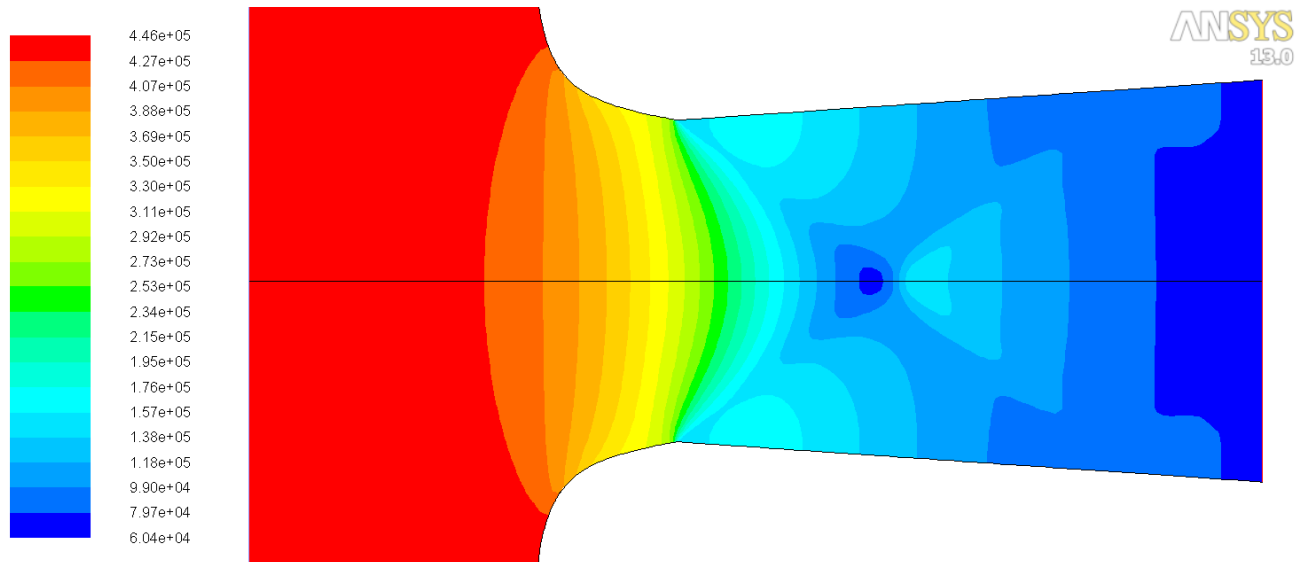
Contours of Static Pressure (pascal)

May 15, 2012
ANSYS FLUENT 13.0 (axi, dp, dbns imp, spe, lam)

Fig A-3.1.17: Static Temperature contours obtained from the CFD model of the nozzle for air using
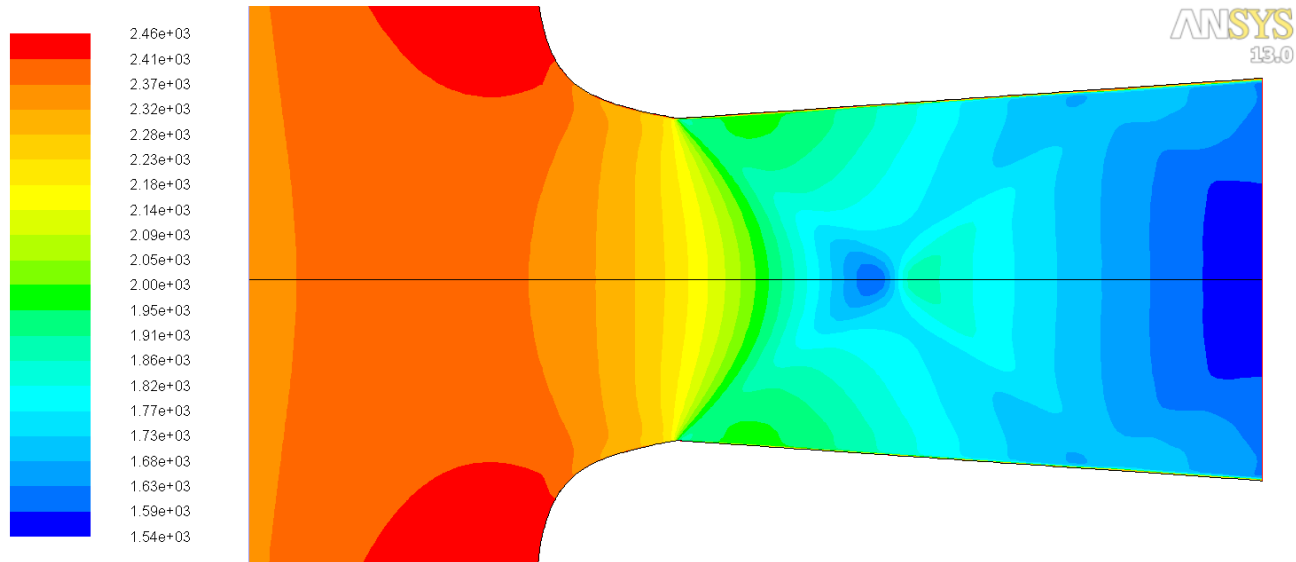
fine-2 grid.

Fig A-3.1.18: Velocity Magnitude contours obtained from the CFD model of the nozzle for air using fine-2 grid.
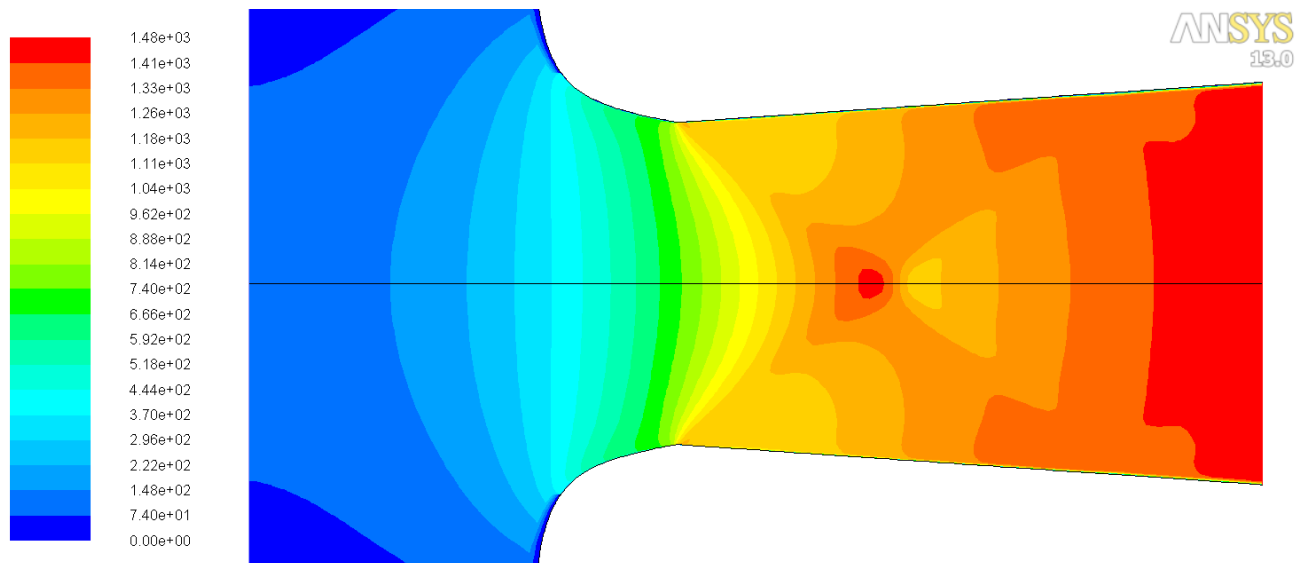
Fig A-3.1.19: Enthalpy along the axis of symmetry obtained from the CFD model of the nozzle for air
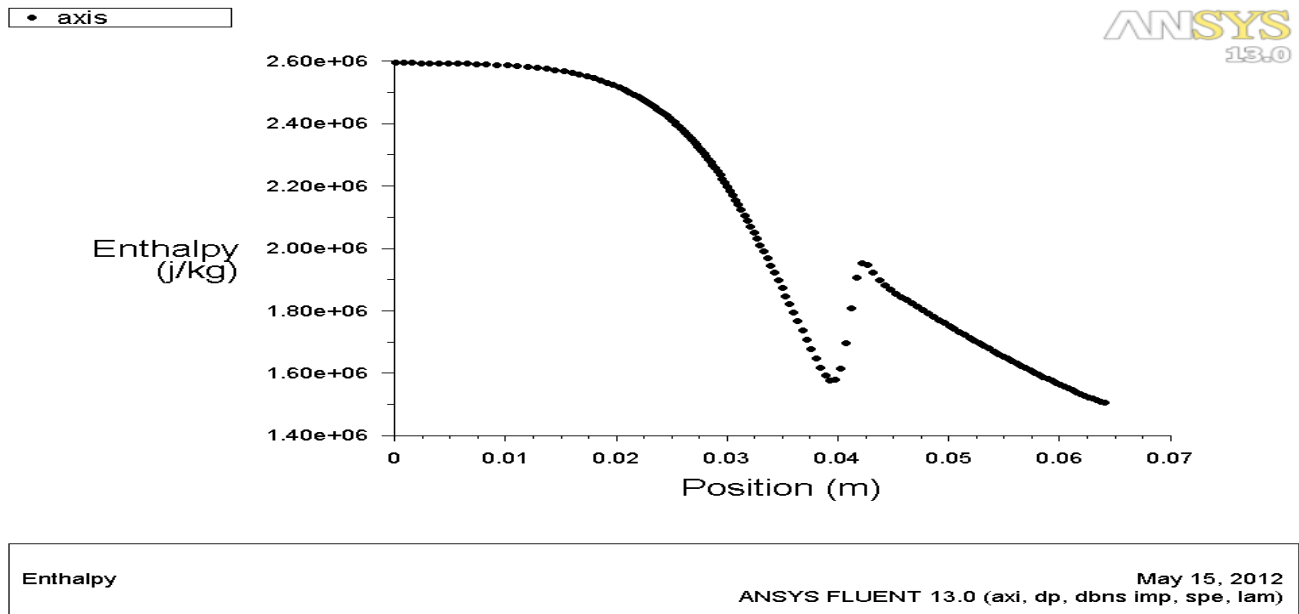
using fine-2 grid.
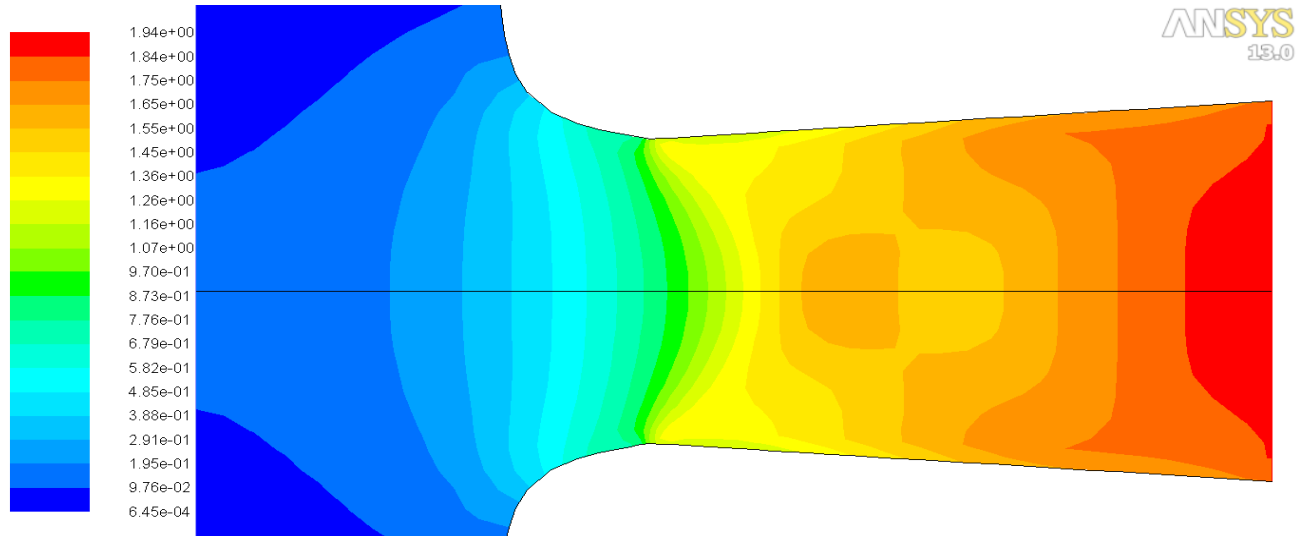
Fig A-3.1.20: Specific heat ratio along the axis of symmetry obtained from the CFD model of the nozzle for air using fine-2 grid.
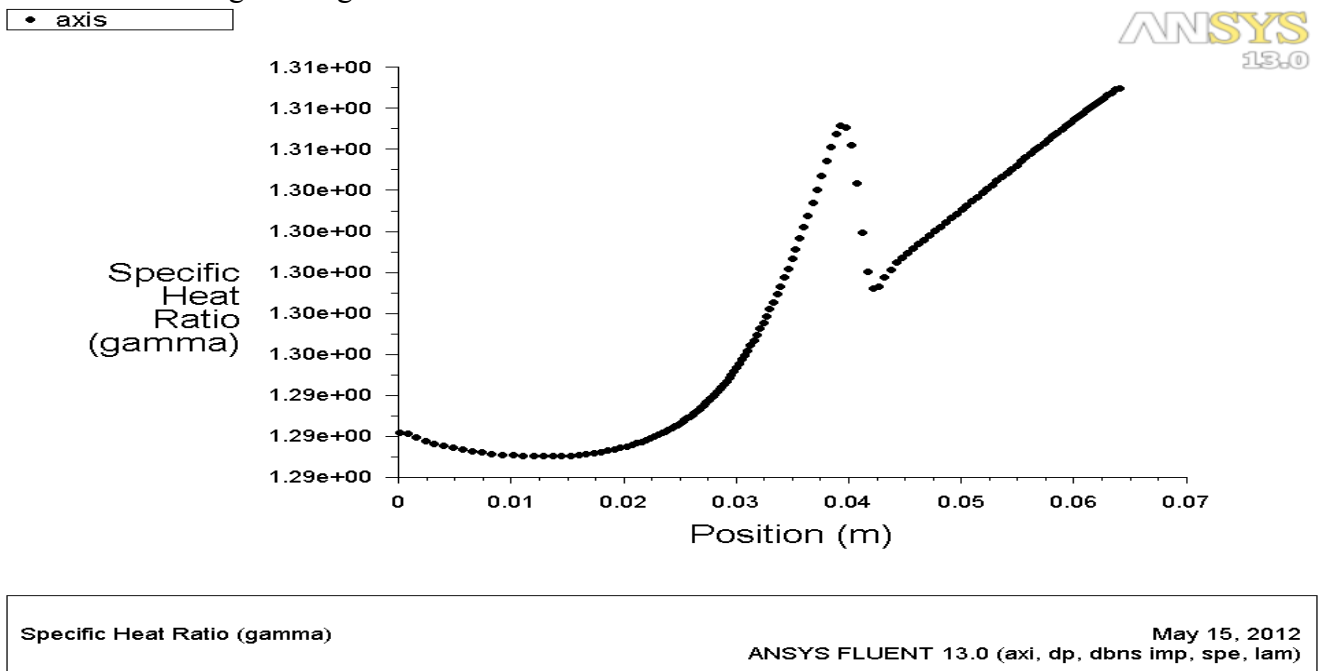
Fig A-3.1.21: Density along the axis of symmetry obtained from the CFD model of the nozzle for air
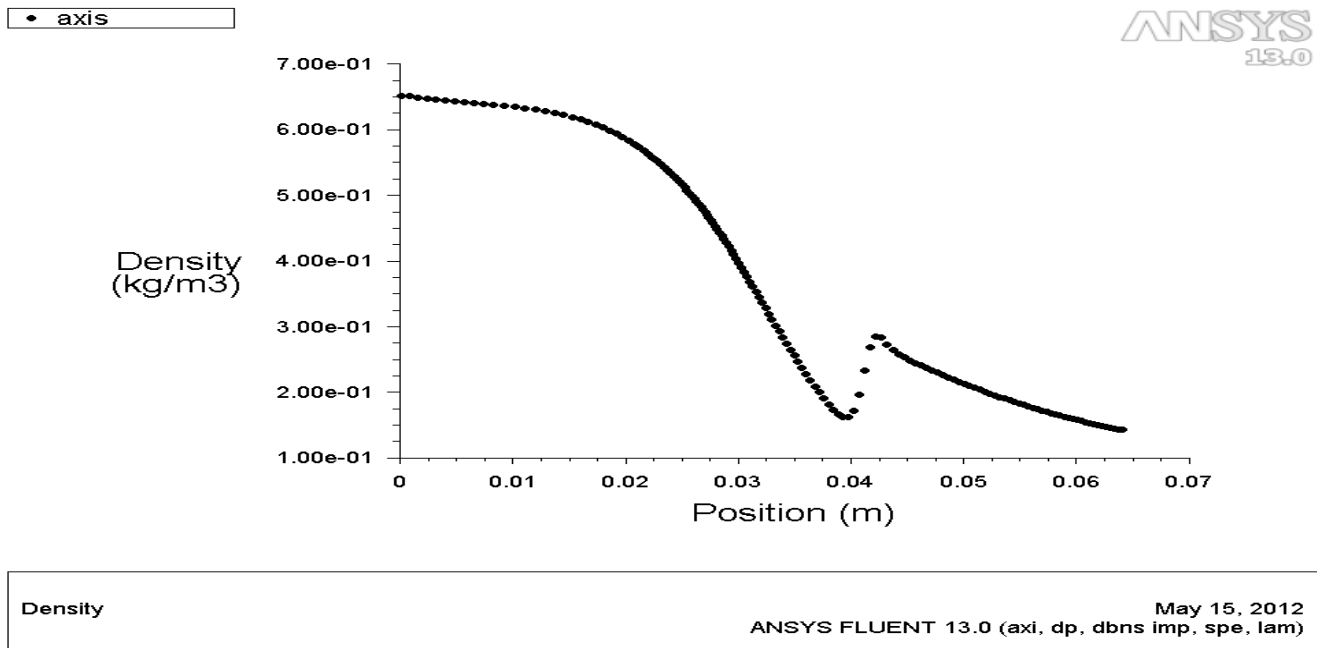
using fine-2 grid.

Fig A-3.1.22: Mass fraction of N along the axis of symmetry obtained from the CFD model of the nozzle for air using fine-2 grid.
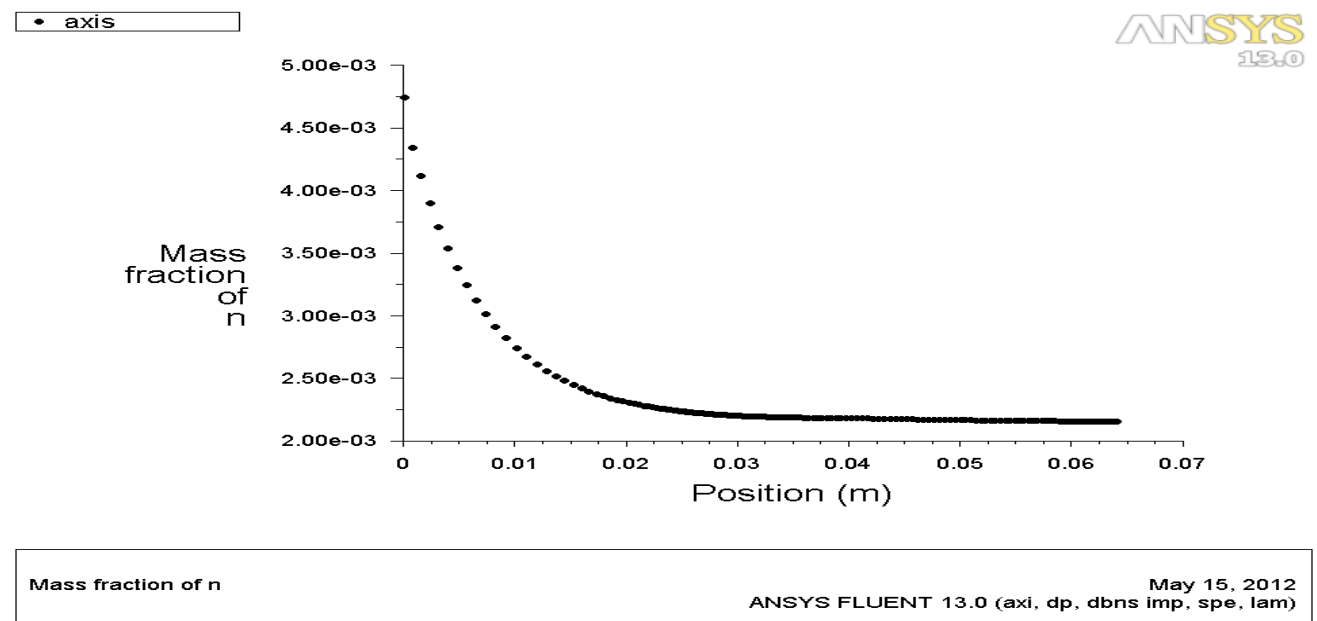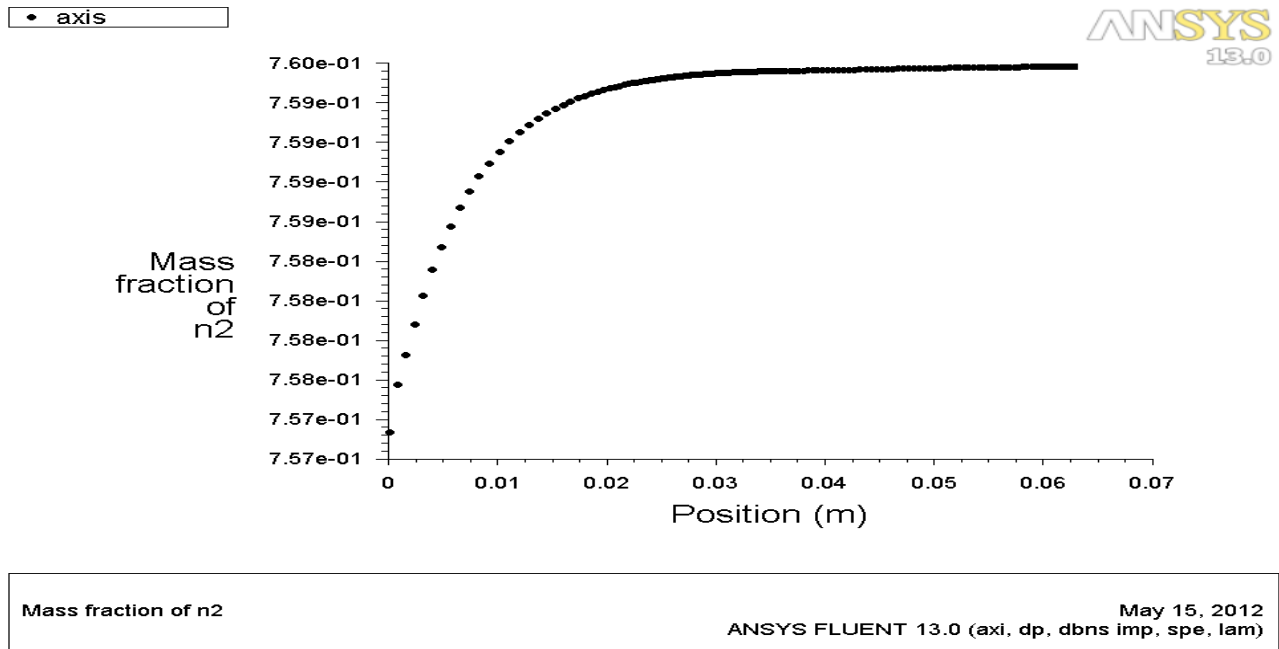
Fig A-3.1.23: Mass fraction of N2 along the axis of symmetry obtained from the CFD model of the nozzle for air using fine-2 grid.

Fig A-3.1.24: Mass fraction of NO along the axis of symmetry obtained from the CFD model of the nozzle for air using fine-2 grid.

Fig A-3.1.27: Scaled residuals obtained from the CFD model of the nozzle for air using fine-2 grid.
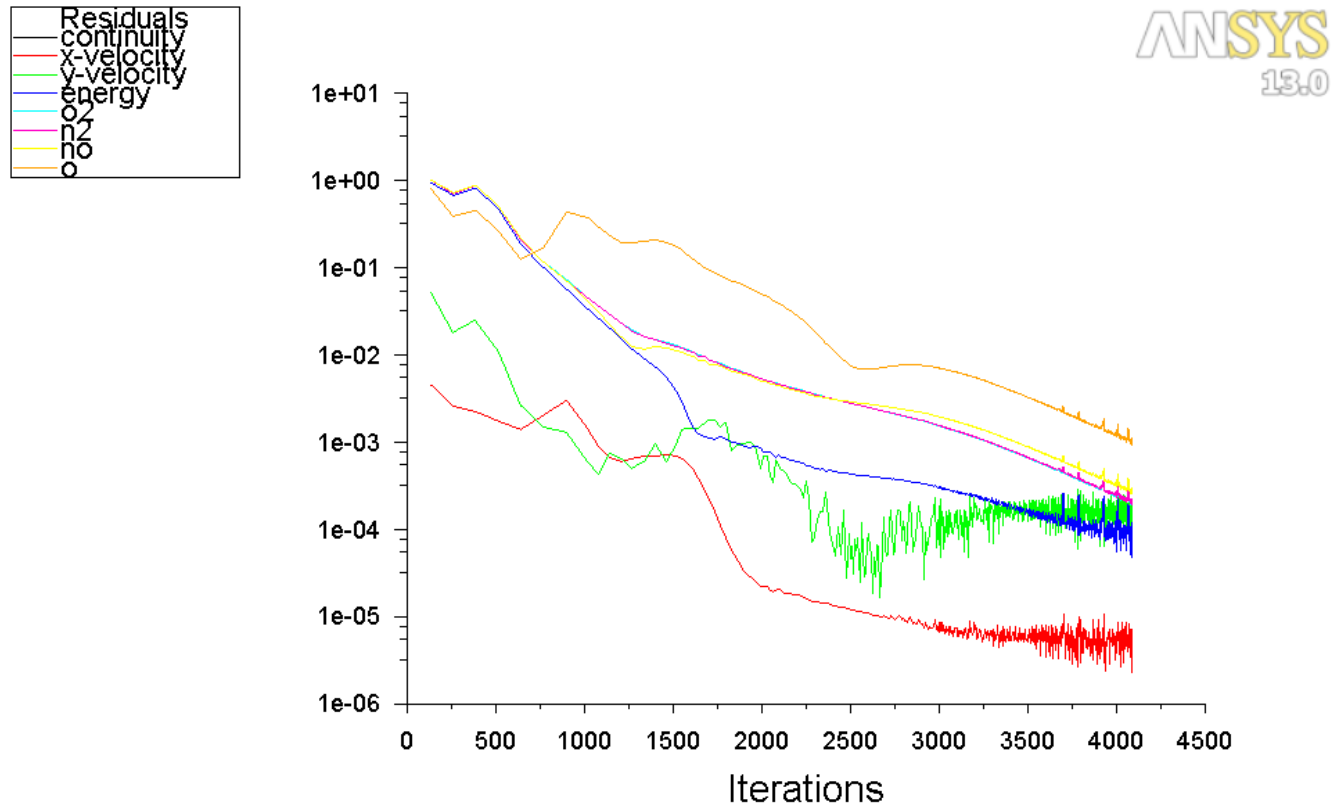
3.2 a) N2-case-1 Coarse grid

Fig A-3.2.1: Mach Contours obtained from the CFD model of the nozzle for N2-case-1 using coarse
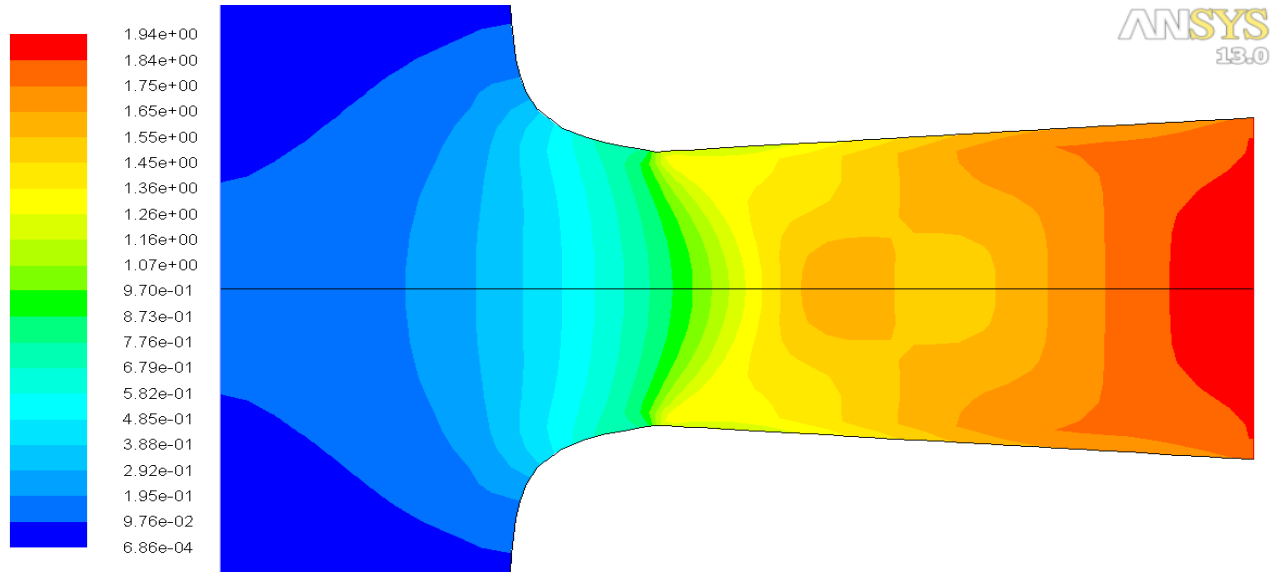
grid.

Fig A-3.2.2: Static Pressure Contours obtained from the CFD model of the nozzle for N2-case-1 using coarse grid.
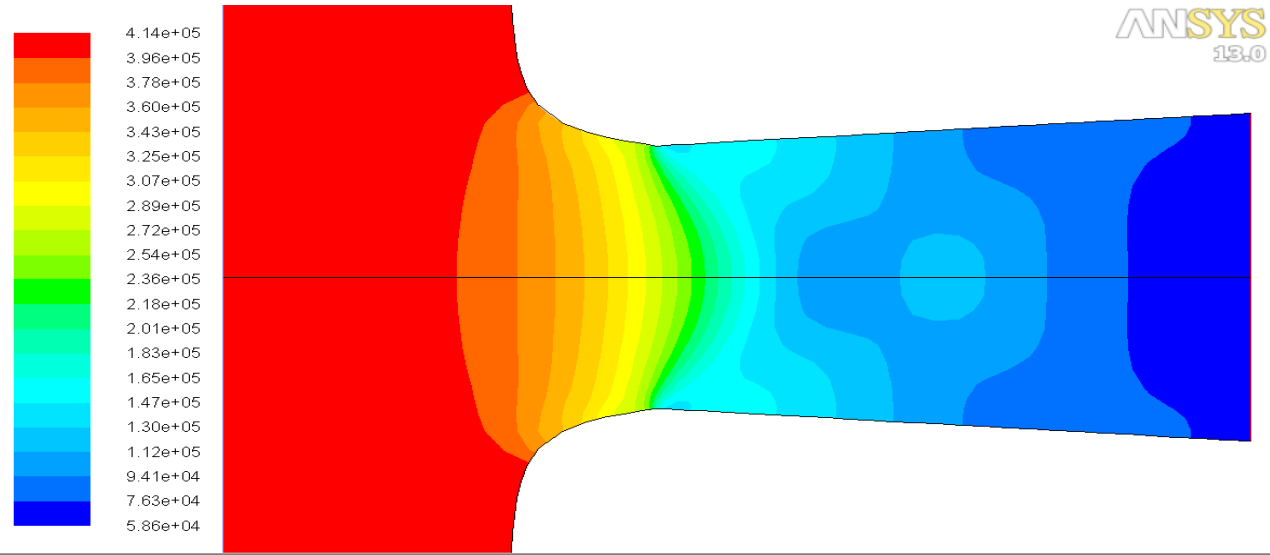
Fig A-3.2.3: Static Temperature Contours obtained from the CFD model of the nozzle for N2-case-1

using coarse grid.

Fig A-3.2.4: Velocity Magnitude Contours obtained from the CFD model of the nozzle for N2-case-1 using coarse grid.
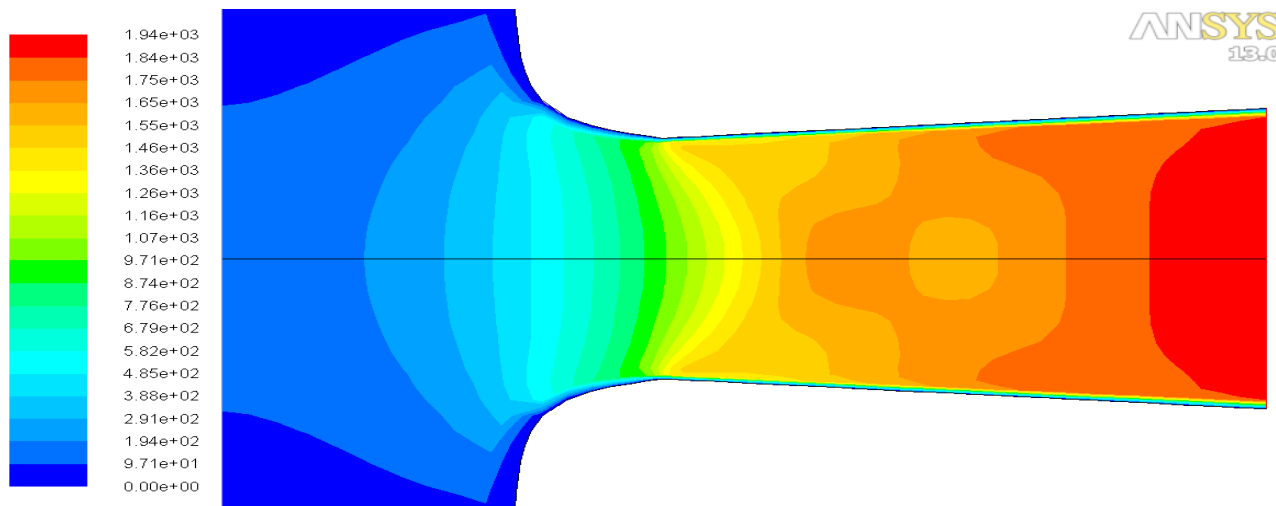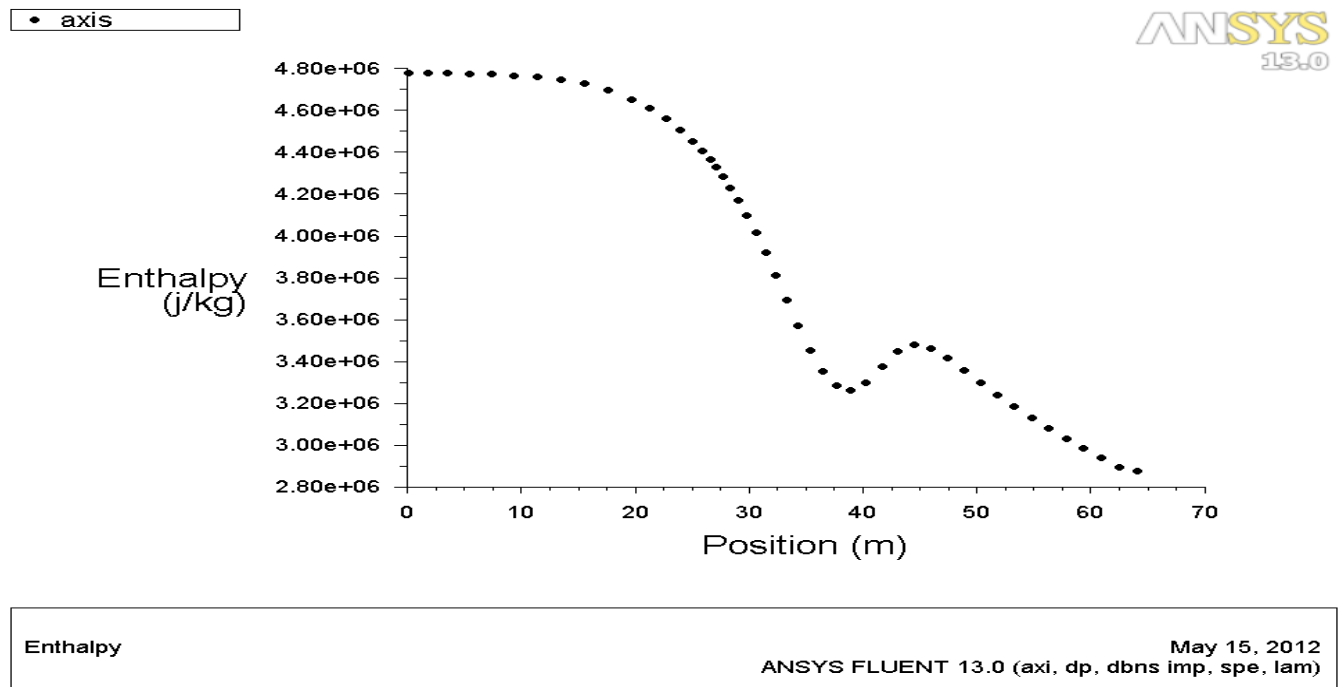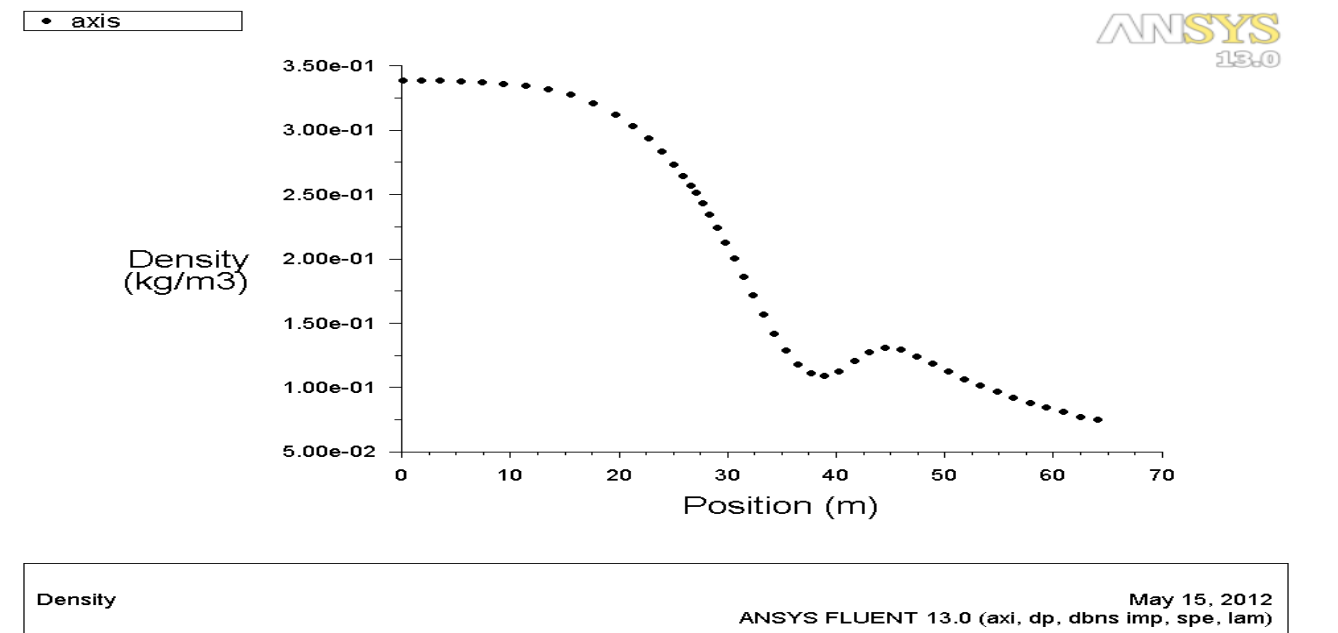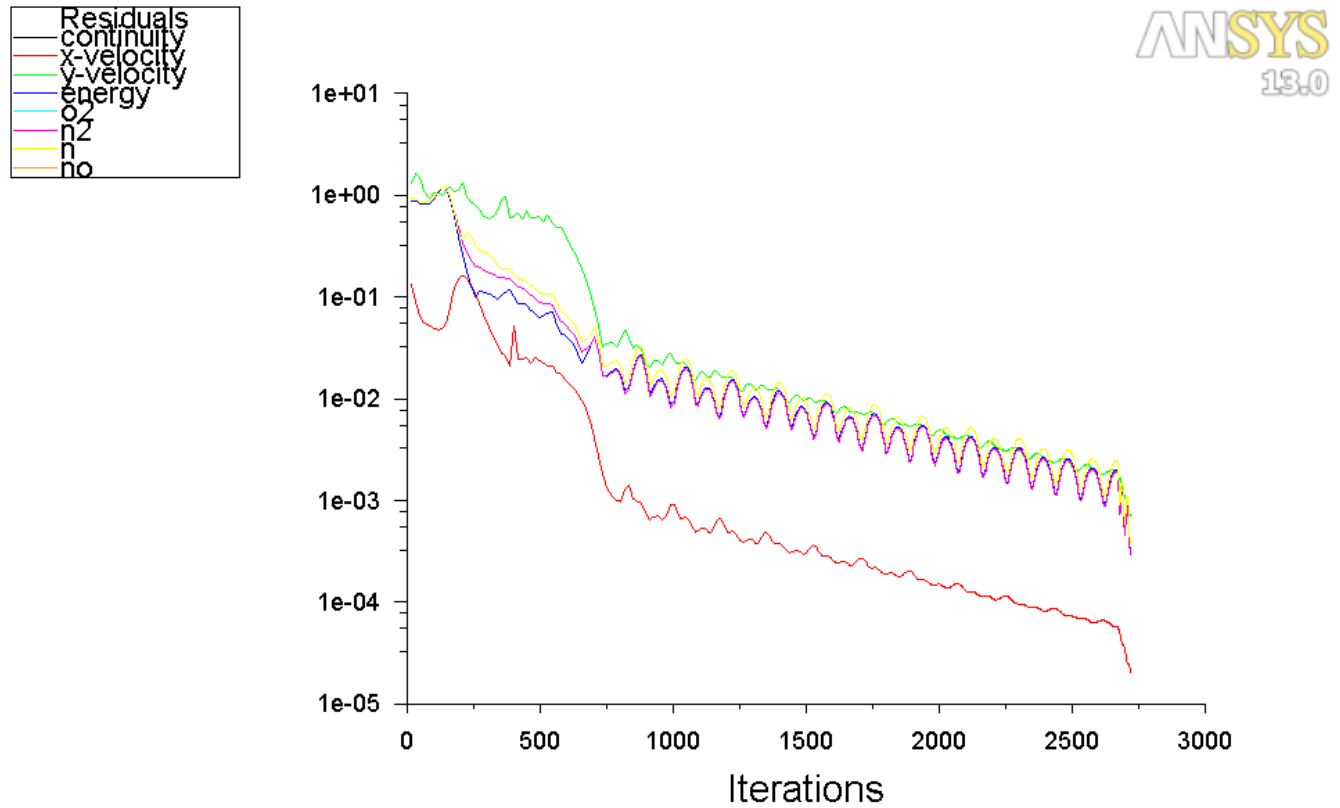
Fig A-3.2.5: Enthalpy along the axis of symmetry obtained from the CFD model of the nozzle for N2-
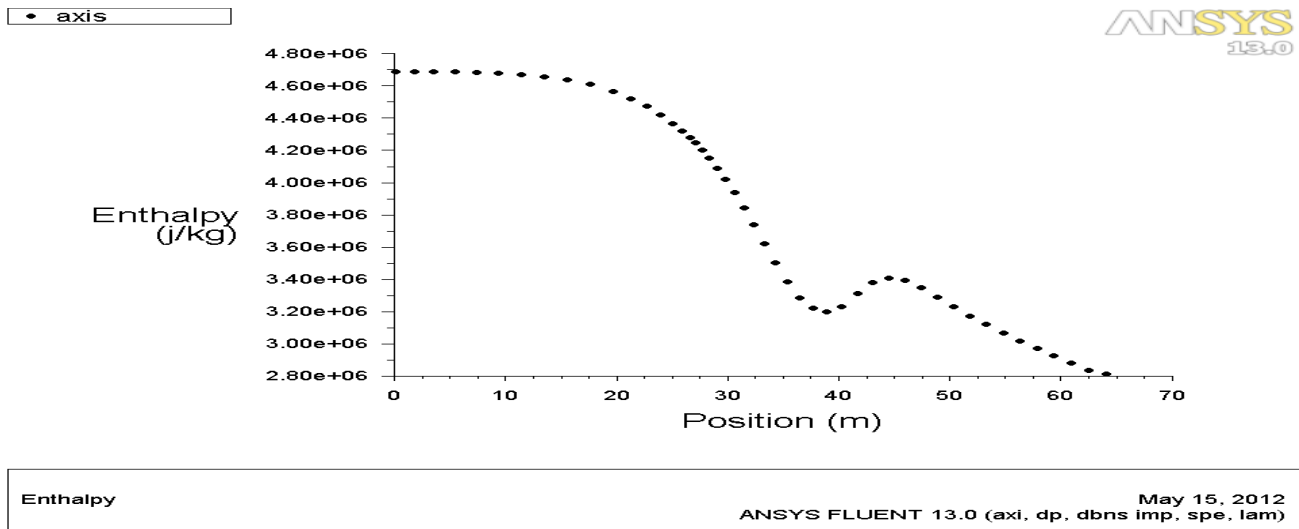
case-1 using coarse grid.

Fig A-3.2.6: Enthalpy along the axis of symmetry obtained from the CFD model of the nozzle for N2-
case-1 using coarse grid.
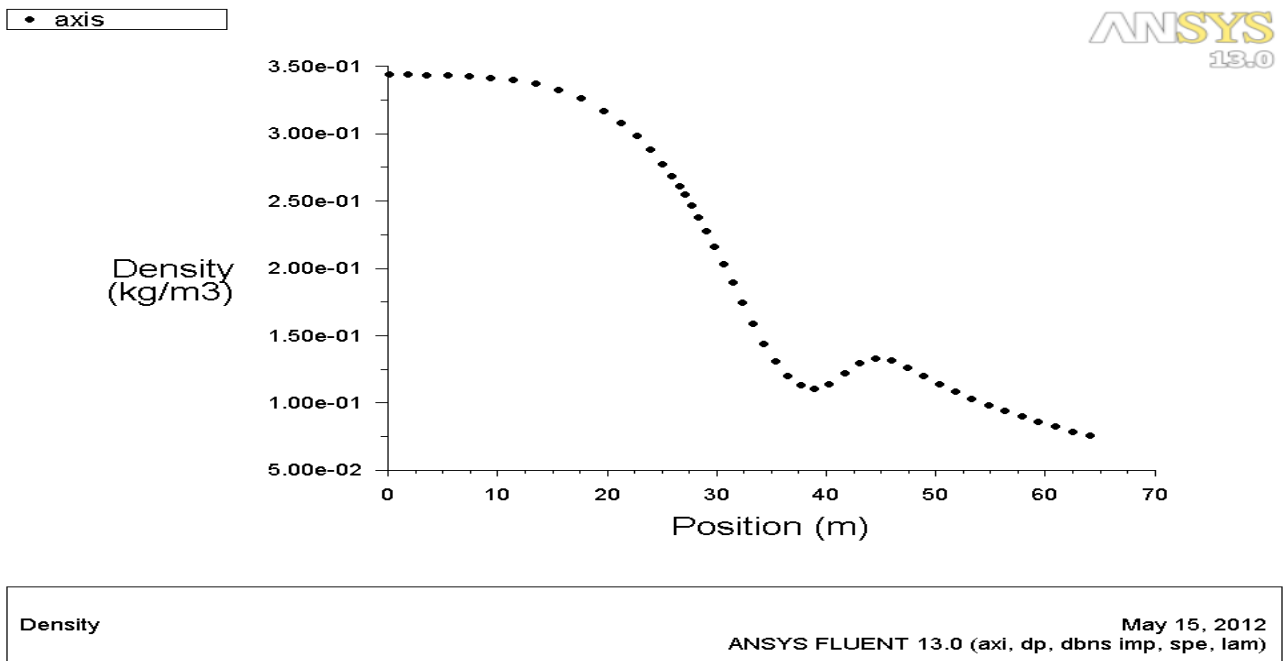
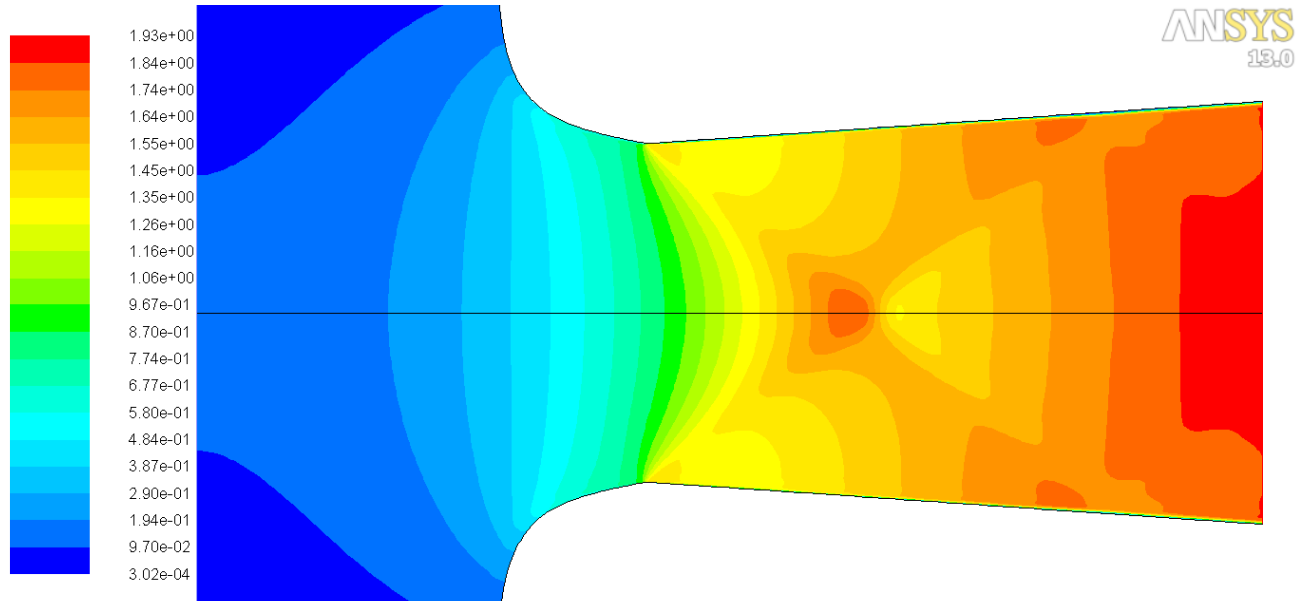**Fig A-3.2.7**: Scaled Residuals obtained from the CFD model of the nozzle for N2-case-1 using coarse
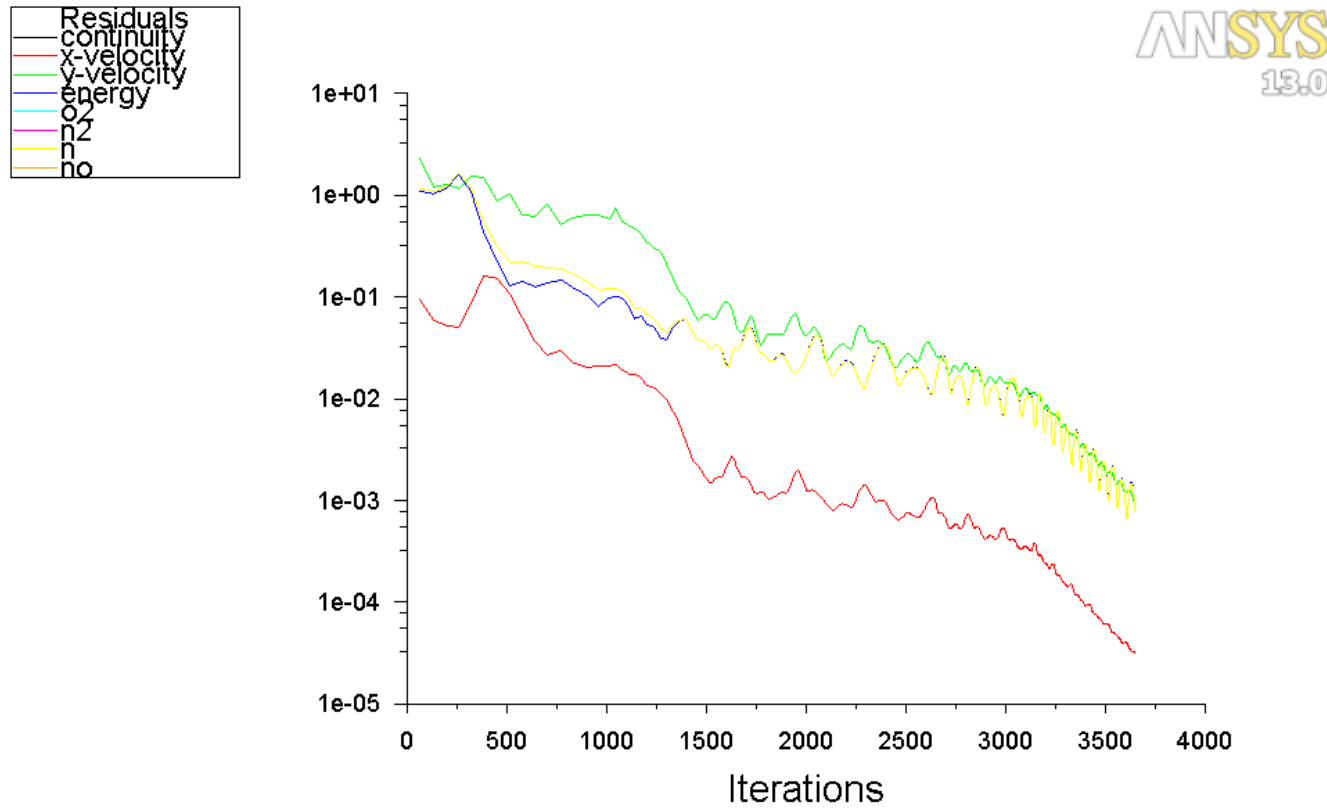
grid.

3.2 b) N2-case-1 Fine-1 grid

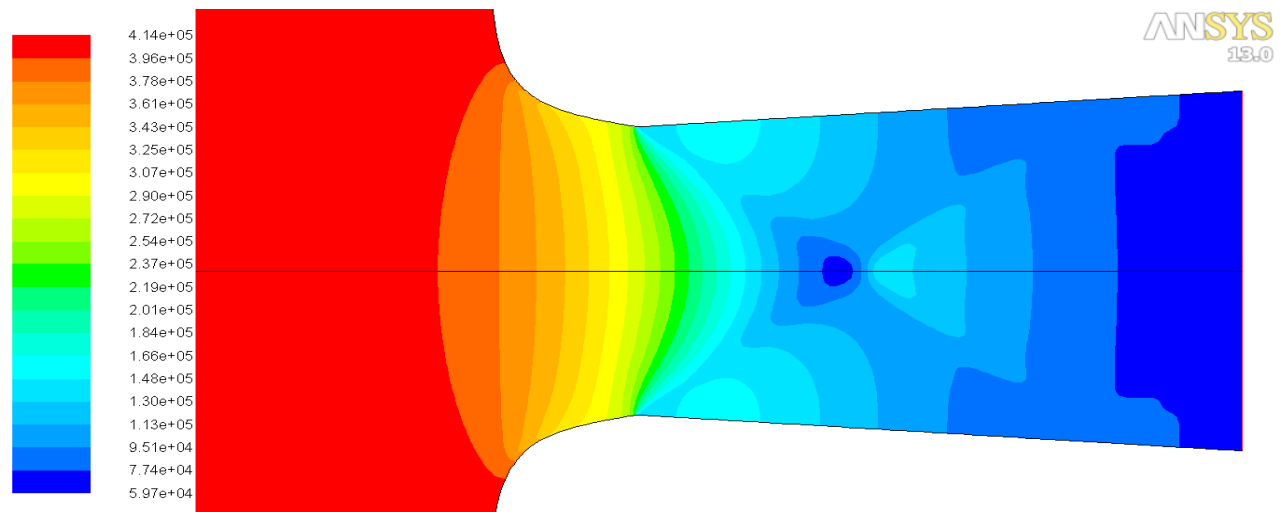**Fig A-3.2.8**: Mach Contours obtained from the CFD model of the nozzle for N2-case-1 using fine-1

grid.

Fig A-3.2.9: Static Pressure Contours obtained from the CFD model of the nozzle for N2-case-1 using fine-1 grid.
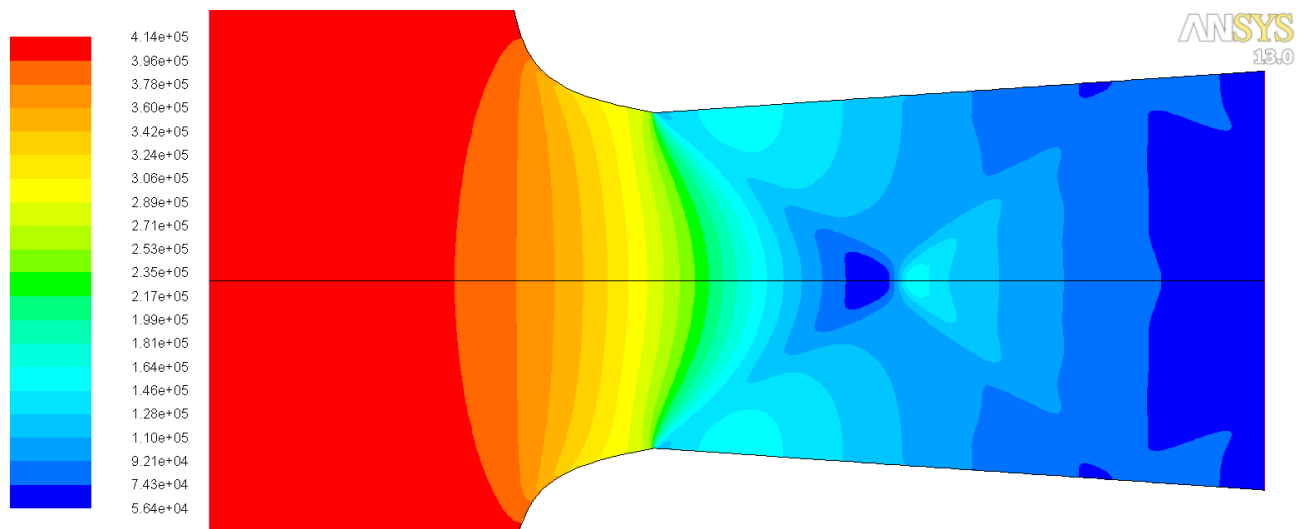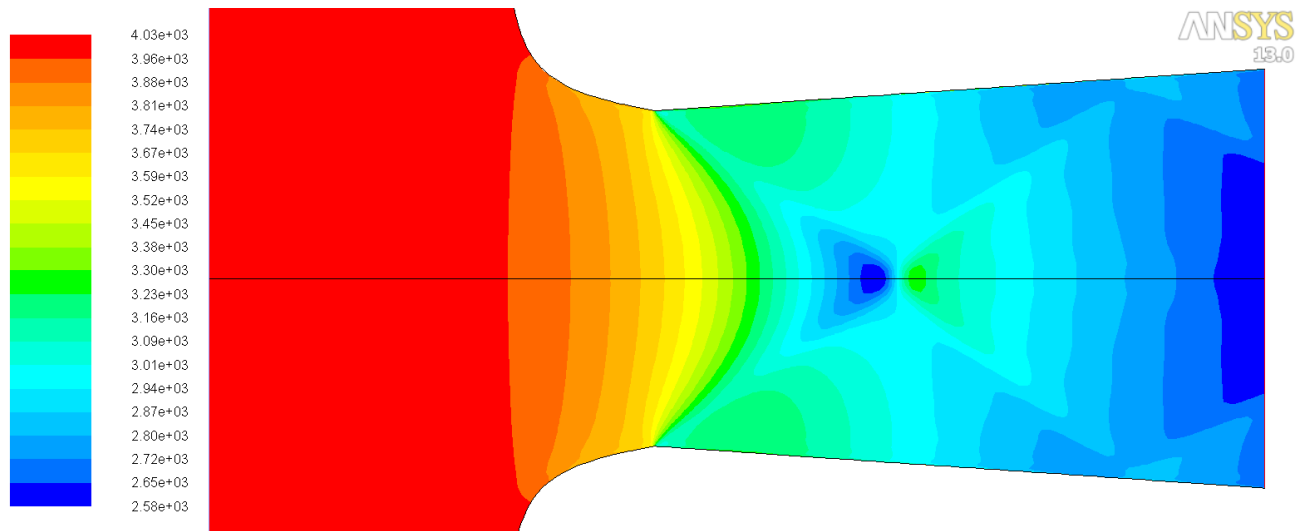
Fig A-3.2.10: Static temperature obtained from the CFD model of the nozzle for N2-case-1 using fine-1 grid.

Fig A-3.2.11: Velocity Magnitude obtained from the CFD model of the nozzle for N2-case-1 using fine-1 grid.
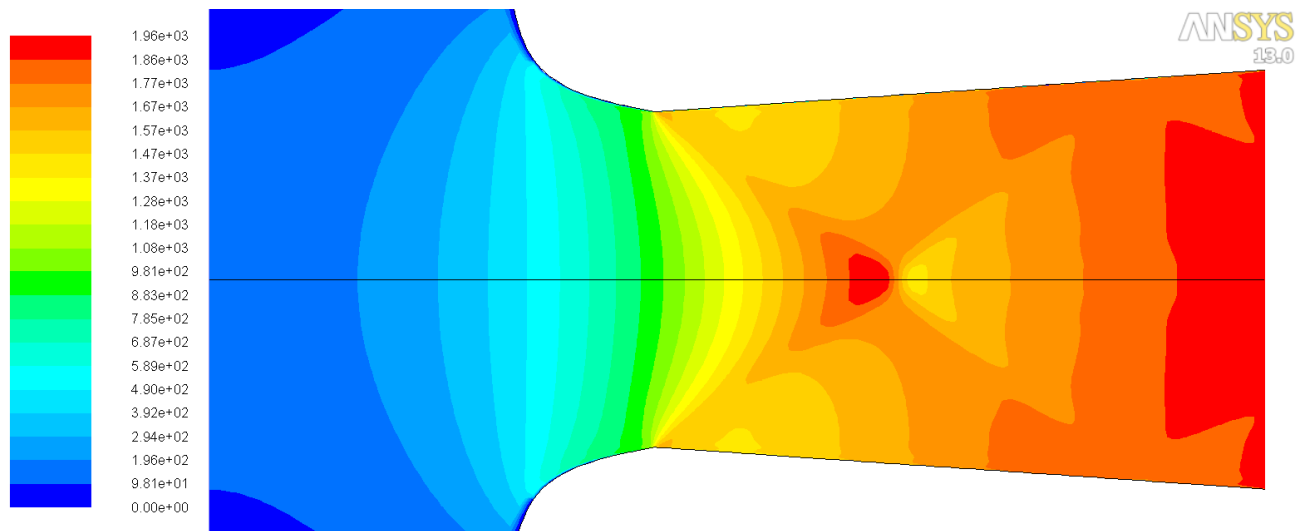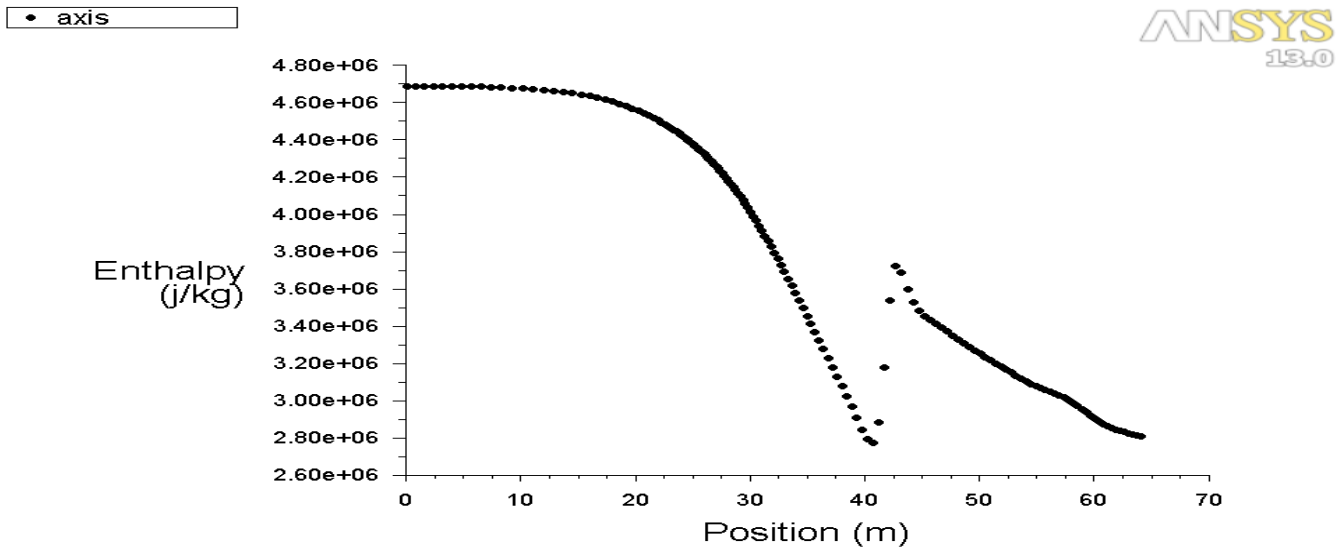
Fig A-3.2.12: Enthalpy along the axis of symmetry obtained from the CFD model of the nozzle for N2-case-1 using fine-1 grid.

Fig A-3.2.13: Density along the axis of symmetry obtained from the CFD model of the nozzle for N2-case-1 using fine-1 grid.
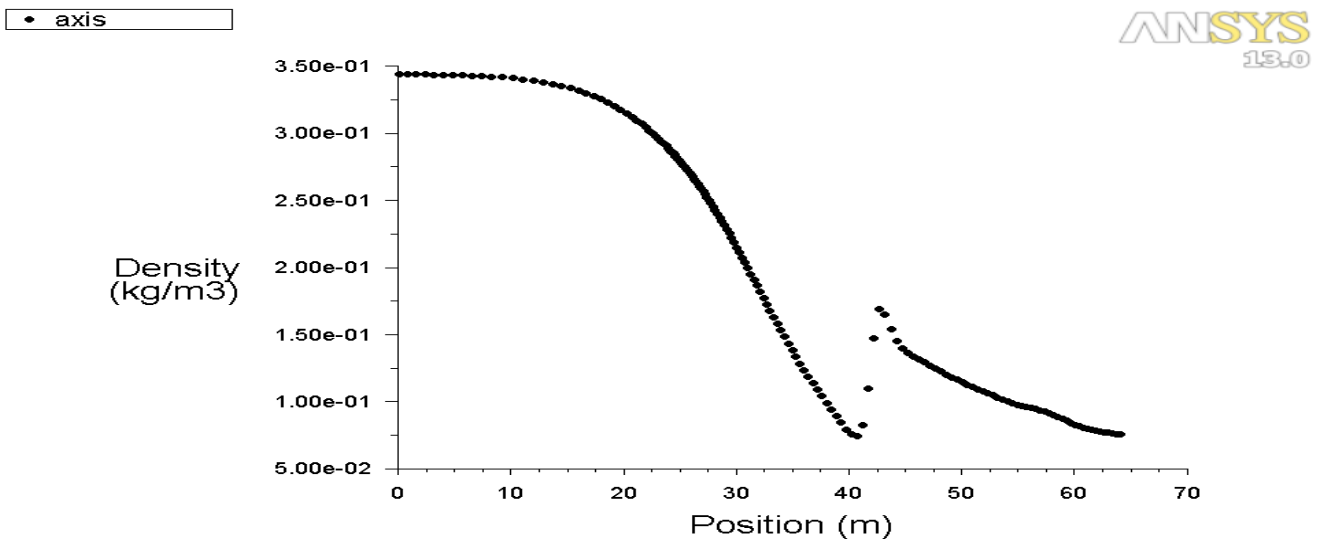
Fig A-3.2.14: Scaled Residuals obtained from the CFD model of the nozzle for N2-case-1 using fine-1

grid.

3.2 c) N2-case-1 Fine-2 grid

Fig A-3.2.15: Mach Contours obtained from the CFD model of the nozzle for N2-case-1 using fine-2
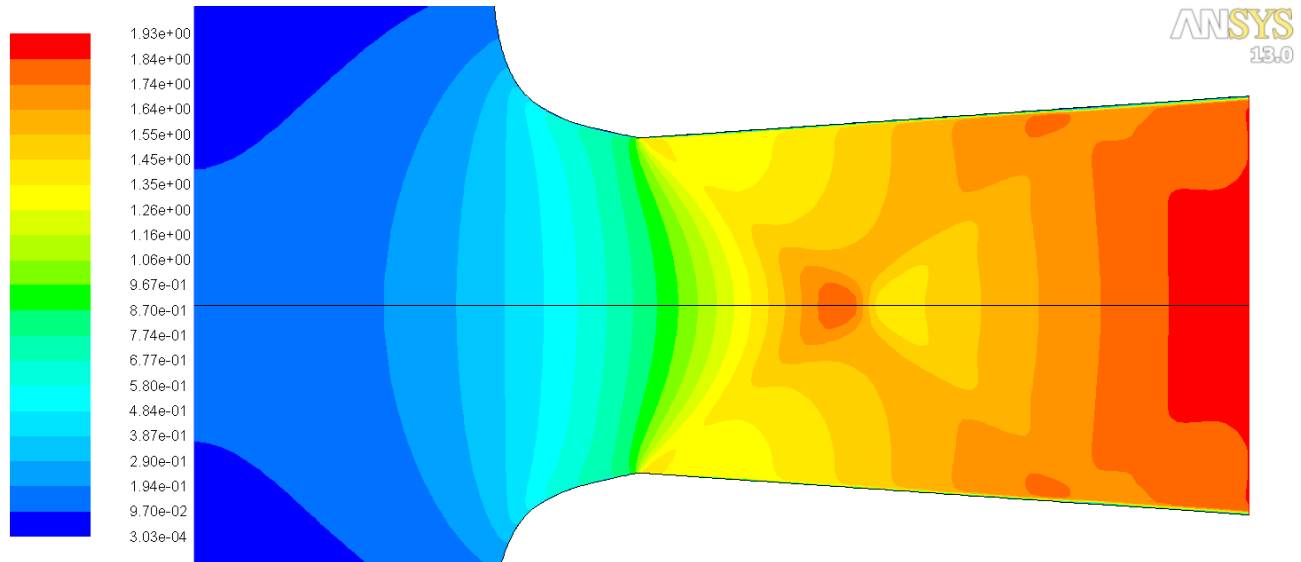
Contours of Mach Number

May 15, 2012
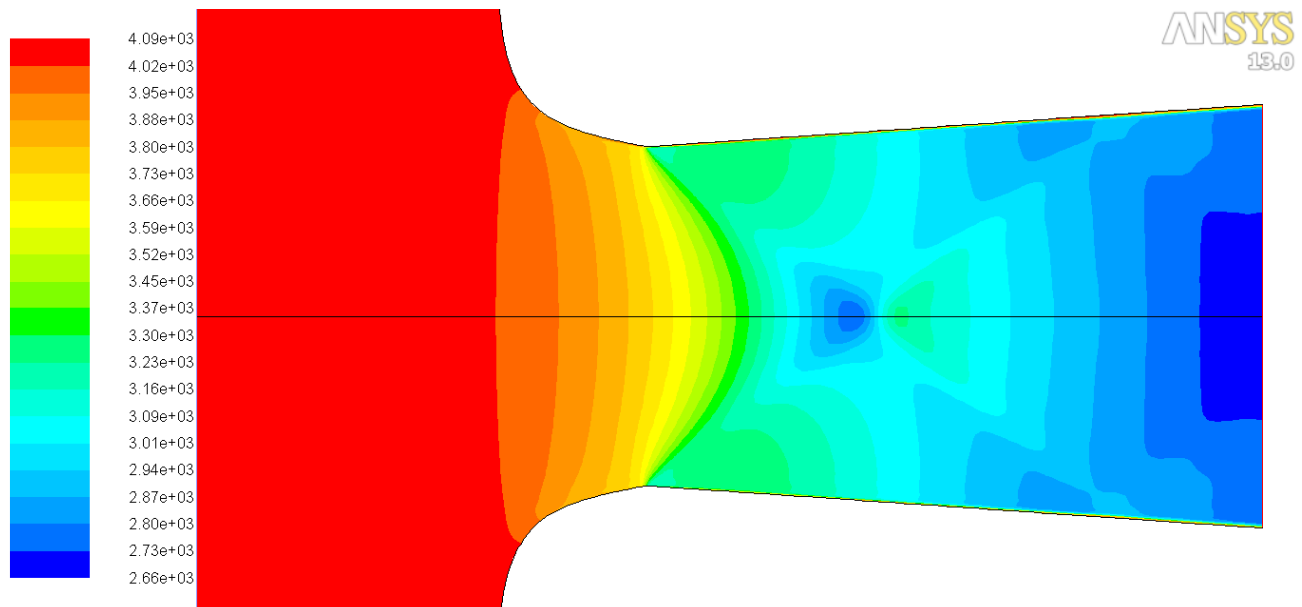ANSYS FLUENT 13.0 (axi, dp, dbns imp, spe, lam)

grid.

Fig A-3.2.16: Static Pressure Contours obtained from the CFD model of the nozzle for N2-case-1 using fine-2 grid.
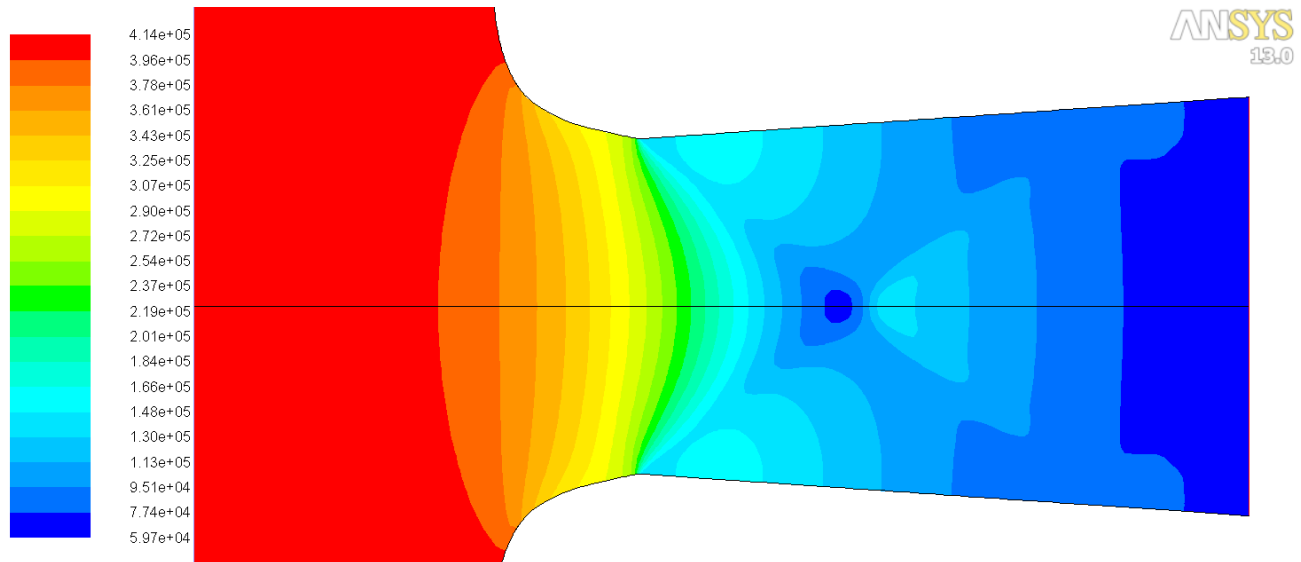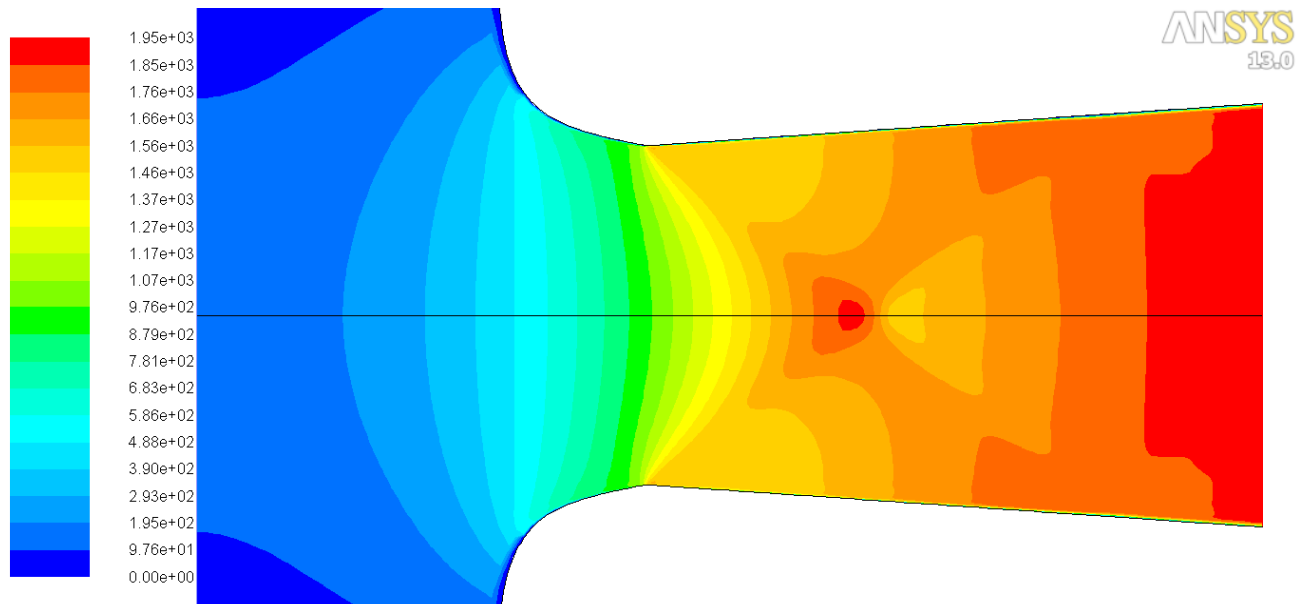

Contours of Static Pressure (pascal)
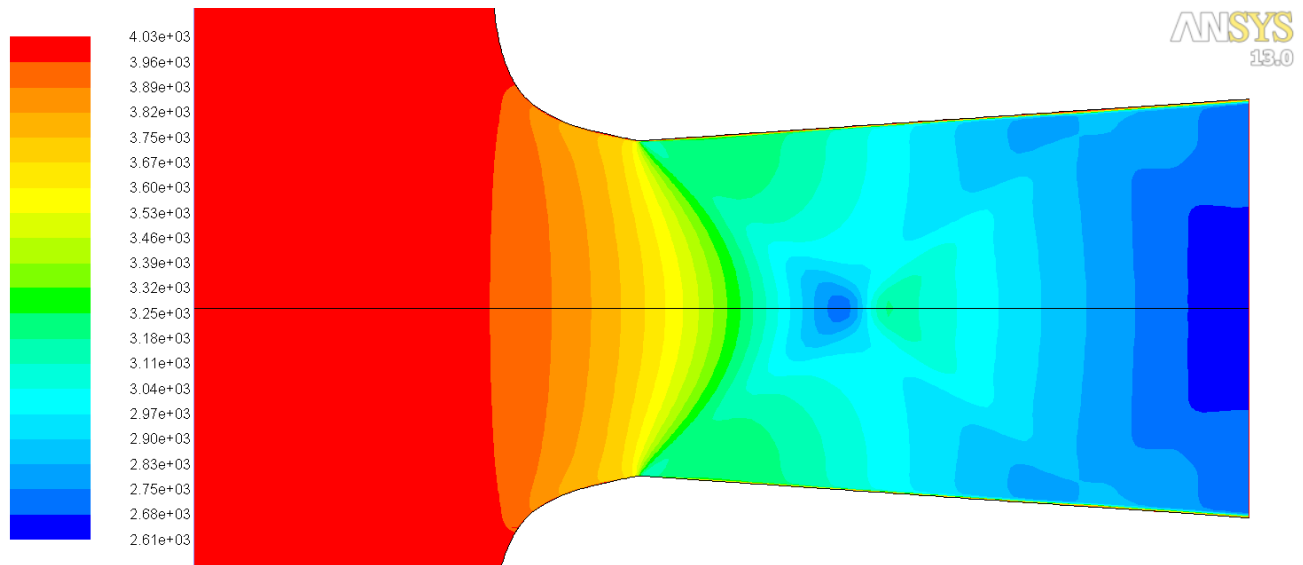
May 15, 2012
ANSYS FLUENT 13.0 (axi, dp, dbns imp, spe, lam)

Fig A-3.2.17: Static Temperature Contours obtained from the CFD model of the nozzle for N2-case-1 using fine-2 grid.

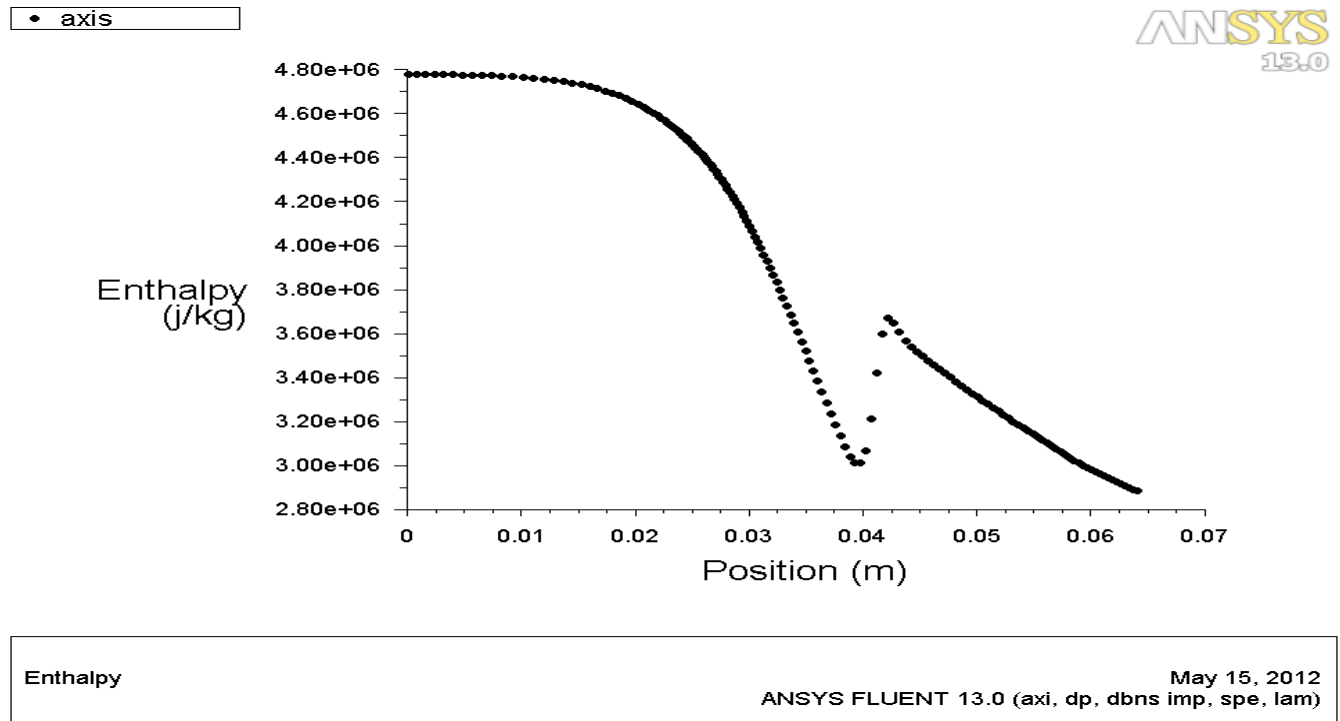**Fig A-3.2.18**: Velocity Magnitude Contours obtained from the CFD model of the nozzle for N2-case-1 using fine-2 grid.
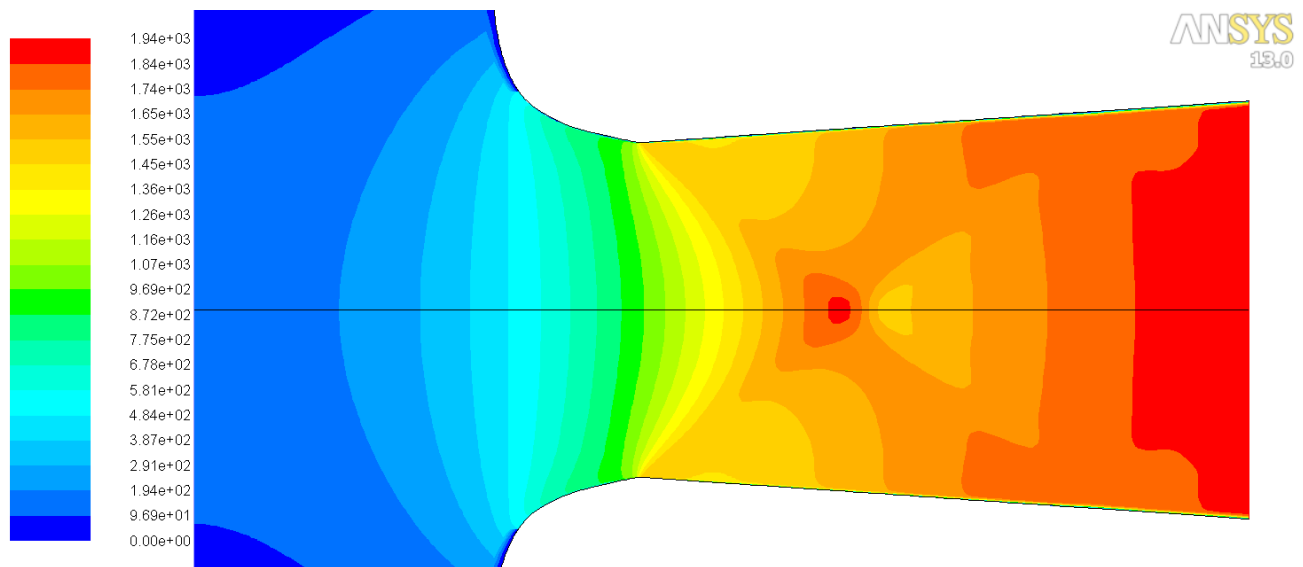
Fig A-3.2.19: Enthalpy along the axis of symmetry obtained from the CFD model of the nozzle for N2-case-1 using fine-2 grid.

Fig A-3.2.20: Density along the axis of symmetry obtained from the CFD model of the nozzle for N2-case-1 using fine-2 grid.

Specific Heat Ratio (gamma)   May 15, 2012
                                    ANSYS FLUENT 13.0 (axi, dp, dbns imp, spe, lam)

Fig A-3.2.21: Specific Heat Ratio along the axis of symmetry obtained from the CFD model of the nozzle for N2-case-1 using fine-2 grid.

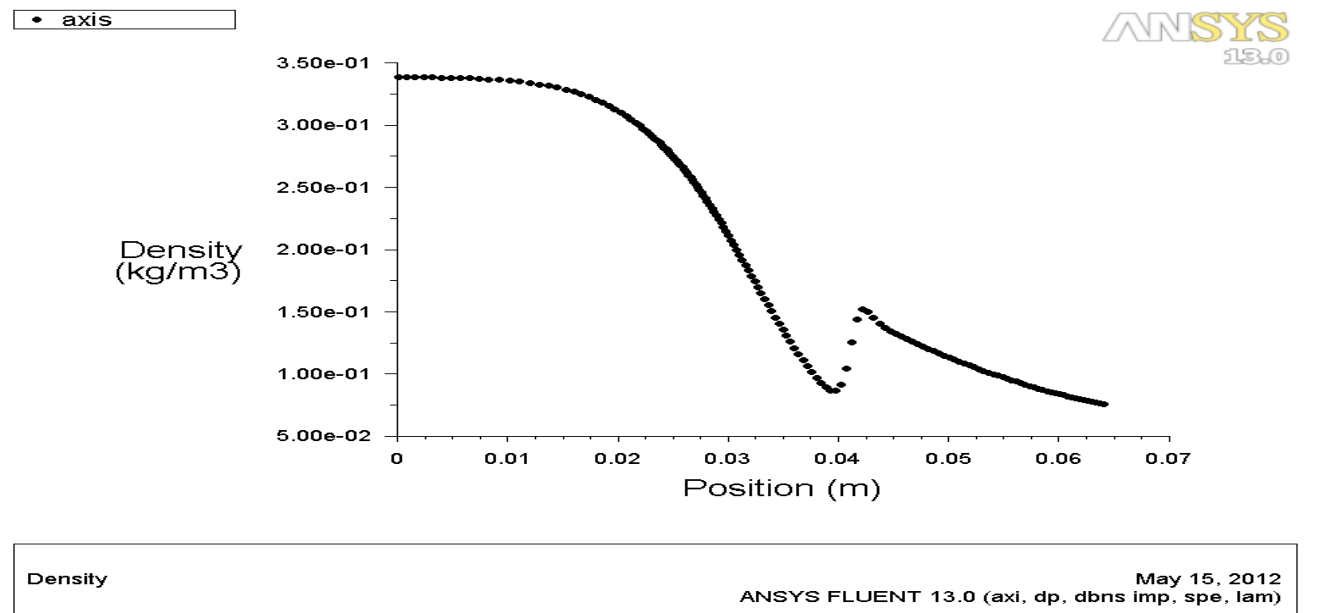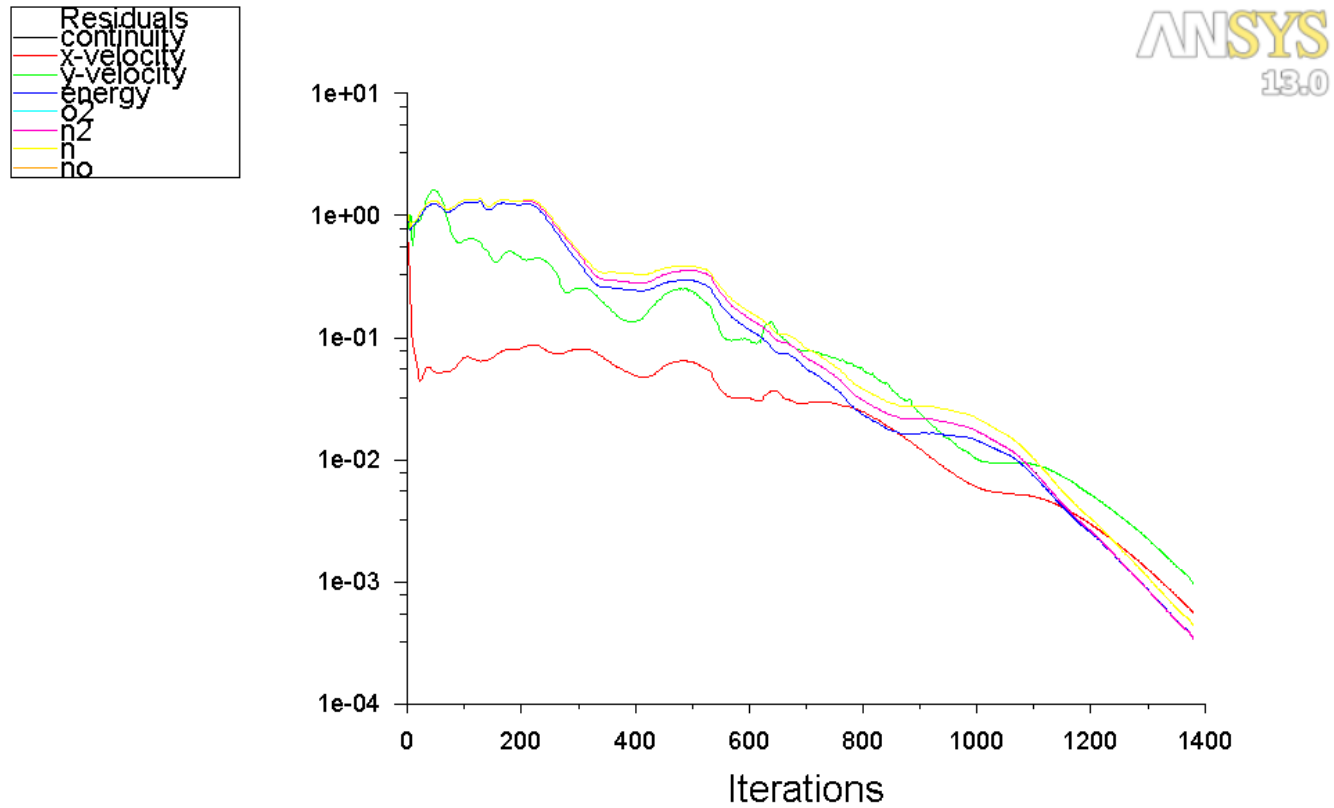**Fig A-3.2.22**: Scaled residuals obtained from the CFD model of the nozzle for N2-case-1 using fine-2 grid.

Scaled Residuals   May 15, 2012
   ANSYS FLUENT 13.0 (axi, dp, dbns imp, spe, lam)

3.3 a) N2-case-2 Coarse grid

Fig A-3.3.1: Mach Contours obtained from the CFD model of the nozzle for N2-case-2 using coarse

grid.

Fig A-3.3.2: Static Pressure Contours obtained from the CFD model of the nozzle for N2-case-2 using coarse grid.
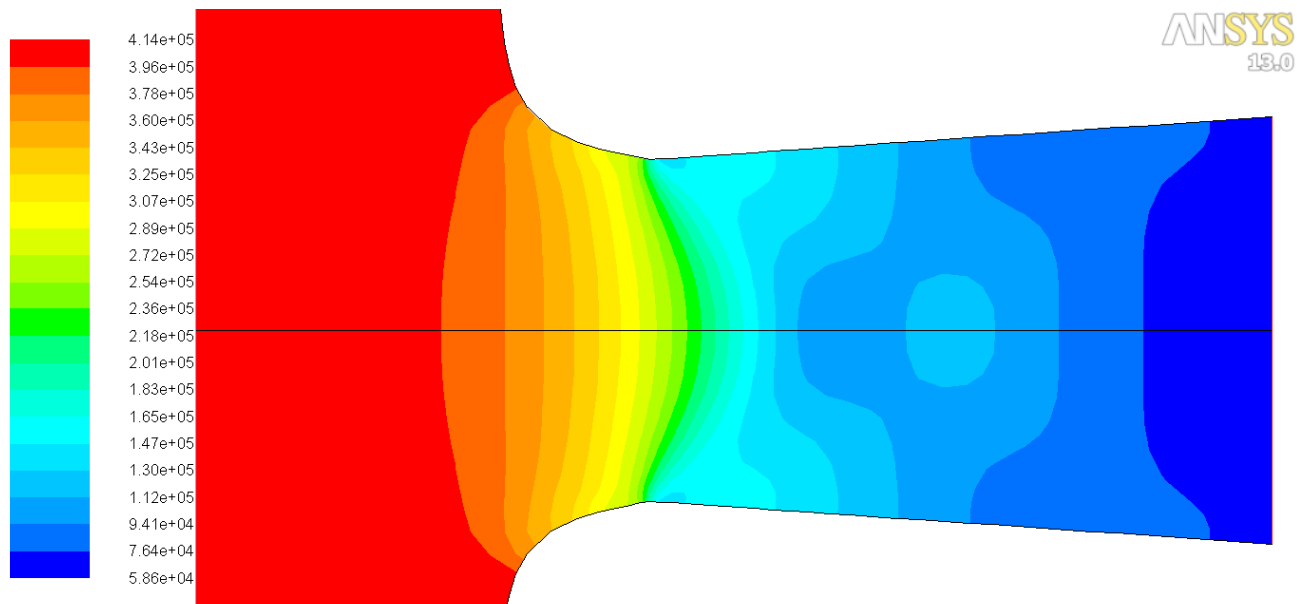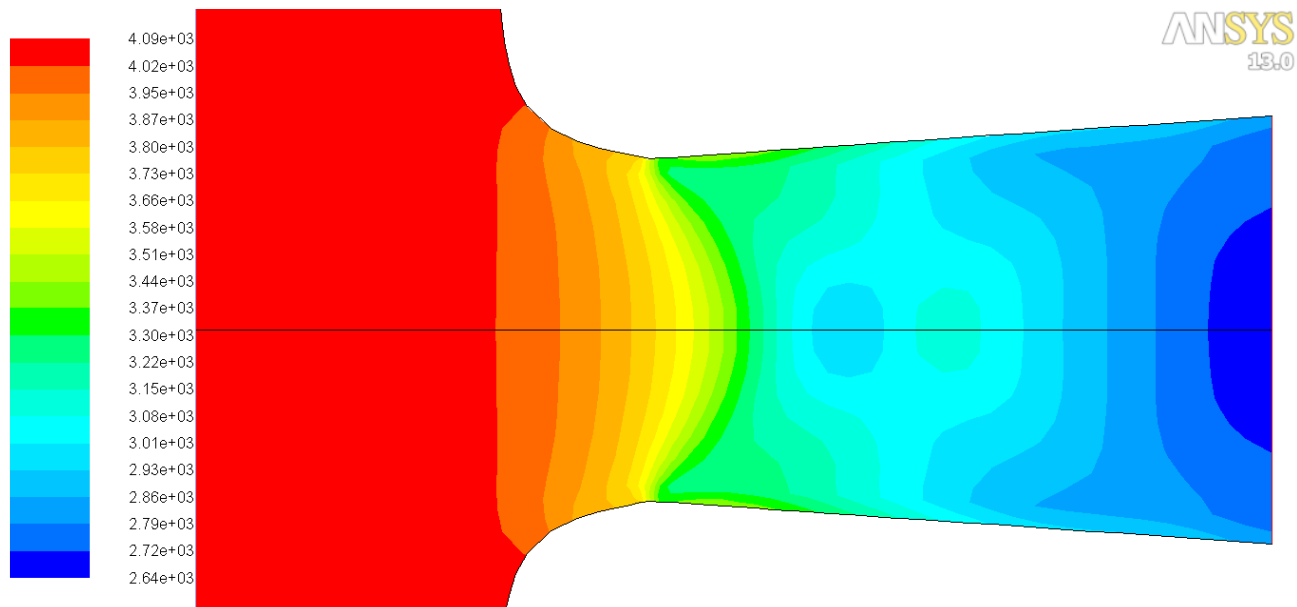
Contours of Static Temperature (k)

May 15, 2012
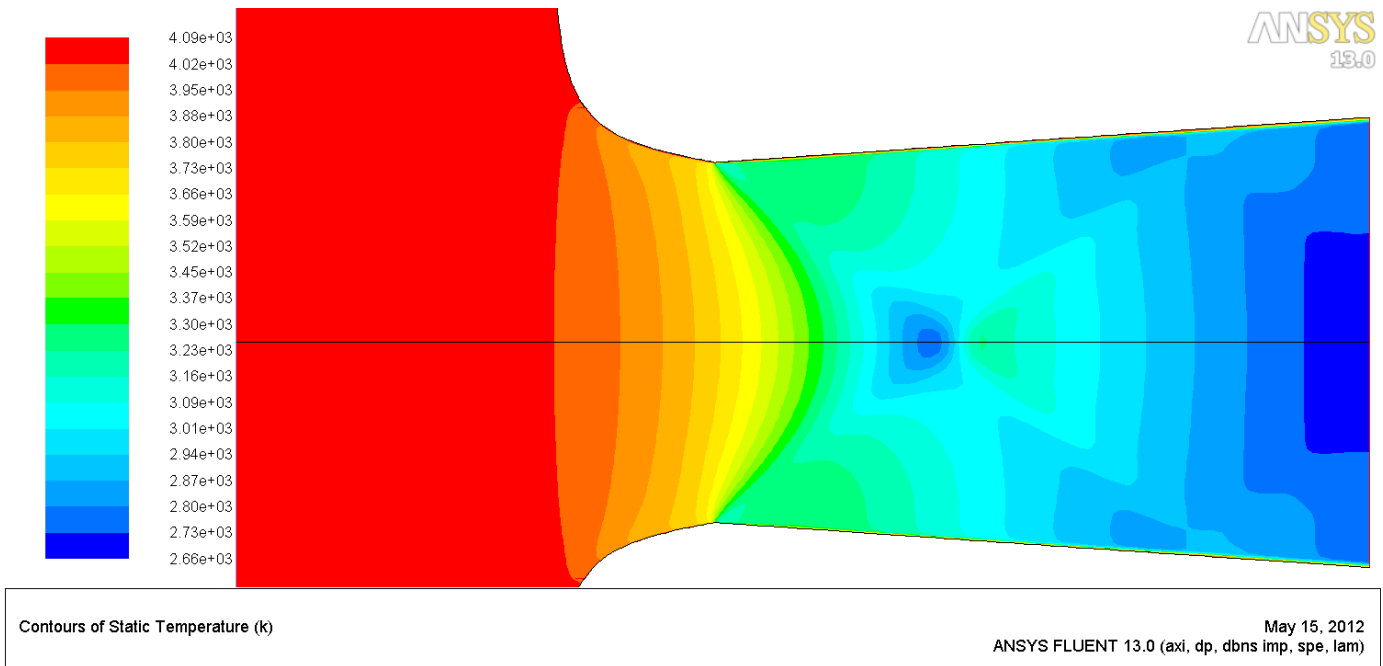ANSYS FLUENT 13.0 (axi, dp, dbns imp, spe, lam)

Fig A-3.3.3: Static Temperature Contours obtained from the CFD model of the nozzle for N2-case-2 using coarse grid.

Fig A-3.3.4: Velocity Magnitude Contours obtained from the CFD model of the nozzle for N2-case-2 using coarse grid.
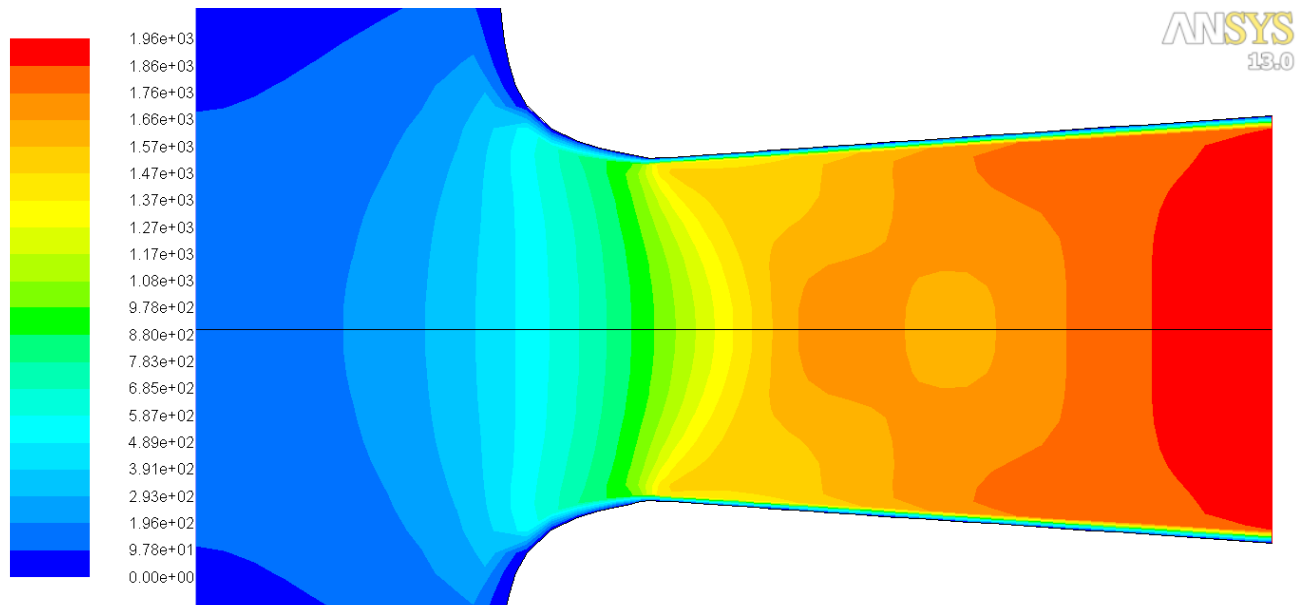
Contours of Velocity Magnitude (m/s)

May 15, 2012
ANSYS FLUENT 13.0 (axi, dp, dbns imp, spe, lam)

Fig A-3.3.5: Enthalpy along the axis of symmetry obtained from the CFD model of the nozzle for N2-case-2 using coarse grid.
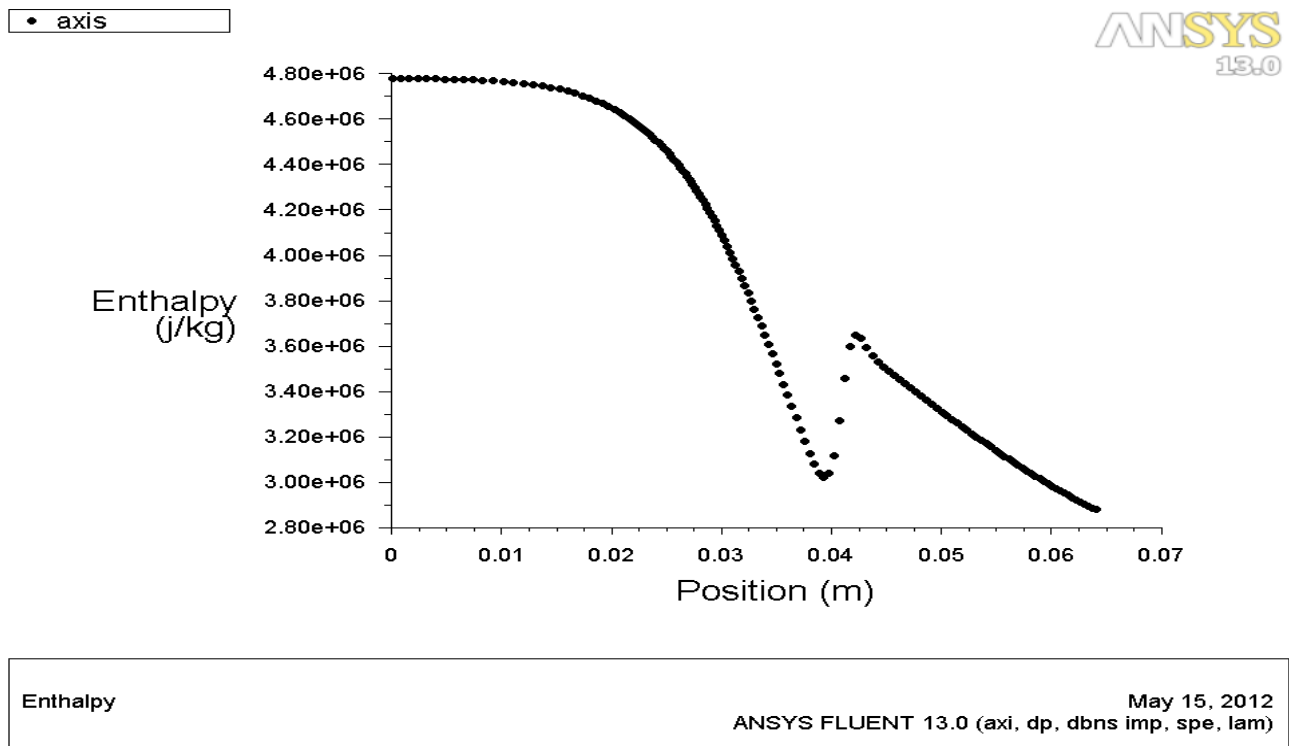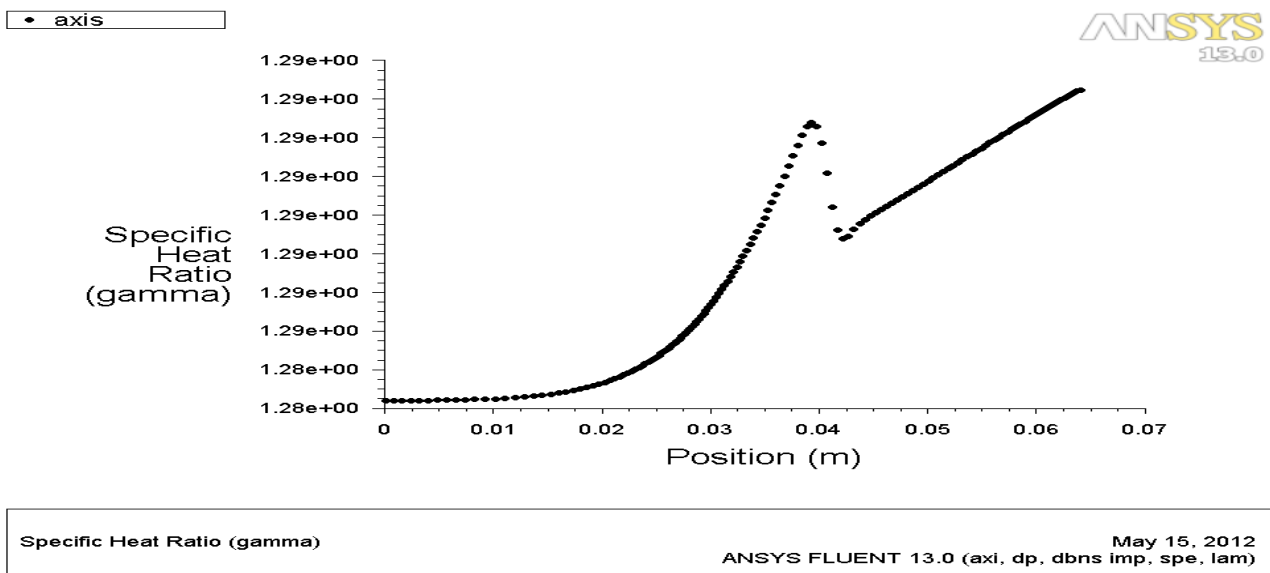
Fig A-3.3.6: Enthalpy along the axis of symmetry obtained from the CFD model of the nozzle for N2-case-2 using coarse grid.

Fig A-3.3.7: Scaled Residuals obtained from the CFD model of the nozzle for N2-case-2 using coarse grid.

3.3 b) N2-case-2 Fine-1 grid

Fig A-3.3.8: Mach Contours obtained from the CFD model of the nozzle for N2-case-2 using fine-1

grid.

Fig A-3.3.9: Static Pressure Contours obtained from the CFD model of the nozzle for N2-case-2 using fine-1 grid.

Contours of Static Temperature (k)

May 15, 2012
ANSYS FLUENT 13.0 (axi, dp, dbns imp, spe, lam)

Fig A-3.3.10: Static Temperature Contours obtained from the CFD model of the nozzle for N2-case-2 using fine-1 grid.

Fig A-3.3.11: Velocity Magnitude Contours obtained from the CFD model of the nozzle for N2-case-2 using fine-1 grid.

Contours of Velocity Magnitude (m/s)

May 15, 2012
ANSYS FLUENT 13.0 (axi, dp, dbns imp, spe, lam)

Fig A-3.3.12: Enthalpy along the axis of symmetry obtained from the CFD model of the nozzle for N2-case-2 using fine-1 grid.
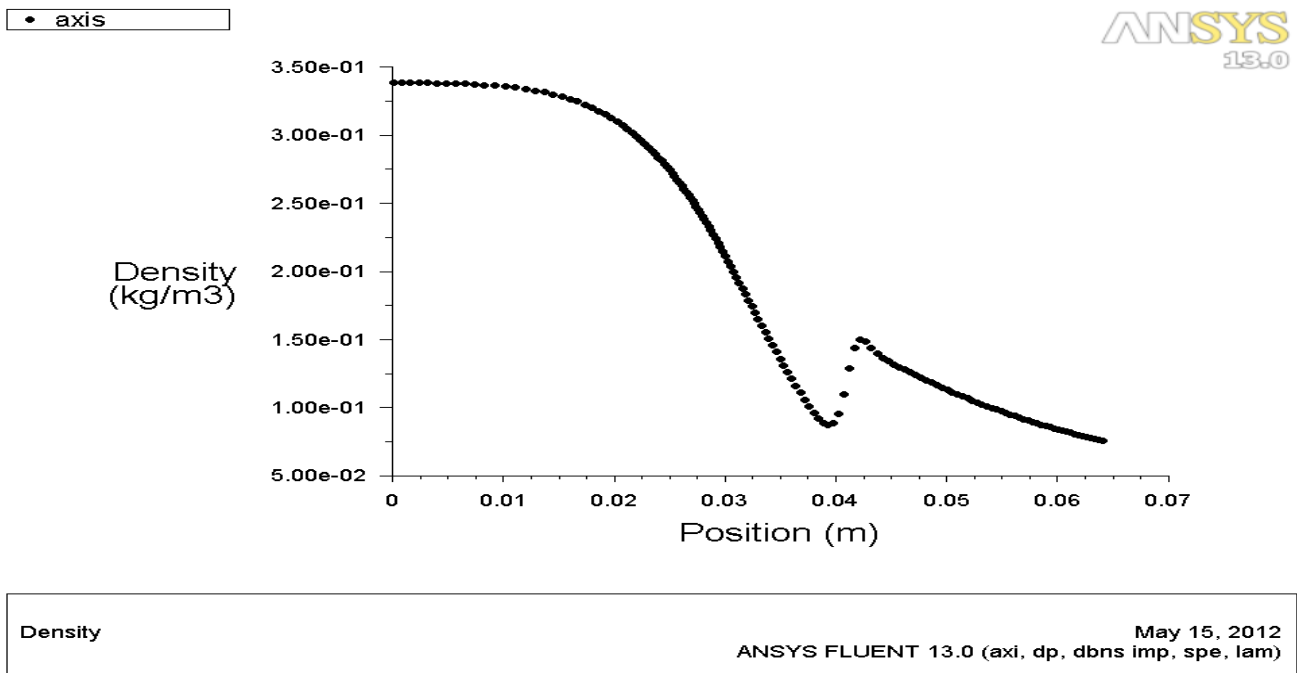
Fig A-3.3.13: Enthalpy along the axis of symmetry obtained from the CFD model of the nozzle for N2-case-2 using fine-1 grid.

Fig A-3.3.14: Scaled Residuals obtained from the CFD model of the nozzle for N2-case-2 using fine-1
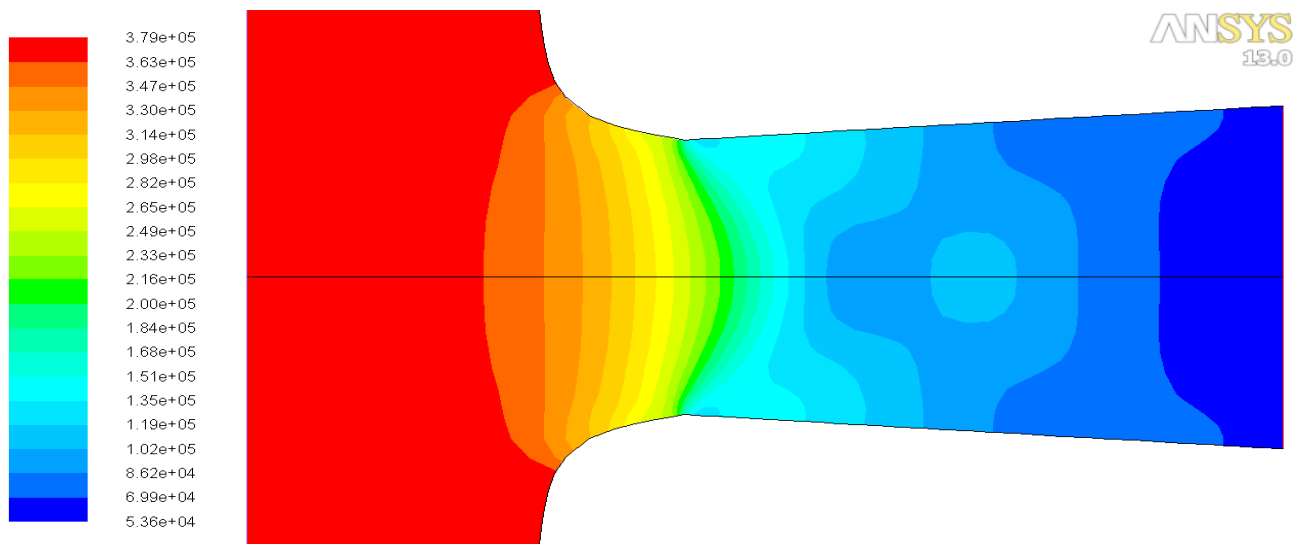

grid.

3.3 c) N2-case-2 Fine-2 grid

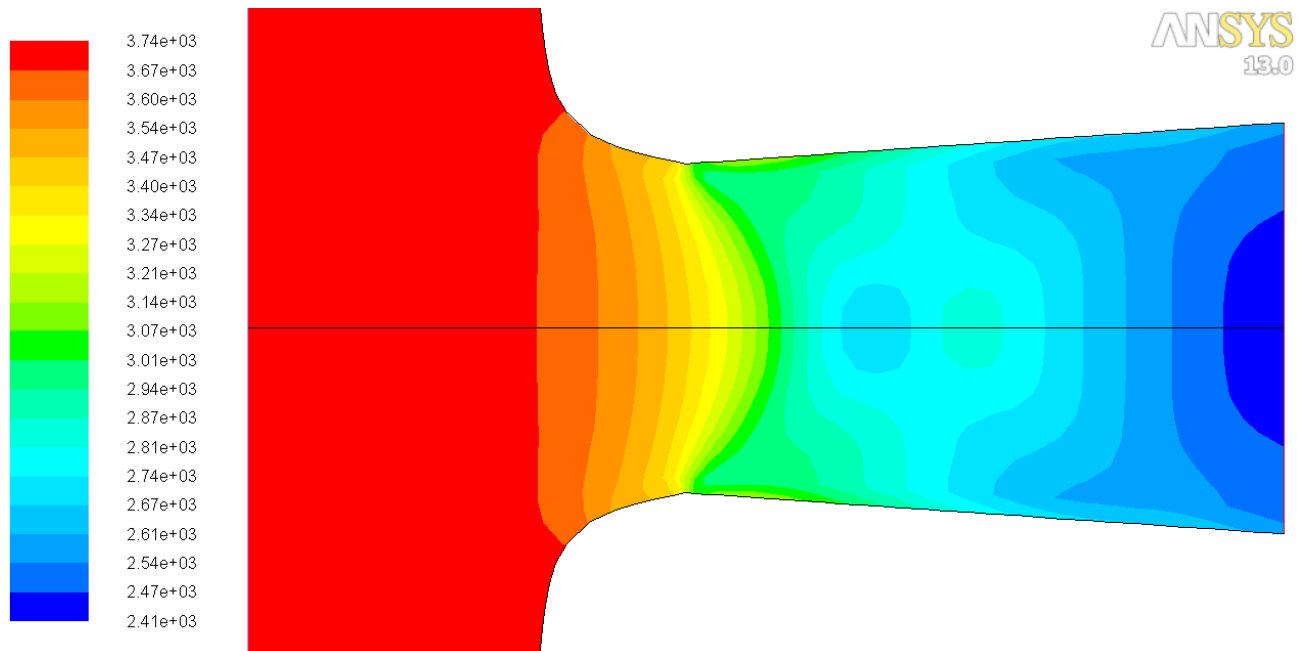**Fig A-3.3.15**: Mach Contours obtained from the CFD model of the nozzle for N2-case-2 using fine-2
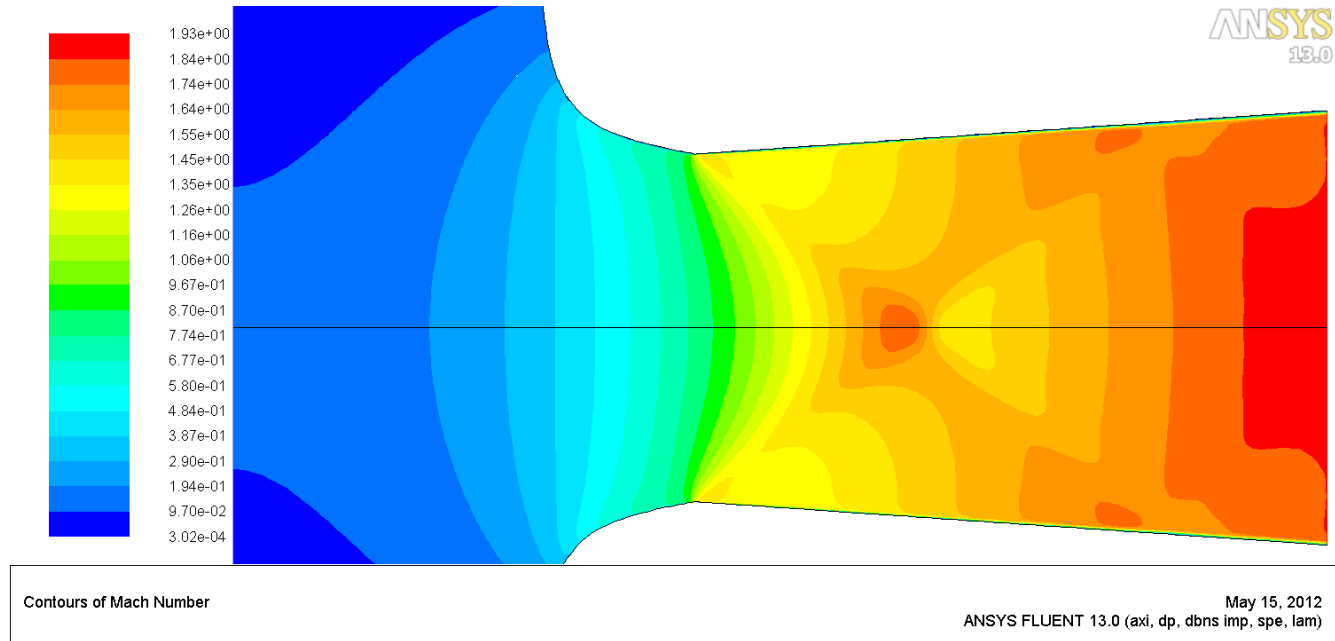
grid.

Fig A-3.3.16: Static Pressure Contours obtained from the CFD model of the nozzle for N2-case-2 using fine-2 grid.
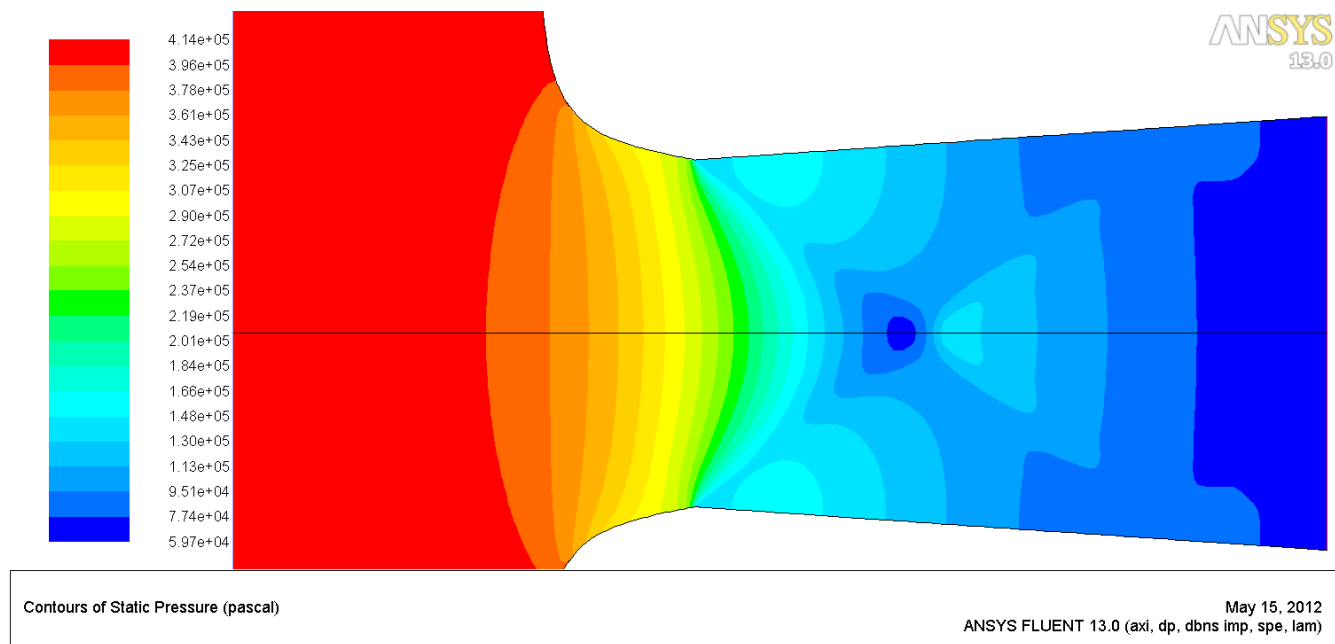
Fig A-3.3.17: Static Temperature Contours obtained from the CFD model of the nozzle for N2-case-2 using fine-2 grid.

Fig A-3.3.18: Velocity Magnitude Contours obtained from the CFD model of the nozzle for N2-case-2 using fine-2 grid.
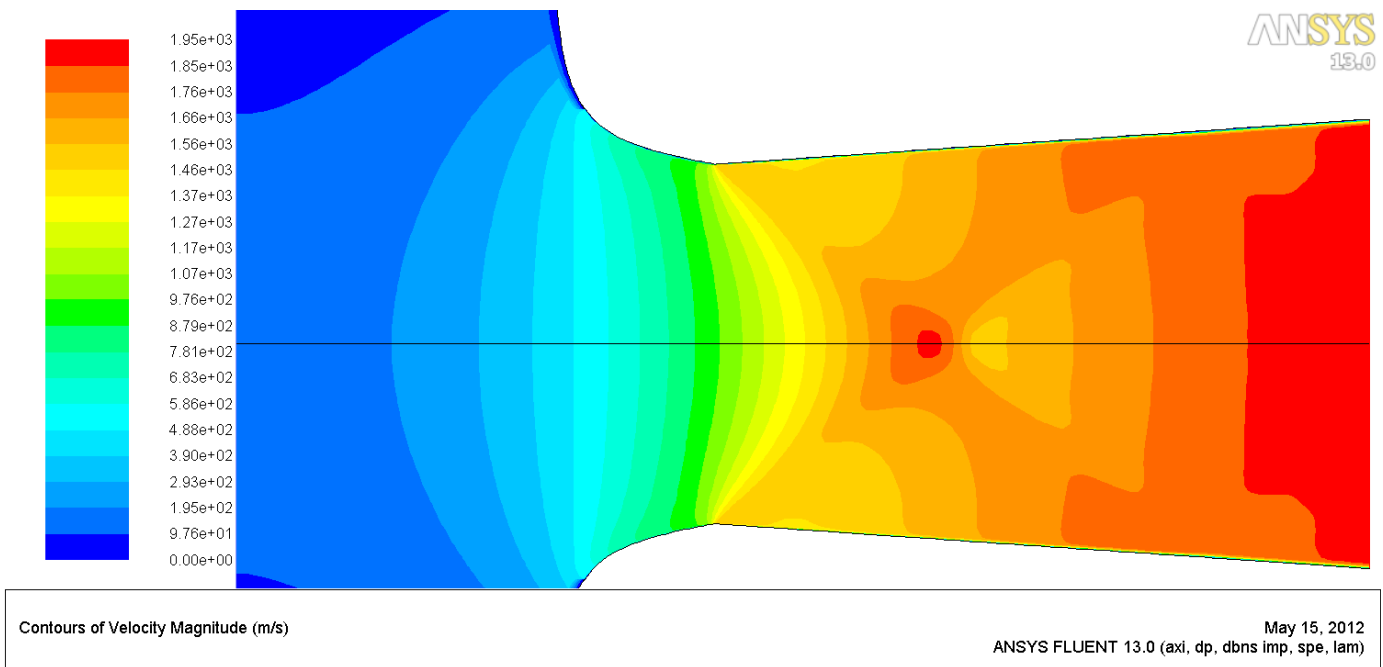
Fig A-3.3.19: Enthalpy along the axis of symmetry obtained from the CFD model of the nozzle for N2-case-2 using fine-2 grid.

Fig A-3.3.20: Specific heat ratio along the axis of symmetry obtained from the CFD model of the nozzle for N2-case-2 using fine-2 grid.

Fig A-3.3.21: Density along the axis of symmetry obtained from the CFD model of the nozzle for N2-case-2 using fine-2 grid.

Fig A-3.3.22: Scaled Residuals obtained from the CFD model of the nozzle for N2-case-2 using fine-2 grid.
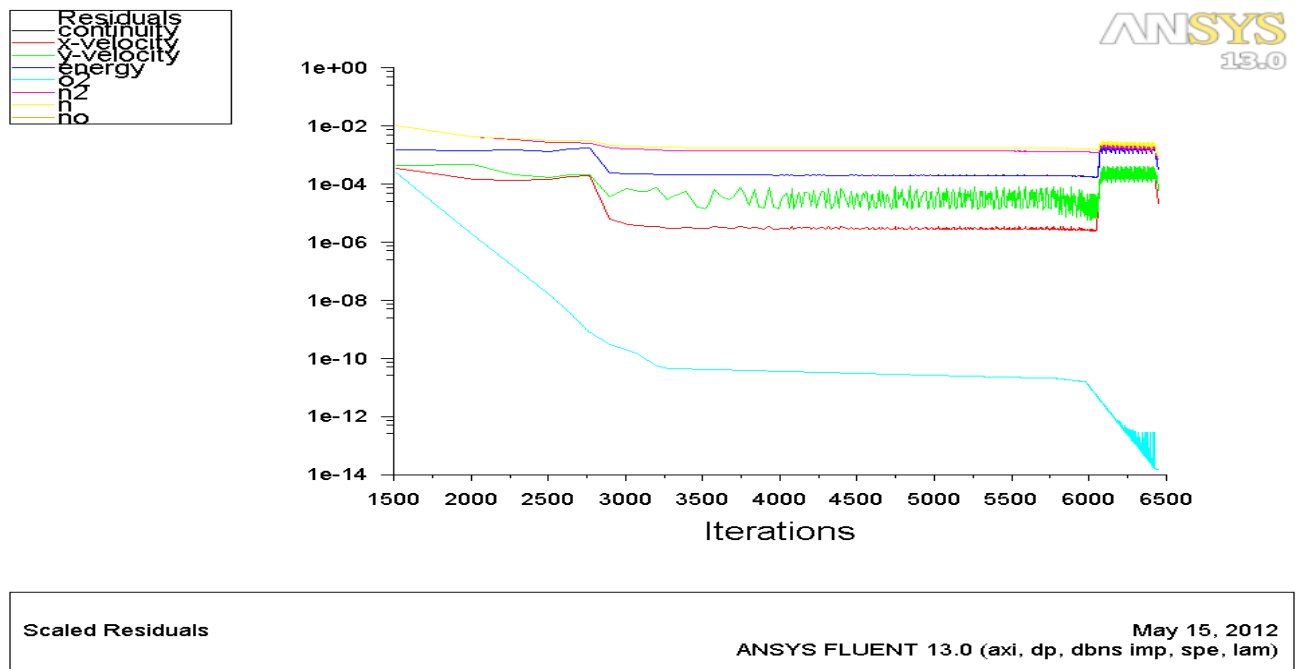
3.4 a) N2-case-3 Coarse grid

Fig A-3.4.1: Mach Contours obtained from the CFD model of the nozzle for N2-case-3 using coarse
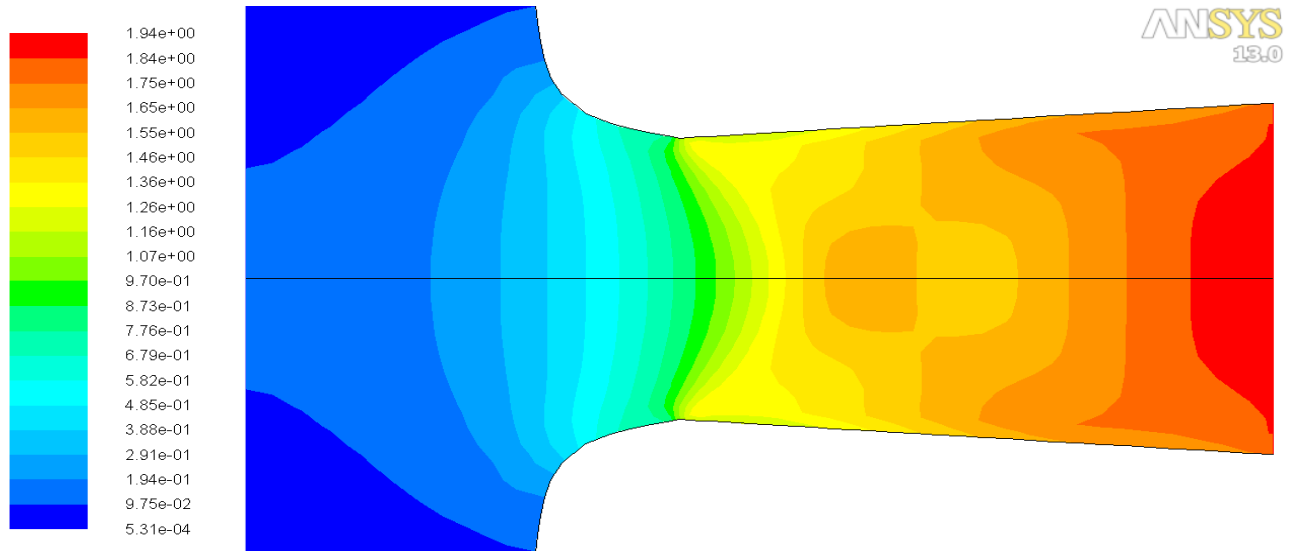
grid.

Fig A-3.4.2: Static Pressure Contours obtained from the CFD model of the nozzle for N2-case-3 using coarse grid.

Contours of Static Temperature (k)

May 15, 2012
ANSYS FLUENT 13.0 (axi, dp, dbns imp, spe, lam)

Fig A-3.4.3: Static Temperature Contours obtained from the CFD model of the nozzle for N2-case-3 using coarse grid.

Fig A-3.4.4: Velocity Magnitude Contours obtained from the CFD model of the nozzle for N2-case-3 using coarse grid.
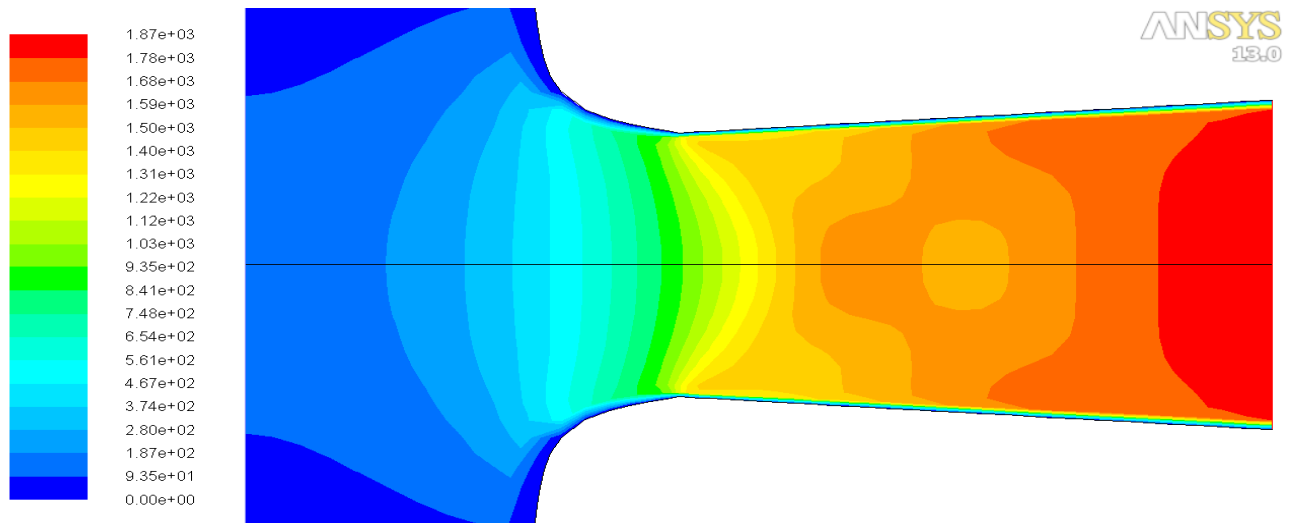
Contours of Velocity Magnitude (m/s)

May 15, 2012
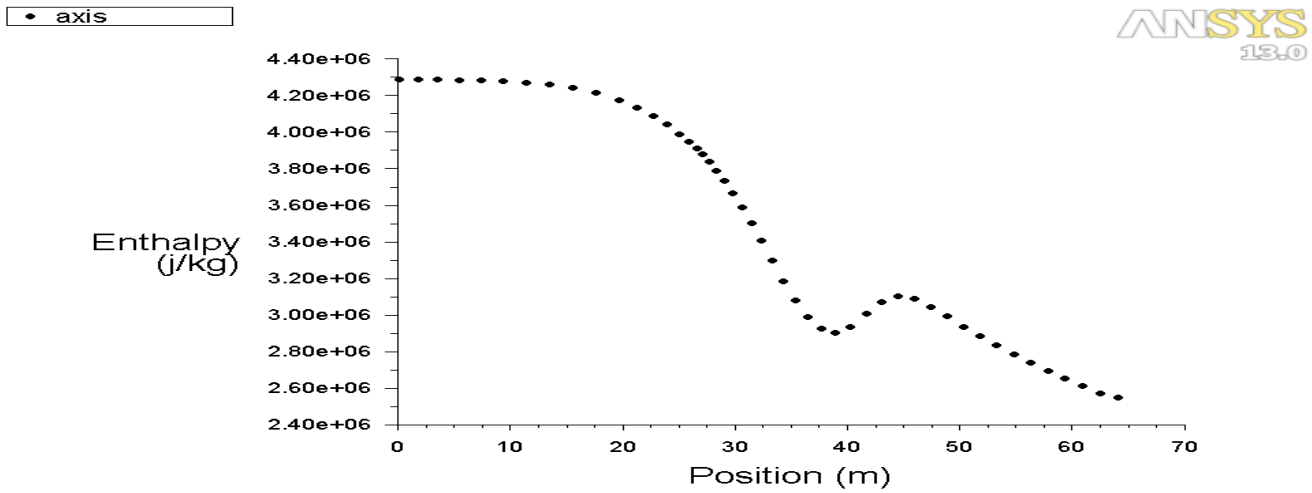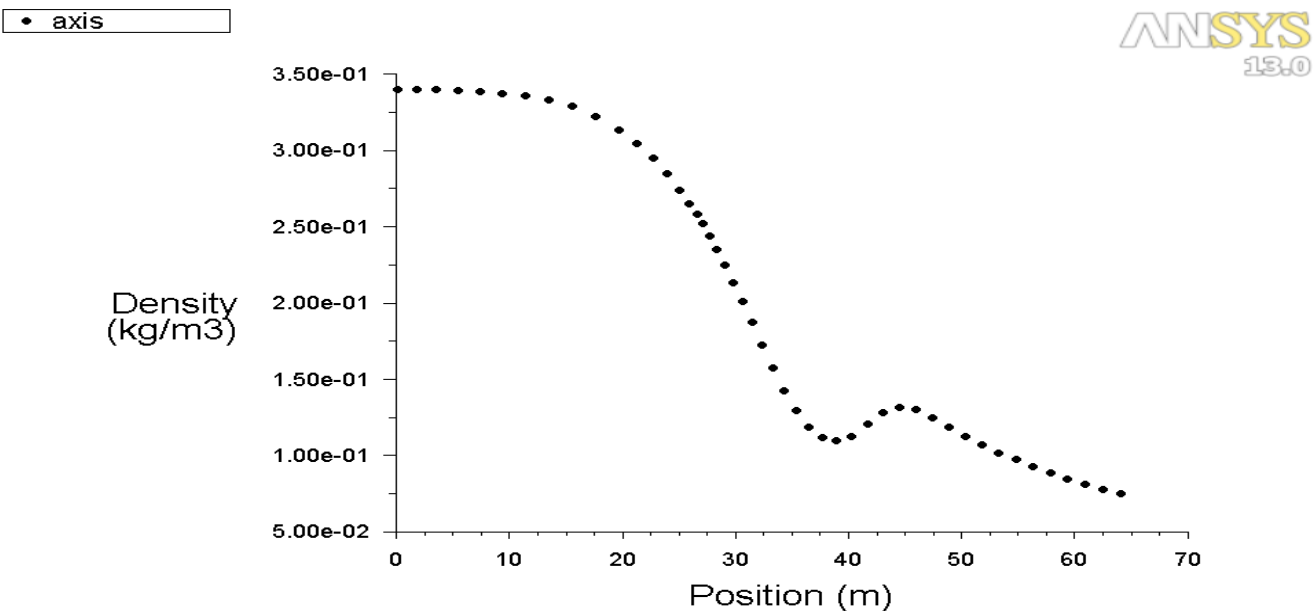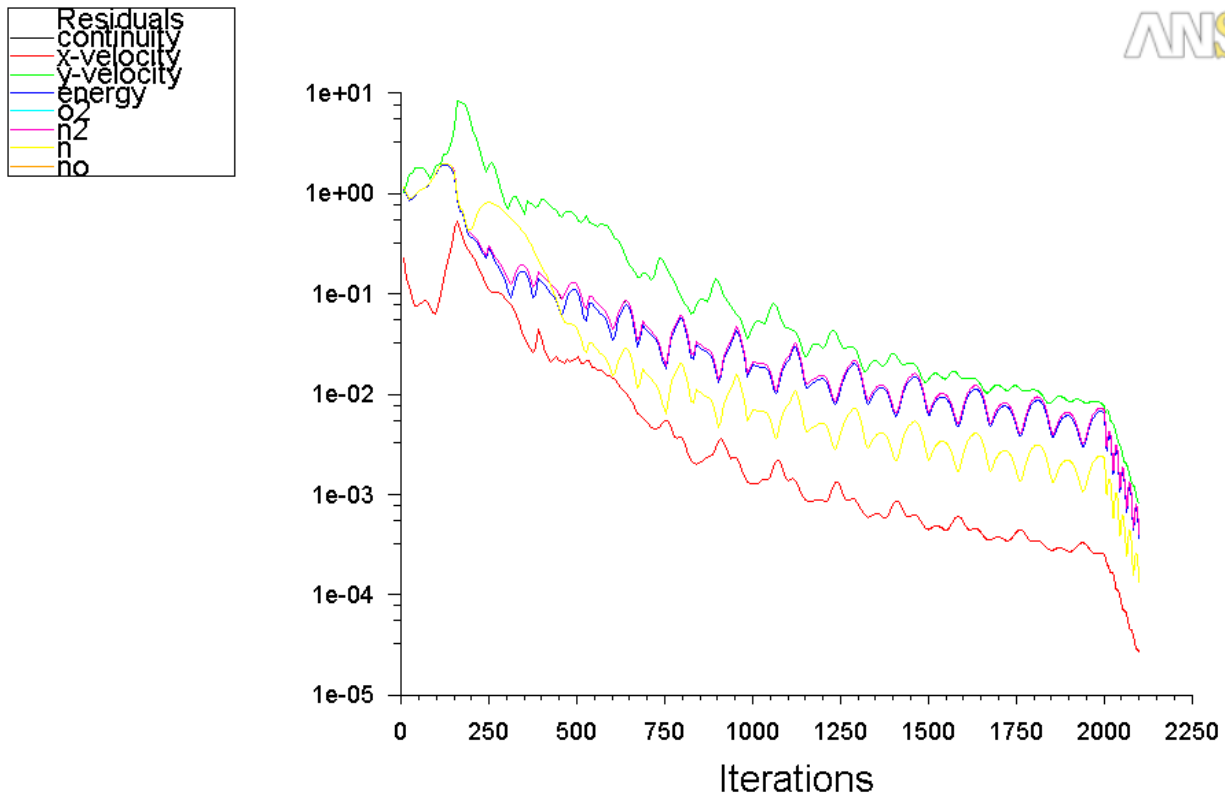ANSYS FLUENT 13.0 (axi, dp, dbns imp, spe, lam)

Fig A-3.4.5: Enthalpy along the axis of symmetry obtained from the CFD model of the nozzle for N2-case-3 using coarse grid.

Fig A-3.4.6: Density along the axis of symmetry obtained from the CFD model of the nozzle for N2-case-3 using coarse grid.
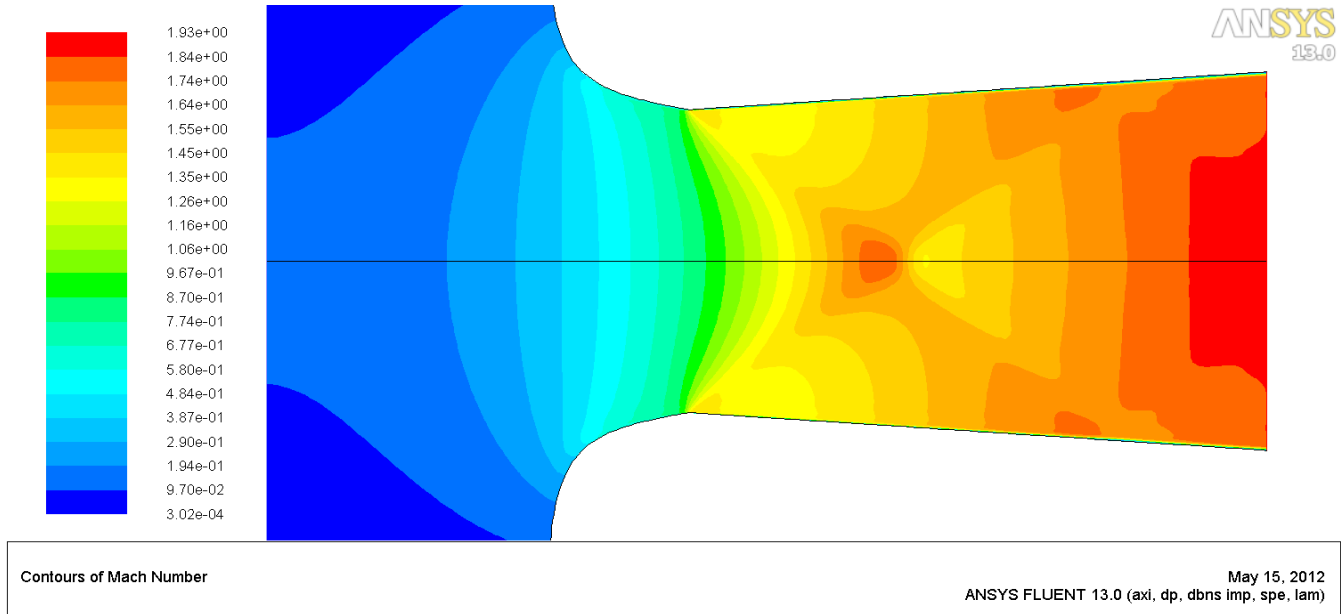
Fig A-3.4.7: Scaled Residuals along the axis of symmetry obtained from the CFD model of the nozzle for N2-case-3 using coarse grid.
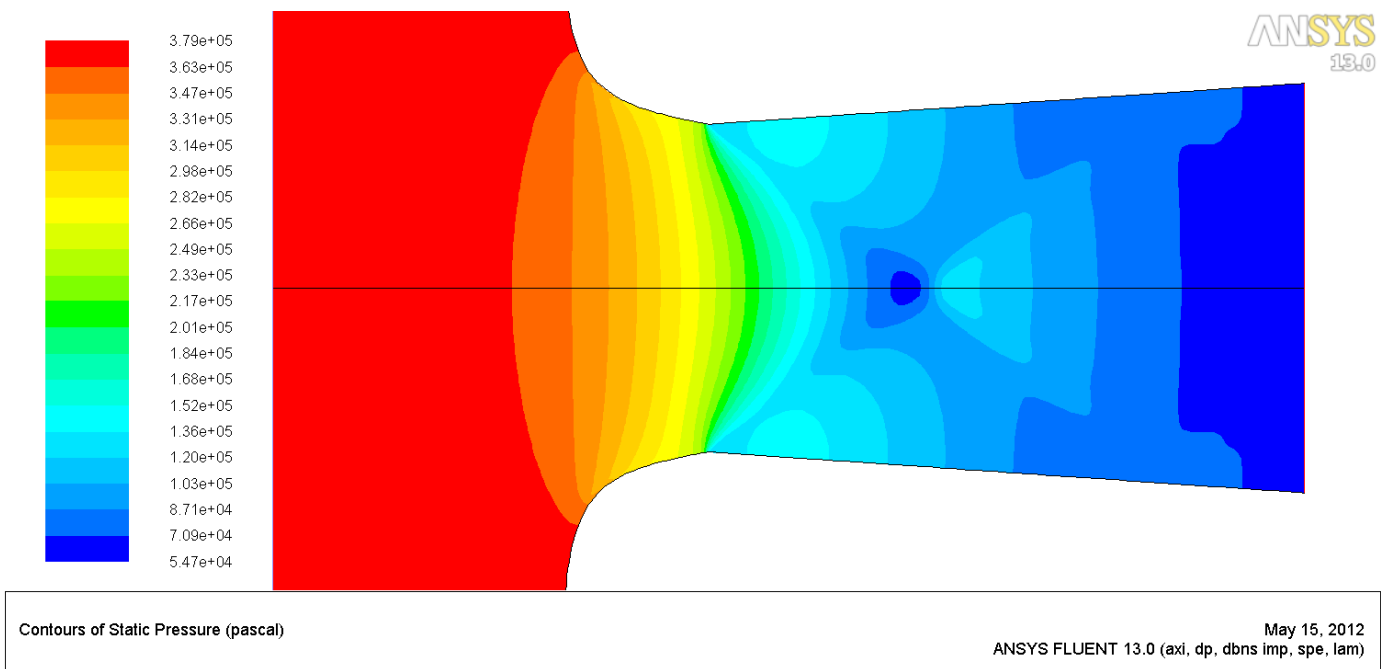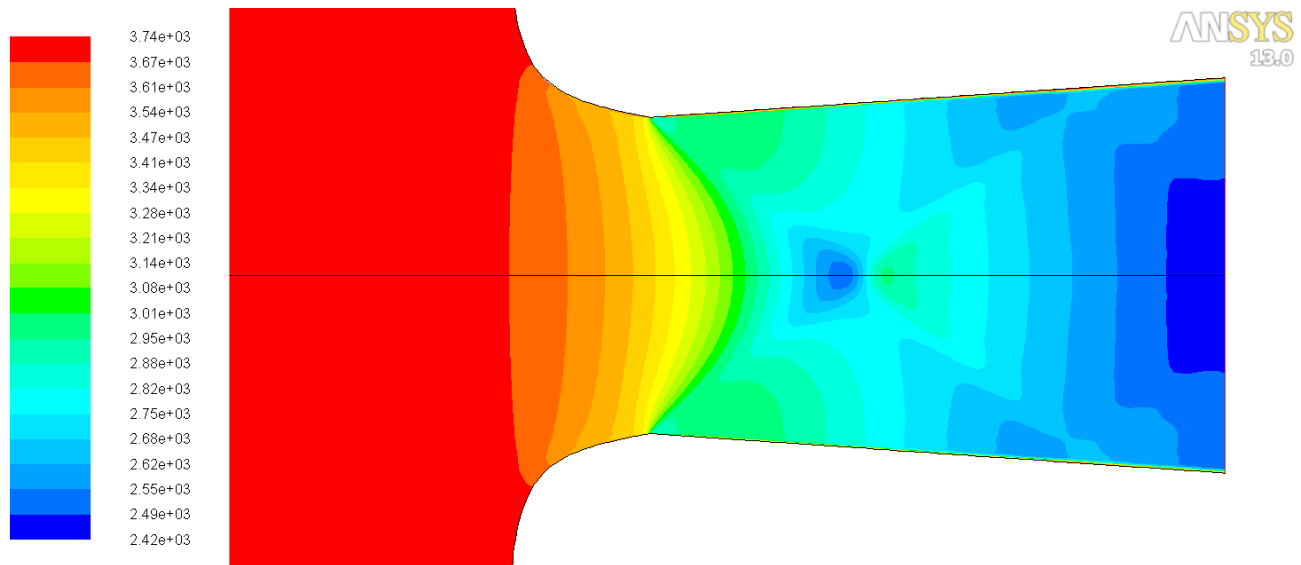
3.4 b) N2-case-3 Fine-1 grid

Fig A-3.4.8: Mach contours obtained from the CFD model of the nozzle for N2-case-3 using fine-1

grid.

Fig A-3.4.9: Static Pressure contours obtained from the CFD model of the nozzle for N2-case-3 using fine-1 grid.
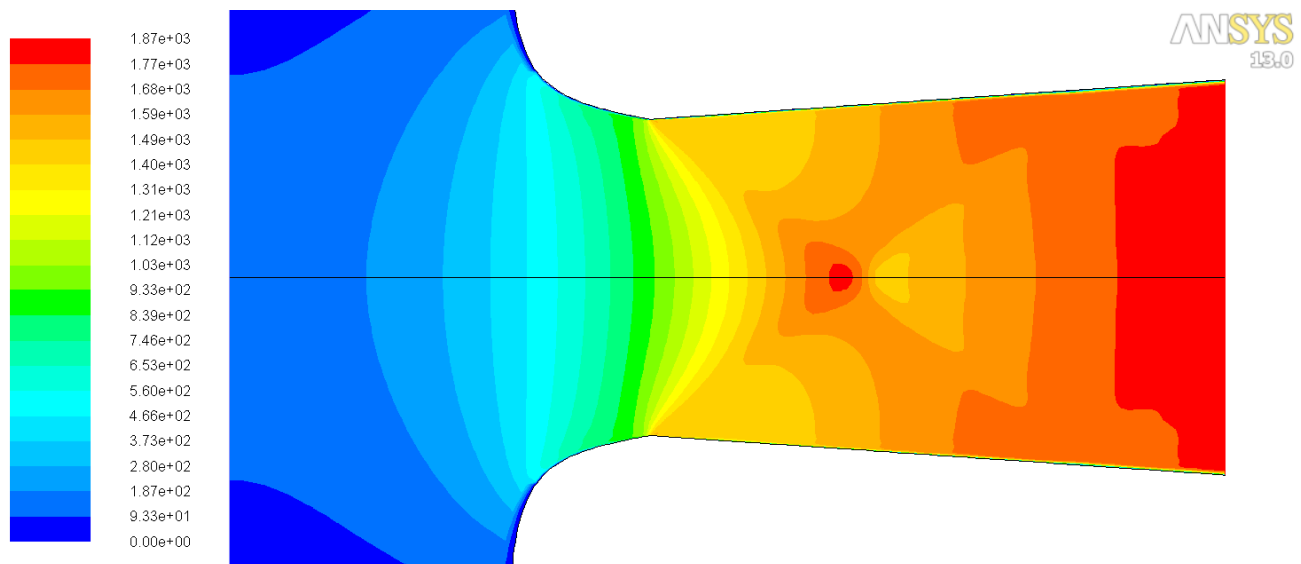
Contours of Static Temperature (k)   May 15, 2012
                                                                                            ANSYS FLUENT 13.0 (axi, dp, dbns imp, spe, lam)

Fig A-3.4.10: Static Temperature contours obtained from the CFD model of the nozzle for N2-case-3 using fine-1 grid.

Fig A-3.4.11: Velocity Magnitude contours obtained from the CFD model of the nozzle for N2-case-3 using fine-1 grid.

Contours of Velocity Magnitude (m/s)   May 15, 2012
                                                                                            ANSYS FLUENT 13.0 (axi, dp, dbns imp, spe, lam)
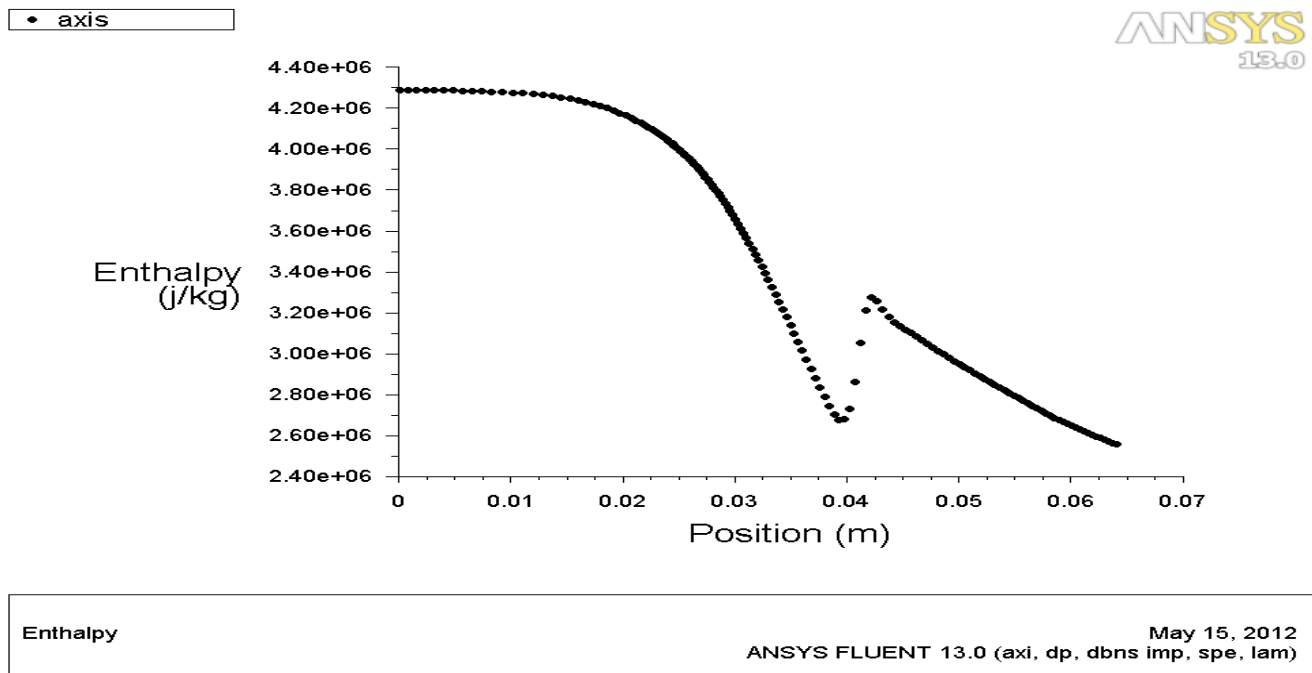
Fig A-3.4.12: Enthalpy along the axis of symmetry obtained from the CFD model of the nozzle for N2-case-3 using fine-1 grid.

Fig A-3.4.13: Density along the axis of symmetry obtained from the CFD model of the nozzle for N2-case-3 using fine-1 grid.
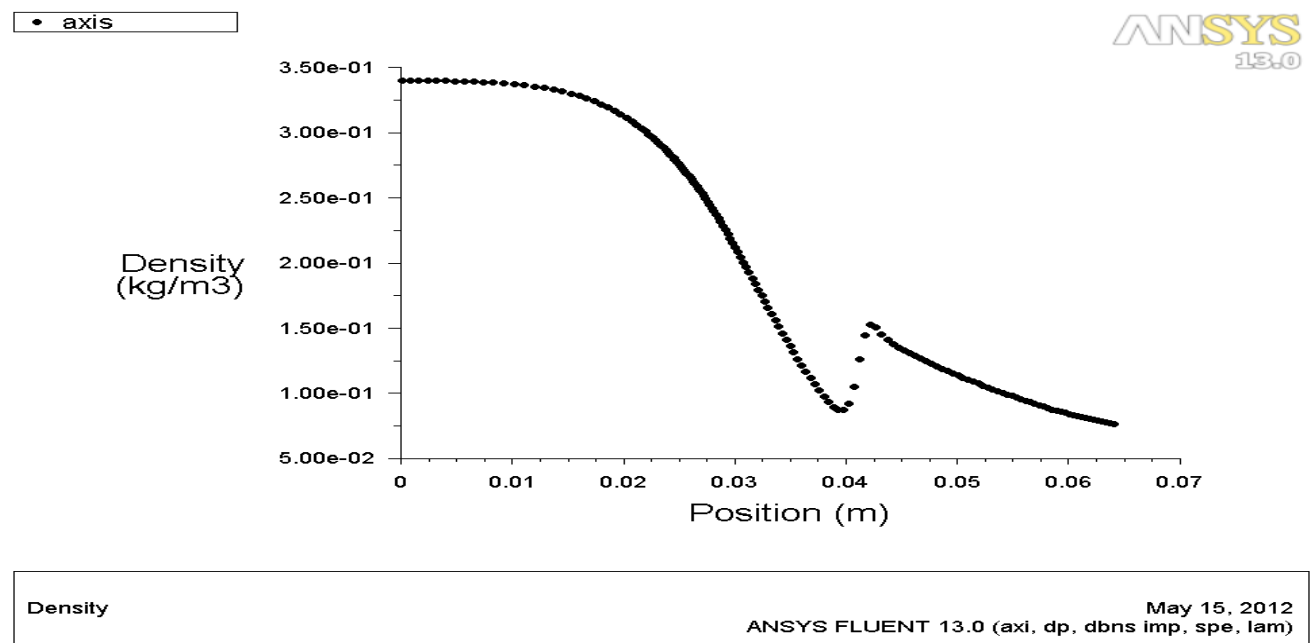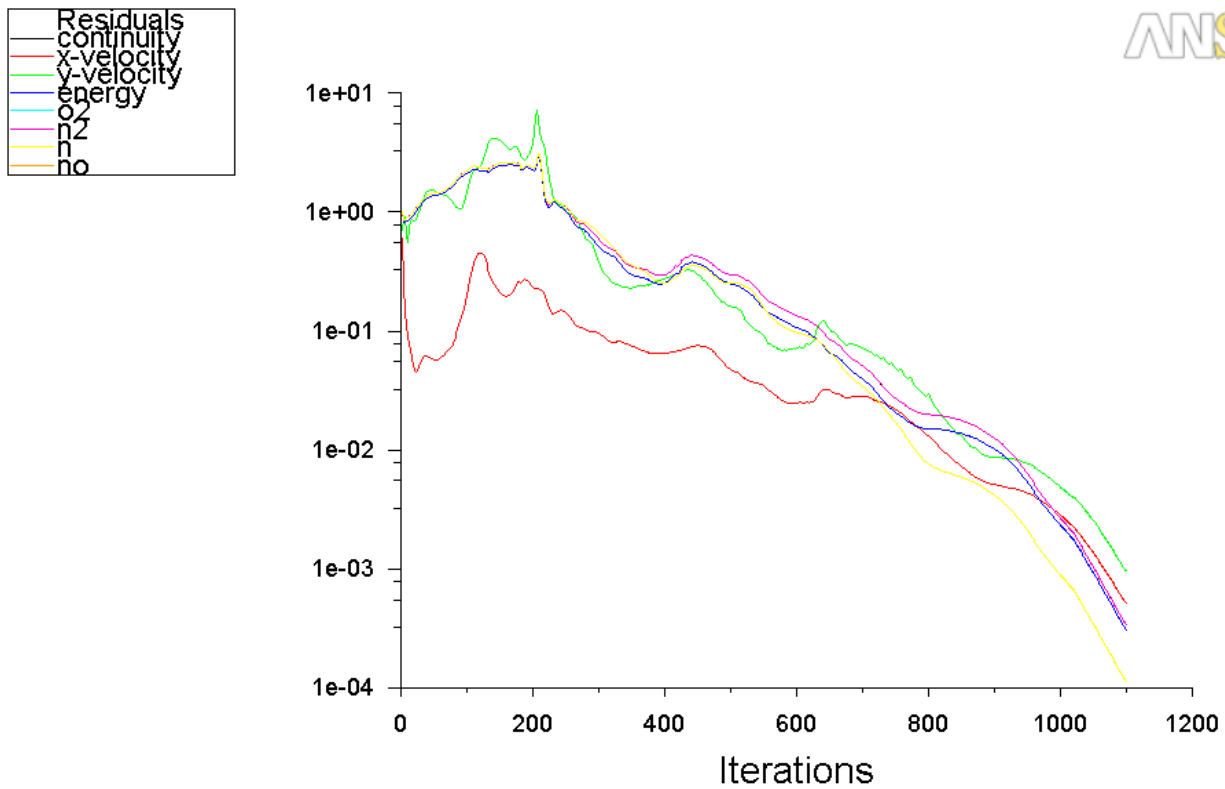
Fig A-3.4.14: Scaled Residuals obtained from the CFD model of the nozzle for N2-case-3 using fine-1

grid.

3.4 c) N3-case-3 Fine-2 grid

Fig A-3.4.15: Mach contours obtained from the CFD model of the nozzle for N2-case-3 using fine-2

grid.

Fig A-3.4.16: Static Pressure contours obtained from the CFD model of the nozzle for N2-case-3 using fine-2 grid.
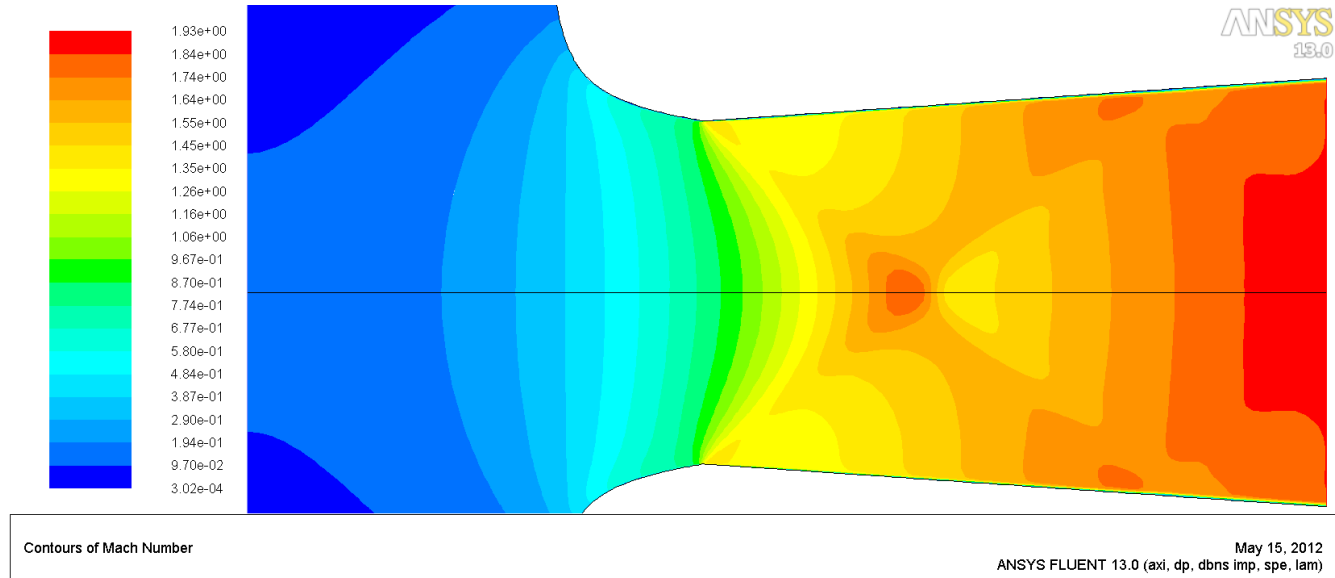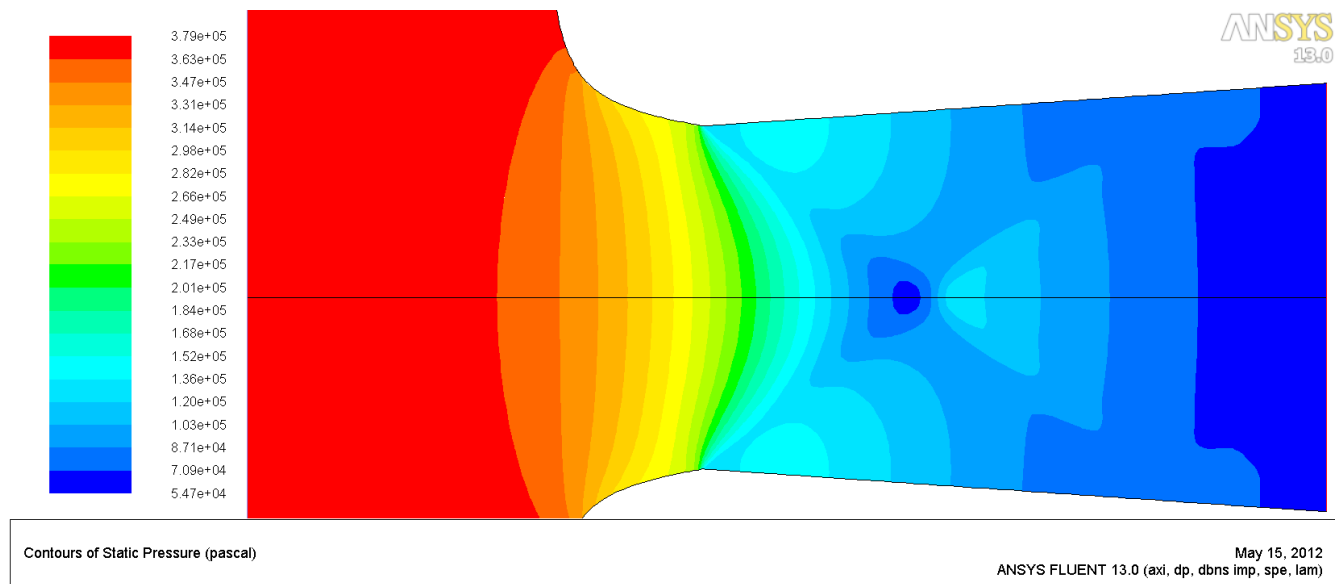
Fig A-3.4.17: Static Temperature contours obtained from the CFD model of the nozzle for N2-case-3 using fine-2 grid.

Fig A-3.4.18: Velocity Magnitude contours obtained from the CFD model of the nozzle for N2-case-3 using fine-2 grid.

Fig A-3.4.19: Enthalpy along the axis of symmetry obtained from the CFD model of the nozzle for N2-case-3 using fine-2 grid.

Fig A-3.4.20: Enthalpy along the axis of symmetry obtained from the CFD model of the nozzle for N2-case-3 using fine-2 grid.

Fig A-3.4.21: Specific heat ratio along the axis of symmetry obtained from the CFD model of the nozzle for N2-case-3 using fine-2 grid.

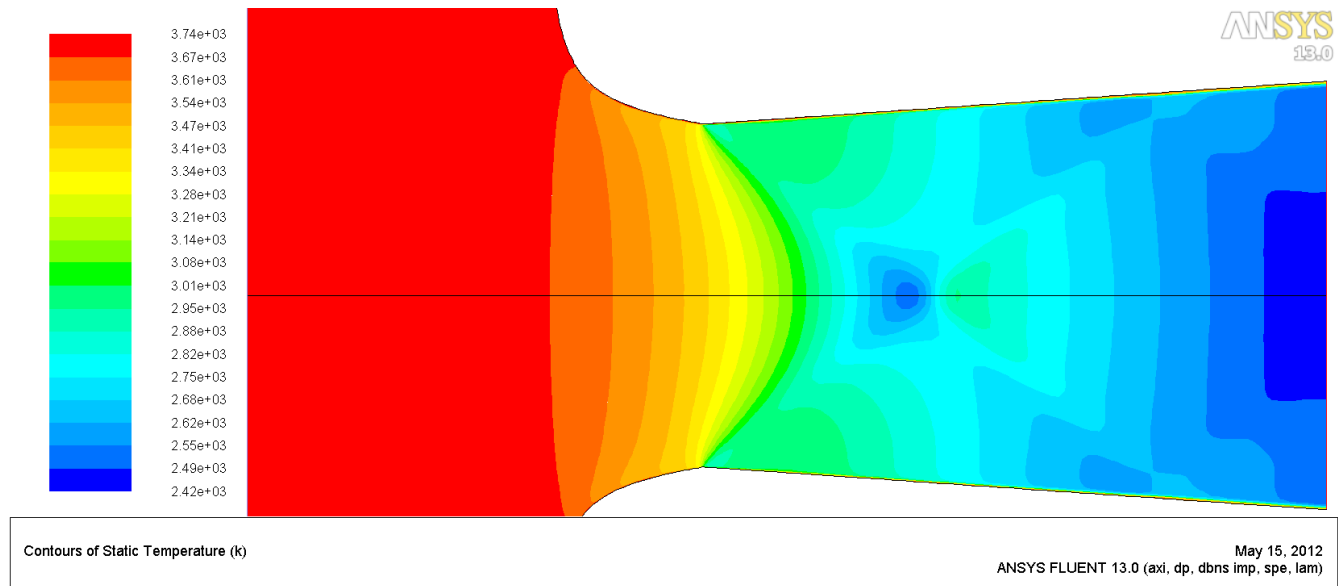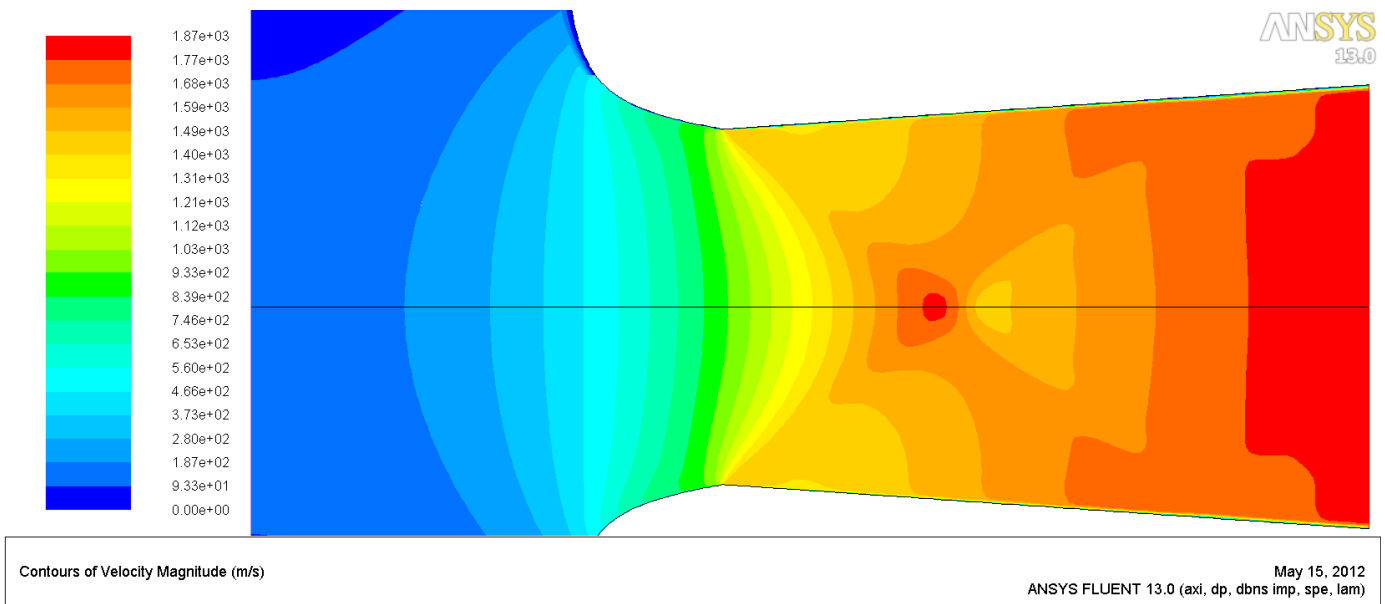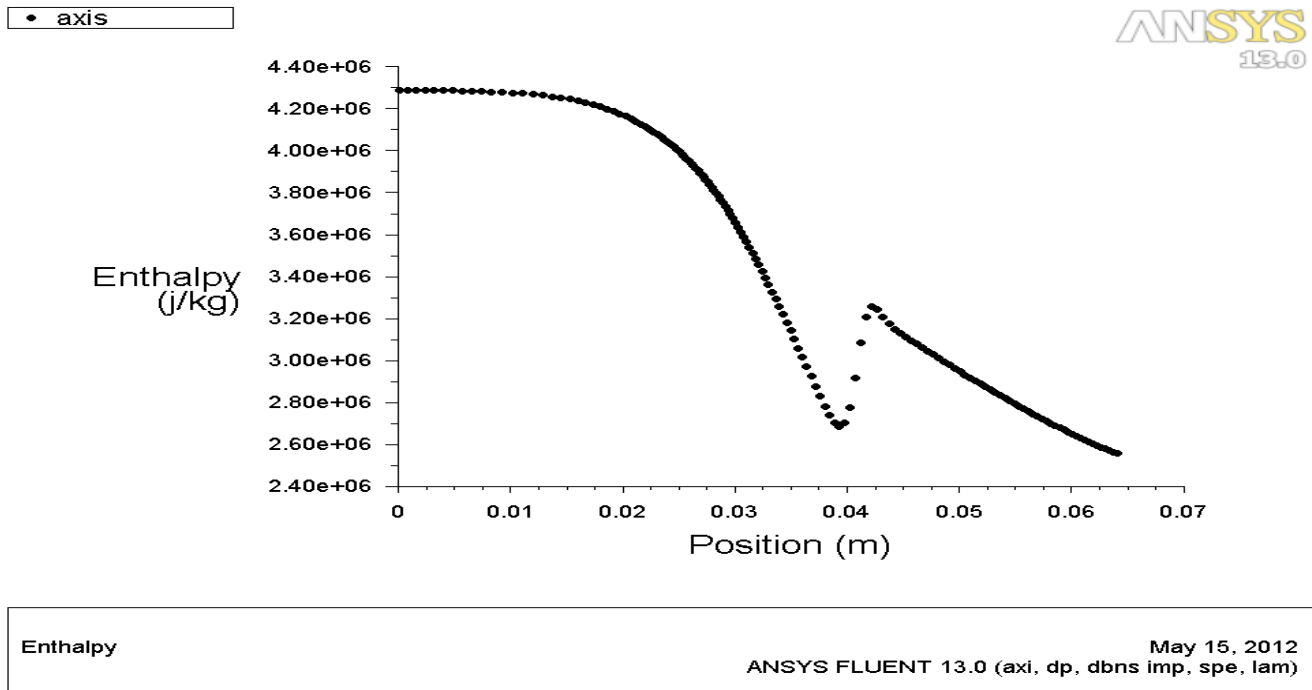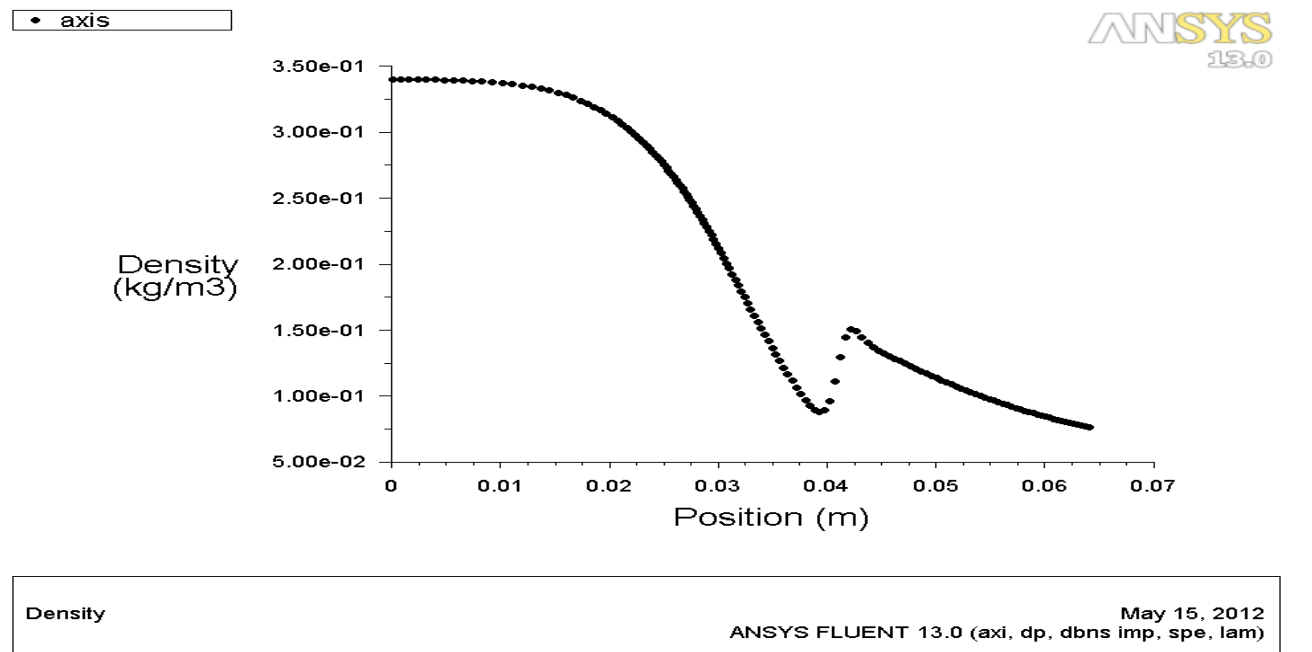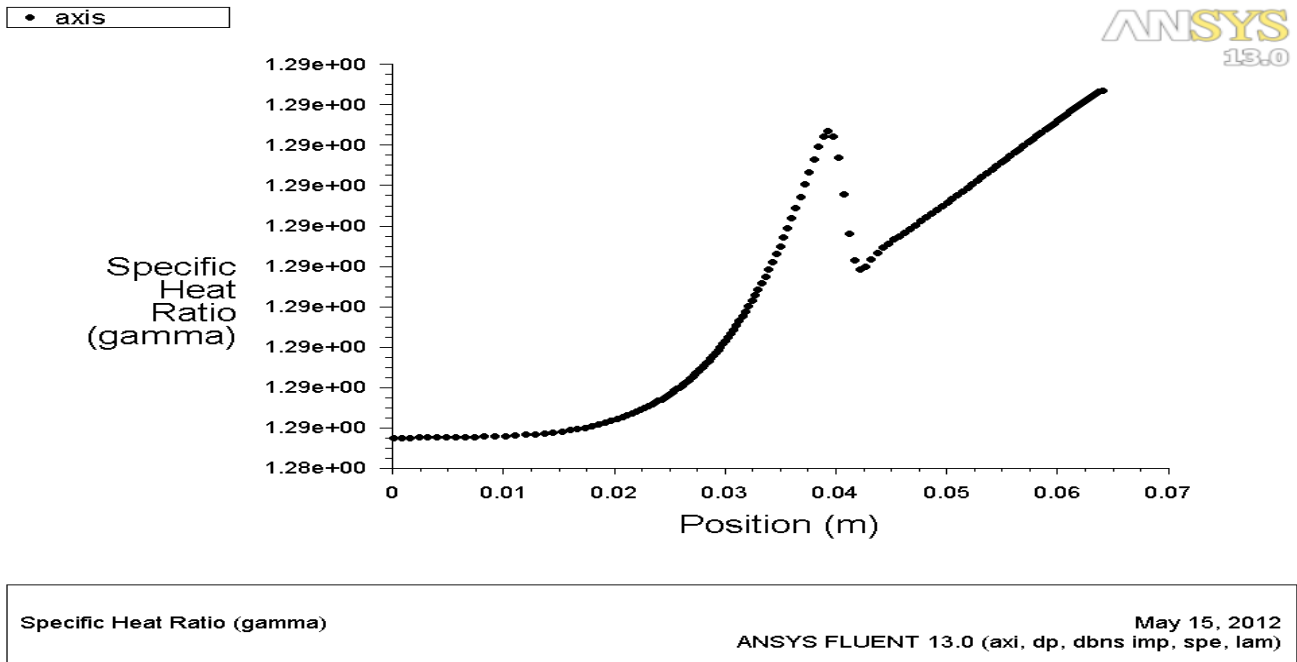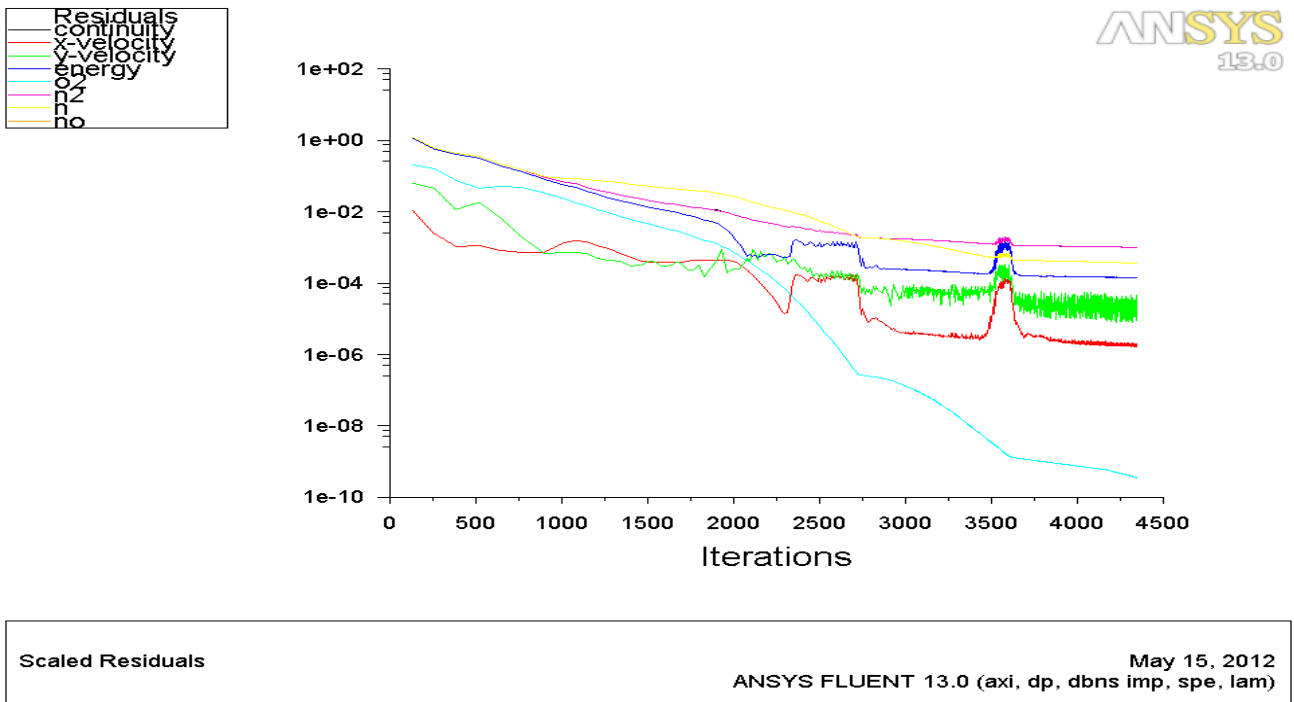**Fig A-3.4.22**: Scaled Residuals obtained from the CFD model of the nozzle for N2-case-3 using fine-2 grid.

A-4 Boundary Layer Analysis- CFD

4.1 Velocity profile analysis

Table A-4.1: Velocity magnitude measured in m/s from the nozzle wall at the exit in the y direction.

Air	Y in mm	N2-case1	N2-case-2	N2-case-3
0	0	0	0	0
6.85202	0.0002	4.00979	3.97336	2.26445
15.446	0.0005	9.10273	9.01944	5.1577
26.1909	0.0008	15.5684	15.4254	8.86002
39.5582	0.0012	23.7703	23.5518	13.6055
56.0855	0.0018	34.1633	33.85	19.6982
76.3639	0.0025	47.3139	46.8821	27.5343
101.012	0.0034	63.9219	63.3435	37.6312
130.637	0.0045	84.8453	84.0877	50.6655
165.78	0.006	111.124	110.151	67.5204
206.837	0.0079	144.003	142.777	89.3412
254.011	0.0103	184.948	183.436	117.645
307.384	0.0133	235.661	233.84	154.452
367.136	0.0172	298.068	295.944	202.372
433.934	0.0223	374.314	371.938	264.606
509.333	0.0287	466.704	464.206	344.779
595.84	0.0369	577.524	575.147	446.462
696.239	0.0474	708.646	706.767	572.214
812.136	0.0608	860.988	860.113	722.868
941.796	0.078	1033.58	1034.28	897.005
1079.39	0.1	1222.2	1225.01	1089.9
1214.08	0.1281	1417.58	1422.91	1292.4
1327.81	0.1641	1601.47	1609.61	1487.12
1402.7	0.2101	1746.28	1757.27	1646.19
1436.33	0.269	1831.51	1844.76	1744.98
1445.03	0.3443	1863.98	1878.39	1785.65
1446.15	0.4406	1870.89	1885.6	1795.58
1445.8	0.5637	1872.2	1886.96	1798.04
1445.4	0.7213	1872.88	1887.63	1799.92
1444.9	0.9228	1873.44	1888.2	1801.71
1444.2	1.1806	1873.66	1888.42	1802.96
1443.38	1.4384	1873.53	1888.29	1803.42
1442.42	1.703	1873.25	1888.01	1803.41
1441.38	1.9744	1872.97	1887.73	1803.25

4.2 Temperature profile analysis

Table A-4.2: Static Temperature measured in K from the nozzle wall at the exit in the y direction.

Air	Y in mm	N2-case1	N2-case-2	N2-case-3
2372.59	0	3884.65	3826.51	3340.08
2372.23	0.0002	3884.65	3826.51	3340.08
2373.23	0.0005	3884.72	3826.65	3340.28
2373.38	0.0008	3884.82	3826.91	3340.64
2373.27	0.0012	3885.03	3827.39	3341.32
2372.85	0.0018	3885.33	3828.16	3342.43
2372.02	0.0025	3885.74	3829.26	3344.07
2370.63	0.0034	3886.25	3830.77	3346.4
2368.43	0.0045	3886.82	3832.73	3349.63
2365.09	0.006	3886.05	3835.18	3354.02
2360.21	0.0079	3884.84	3838.08	3359.95
2353.32	0.0103	3883.91	3841.28	3367.78
2343.94	0.0133	3881.23	3844.42	3377.66
2331.44	0.0172	3875.51	3844.86	3389.18
2314.9	0.0223	3864.71	3841.72	3401.01
2292.65	0.0287	3845.77	3833.55	3410.69
2261.83	0.0369	3814.29	3814.49	3414.04
2218.39	0.0474	3764.35	3777.99	3404.72
2157.74	0.0608	3688.76	3715.79	3374.07
2077	0.078	3580.28	3619.03	3311.85
1976.86	0.1	3434.54	3481.68	3208.91
1864.14	0.1281	3254.37	3305.67	3062.25
1755.83	0.1641	3057.26	3108.83	2884.5
1676.64	0.2101	2881.61	2930.59	2710.8
1637.79	0.269	2768.56	2814.47	2588.58
1626.07	0.3443	2721.83	2766.15	2534.05
1624.71	0.4406	2710.03	2753.85	2518.85
1626	0.5637	2707.7	2751.41	2514.67
1627.57	0.7213	2706.73	2750.43	2511.95
1629.06	0.9228	2705.99	2749.68	2509.38
1629.96	1.1806	2705.76	2749.45	2507.63
1629.86	1.4384	2705.97	2749.67	2506.9
1628.75	1.703	2706.4	2750.1	2506.86

Note: The cells marked in yellow indicate the boundary layer edge at which the local velocity and the local static temperature reach 99% of their respective freestream values.